University of Venda
School of Environmental Sciences
Department of Mining and Environmental Geology

Geology and Geochemistry of Muyexe Magnesite Deposit, Giyani Greenstone Belt, Limpopo Province, South Africa

by

Chauke Tiyani

Student Number: 11622901

A Master's Dissertation Submitted to the Department of Mining and Environmental Geology in the School of Environmental Sciences, in Fulfilment of the Requirements for the Degree of Master of Earth Sciences in Mining and Environmental Geology

Supervisor: Emeritus Professor J.S. Ogola
Department of Mining and Environmental Geology
School of Environmental Sciences, University of Venda

Co-supervisor: Dr. H.R. Mundalamo
Department of Mining and Environmental Geology
School of Environmental Sciences, University of Venda

March 2020

DECLARATION

I, Chauke Tiyani, declare that this research dissertation titled “Geology and Geochemistry of Muyexe Magnesite Deposit, Giyani Greenstone Belt, Limpopo Province, South Africa” is my own work and it has never been submitted for a degree at this or any other university and all reference materials contained therein have been duly acknowledged.

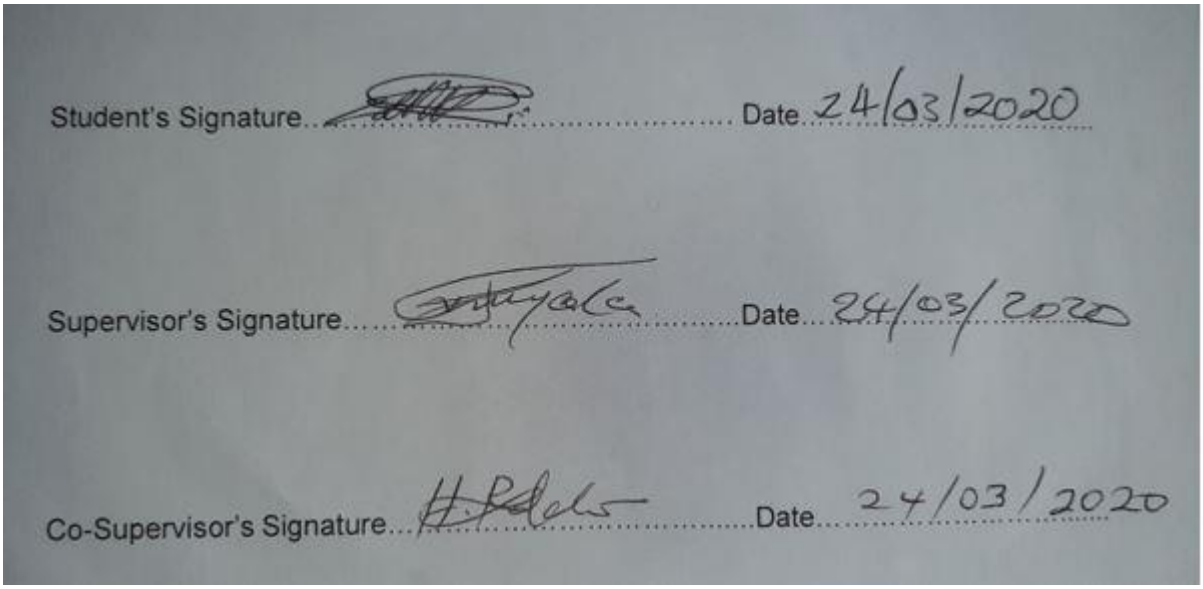

DEDICATION

This dissertation is dedicated to my family. They always believed in me and encouraged me to give my best in education. I believe they are highly honoured to see this work that I did.

ACKNOWLEDGEMENTS

Firstly, I would like to thank my supervisor Emeritus Prof. J.S. Ogola and co-supervisor Dr. H.R. Mundalamo for their support, patience, and meticulous supervision. Without their suggestions and comments, the accomplishment of this dissertation would have been unmanageable. Their guidance greatly helped me conducting this research and writing of this Dissertation. I could not have imagined having better supervisors and mentors for my master's study.

I am grateful to the almighty God for sheltering me and bestowing in me the skills and understanding to pursue studies in geology up to this level.

I would also like to thank my family and friends, my mother Rose Ribisi and my brothers Musa Evans Shivambe and Ockkie Vincent Chauke, my friends, Maringa Matimu, Khosa Hoxani and Nghonyama Ashy for all the support they have provided during executing this work until its completion.

Importantly, I would like to thank the people from the Muyexe magnesite mine. Mine manager Mr. John Lerm and Operations manager Mr. Ivan Freeman and ISCOSA (owner of the mine), for allowing me access to the mine to execute my study. I would also like to thank the Muyexe tribal council for allowing me access to their land during fieldwork.

I would also like to give thanks to the University of Venda, Department of Mining and Environmental Geology for allowing me to use their equipment and their laboratory with assistance from Mr. C. Muzerengi and Mr. Thahala Moses. I would also like to thank Sebabi Orienda form the University of Johannesburg, Spectrum Analytical Facility for assistance in XRD analysis and retrieval.

My special appreciation to my fellow masters and doctorate colleagues under the supervision of Emeritus Prof J.S. Ogola and Dr. H.R. Mundalamo, for their contribution enthusiasm and support in providing relevant assistance and help to complete this study.

The following sponsor is acknowledged for the funding contribution in making this research successful; University of Venda's Research and Publication Committee (RPC).

ABSTRACT

Muyexe magnesite deposit is situated in the Giyani Greenstone Belt in South Africa. Despite mining activities currently taking place at Muyexe magnesite deposit, little information is available about the geology and geochemistry of the deposit. This has resulted in a gap of information about the nature and character of magnesite, namely; its geology, mineralogy, geochemistry and mode of occurrence. Consequently, there is a need for further investigation of the magnesite deposit. The main objective of the study was to establish the geology and geochemistry of the Muyexe magnesite deposit and to ascertain its mode of occurrence. Further work involved undertaking detailed geological mapping, magnesite and rock sampling for petrographic and geochemical studies using petrographic microscopy and X-ray fluorescence spectrometry and identification of minerals in rocks and magnesite through X-ray diffractometry.

A total of 20 magnesite and 4 host rock samples were collected from the Muyexe magnesite deposit. Furthermore, 62 rock samples were collected during geological field mapping of which 16 representative samples were selected for further analysis. X-ray fluorescence spectrometry was conducted on all selected samples of magnesite and rocks. XRD analysis was conducted on 12 rocks and 2 magnesite samples. Mineralogy of the rocks was also confirmed using petrographic microscopy.

Detailed geological map of the Muyexe area revealed that the area is dominated by metamorphic ultramafic and mafic rocks. Basalt and peridotite are intrusions within the rock. The serpentinites and peridotites were found to be the source rock for magnesite mineralization, while the peridotite is the source rock for serpentinites rocks. XRD analysis revealed that magnesite in the Muyexe magnesite deposit is associated with silica and dolomite, while XRF data revealed that the following major oxides are present in magnesite as impurities; silicon dioxide (SiO_2), calcium oxide (CaO), and iron oxide (Fe_2O_3). These oxides reduce the quality of magnesite, thus, their removal is necessary during processing. Magnesite of this deposit was found to be of good quality, with an average value of 54.02 wt. %. Magnesite at Muyexe was formed due to precipitation of Mg^{2+} along the fractures of serpentinites and peridotites due to CO_2rich hydrothermal fluids. Magnesite occurs as a cryptocrystalline of the Kraubath-type.

Keywords: Muyexe magnesite deposit, geological mapping, mode of occurrence.

TABLE OF CONTENTS

DECLARATION i

DEDICATION ii

ACKNOWLEDGEMENTS iii

ABSTRACT iv

TABLE OF CONTENTS v

LIST OF FIGURES ix

LIST OF TABLES xii

ACRONYMS AND ABBREVIATIONS xiii

CHAPTER ONE: INTRODUCTION 1

1.1 Background 1

1.2 Study Area 2

1.2.1 Location 2

1.2.3 Topography and Drainage 4

1.2.4 Soil and Vegetation 4

1.2.5 Land Use 5

1.3 Problem Statement 5

1.4 Justification 5

1.5 Research Questions 6

1.6 Objectives 6

CHAPTER TWO: LITERATURE REVIEW 7

2.1 Geological Setting of Giyani Greenstone Belt 7

2.1.2 Khavagari Branch (Local Geology) 9
2.1.2 Lwaji Branch 10
2.1 Magnesite as a Mineral 11
2.2 Classification of Magnesite Deposit Based on Geology 12
2.2.1 Ultramafic Associated 12
2.2.2 Magnesite Strata-bound in the Sedimentary Environment 13
2.3 Classification of Magnesite Based on Physical Form 13
2.3.1 Crystalline Magnesite Deposits 13
2.3.2 Cryptocrystalline Magnesite Deposits 15
2.4 Genesis of Magnesite Deposit 17
2.4.1 Magnesite Genesis in Ultramafic 18
2.5 Magnesite in South Africa 20
2.7 Economic Importance of Magnesite 23
2.7.1 Magnesite as a Source of Magnesia 25
2.7.2 Caustic-Calcined Magnesia 25
2.7.3 Sinter or Dead-Burned Magnesia 25
2.8 Processing of Magnesite 26
2.9 Quality and Grade of Magnesite 28
2.10 Variation Diagrams for Classification of Rocks 28
2.10.1 Harker Diagram 29
2.10.2 MgO vs Major Oxides 29
2.10.3 Total Alkali-Silica Diagram 30
2.10.4 Ternary Plot 31
2.11 Analytical Techniques for Magnesite Analysis 31
2.11.1 X-ray Fluorescence Spectrometry 31
2.11.2 Inductive Coupled Plasma Emission Spectrometry 33
2.11.3 Atomic Absorption Spectrometry 33

2.11.4 X-ray Diffractometry 34
CHAPTER THREE: MATERIALS AND METHODS 35
3.1 Preliminary Work 36
3.1.1 Desktop Study 36
3.1.2 Reconnaissance Survey 36
3.2 Fieldwork 36
3.2.1 Geological Mapping of Muyexe Area 38
3.2.2 Sampling 41
3.3 Laboratory Work 42
3.3.1 Sample Preparation 42
3.3.2 Sample Analysis 46
3.3.2.1 Petrographic Study 47
3.3.2.2 Loss of Ignition Test 63
3.3.2.3 Geochemical Analysis 65
CHAPTER 4: DATA ANALYSIS AND INTERPRETATION 70
4.1 Geological Map and Cross-Section of Muyexe Area 70
4.3 Mineralogy of Rocks at Muyexe 72
4.4 Whole Rock Geochemistry 74
4.4.3 Trace Elements 76
4.4.4 Rare Earth Elements 82
4.5 Classifications of Rocks and Provenance 85
4.5.1 Alteration Box Plot 85
4.5.2 Classification of Rocks and Magma Type 87
4.6 Geochemistry of Magnesite 90
4.6.1 Major Oxide Geochemistry 90

4.6.2 Trace Elements Geochemistry 92
4.6.3 Rare Earth Elements 100
4.6.4 Mineralogy of Magnesite at Muyexe 102
4.7 Quality and Grade of Magnesite at Muyexe Area 103

CHAPTER 5: DISCUSSIONS, CONCLUSIONS AND RECOMMENDATIONS 105
5.1 Discussions 105
5.1.1 Geological Evidence 105
5.1.2 Petrographic and Mineralogical Evidence 106
5.1.3 Geochemical Evidence 108
5.1.4 Genetic Model 110
5.2 Conclusions 115
5.3 Recommendations 116

REFERENCES 117

APPENDICES 133

LIST OF FIGURES

Figure 1.1: Location of the study area 3
Figure 1.2: Average rainfall measured at Giyani Weather Station 3
Figure 1.3: Common vegetation (Mopani trees) within the Study Area. 4
Figure 2.1: General geology of the Giyani Greenstone Belt 9
Figure 2.2: Lithostratigraphy of the Khavagari branch/arm 10
Figure 2.3: Lithostratigraphy of the Lwaji branch/arm 11
Figure 2.4: Types of cryptocrystalline magnesite deposits 20
Figure 2.5: Magnesite field of the Republic of South Africa 22
Figure 2.6: Global sources of magnesite and producing countries 22
Figure 2.7: Worldwide production of magnesia from magnesite 26

Figure 2.8: Fused magnesia process flow chart 27
Figure 2.9: The Total Alkali vs SiO_2 diagram 30
Figure 2.10: Ternary diagram for tectonic discrimination of igneous rocks..... 31
Figure 2.11: Basic operation of XRD 34
Figure 3.1: Flow chart showing the stages and sequence of the work 35
Figure 3.2: Equipment and implements that were used during fieldwork: 37
Figure 3.3: Topographical map (Base map) 39
Figure 3.4: Sampling of magnesite veins at the mine 41
Figure 3.5: Laboratory equipment used for the preparation of samples 44
Figure 3.6: Laboratory equipment used for thin preparation 46
Figure 3.7: Olympus BX-50 petrographic microscope set-up 47
Figure 3.8: A photograph of: A-Hornblende chlorite schist outcrop 48
Figure 3.9: Photomicrograph of fine-grained hornblende chlorite schist 49
Figure 3.10: A photograph of: A-Quartzite outcrop 50
Figure 3.11: Photomicrograph of quartzite 50
Figure 3.12: A photograph of a: A-Banded iron formation 51
Figure 3.13: Photomicrograph of banded iron formation rock 51
Figure 3.14: A photograph of: A-Amphibolite 52
Figure 3.15: Photomicrograph of amphibolite rock 52
Figure 3.16: A photograph of: A-Fresh serpentinite rock outcrop 53
Figure 3.17: Photomicrograph of fresh serpentinite rock 54
Figure 3.18: Photomicrograph of altered serpentinite rock 54
Figure 3.19: A photograph of: A-Talc schist 55
Figure 3.20: Photomicrograph of talc schist rock 55
Figure 3.21: A photograph of: A-Basalt outcrop 56
Figure 3.22: Photomicrograph of basalt rock 57
Figure 3.23: A photograph of: A-Pillowed amphibolite rock 58
Figure 3.24: Photomicrograph of pillowed amphibolite 58
Figure 3.25: A photograph of: A-Weathered serpentinite schist 59
Figure 3.26: A photograph of: A-Birbirite outcrop 60
Figure 3.27: Photomicrograph of birbirite rock 60
Figure 3.28: A photograph of: A-Altered peridotite outcrop 61
Figure 3.29: Photomicrograph of altered peridotite 62

Figure 3.30: Photomicrograph of peridotite 62
Figure 3.31: Laboratory equipment and tools used for loss of ignition test..... 63
Figure 3.32: A Ranger S2 XRF machine used for geochemical analysis. 66
Figure 4.1: Geological map of the Muyexe area. 71
Figure 4.2: Cross-section view of the Muyexe area. 71
Figure 4.3: Histogram plot showing Major oxides in rock samples 75
Figure 4.4: Histogram plot showing Large Ion Lithophile Elements in rock samples 77
Figure 4.5: Histogram plot showing High Field Strength Elements in rock samples . 79
Figure 4.6: Histogram plot showing Transition Trace Elements in rock samples. 81
Figure 4.7: Trace elements normalised to primitive upper mantle (PUM) 82
Figure 4.8: Histogram plot showing Rare Earth Elements in rock samples 83
Figure 4.9: Spider diagram plot of normalised REE in Rocks 84
Figure 4.10: Alteration box plot of rock samples 86
Figure 4.11: Magma classification AFM diagram 88
Figure 4.12: Total alkali-silica used to determine magma type 89
Figure 4.13: Magma type Nb/Y-Zr/Ti diagram 90
Figure 4.14: Concentration of major oxides and LOI in magnesite samples 91
Figure 4.15: Distribution of Ti in magnesite from the study area 94
Figure 4.16: Distribution of Sr in magnesite from the study area 95
Figure 4.17: Distribution of Ba in magnesite from the study area 96
Figure 4.18: Distribution of Fe in magnesite from the study area 97
Figure 4.19: Distribution of Mn in magnesite from the study area 97
Figure 4.20: Distribution of Cr, Ni and Co in magnesite from the study area 99
Figure 4.21: Trace elements normalised to primitive upper mantle (PUM) 100
Figure 4.22: Spider diagram plot of normalised REE in magnesite 101
Figure 4.23: Histogram showing the mineralogy of magnesite. 102
Figure 4.24: Pie chart illustrating the average concentration of major constituents 104
Figure 5.1: Magnesite veins in different depositional environments at Muyexe 107
Figure 5.2: Cryptocrystalline magnesite texture 107

LIST OF TABLES

Table 2.1: Classification of magnesite deposits based on geology 16
Table 2.2: Comparison of Veitsch type and Kraubath-type models of magnesite 17
Table 2.3: Generalized industrial application of magnesite 24

Table 3.1: Coordinates and elevation of sampled rocks 40
Table 3.2: Characteristics of sampled magnesite and host rocks 42
Table 3.3: Loss of ignition test results 64
Table 3.4: XRF results of major oxides in weight percent (wt. %) 67
Table 3.5: XRF results of selected trace elements in part per million (ppm) 68
Table 3.6: XRD results for the mineralogical composition of magnesite..... 68
Table 3.7: XRD results of the mineralogy of rocks 69
Table 4.1: Statistical analysis of major oxides 75
Table 4.2: Statistical analysis of major oxide and LOI in magnesite 91
Table 4.3: Statistical analysis of trace element data in magnesite 93

ACRONYMS AND ABBREVIATIONS

AAS	: Atomic Absorption Spectrometry
AFM	: Alkalis FeO*total* Magnesium Oxide
Al	: Aluminium
Al_2O_3	: Aluminium oxide
As	: Arsenic
BIF	: Banded Iron Formation
Ca	: Calcium
Cd	: Cadmium
Co	: Cobalt
Cr	: Chromium
DMR	: Department of Mineral Resources
EU	: European Union
Fe	: Iron
Fe_2O_3	: Iron oxide
g	: Gram
GGB	: Giyani Greenstone Belt

GPS : Global Positioning System

Hf : Hafnium

HFSE : High Field Strength Elements

HRSZ : Hout River Shear Zone

K : Potassium

K_2O : Potassium Oxide

Kg : Kilogram

km : Kilometer

La : Lanthanum

LILE : Large Ion Lithophile Elements

LMC : Local Municipality LOI

: Loss of Ingestion

m : Meter

M1 : Mine Site 1

M2 : Mine Site 2

Mg : Magnesium

$MgCO_3$: Magnesite

MgO : Magnesium Oxide

Mn : Manganese

Na : Sodium

Nb : Niobium

Ni : Nickel

P_2O_5 : Potassium Oxide

PPL : Plane-Polarised Light

PUM	: Primitive Upper Mantle
REE	: Rare Earth Elements
Sc	: Scandium
Si	: Silica
SiO_2	: Silica Dioxide
TAS	: Total Alkali Silica
Th	: Thorium
Ti	: Titanium
TTE	: Transition Trace Elements
U	: Uranium
UJ	: University of Johannesburg
Univen	: University of Venda
US$	: United State Dollar
USGS	: United State Geological Society
V	: Vanadium
XPL	: Cross Polarised Light
XRD	: X-ray Diffractometry
XRF	: X-ray Fluorescence
Y	: Yttrium
Zr	: Zirconium

CHAPTER ONE: INTRODUCTION

1.1 Background

Magnesite ($MgCO_3$) is a natural form of magnesium carbonate and a major source of commercial production of magnesium compounds and products (Deer *et al.,* 1992). Theoretically, pure magnesite contains 47.8% MgO and 52.2% CO_2 (Pressacco *et al.,* 2010), but pure magnesite is rare to find in nature (Bashir *et al.,* 2008a). Magnesite falls under the calcite group and occurs as a primary mineral in igneous or sedimentary rocks. Its hardness is 3.5-4.5, with perfect cleavage. Magnesite deposits may occur either as crystalline or cryptocrystalline, with a range of colours that include white, grey, yellow, brown, orange, light pink and even colourless (Strydom, 1998). The mineral magnesite was formerly the source of nearly all magnesia but now shares that with dolomite, brucite, olivine and various sea salts (Birch and Wicken, 1949).

Magnesite is an important mineral in modern industries because magnesite and magnesium compounds are used in a variety of products. There is a lot of possible application of magnesite in all industries, including use in cell phones, cars, aircraft, computers, chemicals and in the agricultural sector (Harben, 2008). Magnesite is also used in the refractory industry of steel and iron. It is also used in refractories in the form of dead-burned magnesia, fused magnesia, and caustic calcined magnesia (U.S. Geological Survey, 2018).

The world demand for magnesite has drastically increased from the year 2000 and it is expected to rise further sharply within the present decade. This is because of its utilisation in the Mg-metal industries and automotive components as, slug conditioner and advance value-added material. Most magnesite resources are mainly used to produce magnesia refractory with low value-added products. Therefore, more effective utilisation of magnesite resources and the development of high value-added products are generally preferred (Wang *et al.,* 2011). A good quality magnesite ore used in different industrial applications consists of 46.6% MgO, 49.9% CO_2, 0.70% SiO_2, 1.35% CaO, 0.85% Fe_2O_3 and AL_2O_3 (Harben and Bates, 1990; Bashir, 2008).

Magnesite deposits are widely deposited around the world, but unevenly. Most of the global magnesite reserves are located in Russia. Other major holders of magnesite reserves include China, North Korea, Austria, Turkey, and Greece, ranked according to the size of their reserves from large to small (U.S. Geological Survey, 2018). The

uneven geological distribution of magnesite means that China has emerged as the dominant producer of magnesite and magnesium compounds and this has affected profitability and market shares of higher-cost producers of magnesite in the world (Kramer, 2005; Indian Mineral Yearbook, 2012). China, Turkey, Russia, and Brazil are among the top producers of magnesite globally (Indian Mineral Yearbook, 2012; DMR, 2013; U.S. Geological Survey, 2018).

Muyexe magnesite mine is one of the mines producing magnesite as its main commodity and currently in operation in South Africa. The other mines include Strathmore mine in Mpumalanga Province and Syferfontein mine in Limpopo Province (DMR, 2013). All these mines apply surface mining method to extract magnesite from the earth (Ratlabala, 2003). In South Africa, magnesite is also produced as a byproduct of other minerals.

The Muyexe magnesite deposit is currently being exploited for its resources and benefiting the economy of South Africa. This has resulted in the deposit being economically important in South Africa, however, there is still a lot of unknown information about its nature and character despite its economic importance. The current study, therefore, focused on the investigation of the geology and geochemistry of the deposit so as to ascertain the mode of formation.

1.2 Study Area

1.2.1 Location

The Muyexe magnesite deposit is located near the Muyexe village, under The Greater Giyani Municipality, in Limpopo Province, South Africa. It is situated about 30 km northeast of Giyani town and about 2 km west of Kruger National Park. It is within the Giyani Greenstone Belt. Geographically, the mine lies at approximately 30°56’13.57’’ E and 23°11’46.14’’ S. (Fig. 1.1).

1.2.2 Climate

The study area is characterized by a warm, dry, and subtropical climate. The average annual rainfall is between 200 – 400 ml per year, with most of the rainfall occurring during mid-summer. Lowest rainfall (0 ml) occurs during June and the highest rainfall (93 ml) occurs during January (Fig. 1.2) (Greater Giyani LMC, 2018-2019). The average mid-day temperatures in greater Giyani ranges between 22^0C to 33^0C, with

June being the coldest month (below 0^0C) and December being the hottest month (33^0C) (Greater Giyani LMC, 2018-2019).

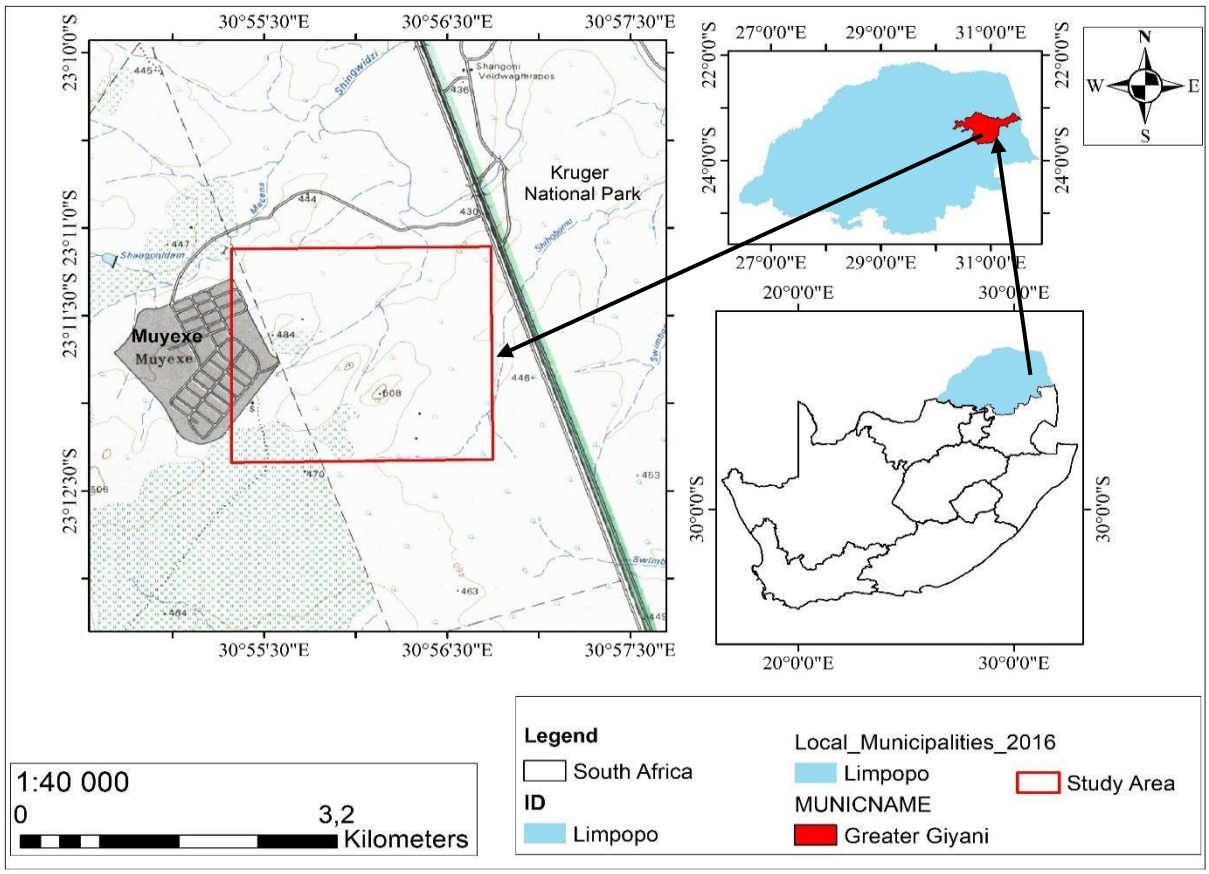

Figure 1.1: Location of the study area (ArcGIS Esri, 2018; Ramovha, 2016).

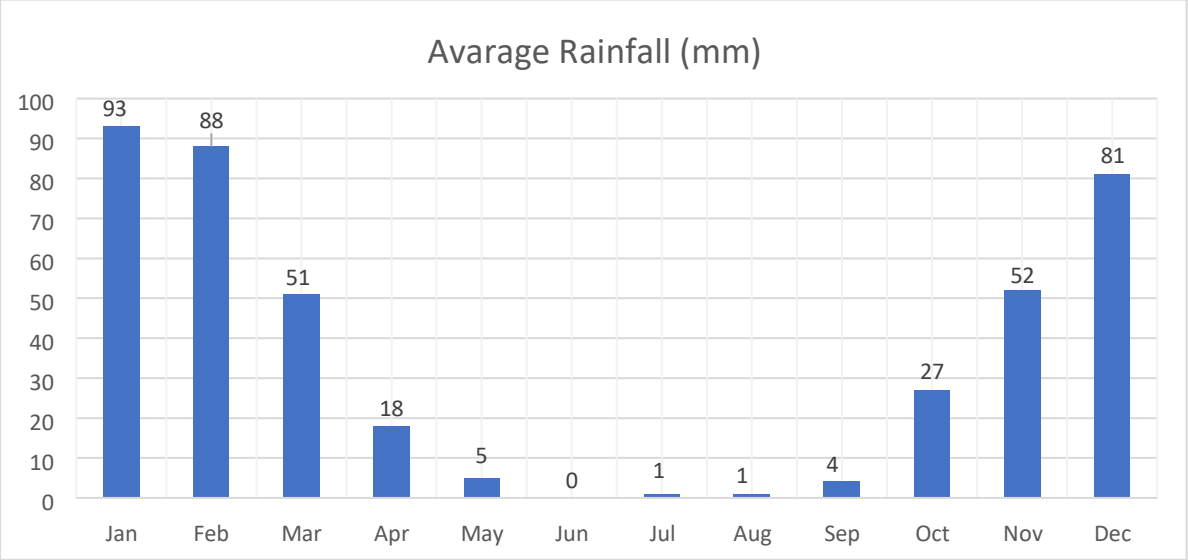

Figure 1.2: Average rainfall measured at Giyani Weather Station (South African Weather Station, 2019).

1.2.3 Topography and Drainage

The area is chiefly characterized by flat topography, with discontinuous hills and ridges which make it easier for development to be implemented. Most of the hills in the area consist mainly of a highly resistant quartzite which was instrumental in shaping the present morphology. The altitude ranges from 440 m to 800 m above sea level in some areas (Greater Giyani LMC, 2018-2019). It is within the Levubu-Letaba river catchment, but the study area is mostly drained by the Shigwedzi river and its tributaries. The flat surface has caused the area to be prone to soil erosion during heavy rainfall which mostly occurs during mid-summer.

1.2.4 Soil and Vegetation

The predominating soil type in the study area is moderately leached loamy soil. There is sandy colluvium at the foot of the hills grading into shallow, reddish coloured sandloam soil. The vegetation in the area is classified as the low veld Mopani and veld savannahs (Rutherford *et al.,* 2006), characterized by a mixture of trees, shrubs, and grasses (Fig. 1.3). The region is covered by bushes and trees, the most common among the trees being Copaifera Mopani, Acacia, Marula (*Scterocayo Caffra*) and occasionally baobab (*Adansonia Digitata)* (Rutherford *et al.,* 2006).

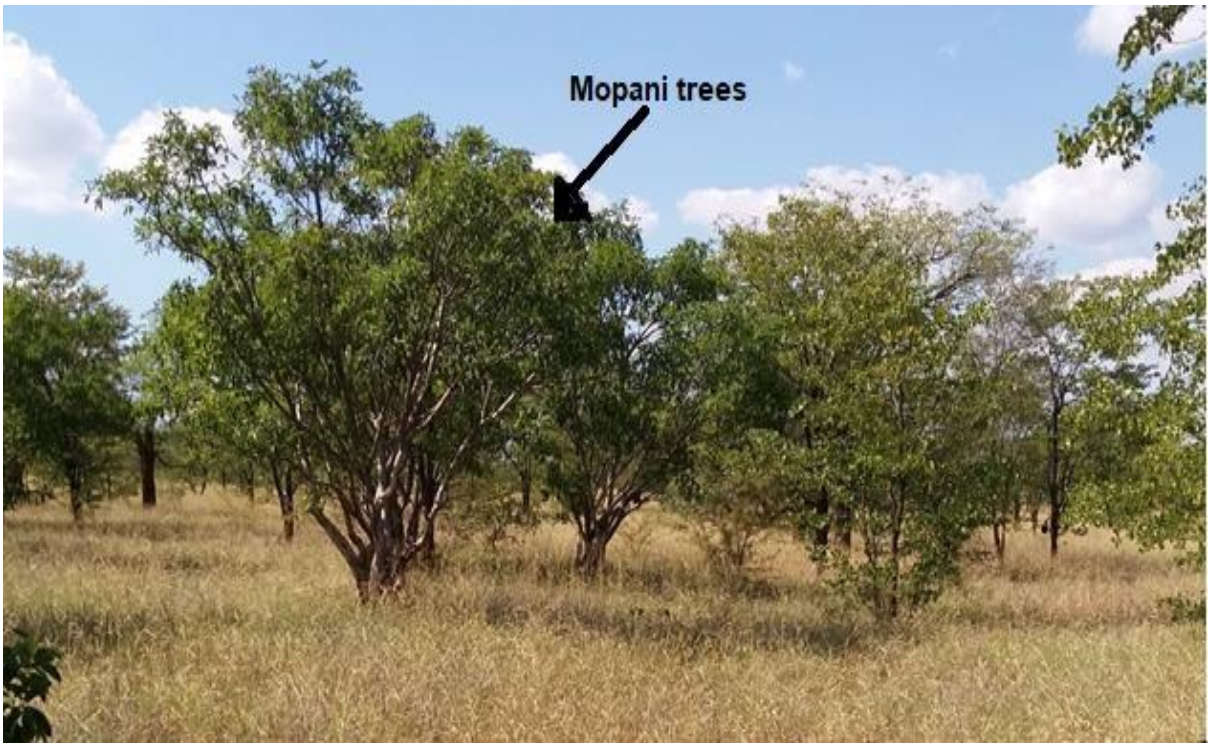

Figure 1.3: Common vegetation (Mopani trees) within the Study Area.

1.2.5 Land Use

The main land use in the area is mostly agricultural and mining activities. Mining activities include the mining of magnesite by the Muyexe Mining Company and sand mining along the Shingwedzi River. The area also consists of game reserves such as the Kruger National Park and Rooikat Nature Reserve. A gate to Kruger National Park is planned in the area and the gate will be known as the Shangoni gate.

1.3 Problem Statement

Despite mining activities currently taking place at Muyexe magnesite deposit, little information is available about the geology and geochemistry of the deposit. This has resulted in a gap of information about the nature and character of magnesite, namely; its geology, mineralogy, geochemistry and mode of occurrence. Consequently, there is a need for further investigation of the magnesite deposit.

1.4 Justification

In modern industries, magnesite has become an important value-added material. According to Bashir *et al.* (2008a), magnesite is used in many products including refractories which are consumed primarily by the iron and steel industry. Magnesite compounds are also used in a variety of material which includes cement, rubber, fertilizers, insulators, fluxes, paper, animal feed, chemicals, and pharmaceuticals. Magnesite is the primary source of magnesia (MgO), which is mainly used in agriculture, mineral processing, paper manufacture, and refractory industries. Magnesia is also used to produce magnesium (Mg), a light metal widely used in the aerospace, automotive and electronics industries (Harben, 2008). Both magnesite and magnesium are included on the EU's latest list of 20 critical materials (European Union, 2014). This has resulted in magnesium being an important mineral in modern industries.

Till now, a limited amount of geological work has been carried out on the magnesite deposits of the area. The initial work only shows major components analysis of the deposit. Considering the importance of magnesite and its value-added material in the modern world, an integrated geological approach comprising of mineralogy, petrography, and geochemistry will be adapted to elaborate on the geology and geochemistry of magnesite deposit and associated host rocks.

The economic utilisation of magnesite is largely dependent upon the physical properties of minerals. The price of fused magnesia depends significantly on its quality. In April 2017, the price of fused magnesia (96%) was around US$360-390 per ton, whereas 97.5% material was US$495-550 per ton and the highest quality fused magnesia with MgO content of greater than 99% was around US$1200-1400 per ton (Li and Ghilotti, 2017). Hence, there is a need to conduct scientific research on the quality of magnesite at the Muyexe magnesite deposit, as this parameter may influence its economic utilisation and price. The information obtained from this study will assist the mining company, industry and the scientific community better understand the nature and value of magnesite at this deposit.

1.5 Research Questions

- What is the geology of the Muyexe magnesite?
- What is the nature and type of rocks associated with magnesite at Muyexe area?
- What is the geochemistry of magnesite at Muyexe area?
- What is the quality of the Muyexe magnesite?
- What is the mode of occurrence of the Muyexe magnesite?

1.6 Objectives

The main objective of the study was to establish the geology and geochemistry of the Muyexe magnesite deposit and to ascertain its mode of occurrence.

The specific objectives were to:

- Undertake detailed geological mapping of the Muyexe magnesite;
- Undertake rock sampling for petrographic and whole-rock geochemical studies using a petrographic microscopy and X-ray fluorescence spectrometry;
- Undertake magnesite sampling for geochemical analysis using X-ray fluorescence spectrometry; and
- Identification of any mineral impurities in magnesite through X-ray diffractometry.

CHAPTER TWO: LITERATURE REVIEW

2.1 Geological Setting of Giyani Greenstone Belt

The Muyexe magnesite deposit is located within the Giyani Greenstone Belt (GGB).

The Giyani Greenstone Belt (GGB) is one of the major greenstone belts located in the Limpopo province. It is an Achaean Greenstone Belt situated on the Northern Kaapvaal Craton immediately adjacent to the Hout River Shear Zone (HRSZ) (Kramers *et al.,* 2014) and close to the contact with the Limpopo Mobile Belt. Like any other greenstone belts in the country, such as Murchison, Pietersburg, and Barberton, the Giyani Greenstone Belt is Archean in age and its lithological succession has been designated as the Giyani Group of the Swazian Super-group (SACS, 1980).

The Archean rocks of the Kaapvaal Craton are dominated by 3.63 Ga granitoid gneisses (Armstrong *et al.,* 1990) and various 2.65 Ga granitoids (Barton and van Reenen, 1990). Meta-volcanic rocks dominate the Giyani Greenstone Belt occurring within the granite-gneiss terrain (McCourt and van Reenen, 1992). The adjacent host rocks of Giyani Greenstone Belt are Swazian age Goudplaats gneiss. It also forms part of the Murchison sequence as the Giyani Group (Steenkamp *et al.,* 2012).

The Giyani Greenstone Belt is approximately 15 km wide and 70 km long in some areas and it bifurcates towards the south-western end into the Khavagari branch and the southern Lwaji branch (Billay *et. al., 2014)*, which are separated by a granitoidgneiss zone (McCourt and van Reenen, 1992; McCourt and Vearncombe, 1992) (Fig. 2.1), but it is contiguous in its eastern region. The thickness of the various members of the Giyani formations shows large variations over short distance because of intense folding and shearing. According to geophysical data (Kleywegt *et al.,* 1987), the Giyani Greenstone Belt indicates a shallow structure of about 1.5 km depth with a maximum depth of 3 km towards its south-eastern margin of the belt.

Gravity and geoelectric profiles across the belt show a 4 km down-dip extension into the crust for the Lwaji, and 1 km depth for the Khavagari branch, whereas the central portion of the belt is shallow (de Beer and Stettler, 1992; Kramers *et al.,* 2014). Kleywegt *et al.* (1987) also concluded that the greenstone belt is not situated along a major crustal boundary.

The Giyani Greenstone Belt (GGB) appears to be dominated by ultramafic and to a lesser extent, mafic rocks with rare iron-formations, felsic schist, and metasedimentary rocks (Fig. 2.1) (Brandl *et al.,* 2006). McCourt and van Reenen (1992) reported mafic and ultramafic meta-volcanic schists, as well as banded iron formation and fine to

medium-grained clastic sediments in the Giyani Greenstone Belt. They found that, due to the structural complexity, no stratigraphic sequence can be defined. However, they noted that ultramafic schists dominate the northwest zone, whereas the meta-volcanic rocks in the central and southeast domains are overall mafic. Various sedimentary units occur throughout the belt (Kroner *et al.,* 2000; Brandl *et al.,* 2006). The lithological strike, as well as that of the schistosity, is between north east–south west and ESE–WSW, with prominent shear zones, developed particularly close to the north-west margin of the belt (Kramers *et al.,* 2014).

Several gold mineralisations, notably the Klein Letaba, Frankie, Fumani, and the Gemsbok prospect, occur within the Giyani Greenstone Belt in the immediate footwall of the Hout River Shear Zone (HRSZ) (Gan and van Reenen, 1995). The mineralisation is associated with fluid-related retrogression of upper amphibolite facies lithologies. In contrast to the north-west margin of the Giyani Greenstone Belt, no marked shear zones have been found to coincide with its south-east boundary. The Giyani Greenstone Belt also host magnesite deposit in its northern part (Prinsloo, 1977).

Towards the southwest part of the belt, the Giyani Greenstone Belt diverges into two branches or arms which are the Khavagari and Lwaji branch which extends towards the westerly direction and the southerly direction respectively (Kroner, 2000; Kramer *et al.,* 2014).

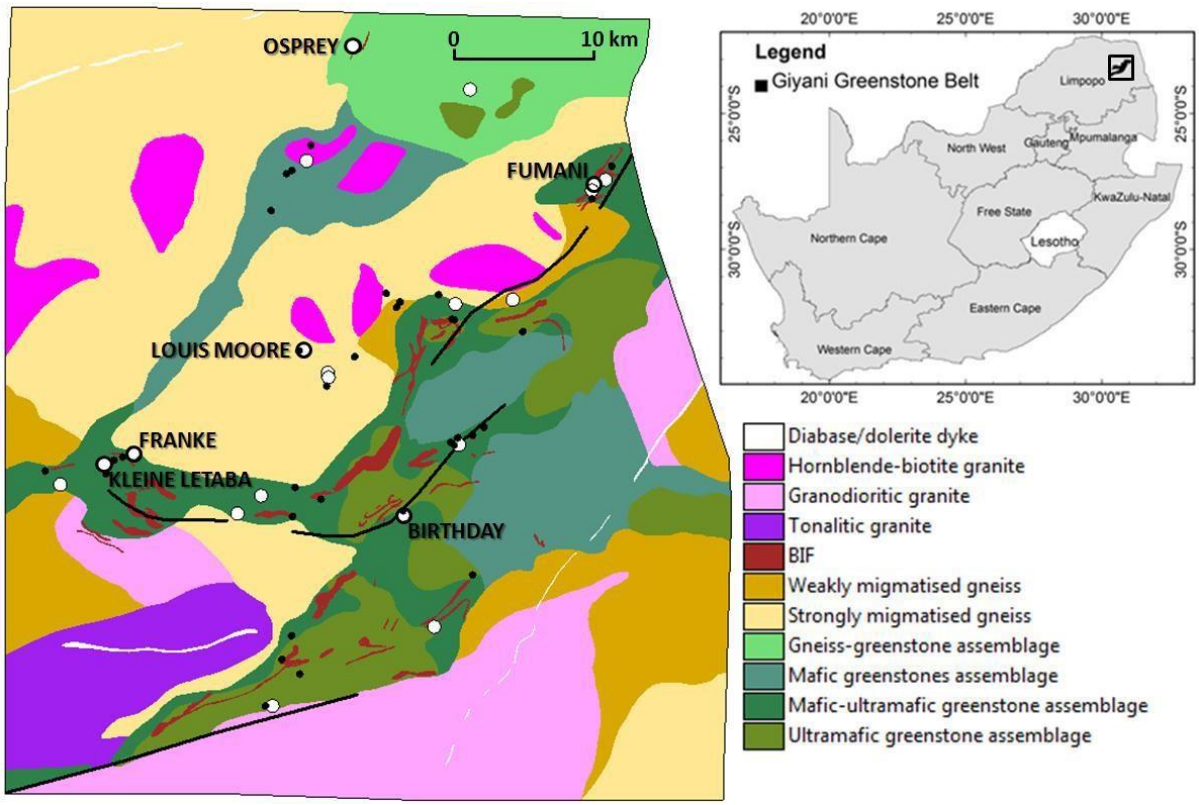

Figure 2.1: General geology of the Giyani Greenstone Belt (Prinsloo, 1977; Vorster, 1979; McCourt and van Reenen, 1992; Billay *et al*., 2014; Carranza *et al.,* 2014).

2.1.2 Khavagari Branch (Local Geology)

In the Khavagari branch a large intrusive body of altered dunite, probably representing part of a layered ultramafic section, is developed at the structural base of the succession. The dunite body is followed by a thick unit of ultramafic schist which in turn is overlain by metapelites (Kroner *et al.,* 2000). The Khavagari branch is dominated by ultramafic schist of tremolitic composition, minor chlorite, and chlorite quartz schist (Fig. 2.2) (McCourt and van Reenen, 1992). It is also overlain by a succession of sedimentary rocks including iron-formation, ferruginous and vitreous quartzite and pelitic schist with mafic tuff and the occurrence of dolomite in the upper section seems to be unique to South African greenstone sequence (Brandl *et al,* 2006). At the top of the succession, an ultramafic unit contains two thin layers of spinifex-textured komatiite inter-layered with coarse and fine-grained amphibolite (Anhaeusser, 2006). The serpentinite, hosted in tremolite-actinolite, talc-tremolite, tremolite-chlorite, and chlorite schists, also contains magnesite which has been mined historically in the belt (Prinsloo, 1977).

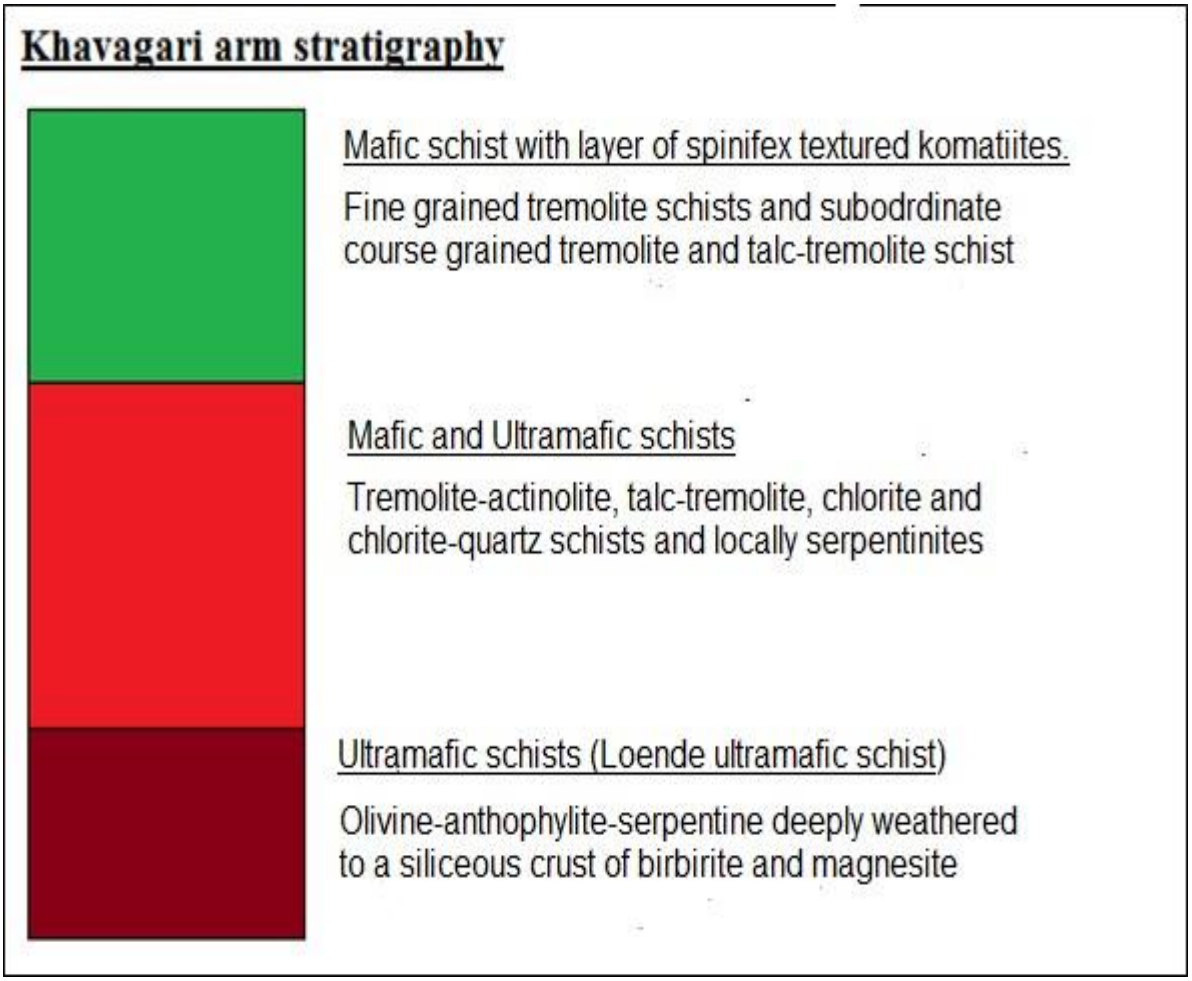

Figure 2.2: Lithostratigraphy of the Khavagari branch/arm in the Giyani Greenstone Belt (McCourt and van Reenen, 1992; Kroner *et al.,* 2000; Anhaeusser, 2006; Billay *et al.,* 2014).

2.1.2 Lwaji Branch

In the Lwaji branch, ultramafic rocks are represented in varying proportions, by tremolite schist, talc schist, chlorite schists, or amphibolite schists (Fig. 2.3). The mafic units are massive with pillowed hornblende-bearing amphibolite. The structural base is formed by ultramafic schists which pass upwards into a thick succession of metasediments, including phyllite, quartz-sericite, chlorite schist, and quartzite (Kroner *et al.,* 2000). The iron-formation is composed of lamina goethite with haematite grading upwards into granite and magnetite rock (Brandl *et al.,* 1993; Kroner *et al.,* 2000). The meta-sediments are overlain by ultramafic schists with a few small serpentinite bodies and then by amphibolite (Kroner *et al.,* 2000).

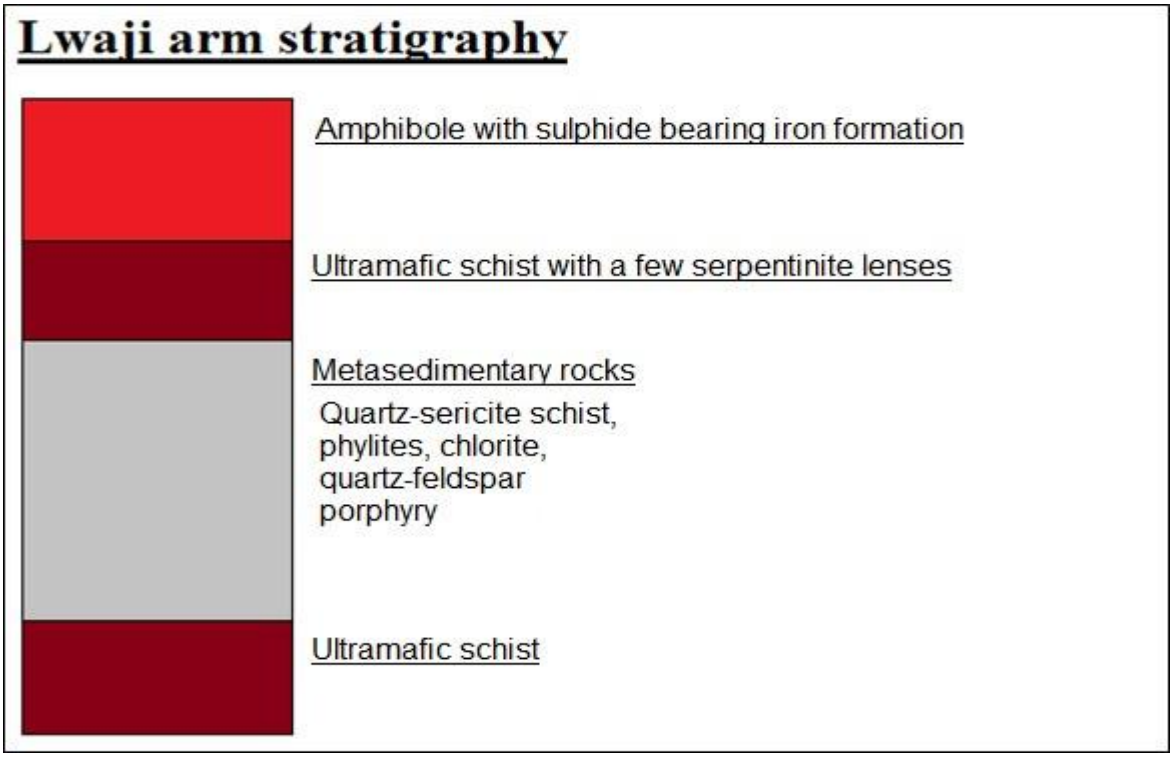

Figure 2.3: Lithostratigraphy of the Lwaji branch/arm in the Giyani Greenstone Belt (McCourt and van Reenen, 1992; Kroner *et al.,* 2000; Billay *et al.,* 2014).

2.1 Magnesite as a Mineral

Most minerals occur as compounds associated with sandy matter and other impurities in the earth's crust. A mineral may be a single compound or a complex mixture of elements. Magnesite, which is a carbonate of magnesium, it is a complex mixture of iron (Fe), silicon (Si), calcium (Ca), magnesium (Mg), carbon dioxide (CO_2), etc. Magnesite ($MgCO_3$) is one of the calcite group of rhombohedral carbonates, which include calcite ($CaCO_3$), siderite (Fe_2CO_3) and rhodochrosite ($MnCO_3$) (Pressacco *et al.,* 2010).

Magnesite is a rare rock-forming mineral compared to calcite and dolomite and it occurs in different marine and non-marine geological units, with relations of silicon, iron, and calcium (Schroll, 2002; Bashir *et al.,* 2008b, Bhilisse *et al.,* 2014). Magnesite has been formed since the Achaean age either as sedimentary beds or carbonated ultramafic rocks (Abu-jaber and Kimberly, 1992). Magnesite is found in crystalline aggregates in metasomatic type deposits, as well as in the form of cryptocrystalline to microcrystalline aggregates in deposits of hydrothermal-vein, hydrothermalsedimentary, and infiltration type (Operta and Bušatlić, 2018).

Magnesite is often intermixed with dolomite, but dolomite is not a member of the calcite group, this is because it occurs when calcium and sodium ions alternate in equal number in an ordered structure among carbonate ions (Pressacco *et al.,* 2010). Pure magnesite contains about 47.8% of magnesium oxide (MgO) and 52.2% of carbon dioxide (CO_2) (Bashir *et al.,* 2009), but pure magnesite is rarely found in nature, it is found with impurities like calcium and silica amongst others.

Many properties of magnesite are moreover undistinguishable or are like those of calcite or dolomite (Wilson and Ebner, 2005). The colour of magnesite is white or grey and can be also tinted yellow or brown with a streak colour of white. The crystal system of magnesite is trigonal, and its crystal habits are usually massive forms such as lamellar, fibrous, and course to fine-grained rocks. The crystals of magnesite are extremely rare, but when found are in the form of rhombohedral or hexagonal prisms. The magnesite lustre is vitreous with a conchoidal to uneven fracture, and its hardness is between 4-4.5. Magnesite specific gravity is approximately 3.0. It is usually associated with mineral calcite, dolomite, aragonite, strontianite, and serpentine. Other characteristics: effervesces easily only in hot dilute hydrochloric acid. The best field indicators are crystal habit, reaction to acid, occurrence, and cleavage.

2.2 Classification of Magnesite Deposit Based on Geology

Classification of magnesite deposits traditionally has been based on “types” from Middle European localities (Pohl and Siegl, 1986). This classification categorises magnesite deposits into two main groups, the ultramafic associated and the strata bound magnesite deposits. The classification system considers the geological setting (Abu-Jaber and Kimberley, 1992) of the magnesite.

2.2.1 Ultramafic Associated

Ultramafic associated magnesite is usually deposited due to the interaction of ultramafic rock or sediments with hydrothermal fluids near the surface or deep-seated areas. They are further divided into two groups based on the mineralisation environment, (a) the surface and near-surface hydrothermal mineralisation and (b) the metamorphic ophiolite environment (Abu-Jaber and Kimberley, 1992). The nearsurface deposits are found in concretions (soil weathering) environment, stratiform mineralisation (lacustrine/ evaporitic environment), vein-type, and vein-type

in a submarine environment (Pohl and Siegl, 1986). Their examples include the Bela Stena type and Kraubath type. The metamorphic ophiolites are located in a metamorphosed mineralised environment, such as greenschist facies mineralisation and amphibole facies mineralisation. Their examples include the hochfilzen and Greiner type (Pohl and Siegl, 1986).

2.2.2 Magnesite Strata-bound in the Sedimentary Environment

Magnesite strata-bound in the sedimentary environment is associated with sedimentary chemical rocks. They are formed due to precipitation or metasomatism of sedimentary rocks such as dolomite due to its interaction with hydrothermal fluid (Pohl, 1980). They are located within the environment such as terrestrial, playa/sabkha, modern and quaternary ancient and marine-sedimentary rocks, among others. Their examples include the Veitch type and Redbed type deposit (Pohl and Siegl, 1986).

The classification presented in Table 2.1 summaries these two concepts and gives examples of each deposit.

2.3 Classification of Magnesite Based on Physical Form

Generally, the use of ‘’type’’ of deposits to classify magnesite is unsatisfactory and that is why a better classification system, which is based on the physical form (crystallinity) of magnesite was created. Equally, the usage of crystallinity is problematic to classify magnesite deposits, distinguishing macroscopically into cryptocrystalline, fine-grained, and coarse-crystalline (sparry) magnesites (Abu-Jaber and Kimberley 1992). Nevertheless, the grain size is an important mineralogical property and the transition from type-localities to new terms should be favoured.

Due to their complex genesis, magnesite deposits are distinguished in nature by two distinct physical forms, namely, crystalline (microcrystalline) (Veitsch type) and cryptocrystalline (kraubath type) (Nasedkin *et al.,* 2001; Pressacco *et al.,* 2010; Harraz, 2017). A comparison between the two examples (Veitsch and Kraubath) is given in Table 2.2.

2.3.1 Crystalline Magnesite Deposits

Crystalline magnesite deposits are characterized by a wide range of visible crystal sizes, varying between 0.5-20 mm (rarely 5-6 cm) (Nasedkin *et al.,* 2001). The

individual crystals have a well-pronounced cleavage; hence the rock name is sparry magnesite (Nasedkin *et al.,* 2001). They are generally of large sizes and several million tons of ore (Harraz, 2017). They have a hardness of 3.5 to 4 and are often pure, but usually contains amounts of iron, lime, silica, and manganese (Pressacco *et al.,* 2010). Crystalline magnesite has low to medium applications in the industry (Wilson, 2013). They have a common mechanism of formation due to their striking resemblance to each other. Dolomite is usually the host rock for these types of magnesite deposits, but some, such as those in Brazil, are in limestone formations (Pressacco *et al.,* 2010). The host rock and magnesite mineralisation are usually not in direct contact with limestone/dolomite but are separated by a zone of dolomitisation. Major deposits of crystalline magnesite are found in Austria, Brazil, Canada, Nepal, Spain, and the United States (Pressacco *et al.,* 2010). The example of this deposit includes the Veitsch type magnesite deposit, which is discussed below.

Veitsch Type

The Veitsch type sparry magnesite deposit is located at the Veitsch area in Austria/Styria in the Veitsch Nappe of the Austroalpine greywacke zone (Pohl, 1980). The Veitsch type magnesite hosted in carbonate rocks, mostly dolomitic, represents marine shallow-water environments of Proterozoic and Paleozoic ages. Sometimes it is associated with pelite, sandstone, conglomerate, and basic volcanic and often it occurs in metamorphic terrains. The sparry magnesite deposit is white to black, grey, blue, reddish, and fine to coarse-grained, with mono and bipolar crystal growths. Often it displays decorative pictures like box and rosette texture, pinolitic texture (large elongated cm-sized light magnesite crystals in a fine-grained dark matrix), or zebra banding. Veitsch type sparry magnesite forms layered and lens-shaped deposits and irregular stocks. Often the layered texture and the magnesite dolomite boundaries are angular to the sedimentary bedding that mostly can hardly be recognized. Often there are transitions of the ore body to dolomite and the host limestone (Wilson and Ebner, 2005). Veitsch type magnesites are characterized by an elevated Fe-content of several percent (although true breunnerites with more than 10 % mole of $FeCO_3$ are slightly rare), MnO to about one-tenth of FeO, low Al_2O_3 and variable SiO_2 and CaO_3, depending on quartz, talc, and dolomite contents.

2.3.2 Cryptocrystalline Magnesite Deposits

Cryptocrystalline magnesite deposits, also known as amorphous are an alteration of serpentine or allied magnesium-bearing rocks, which were subjected to the actions of carbonated seawater (Pressacco *et al.,* 2010). Individual crystals are not seen in the polarised light under the optical microscope because it is fine grain and compact showing no cleavage and practically opaque in cross Nicolls (Nasedkin *et al.,* 2001). The size of the individual grains is about 1-5 microns, and this can be seen under a scanning electron microscope and their hardness is 3.5 to 5. Serpentine lies near or surrounds the magnesite itself and the magnesite is an alteration product of ultrabasic rocks (Pressacco *et al.,* 2010). Mode of formation of cryptocrystalline magnesite limits the amounts of impurities to relatively small quantities of iron, lime, and silica. The occurrence of cryptocrystalline magnesite deposits is common throughout the world but because of their usually limited size, only a small number of these cryptocrystalline deposits, except for those in Greece, India, Turkey, and Australia are exploited commercially (Pressacco *et al.,* 2010; Harraz, 2017). There are two types of cryptocrystalline magnesite; the first is closely associated with serpentine mass, where the magnesite occurs in veins of various thickness and as massive bodies, and lenticular masses or as stockwork with irregular veins from a few centimetres to several meters in thickness. The second one is also associated with ultramafic rocks, as the magnesium source, but here the rock was weathered, eroded, transported, and deposited in a lacustrine environment (Nasedkin *et al.,* 2001; Pressacco *et al.,* 2010). Cryptocrystalline magnesite has low to a high industrial application (Wilson, 2013). The example of this deposit includes the Kraubath type magnesite deposit, which is discussed below.

Kraubath Type

Kraubath type magnesite deposit type is located in the ophiolitic ultramafic massif of Kraubath (Austria/Styria), which is part of the Middle Austria pine crystalline complex of the Eastern Alps (Neubauer and Frisch, 1993). Important host lithologies of Kraubath type magnesite are olivine-rich rocks (dunite, peridotite) of ophiolite zones or other ultrabasic magmatic intrusive complexes. Kraubath type magnesite is snow white with tints to yellow, yellow, or buff and occurs in cryptocrystalline texture with a

conchoidal fracture, sometimes cauliflower-shaped and with transitions to fibrous and granular types. Magnesite occurs in veins and stockworks aligned with secondary faults of this fracture zone, and underneath a pre-Neogene lateritic alteration surface. Mineralisation in shallow niveaus (extending only some 10 m to the depth) occur close to the recent or paleo surfaces in networks or layers or as thicker veins rarely extending some km in a strike and some 100 m to the depth. In comparison to sparry magnesite deposits, the potential of cryptocrystalline magnesite deposits is smaller (up to several tens of 106 t: Wilson and Ebner, 2005).

Table 2.1: Classification of magnesite deposits based on geology (Pohl, 1990; Schroll, 2002)

Geological Setting	**Examples**
1. Magnesite ultramafic association	
a. Surface and near-surface to hydrothermal mineralisation	
Concretions (soil weathering)	
Stratiform mineralisation (lacustrine/ evaporitic)	Bela Stena type
Vein type (with a transition to CO_2 and fluid from deep sources	Kraubath type
Vein-type in a submarine environment	
b. Metamorphic ophiolitic environment	
Mineralisation in greenschist facies	Hochfilzen, Breltenau
Mineralisation in amphibolite facies	Greiner type
2. Magnesite strata bound in a sedimentary environment	
Mineralisation in the terrestrial environment	Redbend type (Alpine Permian)
Mineralisation in the playa/sabkha environment Modern and Quaternary ancient	Carrorong L., Sebkha el Melah Barton Farm, Aldelaide Syncline
Associated with evaporates	Kaswasser (Hall) type
Mineralisation in marine sedimentary rock series	Sabka el Melah

Mineralisation in metasedimentary rock series	Veitsch type

Table 2.2: Comparison of Veitsch type and Kraubath-type models of magnesite (Jansen and Bateman, 1981; Pohl, 1980; Bashir, 2008)

Veitsch Type	**Kraubath Type**
Crystalline in nature	Cryptocrystalline (porcelain mass)
Granular aggregate	Compact with a conchoidal fracture
Vitreous lustre	Dull opaque
Perfect rhombohedral (3set) cleavage	No cleavage
Larger size bedded deposit/ lens-shaped	Small-sized, veins fill on ultramafic rocks
Geochemical signature: Fe^{++}	Geochemical signature: Ni^{++} Cr^{++} and Co^{++}
Host rock: limestone-dolomite	Host rock: serpenitised harzburgite
Min. association: siderite, pyrite, calcite	Min. association: opal, chlorite, chalcedony

2.4 Genesis of Magnesite Deposit

Magnesite ($MgCO_3$) is formed in a sedimentary and/or magmatic environment (Pohl, 1990; Abu-Jaber and Kimberley, 1992; Schroll, 2002; Kadir *et al.,* 2013). Two major models are used to explain the genesis of magnesite deposits. These are evaporitic or early diagenetic formation (syngenetic) (Lambert *et al.,* 1984; Melezhik *et al.,* 2001; Frank and Fielding, 2003) and metasomatic replacement of host carbonates (epigenetic) (Valdiya, 1968; Aharon, 1988; Ellmies *et al.,* 1999). Similar explanations have been applied to Palaeozoic strata bound magnesite occurrences, and different opinions have given rise to the so-called “magnesite problem” (Kralik *et al.,* 1989). The controversy between syngenetic and epigenetic has until this day not been fully resolved (Hogmalm *et al.,* 2012). Uncertainties concerning the genesis of ultramafichosted deposits are discussed by Abu-Jaber and Kimberley (1992) while the genesis of sparry magnesite deposits is discussed by Schroll (2002), where he concluded that the origin of sparry magnesite hosted by meta-sediments is to be considered as a sedimentary enrichment influenced by diagenetic and metamorphic processes. An approach to the best genetic model of each magnesite deposit needs

the synopsis of all geological facts and geochemical data (Schroll, 2002). The genesis of magnesite in the ultramafic environment is further explained below.

2.4.1 Magnesite Genesis in Ultramafic

There is a major controversy regarding the genesis of cryptocrystalline magnesite deposits. The main disagreement is whether they originate as a result of (i) metasomatic replacement 'in situ' of serpentinized peridotite by magnesite and silica under the supergene and/or hydrothermal conditions (Metasomatic/weathering) (O'Neil and Barnes, 1971; Moller, 1989; Zachmann and Johannes, 1989) or by filling of fractures by precipitation of magnesite from a magnesium-rich carbonic fluid due to the pressure decrease (Hydrothermal processes) (Ilich, 1968; Griffis, 1972; Dulski and Morteani, 1989; Abu-Jaber and Kimberley, 1992; Fallick *et al*., 1991) (Fig. 2.4).

Metasomatic Replacement

Meteoric waters containing carbon dioxide (dissolved from the atmosphere) may be expected to react with ultramafic rocks and to take magnesium and silicon into solution, leaving the iron behind. As these percolates downwards they leach more and more Mg^{2+} and Si^{2+} and thus become supersaturated. The precipitation of magnesite takes place when the solutions lose carbon dioxide and thus change pH as they approach the surface again. O'Neil and Barnes (1971) pronounced a variety of magnesium and calcium carbonate deposits in California, understood to have been formed as a result of surficial metasomatic replacement. In these, the interaction between ultramafic rocks and groundwater drives near-surface carbonate precipitation at temperatures of 15-25°C. Barnes and O'Neil (1969) distinguished two types of water. The first water being of $Ca^{2+}OH^{-1}$-type water (formed as a result of the reaction between pyroxenes relatively rich in calcium, and groundwater) is held to be responsible for the deposition of travertine (calcite), and the second water being $Mg^{2+}HCO_3^{-1}$ type water (formed by the reaction between serpentinites and groundwater) is argued to be responsible for nesquehonite precipitation.

Metasomatic Hydrothermal Alteration

According to Ilich (1968), the formation of both lacustrine sedimentary and ultramafichosted vein-stock work-type magnesites results from CO_2-rich volcanogenic exhalations. Fractured ultramafic rocks are leached by these CO_2-bearing

hydrothermal solutions, becoming rich in Mg^{2+}. Magnesite is precipitated by the release of CO_2 as a result of rapidly falling pressure as the solutions move towards the surface. This precipitation mechanism has been accepted by Fallick *et al*. (1991), Abu-Jaber, and Kimberley (1992) and others. Ilich (1968) also suggested that similarities in Hg concentration in lacustrine-sedimentary and ultramafic-hosted vein stockwork magnesites indicates that both formed from hydrothermal sources. In Serbia, vein-stockwork, and lacustrine magnesites, both have high Hg (700 ppb) concentrations whilst ultramafic rocks in the area have only 9 ppb (Abu-Jaber and Kimberley, 1992). In areas where mercury is present, hydrothermal solutions at depth are rich in both mercury and magnesium. When these solutions find a suitable fractured-faulted zone, which may emerge at the base of a lake, the pressure drop leads to a release of CO_2 from the solution and the precipitation of mercury (as cinnabar) as well as magnesite.

In both Metasomatic and hydrothermal processes, there are three general requirements: a) there must be a magnesium source, b) there must be a suitable water supply, and c) there must be a carbon dioxide source.

Source of Magnesium

Ultramafic rocks, minerals with a high concentration of magnesium, salinity, meteoric water, and magnesium-rich hydrothermal solutions are considered to be the source of magnesium (Mg) required for the magnesite deposits in several parts of the world (Prasannakumar *et al.,* 2002; Dar and Dubey, 2012). Though magnesium is released during weathering and serpentinisation of dunite and peridotite, it is insufficient to account for the magnesite deposits at depth, especially in the zone of less weathering and serpentinisation (Prasannakumar *et al*., 2002), so magnesium is released by the breakdown of silicates due to hydrothermal activity associated with ultramafic-mafic magmatism.

Source of Water

Meteoric water is a striking fluid source since it potentially provides large volumes near the surface. Fallick *et al*. (1991) suggested that generally the large amount of water needed for magnesite mineralisation can only be satisfied by meteoric water recharge.

Source of Carbon

Various models are in vogue regarding the source of CO_2 for the formation of veintype magnesite deposits. Of these, magnesite formation as a result of the reaction of ultramafic rocks with ascending CO_2- rich diagenetic metamorphic fluids derived from decarbonisation of deep-seated carbonates or decarboxylation of organic-rich sediments was in wider acceptance (Pohl, 1990). The other mechanisms include meteoric waters enriched with atmospheric or biogenic carbon (Jedrysk and Halas, 1990) a mantle source for the carbon (Gold, 1979), and mixing of ascending fluids with near-surface meteoric water constituting the mineralizing solution. The source of carbon is unclear. The source may be atmospheric (including plant respiration and degradation), volcanic, or metamorphic (degassing) (Abu-Jaber and Kimberley, 1992). The complexity and proliferation of models often make it difficult to suggest a model without ambiguity and in recent years carbon isotope studies have been reported to constraining the genetic model.

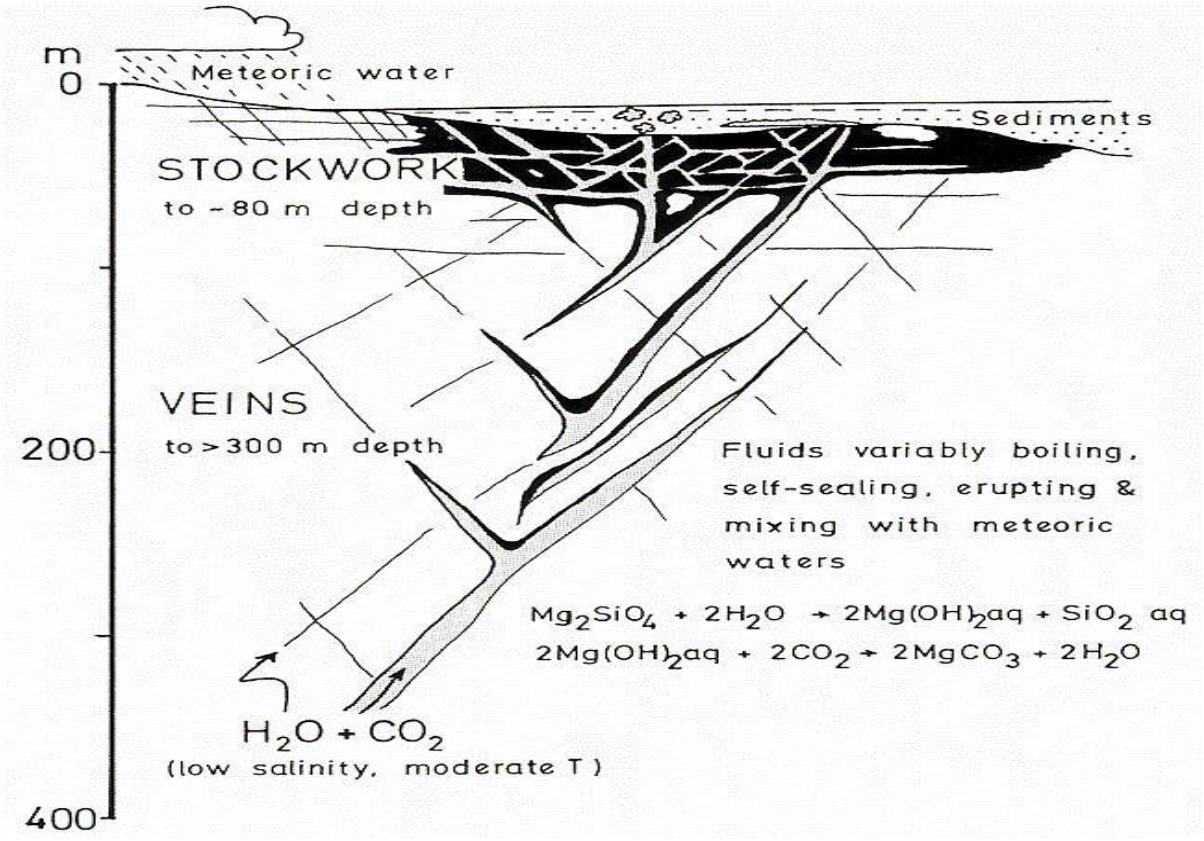

Figure 2.4: Types of cryptocrystalline magnesite deposits (Pohl, 1990; Zadeh, 2009).

2.5 Magnesite in South Africa

South Africa is the leading supplier of a range of minerals and mineral products, but when it comes to magnesite production, South Africa does not even make up the top 10 of the world's magnesite (magnesite compound) production. South Africa's economically viable deposits of magnesite occur as weathering products of rocks with high magnesium content (Masindi, 2015). The main magnesite deposits are in Mpumalanga and Limpopo provinces, this is, in the Malelane area, near Lydenburg, an area north of Soutpansberg, in the Burgersfort and Giyani districts (Fig. 2.5) (Naidoo, 2008; DMR, 2013). There are only a few mines that are exploiting magnesite as the main commodity and these mines include the Muyexe magnesite mine, Strathmore magnesite mine, and Syferfontein magnesite mine (Ratlaba, 2003; Naidoo, 2008). Magnesite in South Africa's mined using an open cast mining method. Magnesite in South Africa is primarily used for amendments to agricultural soil. The other magnesite production is from by-products of other mineral deposits and products of various sea salts. In 2013 South Africa's production of magnesite was 8219 Mt (DMR, 2013). The deposits of natural magnesite in South Africa have been estimated to be 18 Mt in total (Afonin and Maryasev, 2006, Jeleni *et al.,* 2012, Sibanda *et al.,* 2013, Masindi *et al.,* 2015). This was only 0.9% of the total world's production of magnesite which was 910000 Mt (U.S. Geological Survey, 2013).

2.6 Magnesite Global Production and Reserves and Markets

The world's total magnesite reserve as of 2017 has been estimated to be 8,500,000 Mt (U.S. Geological Survey, 2018). According to United States Geological Survey (USGS) in 2018, global magnesite production totalled 270 million Mt, with 67% of these resources held by China, Russia, North Korea, and Brazil (Fig. 2.6). USGS data show that in 2017 China produced 70% of the world's magnesite and 88% of global magnesium metal. China is the top producing country than Russia, Turkey, Slovakia, and Korea, respectively. The main exporters of magnesite are China, Slovakia, and Turkey. Although Slovakia is the fourth major producer, it is the second major exporter of the magnesite in the world (U.S. Geological Survey, 2018). Due to its strong forecast growth in demand for magnesium and magnesite, the European Union (EU) has included both magnesium and magnesite in their list of 20 EU critical material, published in May 2014 (European Union, 2014).

The price of fused magnesia depends significantly on its quality. In April 2017, the price of fused magnesia (96%) was around US$360-390 per ton, whereas 97.5% material was US$495-550 per ton and the highest quality fused magnesia with MgO content of greater than 99% was around US$1200-1400 per ton (Li and Ghilotti, 2017).

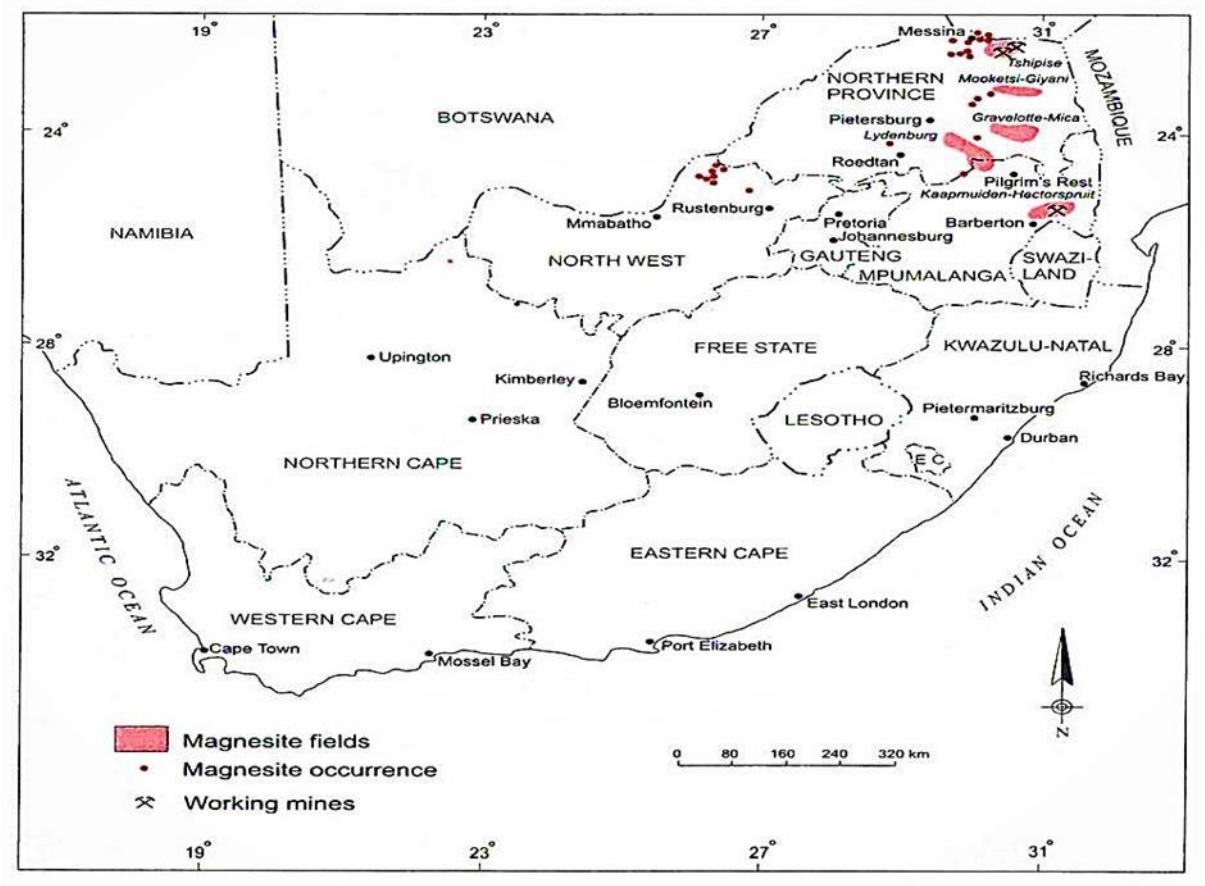

Figure 2.5: Magnesite field of the Republic of South Africa (Masindi, 2015).

Figure 2.6: Global sources of magnesite and producing countries (Wilson, 2013).

2.7 Economic Importance of Magnesite

Magnesite is an important mineral in the modern-day industry, as it is used in a variety of products. The economic utilisation of magnesite is largely dependent upon the physical properties of minerals and its impurities. Magnesite is the primary source of magnesia. Magnesia is mainly used in agriculture, mineral processing, paper manufacturing, and refractory industries (Table 2.3) (Harben, 2008). Magnesite is also used to produce magnesium (Mg) a lightweight earth metal widely used in aerospace and automotive industries. There is a surplus of possible applications of magnesite and these are summarised in Table 2.3 below. These include mobile telephones, cars, trucks, motorcycles, aircraft engines, and other aircraft components and high impact resistance portable (Bashir *et al.,* 2009).

The main proportion (about 98%) of magnesite mined is used for conversion in the calcined form which finds many applications (Indian Yearbook, 2012; Hazzar, 2017). The other industries where raw magnesite is used are mosaic tiles, electrodes, chemicals, and manufacture of magnesium metal. Magnesite is also used in fertilizers and by the food processing industry (Harben, 2008). Raw magnesite is dead-burnt for making basic refractory bricks, basic refractory mortars, ramming mass, tar/pitch impregnated magnesite, magnesia carbon bricks, slide-gate plates, and other refractories (U.S. Geological Survey, 2018).

Caustic calcined magnesite is used for manufacturing sorel cement (magnesium oxychloride), castable refractories, and extraction of magnesium metal. It is also the source material for the manufacture of magnesium compounds like magnesium sulphate (Epsom salt) and other salts used in paper and pharmaceutical industries (Indian Yearbook, 2012). In the paper industry, magnesium bisulphate produced from magnesite was used as cooking liquor for preparing pulp (Bashir *et al.*, 2008a). It is also used in textile, rubber, glass, ceramic industries, and animal feedstuff. Fused magnesia finds application as an insulating material in tubular heating elements in the electrical industry and refractory brick linings in steel furnaces. The uses of magnesite are simplified in Table 2.3 below.

Table 2.3: Generalized industrial application of magnesite (Harben, 2008)

USES	**END-USER INDUSTRY**	**PRODUCT/FICTION**
Chemicals	Chemical manufacture	Feedstock, magnesium salts, magnesium metal, and alloys
	Fire Retardants/Wood preservatives	Feedstock
	Pulp and paper	Pulping liquors
	Rubber	Catalyst and filler
Refineries/Refractories	Steel, copper, and nickel refining	Slag conditioners, insulators
	Fluxes (soldering, welding, and smelting)	Fluxing agents
Glass and ceramics	Fiberglass	Feedstock
	Speciality additives including frits, glasses enamels	Additives
	Sealants and adhesives	Cement

Building compounds/speciality cement	Construction/Building industry	Cement, typically used in the production of fireproof materials and coating wallboards, flooring, and grinding wheels
Pharmaceutics	Pharmaceutical industry	Medicines, disinfectants
Fertilizer/Agriculture	Fertilizer	Secondary/micronutrients
	Animal feed	Nutritional minerals
Environmental, Water treatment, filtration	Waste and effluent treatment	Chemical additives
		FGD
Energy	Oil and gas	Drilling muds
Automobile	Automobile/Aircraft manufacturers	Engine alloys, car, truck, motorcycle, aircraft engines, light aircraft parts

2.7.1 Magnesite as a Source of Magnesia

Magnesite is the world's most important source of magnesia because it provides magnesia (MgO) upon calcination. Magnesium (Mg) is the eighth greatest plentiful element and constitutes about 2% of the Earth's crust, and it is the third most abundant element dissolved in seawater (Erdogan, 2016). Though magnesium originates in over 60 minerals, only dolomite, magnesite ($MgCO_3$), brucite $Mg(OH)_2$), carnallite ($KMgCl_3 \cdot 6(H_2O)$), and olivine ($(Mg, Fe)_2SiO_4$) are of commercial importance (Erdogan, 2016). Of these minerals, magnesite (MgCO3) and dolomite ($MgCO_3.CaCO_3$) are the largest sources of magnesium (Mg) and magnesium compounds. Magnesium compounds which are MgO (Caustic Magnesia and Sinter or Dead-burnt magnesia), $MgCl_2.6H_2O$ (Bischofite), Mg(OH) (Brucite), $MgCO_3$ (Magnesite) are produced from seawater, lake brines and minerals deposits (Harben, 2008). Magnesium oxide (MgO), has several categories, namely, light-burned, or caustic-calcined MgO, hard-burn MgO, and dead-burn MgO, or as it is otherwise known, periclase: and the last category, fused magnesia. Most magnesite resources are mainly used to produce magnesia refractory with low value-added products (Bashir *et al.,* 2008b; Harben, 2008).

2.7.2 Caustic-Calcined Magnesia

Caustic-calcined magnesia is magnesia which is calcined (burned) at a relatively low temperature (600-1000^{o}C). It is also known as lightly burned magnesite (MgO), with a relatively high specific surface area of 1.0-250 m^2/g. It is a concentrated source of chemically active magnesia (Pressacco *et al.,* 2010). It is mostly used in the agricultural sector, environmental sectors, manufacturing and chemical source, and feedstock (Harben, 2008; Erdogan, 2016). About 22% of the total magnesia is used in the production of Caustic-calcined magnesia (Fig. 2.7).

2.7.3 Sinter or Dead-Burned Magnesia

Dead-burned magnesia refers to magnesia which was calcined (burned) at a higher temperature (greater than 1450^{o}C) and yielded dead-burned magnesia (Pressacco *et al.,* 2010). It is also known as double calcined magnesite, sintered magnesia, magnesia clinker, or periclase. The magnesite when burned has a surface area greater than 0.1 m^2/g. It is a dense, hard, and chemically non-reactive product with the highest melting point of all common refractory oxides. Dead burned magnesia can resist chemical (slag) attack, it is highly refractory (melting point 2800^{o}c for pure periclase) and withstands mechanical abrasion (mag-chrome or mag-carbon bricks) castable refractories and gunning mixers for smelting, glass melting and cement production (Indian Mineral Yearbook, 2012; Harben, 2008). About 69% of the total magnesia is used in the production of Dead-Burned Magnesia (Fig. 2.7).

2.7.4 Fused Magnesia

Fused magnesia is produced by the fusion of the high-grade magnesite in Higgins or electric arc, tilt furnaces between 2500 and 3000^{o}C (Indian Mineral Yearbook, 2012).

It has the highest grade of periclase with 96 % to ≥99 % MgO, a bulk density near the theoretical limit of 3.58 g/cm^3 and it is resistant to the action of molten metals, basic slags and fluxes and high temperatures (Pressacco *et al.,* 2010). 9% of the total magnesia is used in the production of fused magnesia (Fig. 2.7). Fused magnesia is superior to Dead Burned Magnesia in abrasion resistance and chemical stability (Harraz, 2017). It is mostly used in refractory and electrical insulators (Harben, 2008).

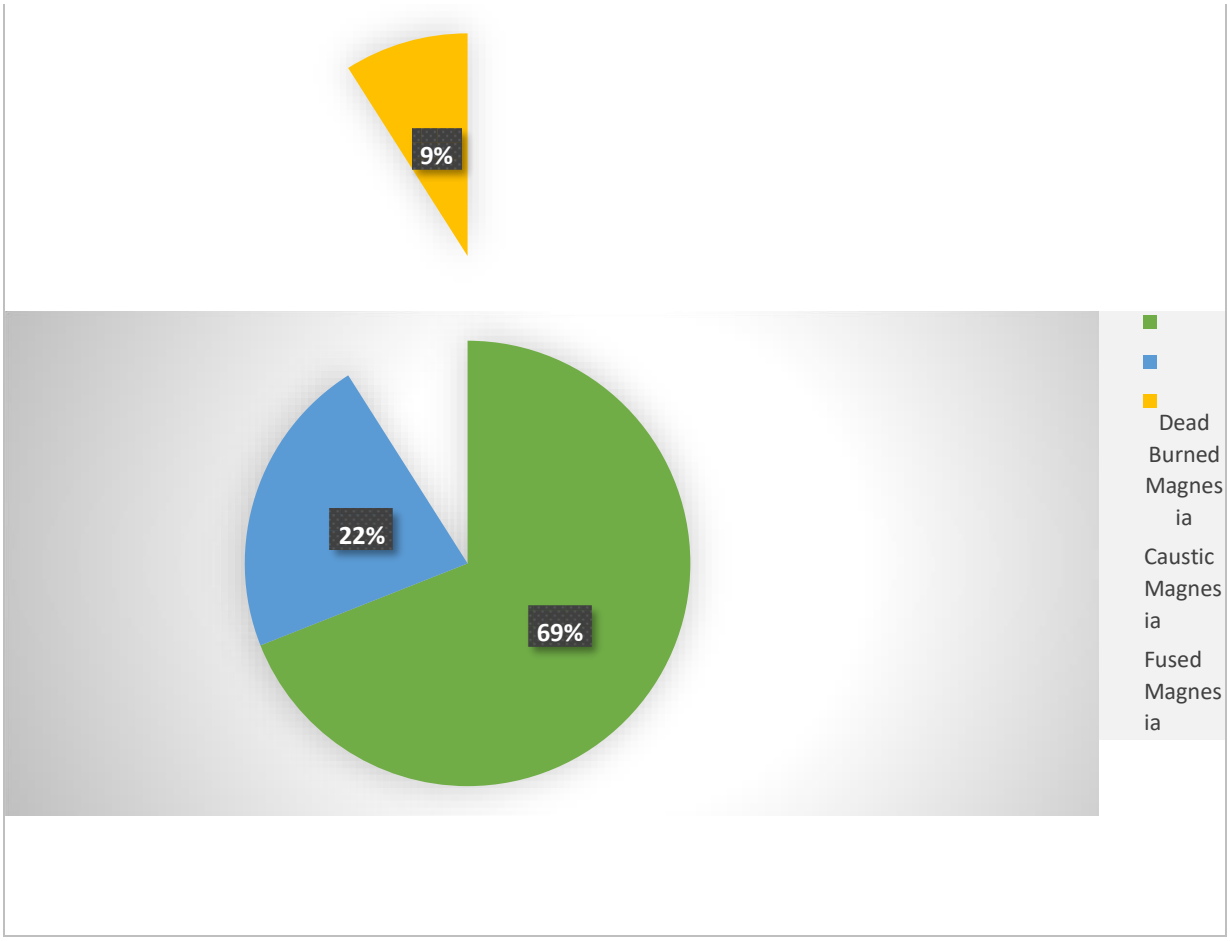

Figure 2.7: Worldwide production of magnesia from magnesite (Wilson, 2013; Hazzar, 2017).

2.8 Processing of Magnesite

Beneficiation of magnesite ore is performed using physical and chemical methods to produce a high-grade product to be used in the manufacture of magnesium compounds. Magnesite ore is separated from impurity silica and iron by crushing, grinding, screening, and beneficiation methods (Erdogan, 2016). The processing of magnesite ore starts with crushing, screening, and washing (Fig. 2.8). Magnesite is transformed into magnesia by the application of heat which drives off carbon dioxide (CO_2), thereby converting the carbonate to the oxide of magnesium (MgO) (Bashir, 2008; Hazzar, 2017).

When raw magnesite is heated, between 700-1000^{0}C produces caustic-calcined magnesia (caustic magnesia). It is both an end product and an intermediary step in the chain of magnesia products (Fig. 2.8). When calcined magnesia is heated, between 1530-2300^{0}C the product is non-reactive and exhibits exceptional

dimensional stability and strength at high temperatures (Hughes, 2008) This product is known as dead-burned or sintered magnesia.

It is mainly used as a refractory material because of its inertness and high melting point (Hazzar, 2017). Heating to this level drives off all but a small fraction of the remaining carbon dioxide to produce a hard-crystalline non-reactive form of magnesium oxide. When calcined or dead-burned magnesia is heated over an electric arc furnace, electro-fused magnesia is produced. It has higher strength, resistance to abrasion, and chemical stability than dead-burned magnesia. It is used in the manufacture of premium grade refractory bricks used in the high wear hot spots of basic oxygen furnaces, electric arc, or similar furnaces where temperature can approach 950^0C.

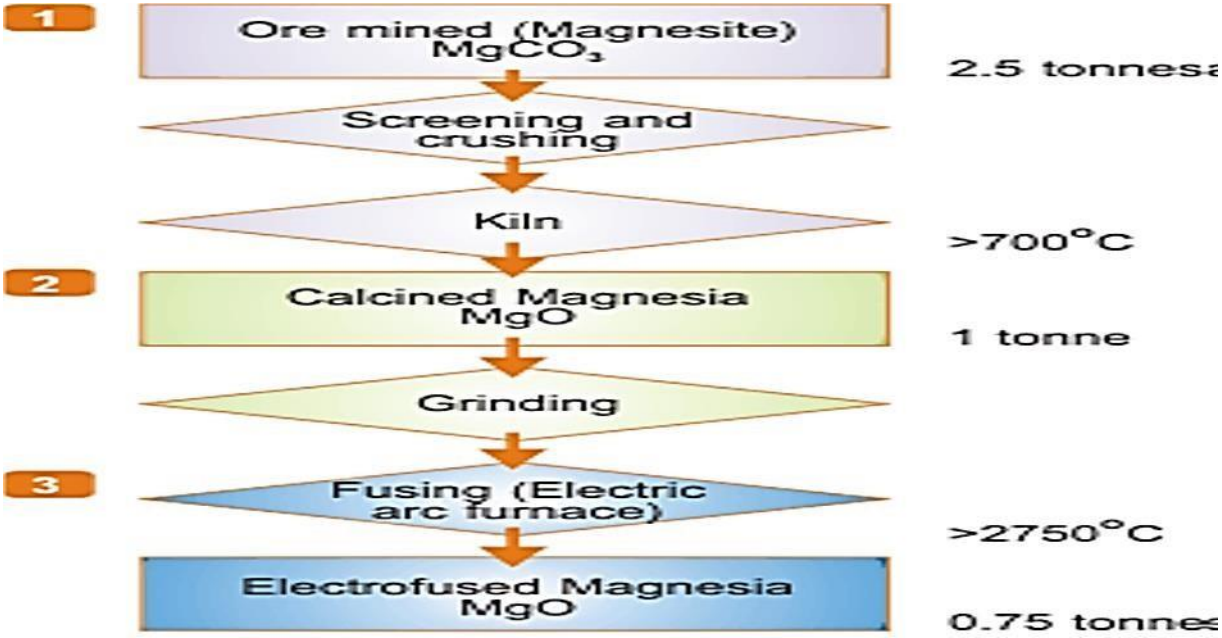

Figure 2.8: Fused magnesia process flow chart (Hughes, 2008).

2.9 Quality and Grade of Magnesite

According to Harben and Bates (1990), the requirement in terms of the chemical composition of good cryptocrystalline magnesite for used in different industrial applications is 46.6% magnesium oxide (MgO), 49.9% carbon dioxide (CO_2), 0.70% silica (SiO_2), 1.35% calcium oxide (CaO), 0.85% iron oxide (Fe_2O_3) and aluminium oxide (Al_2O_3). However, the Bureau of Indian Standards specification (IS: 3607-1979, First Revision, Reaffirmed, 2010) has prescribed the following specifications for magnesite for use in the chemical industry: loss on ignition percent by mass minimum 48.0, silica (as SiO_2) percent by mass max 2.0, aluminium (as Al_2O_3) percent by mass

max 0.3, iron oxide (Fe_2O_3) percent by mass max 0.4, magnesium (as MgO) percent by mass min 45.0, calcium (as CaO) percent by mass max 1.0 (Indian Yearbook, 2012).

Cao *et al.* (2016) mention the following concentration of magnesium oxide in magnesite to classify the magnesite into grades. High-grade magnesite has a minimum concentration of 46% MgO, middle-grade magnesite has a concentration of MgO between 43-46% and lower grade magnesite has a magnesium oxide concentration of less than 43%.

2.10 Variation Diagrams for Classification of Rocks

Variation diagrams are used to present geochemical data that has been collected from a suite of samples. They are diagrams that are constructed by plotting the chemical compositions of rocks to display and convey important clues to the processes that took place whether they may be geochemical or Petro-genetic and help to show a range of petrologic processes (Rollinson, 1993).

A well-correlated trend within the variation diagrams does not provide the ability to identify a unique geochemical process. This is due to that similar trends that may be found may be a result of more than one process. As such, additional data in the form of trace elements, rare earth elements or isotope data may assist in discriminating between various processes. This can be done in the absence of unambiguity from major element variation diagrams (Rollinson, 1993).

2.10 .1 Harker Diagram

This is the oldest method in the variation diagram and has been in use since 1909. The Harker diagram uses only the major elements (major oxides) and plots them graphically against the % weight of SiO_2. The abscissa (X-axis) of the graphs is usually chosen as SiO_2 because of all the major oxides in igneous rocks, this is the most abundant and exhibits the widest variation within a specific suite of samples. SiO_2 can be used as a measure of the evolution of magma forming that rock and also, it increases its concentration following a series of successive fractional crystallization of the liquid forming the rock (Wilson, 2007). The abscissa of the graph can be replaced with Zr and plotted against any element that can be mobilized from the magma and the plot now becomes a Binary plot.

Any major element or oxide can be chosen and used as an abscissa given that it has a wide variation in abundance. If the Harker diagram exhibits a certain correlation or trend within the same igneous suite, then all the rocks within that suite can be said to be genetically related or comagmatic (Brock University, 2017). To observe a trend within a Harker diagram, a trend line or best fit line needs to be constructed in the plot.

In the case of the binary plot, Zr is plotted against a series of various elements of various ionic potential. These elements can be composed of lithophile elements that may include major elements and less mobile trace elements. If the plots exhibit a wide dispersion of scattering, this shows that a particle element had been remobilized during the crystallization of magma and if a certain trend exists then the elements can be said to immobile. This mobilization of elements may be caused by either alteration of the magma as it crystallizes or by magma differentiation during crystallization.

2.10.2 MgO vs Major Oxides

This is a variation diagram wherein MgO is the abscissa and any other major oxides are plotted on the Y-axis of the diagram. These types of diagrams are most suitable for mafic units preferably basalts. MgO is plotted in the X-axis instead of the traditional SiO_2 because MgO has a tendency of decreasing as the magma differentiates further while the SiO_2 exhibits little change among the various types of basalts. These

2.10

variation diagrams can be used to measure the degree of evolution of the rock suites (Nelson, 2011).

.3 Total Alkali-Silica Diagram

This is a variation diagram that is used for volcanic rocks classification and to distinguish between various two types of parental magma namely tholeiitic magma and alkali magma based on the relationship between the combined alkali content and the silica content. It can also be used to distinguish between trends that may exist within a rock series (Nelson, 2011). The abscissa of the diagram is given by silica (SiO_2) while the Y-axis is composed of $Na_2O + K_2O$ in weight percentage.

The TAS diagram fields consist of basalt, trachyte, basanite, basaltic andesite, andesite, dacite, rhyolite, tranchybasalt, tranchyandesite, picrobasalt, tephrite, phonotephrite, tephriphonolite, and foidite which can be named according to the dominant feldspathoid minerals (Fig. 2.9). more studies are maybe required in some of the magma types like a normative mineralogy test may be required to further subdivide basalt and trachyte into subgroups and this may allow for further division of the Basalt (Nelson, 2011).

2.10

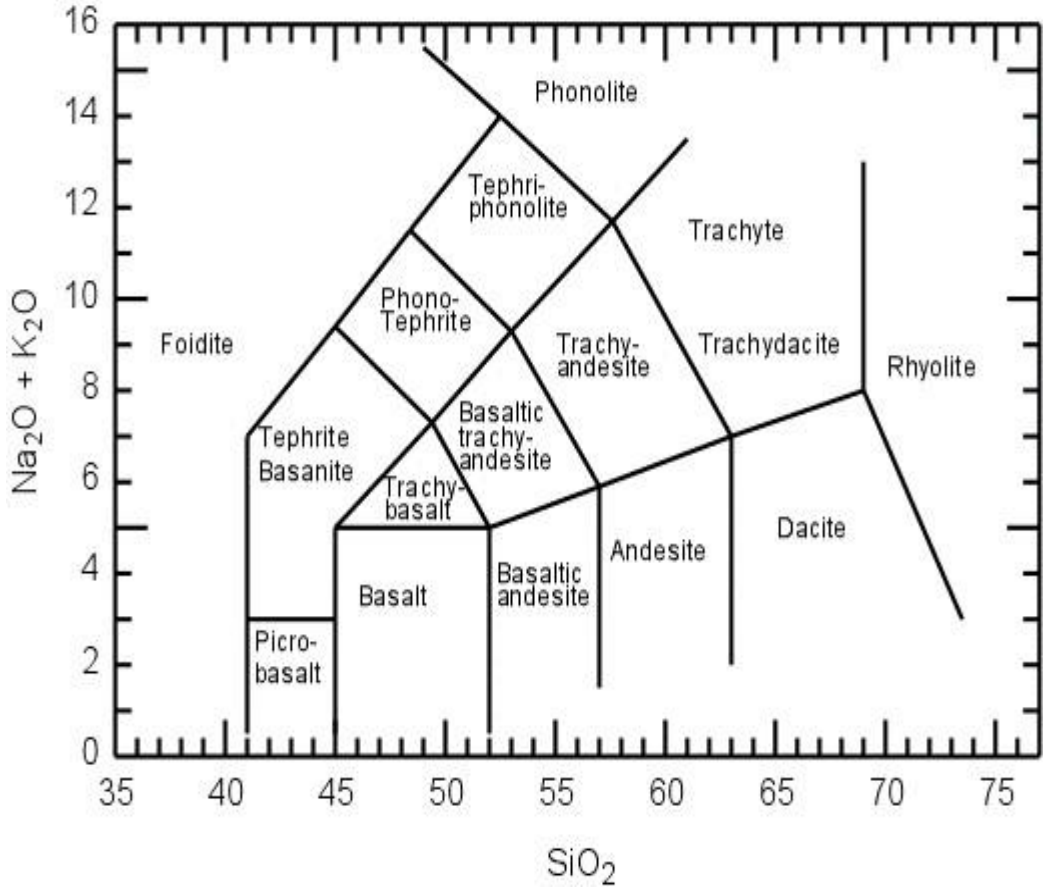

Figure 2.9: The Total Alkali vs SiO_2 diagram (Nelson, 2011).

.4 Ternary Plot

The ternary plot is a triangular diagram used for various purposes that include geochemical classification of igneous rocks and to distinguish the tectonic setting of various rock units (Fig. 2.10). These plots consist of 3 axis a, b, and c located within the vertex of the triangular structures, but with differences in what each axis represented by. A ternary diagram that uses TiO_2, MnO and P_2O_5 can be used to discriminate between five tectonic environments of basaltic rocks which are midoceanic ridge, island arc tholeiite, island arc calc-alkaline, oceanic island tholeiitic, and ocean island alkali rocks and boninites which can be classed in island arc fields (Marshall, 1996).

2.10

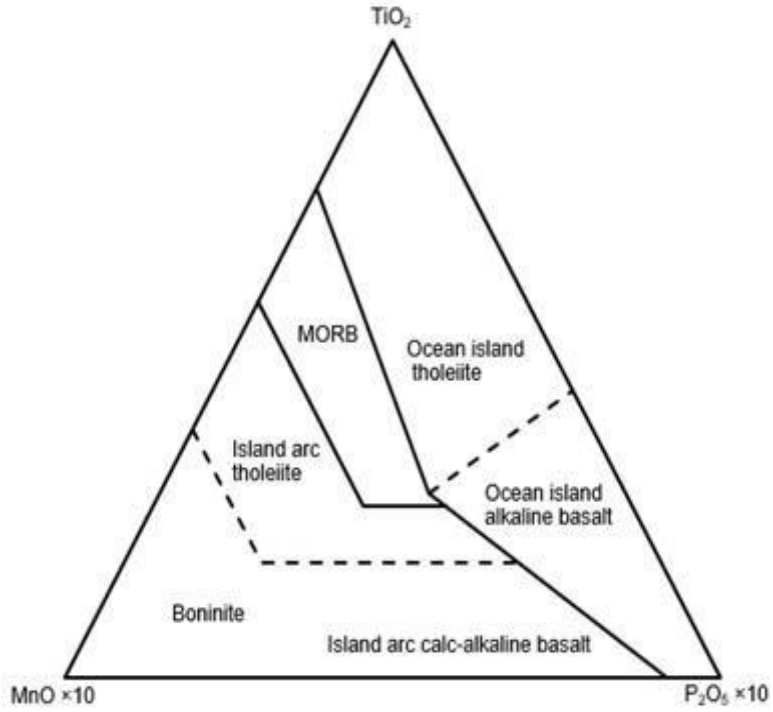

Figure 2.10: Ternary diagram for tectonic discrimination of igneous rocks.

2.11 Analytical Techniques for Magnesite Analysis

2.11.1 X-ray Fluorescence Spectrometry

This is the most widely used method in the analysis of whole-rock geochemical data because it has the capacity to analyse for both major and trace element chemistry within a rock sample. The concentration of detection ranges from 100 % in the major oxides/element to a few parts per million for trace elements. This method can analyse a wide range of sensitivity able to analyse up to 80 elements (Rollinson, 1993).

Analysis using this method is rapid and allows for a large number of samples to be analysed within a very short period with high precision in data obtained. It is limited by the inability to analyse elements that are lighter than Sodium (Na) within the periodic table (Williams, 1987). The way in which X-ray Fluorescence works is that it uses an x-ray beam to excite a sample. A primary X-ray is used to excite a secondary X-ray beam. This secondary ray contains the wavelengths characteristics of the elements that may be present within that sample and the wavelength's intensity is used to determine the concentration of the element.

Analysis of rock samples in X-ray Fluorescence involves the process of first preparing the sample into two different forms of which any one of them can be chosen. Sample can be prepared into a pressed powder disk pellet or prepared into a glass bead using the powder sample fused with lithium tetra-borate or metaborate (Takahashi, 2015).

Merits

- Rapid results, well suited for bulk chemical analysis or major and trace elements in rocks and sediments.
- Requires minimum sample preparation.
- A clean and safe method, without the use of environmentally hazardous chemicals and due to the design of instrument X-radiation poses no risk for the operator.
- High sensitivity (from parts per billion) levels to 100%; and
- Non-destructive (Peter, 2010).

Limitations

- X-ray fluorescence is limited to large samples, typically >1 gram, and the materials that can be prepared in powder form and effectively homogenized.
- Analyses cannot differentiate variation among isotopes of an element; therefore, these analyses are routinely done with other instruments.
- It is limited to materials for which compositionally similar, the well-characterized standard is available; and
- Limited at small spot sizes analyses typically of 2-5 microns, therefore typically for bulk analyses of larger samples of geological materials (Peter, 2010).

2.11.2 Inductive Coupled Plasma Emission Spectrometry

The ICP method has a low detection limit with high precision within various ranges of elemental concentrations. It allows simultaneous measurement of elements within a space of time of approximately 2 minutes making it a rapid method of analysing elements. The ICP method utilizes a flame that burns at an average temperature of about 6000-10 000 K requiring the sample to be in solution and a standard silicate dissolution technique may be employed. The principle behind the method is based on that the solution is passed into an argon plasma as an aerosol (Rollinson, 1993).

A stream of argon atoms forms the plasma that is heated by the inductive heating of a radio-frequency coil using a tesla spark to ignite it. The argon plasma dissociates the samples resulting in many exciting atomic and ionic spectral lines. There is a range of photomultipliers within the ICP that detect these spectral lines and then compares them with the calibrated lines and finally convert the intensities of the spectral line into concentrations (Thompson and Walsh, 1983).

2.11.3 Atomic Absorption Spectrometry

The principle within this method is based upon that atoms of a specific element can absorb electromagnetic radiation when atomized and the wavelength of this radiation that is absorbed is specific to each element. The equipment itself consists of an atomizer, detector, and a light source. It requires the sample to be in solution so that the sample can be atomized using an acetylene nitrous oxide flame or an acetylene air flame (Price, 1972).

The AAS is limited to that it can only analyse samples in solution and that it is limited to the analysis of one element at a time although other instruments can be fitted with multiple torrent lamp holders. It has the capability of analysing all major oxides except for phosphorus (P). This method also exhibits a low detection limit for sodium (Na), potassium (K), magnesium (Mg) and calcium (Ca). This method is the cheapest method of all both in running cost, capital outlay and is mostly used to detect elements that exhibit an atomic number that is too low to be measured by other methods mostly XRF method (Rollinson, 1993). It is also used to analyse transition metals that can be leached from the soil such as in geochemical exploration.

2.11.4 X-ray Diffractometry

Diffraction of X-rays by matter is most powerful when applied to crystalline materials. However, it can also provide important information when applied to amorphous solids or liquids. In diffraction experiments, wavelengths used to lie between approximately 0.5 and 2.5 Å (Nesse, 2012). Because it considers the crystal structure of a sample of matter, XRD spectroscopy can be used to identify minerals in the sample under investigation. The diffraction of X-rays from a fine-grained crystalline powder is based on the principle that a beam of X-rays that strikes a crystal will pass through it, but with scattering or diffraction of the photons in the beam (Fig. 2.11).

Since the particles in the crystal are in a regular or symmetrical arrangement, the Xrays will be scattered in a regular pattern. X-ray crystallography is a technique in which the pattern produced by the diffraction of X-rays through the closely spaced lattice of atoms in a crystal is recorded and then analysed to reveal the nature of that lattice (Nuffield, 1966). This generally leads to an understanding of the material and its molecular structure. The spacing in the crystal lattice can be determined by using
Bragg's law. In the case of XRD, the system is set up similarly to an XRF spectrometer. The main differences are that the sample gets irradiated by monochromatic radiation (one wavelength) and that it has no analysing crystal. The sample itself acts as the analysing crystal and limits XRD analysis to crystalline materials. Since it considers the crystal structure, XRD can identify minerals where XRF is limited to identifying the elements present. Some of the merits of XRD include the following; it is nondestructive, fast, easy sample prep, has a high-accuracy for d-spacing calculations, can be done in-situ, single crystal, poly, and amorphous materials, standards are available for thousands of material systems.

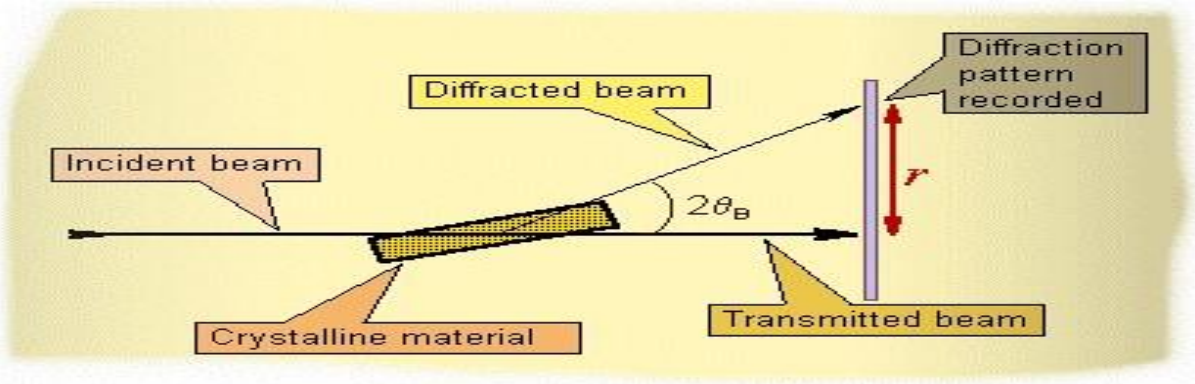

Figure 2.11: Basic operation of XRD (Nesse, 2012).

CHAPTER THREE: MATERIALS AND METHODS

This chapter deals with the materials, methods, and procedures that were applied in the current work. The work was divided into three stages: Desktop study (Stage 1), Fieldwork (Stage 2) and Laboratory work (Stage 3) (Fig. 3.1).

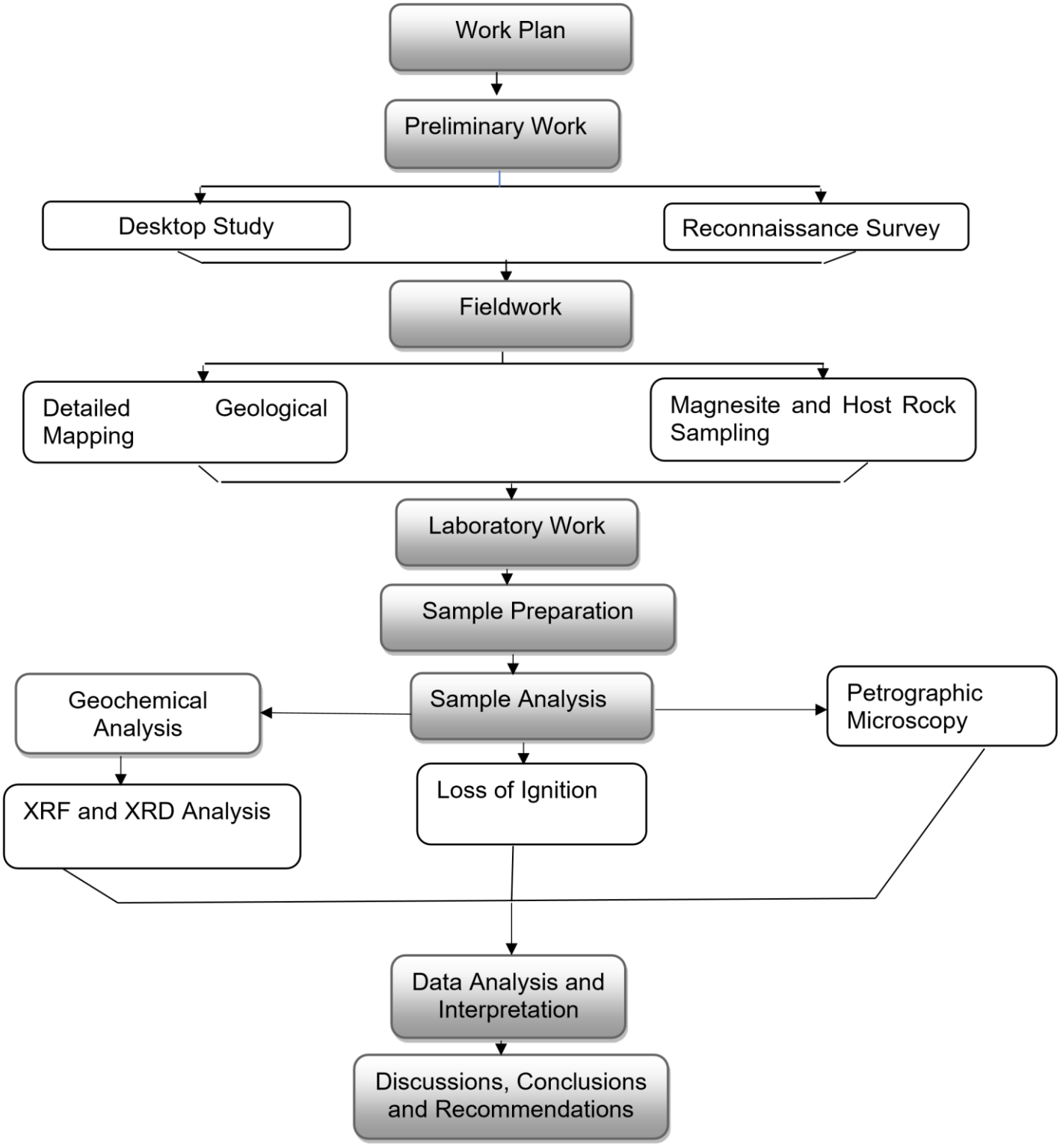

Figure 3.1: Flow chart showing the stages and sequence of the work.

3.1 Preliminary Work

Preliminary work is the procedure of preparation for undertaking actual fieldwork. The common idea of the procedure was to outline methods and materials compulsory to embark on the study before actual fieldwork was carried out. The preliminary work provided knowledge about the study area and the possible constraints that may have an impact on accomplishing the set objectives. Preliminary work comprises of both desktop study and reconnaissance survey.

3.1.1 Desktop Study

The desktop study is the type of work that includes all materials used before undertaking a reconnaissance survey. The desktop study provided a preliminary, yet comprehensive analysis of the project efficiency and reduce costs by providing a clear understanding of future challenges by identifying the potential problem areas and to learn more about the study area. The materials used included the internet, books, journals, geological reports, and topographic and geological maps

3.1.2 Reconnaissance Survey

A reconnaissance survey was conducted before the fieldwork. The purpose of the reconnaissance survey was to obtain preliminary information about geology, topography and to be familiarised with the study area. For example, to know the type of soil, vegetation, and drainage of the study area. A reconnaissance survey was also conducted to ensure safety during fieldwork and to ascertain accessibility of any point in the study area, thus it provided the initial insight into planning.

3.2 Fieldwork

The fieldwork comprised of a collection of information within the study area. The information acquired includes the following: identification of types of rocks, their attitudes, and their structural features. Geological field mapping and magnesite sampling were carried out to collect field data. The primary objective of carrying out fieldwork was to provide a description of outcrops in the area; in addition, sampling was accomplished to collect samples for laboratory analysis.

The following field gears were used during fieldwork (Fig. 3.2):

- GPS was used to take coordinates (longitude and latitude) of the sampling points and the elevation of the sampling points;
- Topographic map was used as a base map during geological mapping;
- Sample bags were used for collecting samples;
- Permanent marker was used to mark the sample number on the sample bag;
- Geological hammer and sledgehammer were ideal for collecting magnesite samples and rock specimens;
- Compass was used to measure the attitude (Strike, Dip angle and Dip direction) of the outcrops during fieldwork;
- Tape measure was used to measure the thickness and length of the magnesite veins within the host rock; and
- Hand lens was used as a magnifier for mineralogical identification in the field.

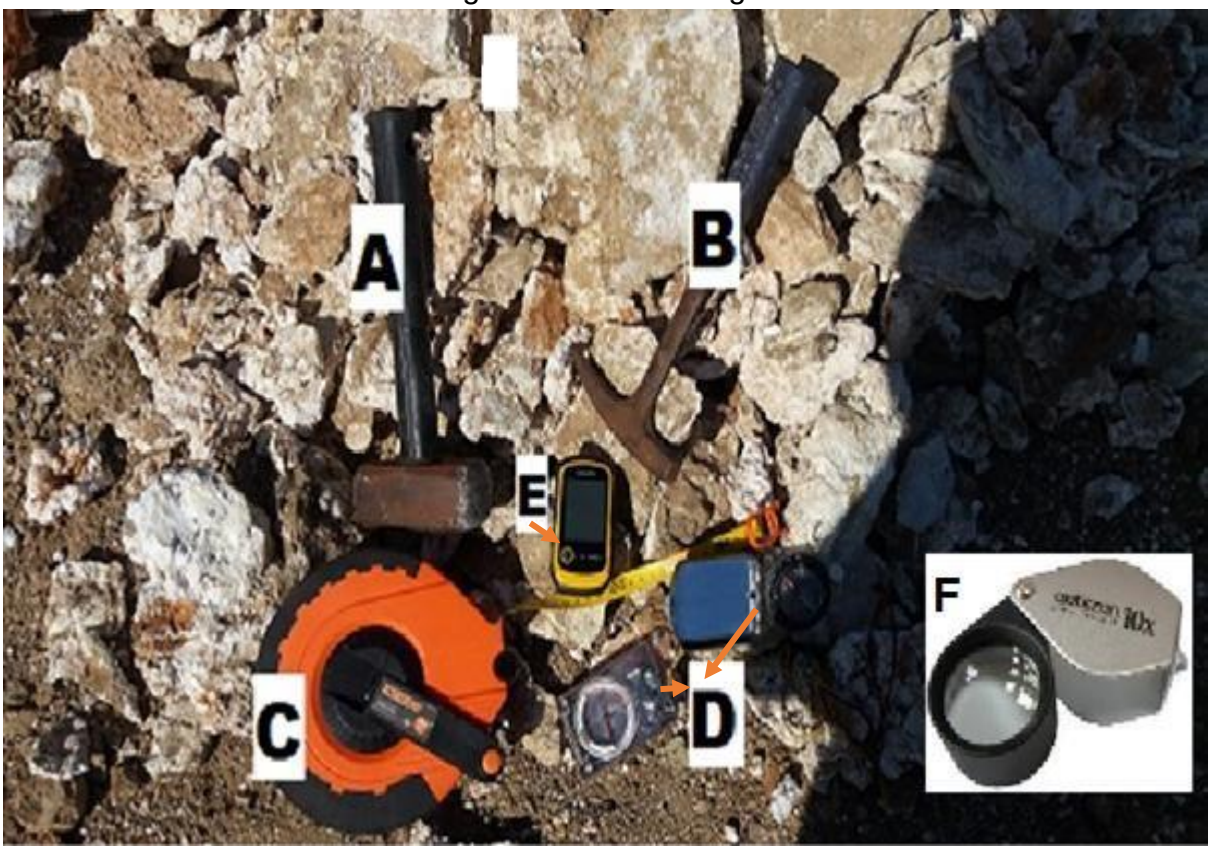

Figure 3.2: Equipment and implements that were used during fieldwork: A-Sledgehammer; B-Geological hammer; C-Tape measure; D-Compasses; E-GPS; and F-Handheld lens.

3.2.1 Geological Mapping of Muyexe Area

Geological field mapping was carried out to produce a geological map of the study area. Field data was compiled by studying outcrops as well as their immediate environment. The study area (Fig. 3.3) was divided into five traverses of 500 m wide each that along 7 profiles cut across the general strike of lithologies in the area. The study area had a total area of 6.25 km^2 with dimensions 2.5 km by 2.5 km. Field data was collected by mapping each outcrop within the traverses.

Brunton compass and GPS were used to locate ourselves in the field. However, the compass was also used to measure the attitudes of lithologies while the GPS was used to record the location of outcrops and altitude of the outcrop.

During geological field mapping, the description of texture and mineralogy of the rock specimens was done with the aid of a hand lens and recorded in a notebook. The contact between the rock outcrop and encountered geological structures were recorded in the field notebook and photographed for later referencing when compiling a geological map of the study area.

A total of 62 rock specimens were collected using a sledgehammer and geological harmer by chip sampling method and placed inside a sample bag marked with a permanent marker. The collected rock specimen weighed about 2 kg. The rock spacemen were collected for further laboratory analysis using petrographic study and whole-rock geochemistry.

Data collected from the geological mapping was used to compile a geological map of the area as well as a cross-section.

The coordinates and elevation of sampled rocks during geological mapping are presented in Table 3.1, while the more detailed description of the rocks is presented in Appendix A.

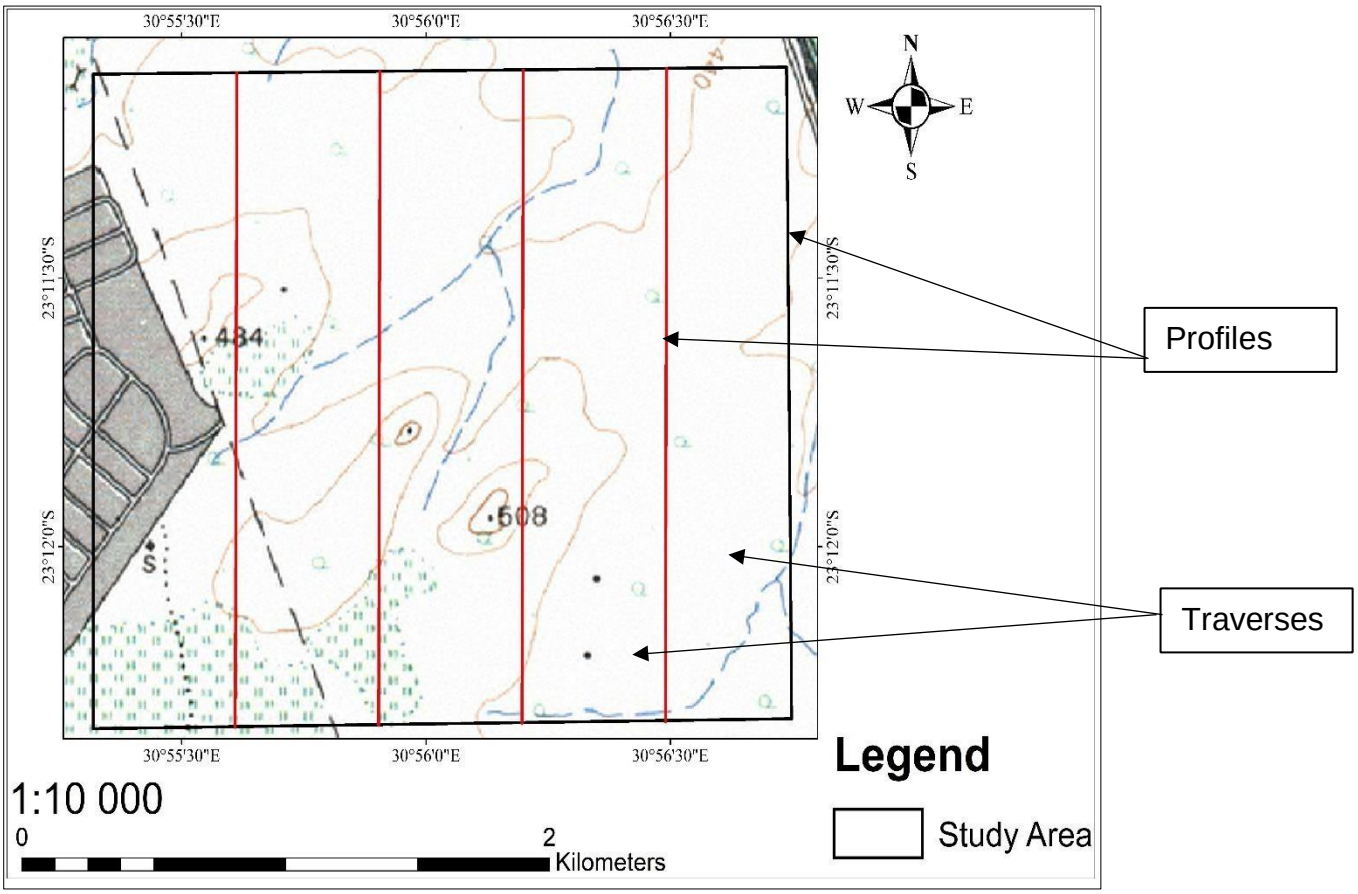

Figure 3.3: Topographical map (Base map) (ArcGIS Esri, 2018).

Table 3.1: Coordinates and elevation of sampled rocks during geological mapping

Sample I. D	Latitude	Longitude	Elevation
T1S1	23^{0}11'25.1''S	30^{0}55'28.3''E	458 m
T1S2	23^{0}11'26.1''S	30^{0}55'29.0''E	459 m
T1S3	23^{0}11'26.6''S	30^{0}55'29.2''E	462 m
T1S4	23^{0}11'27.0''S	30^{0}55'29.4''E	462 m
T1S5	23^{0}11'27.7''S	30^{0}55'30.3''E	464 m
T1S6	23^{0}11'21.6''S	30^{0}55'31.1''E	465 m
T1S7	23^{0}11'31.1''S	30^{0}55'32.3''E	470 m
T1S8	23^{0}11'34.4''S	30^{0}55'32.2''E	476 m
T1S9	23^{0}11'36.1''S	30^{0}55'32.0''E	476 m
T1S10	23^{0}11'37.9''S	30^{0}55'32.7''E	477 m
T1S11	23^{0}11'43.7''S	30^{0}55'35.1''E	465 m
T1S12	23^{0}11'47.9''S	30^{0}55'40.0''E	457 m
T1S13	23^{0}11'54.7''S	30^{0}55'40.8''E	476 m
T1S14	23^{0}12'04.4''S	30^{0}55'44.9''E	486 m
T1S15	23^{0}12'10.09'' S	30^{0}55'45.1''E	470 m
T1S16	23^{0}12'12.2''S	30^{0}55'46.0''E	470 m
T1S17	23^{0}12'13.2''S	30^{0}55'46.8''E	470 m
T1S18	23^{0}12'15.3''S	30^{0}55'48.5''E	470 m
T2S1	23^{0}11'17.8''S	30^{0}55'37.0''E	450 m
T2S2	23011'21.2''S	30055'44.5E	457 m
T2S3	23011'19.9S	30055'43.58''E	457 m
T2S4	23^{0}11'22.2''S	30^{0}55'44.6''E	457 m
T2S5	23^{0}11'21.8S	30^{0}55'45.2E	459 m
T2S6	23^{0}11'26.4''S	30^{0}55'47.1''E	454 m
T2S7	23^{0}11'29.5''S	30^{0}55'48.7''E	456 m
T2S8	23^{0}11'36.8''S	30^{0}55'52.4''E	451 m
T2S9	23^{0}11'40.3''S	30^{0}55'53.2''E	455 m
T2S11	23^{0}11'47.0''S	30^{0}55'55.4''E	485 m
T2S12	23^{0}11'50.5''S	30^{0}55'58.8''E	479 m
T2S13	23^{0}11'56.9''S	30^{0}56'01.6''E	473 m
T2S14	23^{0}12'01.1''S	30^{0}56'03.0''E	475 m
T2S15	23^{0}12'10.9''S	30^{0}56'04.2''E	463 m
T2S17	23^{0}12'12.2''S	30^{0}56'08.7''E	459 m
T3S1	23^{0}11'56.1''S	30^{0}56'15.0''E	464 m
T3S2	23^{0}11'52.4''S	30^{0}56'16.1''E	467 m
T3S4	23^{0}11'38.7''S	30^{0}56'07.0''E	450 m
T3S5	23^{0}11'32.9''S	30^{0}56'04.9''E	441 m
T3S6	23^{0}11'31.1''S	30^{0}56'01.4''E	444 m
T3S7	23^{0}11'29.5''S	30^{0}56'00.4''E	445 m
T3S8	23^{0}11'27.6''S	30^{0}55'56.5''E	453 m
T4S1	23^{0}11'14.5''S	30^{0}55'58.2''E	411 m
T4S2	23^{0}11'30.9''S	30^{0}55'58.0''E	449 m
T4S3	23^{0}11'36.7''E	30^{0}56'20.1''E	454 m
T4S4	23^{0}11'28.2''S	30^{0}56'77.1''E	457 m
T4S5	23^{0}11'48.3''S	30^{0}56'17.3''E	466 m
T4S6	23°11'51.30"S	30°56'23.14"E	462 m
T4S7	23°11'53.61"S	30°56'24.95"E	458 m
T4S8	23°12'11.13"S	30°56'22.57"E	458 m
T5S1	23^{0}11'09.7''S	30^{0}56'25.6''E	416 m
T5S2	23^{0}11'10.2''S	30^{0}56'27.6''E	420 m
T5S3	23^{0}11'12.3''S	30^{0}56'28.1''E	423 m
T5S4	23^{0}11'14.7''S	30^{0}56'30.0''E	427 m
T5S5	23^{0}11'23.6''S	30^{0}56'30.9''E	429 m
T5S6	23°12'10.77"S	30°56'33.79"E	450 m
TRS1	23^{0}12'03.''S	30^{0}55'45.5''E	482 m
TRS2	23°11'54.14"S	30°55'33.35"E	470 m
TRS3	23°11'42.19"S	30°56'16.78"E	468 m
TRS4	23°11'23.9"S	30°55'33.2"E	450 m
TRS5	23°11'39.9"S	30°55'47.8"E	450 m
TRS6 (T2S)	23°11'52.80"S	30°55'51.60"E	487 m
TRS7 (T3S9)	23°11'52.80"S	30°56'6.00"E	485 m

3.2.2 Sampling

A total of 20 magnesite samples and 4 host rock specimens were collected at the mine (Fig. 3.4). The size of the magnesite samples ranged from 0.5 kg to 2 kg, while host rock specimens were about 2 kg. Magnesite was sampled, using a chip sampling method for vein deposits. Collected magnesite samples were marked according to where they were sampled. Those that were sampled at the first mine site were marked M1, while those sampled from the second mine site were marked M2. Host rocks were marked according to their sequence of sampling. A permanent marker was used to mark the sample during sampling, and the sample was then stored in a sample bag. Both rock specimens and magnesite samples were collected from locations where magnesium mineralisation was intensive, thus, consideration was given to the geological setting of the magnesite mineralisation. Then sampling was done along a profile, across the magnesite veins in such a way that the underlying host rock was also covered (Bashir, 2008). The samples were also collected from contacts of host rocks and veins filled with magnesite. Physical characteristics such as colour, texture, structure, and alteration of the samples were recorded and presented in Table 3.2. The samples were then taken to the laboratory for geochemical investigations.

Figure 3.4: Sampling of magnesite veins at the mine: A-Tape measure; BSledgehammer; and C-Geological hammer.

Table 3.2: Characteristics of sampled magnesite and host rocks

Sample. ID	Colour	Texture	Structure	Alteration
M1S1	Milky white	Cryptocrystalline	Vein type	None
M1S2	Milky white	Cryptocrystalline	Vein type	None
M1S3	Milky white	Cryptocrystalline	Vein type	None
M1S4	Milky white	Cryptocrystalline	Vein type	None
M1S5	Milky white	Cryptocrystalline	Vein type	None
M1S6	Milky white	Cryptocrystalline	Vein type	None
M1S7	Yellowish white	Cryptocrystalline	Vein type	None
M1S8	Milky white	Cryptocrystalline	Vein type	None
M1S9	Milky white	Cryptocrystalline	Vein type	None
M1S10	Milky white	Cryptocrystalline	Vein type	None
M2S1	Yellowish white	Cryptocrystalline	Vein type	None
M2S2	Milky white	Cryptocrystalline	Vein type	None
M2S3	Milky white	Cryptocrystalline	Vein type	None
M2S4	Milky white	Cryptocrystalline	Vein type	None
M2S5	Milky white	Cryptocrystalline	Vein type	None
M2S6	Milky white	Cryptocrystalline	Vein type	None
M2S7	Milky white	Cryptocrystalline	Vein type	None
M2S8	Milky white	Cryptocrystalline	Vein type	None
M2S9	Milky white	Cryptocrystalline	Vein type	None
M2S10	Brownish white	Cryptocrystalline	Vein type	None
HR1	Greenish grey	Serpentinite	None	Medium
HR2	Greyish	Serpentinite	Weathered	High
HR3	Brownish to whitish	Serpentinite	Weathered (Magnesite Veins)	High
HR4	Greenish to brownish	Elephant skin type	None	High

3.3 Laboratory Work

Samples collected at the field were taken to the University of Venda, Department of Mining and Environmental Geology laboratory for preparation and laboratory analysis.

3.3.1 Sample Preparation

Preparation of samples for geochemical analysis involved the following steps: cutting, crushing, milling, pelletization for X-ray spectrometry analysis.

Cutting of Rocks Specimens and Magnesite Samples

Rock specimens and magnesite samples that were brought back from the field were cut in half using a diamond blade rock cutter. The objective of this was to split the rock and magnesite into halves, where one half can be used for petrographic study while the other half can be used for geochemical study.

Magnesite and Rock Crushing

Magnesite and rock samples were crushed using a jaw crusher (Fig. 3.5A) to further downsize the samples. The crusher was cleaned thoroughly with a wiper cloth and acetone prior to crushing to remove residual samples material to avoid crosscontamination of the samples. The crushed samples were then split using a riffle splitter.

Milling

Samples for X-ray fluorescence spectrometry and X-ray Diffractometry are needed to be in powdered form and as such a RS 200 milling machine (Fig. 3.5B) was utilised to mill and pulverize the crushed rock specimen and magnesite samples into a fine powder. The machine was set to operate at a rotational speed of 700 rpm and rotate for a minimum of 5 min per sample. After milling each sample, the milling pot was cleaned thoroughly prior to milling a new sample. The milling pots were cleaned using quartz to prevent contamination, the pots were also cleaned using acetone and the sample to be milled to ensure quartz did not affect the SiO_2 content during analysis. The milled samples were then stored in a new sampling bag and tagged with its respective sample labels.

Pelletisation of Samples for XRF

The XRF (the Bruker S2 ranger) uses a pressed pellet for analysis. The pressed powder pellet was made using a binding agent of approximately 2.5 grams (Boric acid) and about 10 grams of the milled sample. A total of 16 rock samples and 20 magnesite samples were pelletised. The sample was placed in an aluminium cup of 40 mm diameter and with boric acid (Fig. 3.5C) as the binding agent, used to form pellets. A 30-ton pressing machine was used to press and compress the samples into pellets. The compressing period was a minute for each sample. After the sample was pelletized, the equipment was cleaned using Acetone.

Figure 3.5: Laboratory equipment used for the preparation of samples for XRF analysis: A-Jaw crusher; B-Milling machine and C-Pellets making products.

Preparation of Samples for XRD Analysis

The representative portion (± 10 g/sample) of crushed and milled magnesite samples and rock specimen were taken to the University of Johannesburg (UJ), Analytical Laboratory (Spectrum), in Johannesburg for X-ray diffraction analysis. These samples included 12 rock samples and 2 magnesite samples. At the University of Johannesburg, crushed and milled samples (<75µm) were further milled to a size of 10µm using a small mill and measured to 1g of sample for analysis. The powdered samples were then filled in the sample holder by using a backfill method, i.e. locking the sample holder onto the stand and then filling it from the backside. For this, the

sample was uniformly spread on top of the stage and pressed gently to prepare a flat surface filled in a sample holder.

Thin Section Preparation

The samples to be used for the petrographic study were obtained through the preparation of thin sections of rock specimens. Several steps were followed for the preparation of thin sections, which included the cutting of rock specimens, trimming, bonding, cutting of bonded samples, grinding, and polishing.

Cutting

Large rock specimens from the field were cut through a rock cutter into a rectangular manageable slab of approximately 50 X 80 mm size and trimmed to 30 X 40 mm size, using a diamond rock saw cutter (Fig. 3.6A). The specimen was cut into two equal parts, whereby one part was kept as a duplicate for future work, while the other half was used to produce a thin section.

Polishing and Bonding Slabs

The samples were then polished, using silicon carbide grit in a sequence of 120, 220, 400, 800 and 1000 grit sizes until samples were smooth for the bonding process. The polished samples were then cleaned by washing in an ultrasonic bath before they were oven-dried at 80^{o}C for 15 minutes (Fig. 3.6E). After drying, samples were cooled to room temperature before bonding. The epoxy bonding agent was prepared by mixing hardener and resin at a ratio of 2:15 (2 parts hardener and 15 parts of resin). Samples were bonded on frosted glass slides using epoxy, then placed on a bonding jig for 24 hours for effective bonding (Fig. 3.6B).

Cutting and Grinding

The bonded samples were first cut to reduce the thickness from 40 mm to 10 mm using Streuers Accutum-50 cutting machine (Figure 3.6C). Cutting process took approximately 8 to 20 minutes. The samples were then grinded to 50 micrometers for approximately 30 minutes. The instrument was programmed to grind and stop the process automatically when the 50-micrometer size was achieved.

Polishing

Ground samples were placed into a polishing machine called a Rotopol-35 polishing machine (Fig. 3.6D). Samples were polished using the polishing disk for 2 hours. Once polished, the sample thickness was checked using a micrometer gangue to confirm the required thickness of approximately 30µm. The thin section was then cleaned with deionized water, air-dried, ready for study.

Figure 3.6: Laboratory equipment used for thin preparation: A-Diamond saw cutter; BBonding jig; C-Struers Accutum-50 cutting machine; D-Struers Rotopol-35 polishing; and E-Drying oven.

3.3.2 Sample Analysis

Samples were analysed by, Petrographic microscope, X-Ray Fluorescence, and Xray diffractometer.

3.3.2.1 Petrographic Study

Petrographic microscopy was used to investigate the optical properties of rocks collected during fieldwork. These properties are extremely important in identifying the host rocks associated with magnesite mineralisation. The optical properties of rocks include colour variations under plane-polarized light, fracture characteristics of the grains, grain size, refractive index, relief, extinction angle, pleochroism, and birefringence, as well as mineral assemblages.

An Olympus BX-50 petrographic microscope (Fig. 3.7) was used to provide highresolution detail of the thin sections.

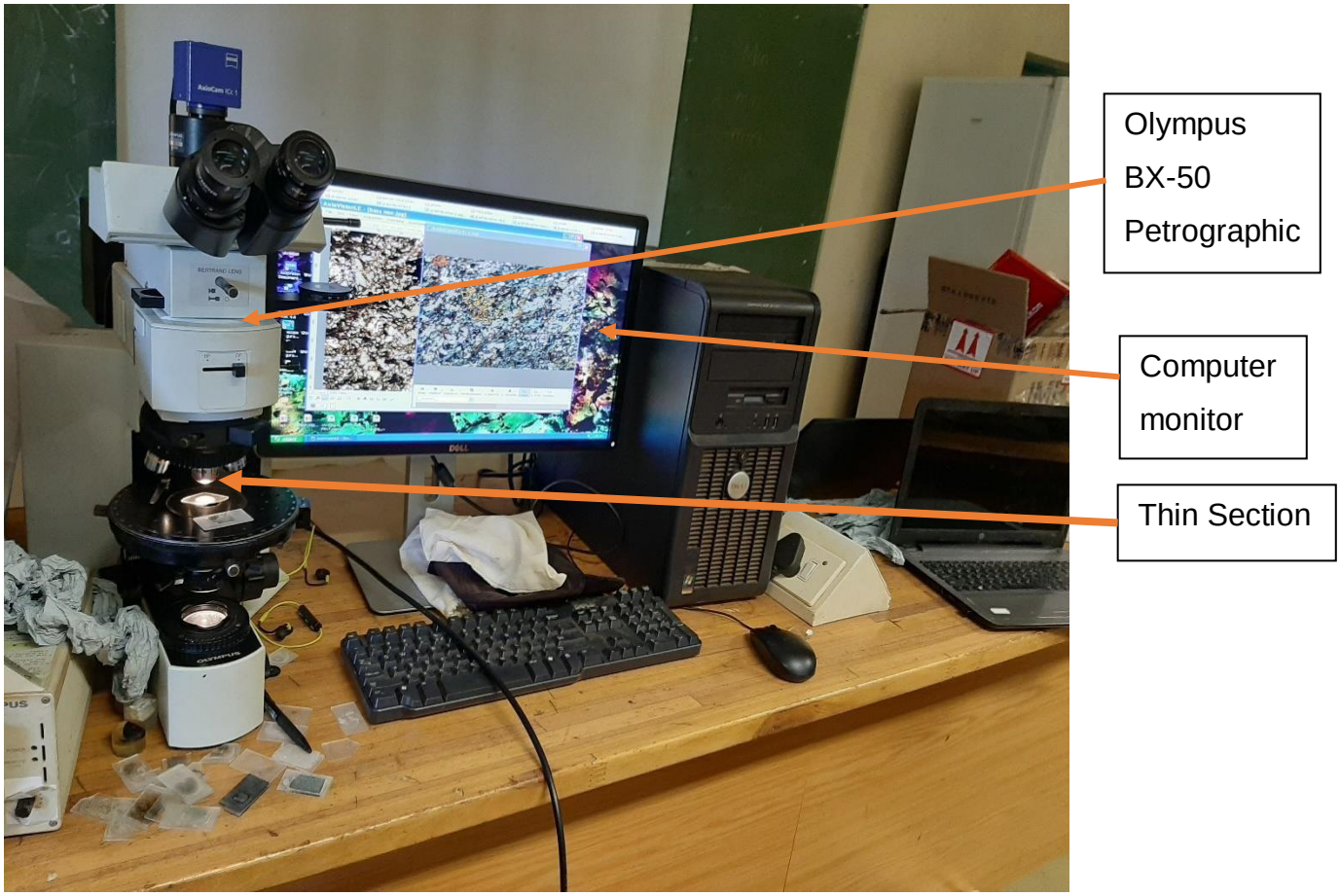

Figure 3.7: Olympus BX-50 petrographic microscope set-up showing the components parts.

A detailed description of 14 rock specimens and their thin sections, that are representative specimens of about 63 rocks that were identified in the study area are presented below.

Hornblende Chlorite Schist

The hornblende chlorite schist outcrop was generally grey to light brown (Fig. 3.8). It was well foliated and had a sharp contact with basalt, talc schist, and quartzite throughout the Muyexe area. The hand specimen of the rock had a vitreous to silky lustre. It was pale green to grey in colour and fine to medium-grained. It comprises mainly of hornblende minerals and fine-grained carbonate crystals. It had a lepidoblastic texture with well-developed schistosity. Occasionally the rock was well sheared.

Under the microscope (Fig. 3.9), the rock sample showed foliations of hornblende and chlorite grains. The brownish mineral grains are of hornblende, the whitish minerals are chlorites, while the blueish mineral is anthophyllite. The opaque mineral chromite is present as an accessory phase within the rock. The mineralogy of the rock was confirmed with XRD analysis and the rock contains the following minerals: magnesiohornblende, anthophyllite, and clinochlore.

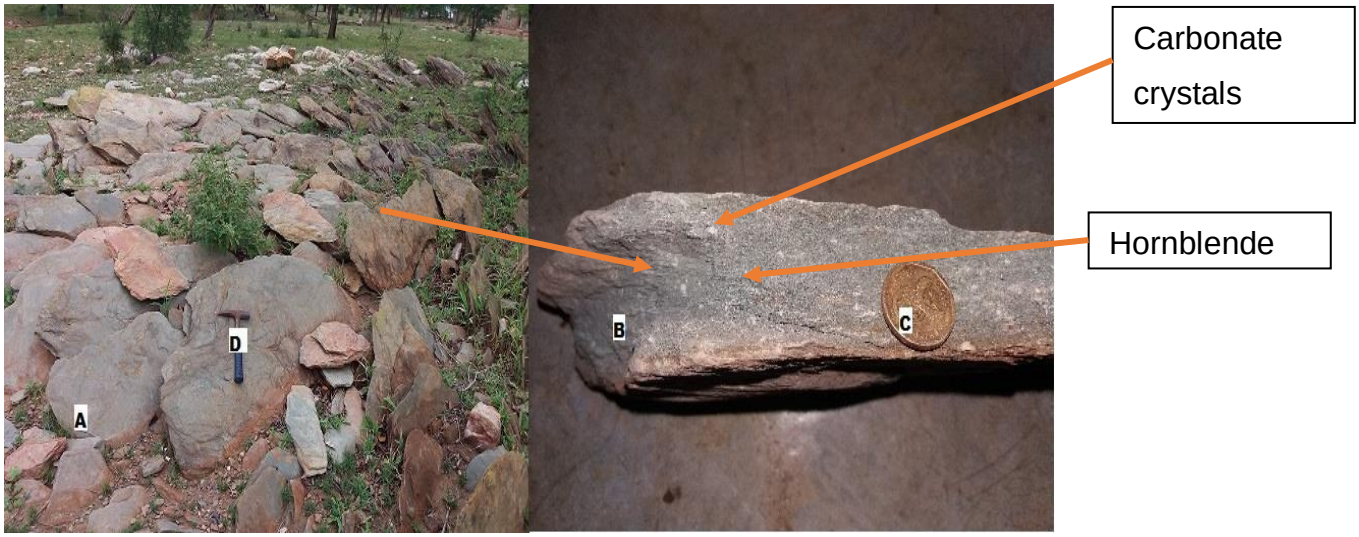

Figure 3.8: A photograph of: A-Hornblende chlorite schist outcrop; B-Hand specimen; C-Coin; and D-Geological hammer as a scale.

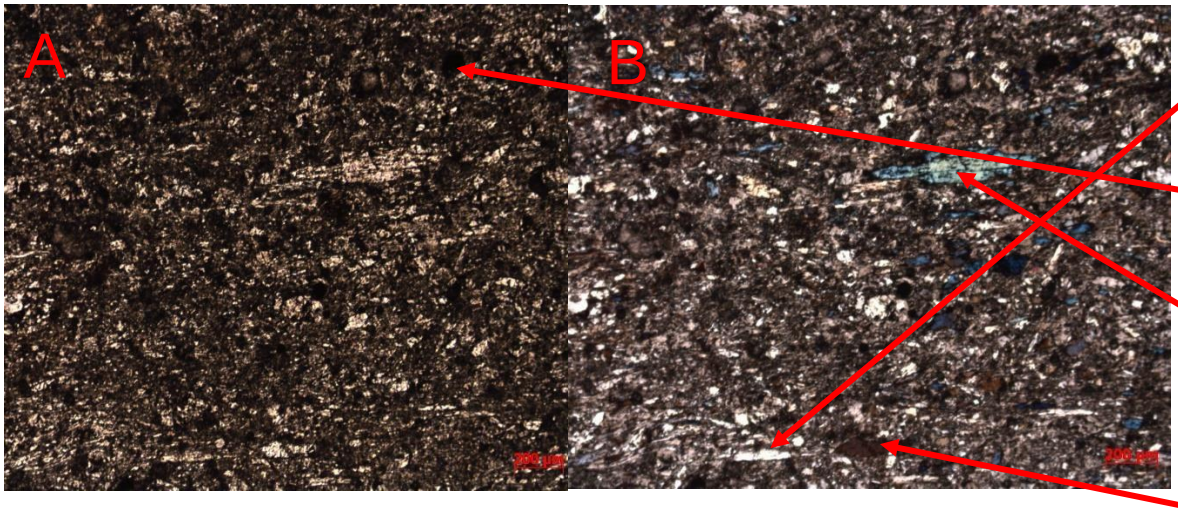

Figure 3.9: Photomicrograph of fine-grained hornblende chlorite schist with chlorite grains dominating the rock and being aligned display schistosity. Photomicrography are in a plane polarised light (A) and cross polarised light (B).

Vitreous Quartzite

Vitreous quartzite was generally the most dominant rock along the north-eastern part of the Muyexe area. The quartzite outcrop (Fig. 3.10) was generally white to pink in colour. The pink stain being the result of oxidation of iron. It was hard and tough to break because of the interlocking crystalline structure of quartz which is cemented by silica. The hand specimen of the quartz was white to pink in colour and had a granular texture with medium grain sizes, which can be seen with naked eyes.

In a thin section (Fig. 3.11), when viewed in plane-polarized light (PPL), quartz was colourless with low relief and had no cleavage. Under cross-polarized light (XPL) quartz displays low interference birefringence colours. When the stage was rotated, the quartz grains displayed a change in colours, thus presenting a phenomenon known as birefringence in quartz grains. The black opaque mineral was iron oxide, which usually stains the rock into a pinkish colour.

Figure 3.10: A photograph of: A-Quartzite outcrop; B-Hand specimen; C-Ruler; and DGeological hammer for scale.

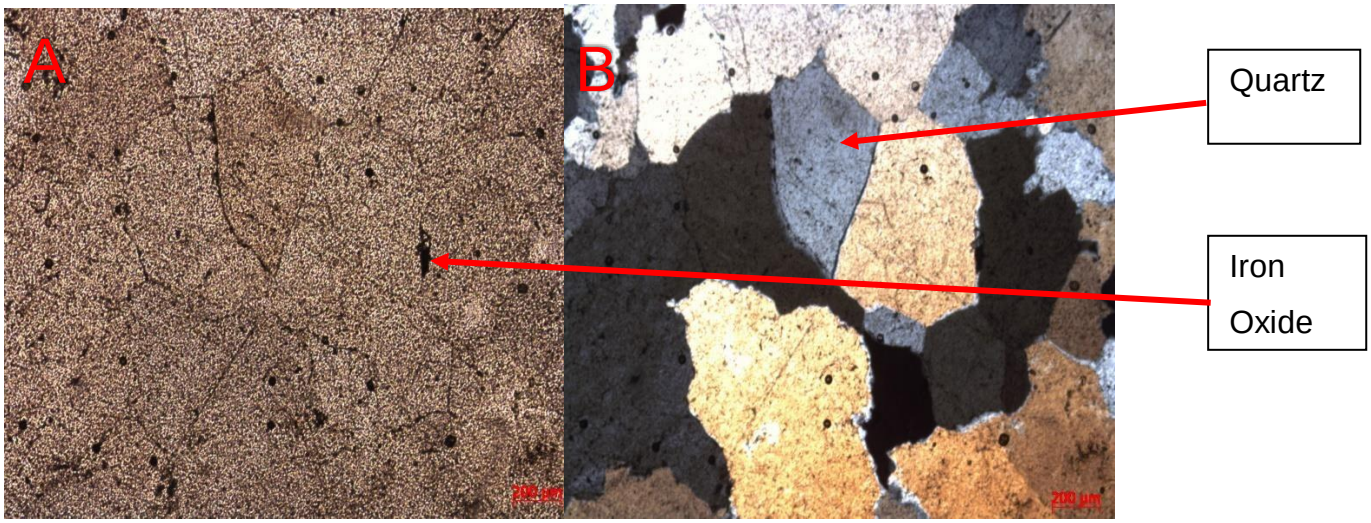

Figure 3.11: Photomicrograph of quartzite with quartz grains dominating the rock and opaque grains are chromite and magnetite. Photomicrography are in a plane polarised light (A) and cross polarised light (B).

Banded Iron Formation

The banded iron formation (BIF) was partially weathered and it consisted of alternating layers of different minerals (Fig. 3.12). The length of the outcrop was very short, and it did not extend to a large area. The hand specimen of the BIF was red to dark grey, with white fibrous. It consists of alternating layers of cherts, iron oxide and jasper. The fibrous vein may consist of carbonate minerals such as asbestos. It had a course to large-grained and a bended, trellis texture with an uneven fracture.

In the thin section (Fig. 3.13) the rock exhibits bladed quartz and iron oxide grains. The grains were elongated and ranging from 100 mm to 300 mm. When viewed in plane-polarized light (PPL), quartz is colourless with low relief and with no cleavage. Quartz also shows a systematically oriented crystal in the iron oxide matrix. Under cross-polarized light (XPL) quartz displays low interference birefringence colours. The iron oxide was present in some parts of the microcrystalline quartz (Chert).

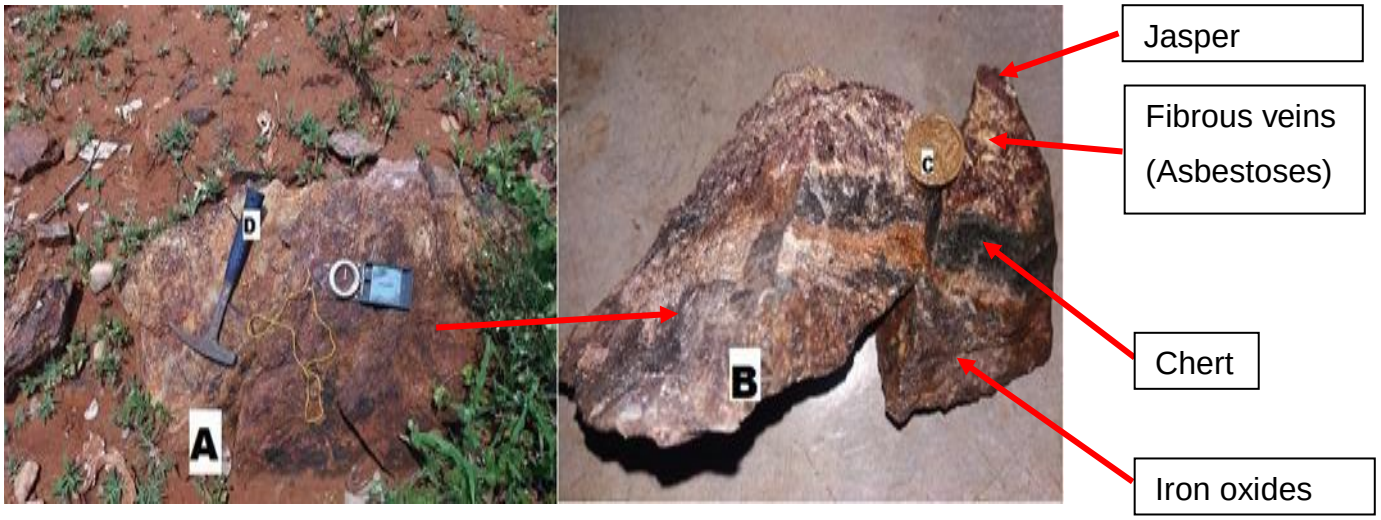

Figure 3.12: A photograph of a: A-Banded iron formation; B-Hand specimen of BIF; CCoin; and D-Geological hammer as a scale.

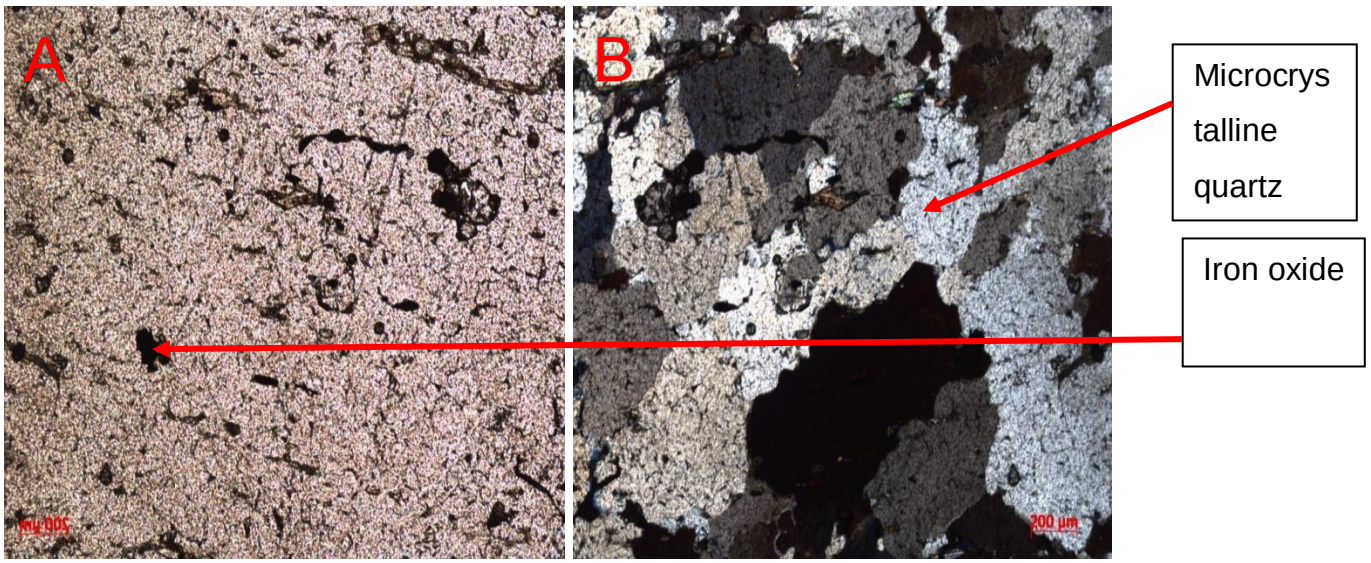

Figure 3.13: Photomicrograph of banded iron formation rock with microcrystalline quartz grains dominating the rock and opaque grains are iron oxide. Photomicrography are in a plane polarised light (A) and cross polarised light (B).

Amphibolite

The outcrop of this rock was dark grey. It was compact and hard to break where it was not weathered. The outcrop extended parallel to the other rocks in the area, forming a dyke or sills (Fig. 3.14). The outcrop was located near the top of a hill. The hand specimen was greenish to dark grey. It was glassy, rough, and shiny. It was heavy and this was due to the presence of iron and magnesium. It had a mixture of phaneritic and porphyritic texture. It composes of dark and light minerals such as hornblende and quartz.

The thin section (Fig. 3.15) indicated that the rock was dominated by the hornblende, quartz, and plagioclase minerals. According to XRD analysis, the hornblende mineral is magnesio-hornblende and the plagioclase mineral is the anorthite.

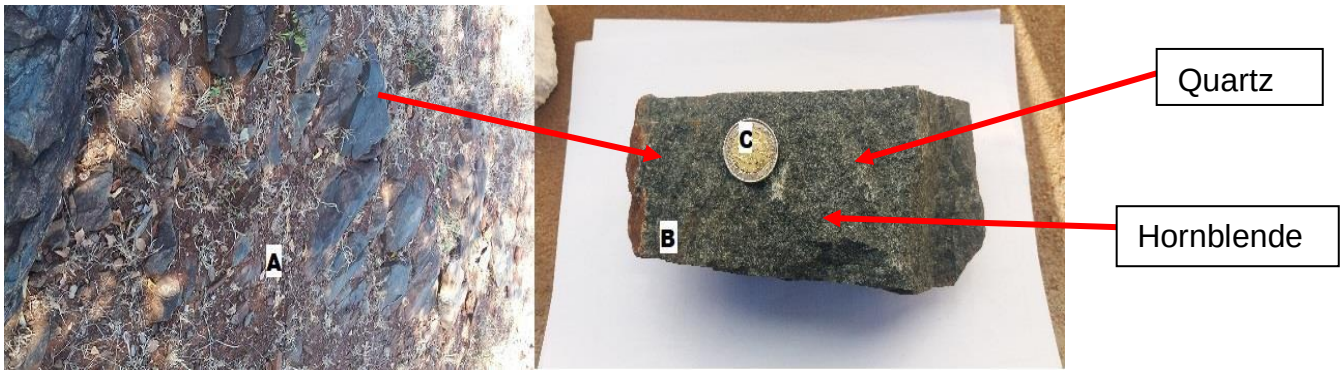

Figure 3.14: A photograph of: A-Amphibolite; B-Hand specimen; and C-Coin (C) as scale.

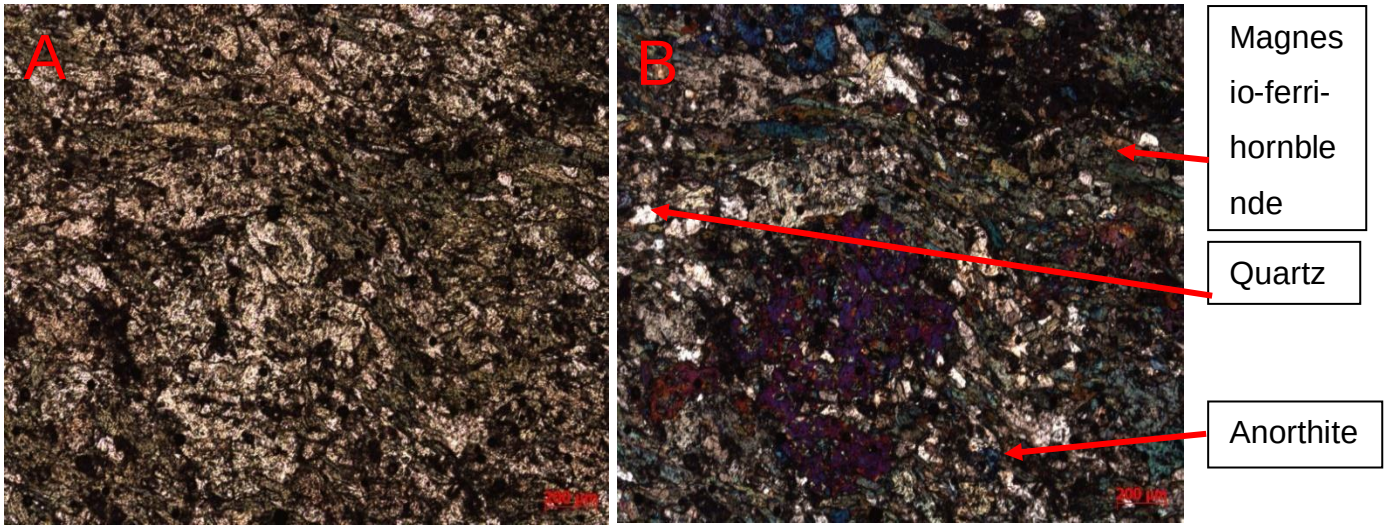

Figure 3.15: Photomicrograph of amphibolite rock. Photomicrography are in a plane polarised light (A) and cross polarised light (B).

Serpentinites

The serpentinite outcrop (Fig. 3.16) was grey and showed signs of weathering. The rock was mostly found in high elevation areas, mostly along the hills. The weathering left a stain of grey to brown layer, this was due to being chemically altered by hydrothermal fluid. The hand specimen (Fig. 3.16) was generally pale green to grey. It had a coarse grain size and a serpentine texture. Composed of serpentine minerals and it was light and not heavy, with some of the serpentines having magnesite veins on it.

Under the microscope (Fig. 3.17 and Fig. 3.18), the rock was dominated by a finegrained matrix of serpentine, with a large crystal of olivine, cummingtonite, tremolite and actinolite. Opaque grains of chromite were present in the thin section. The olivine was showing signs of serpentinisation. According to XRD data, the rock is composed of actinolite, tremolite, cummingtonite, and chromite. This was also confirmed by thin section analysis.

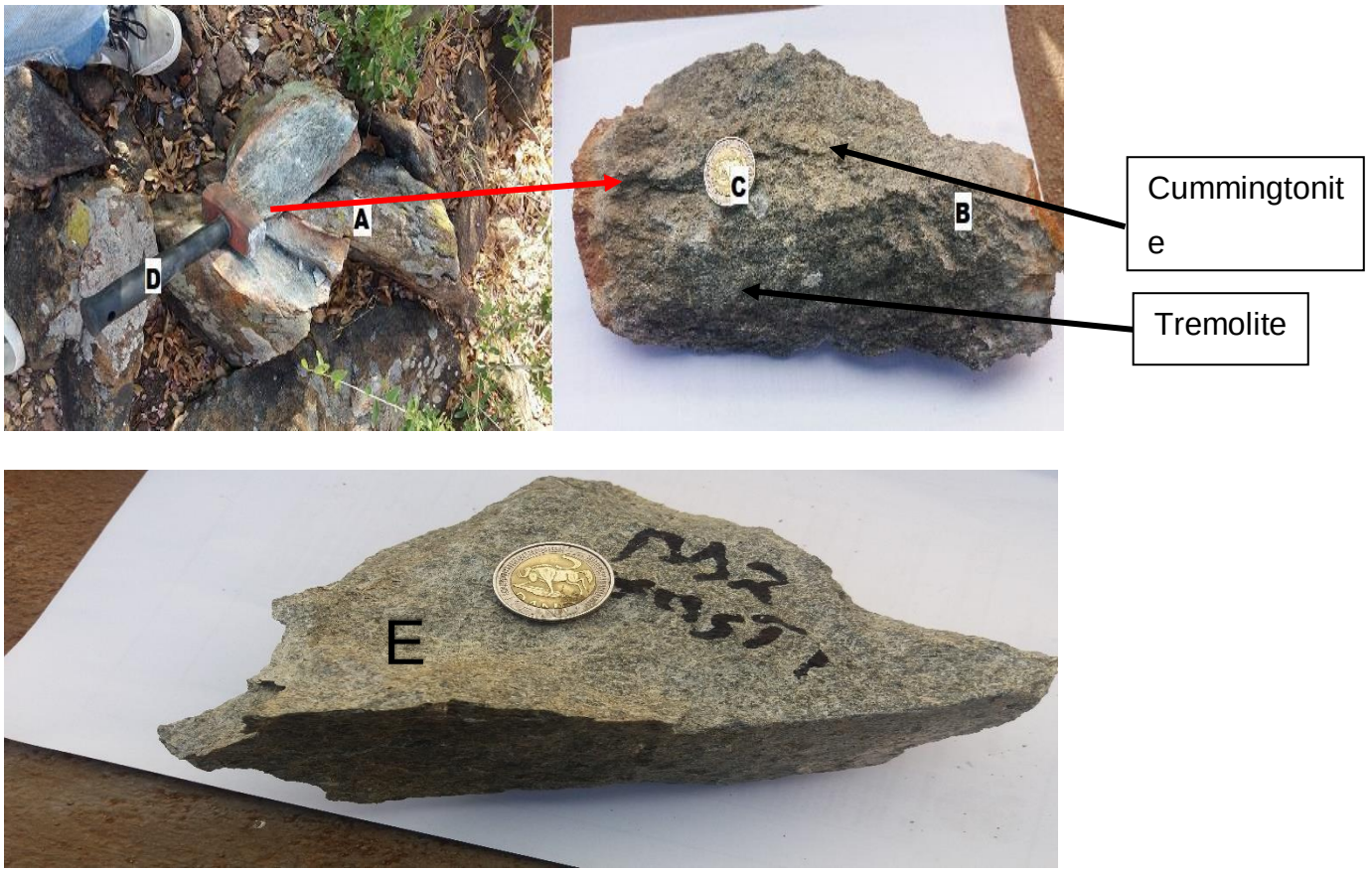

Figure 3.16: A photograph of: A-Fresh serpentinite rock outcrop; B-Hand specimen; C-Coin; D-Sledgehammer as a scale; and E-Hand specimen of altered serpentinite.

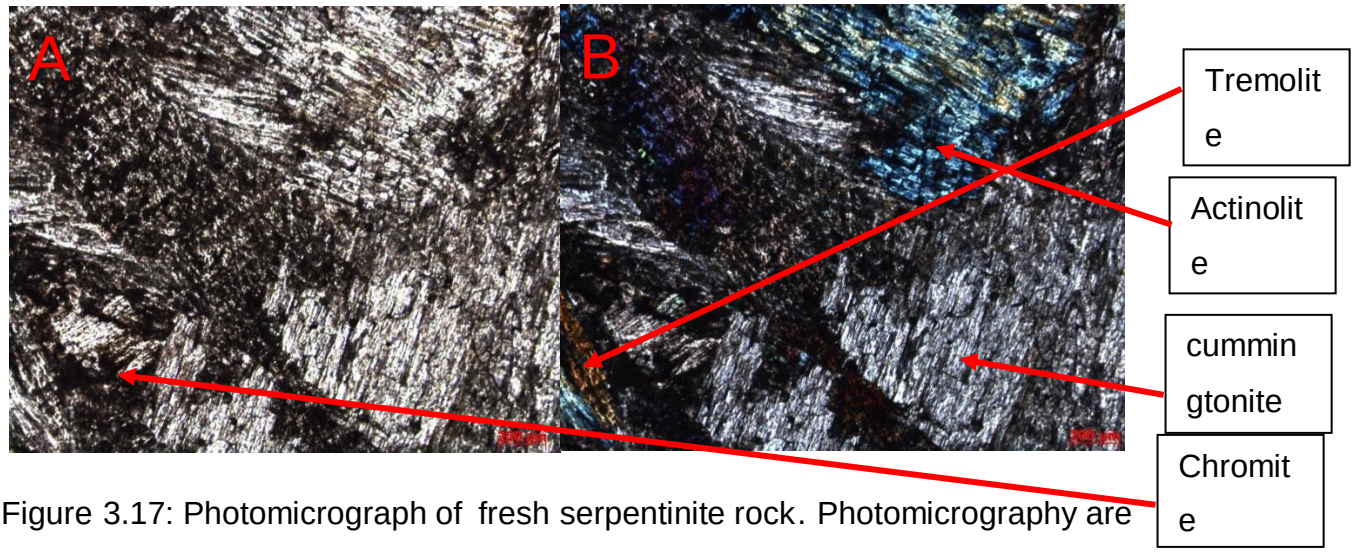

Figure 3.17: Photomicrograph of fresh serpentinite rock. Photomicrography are in a plane polarised light (A) and cross polarised light (B).

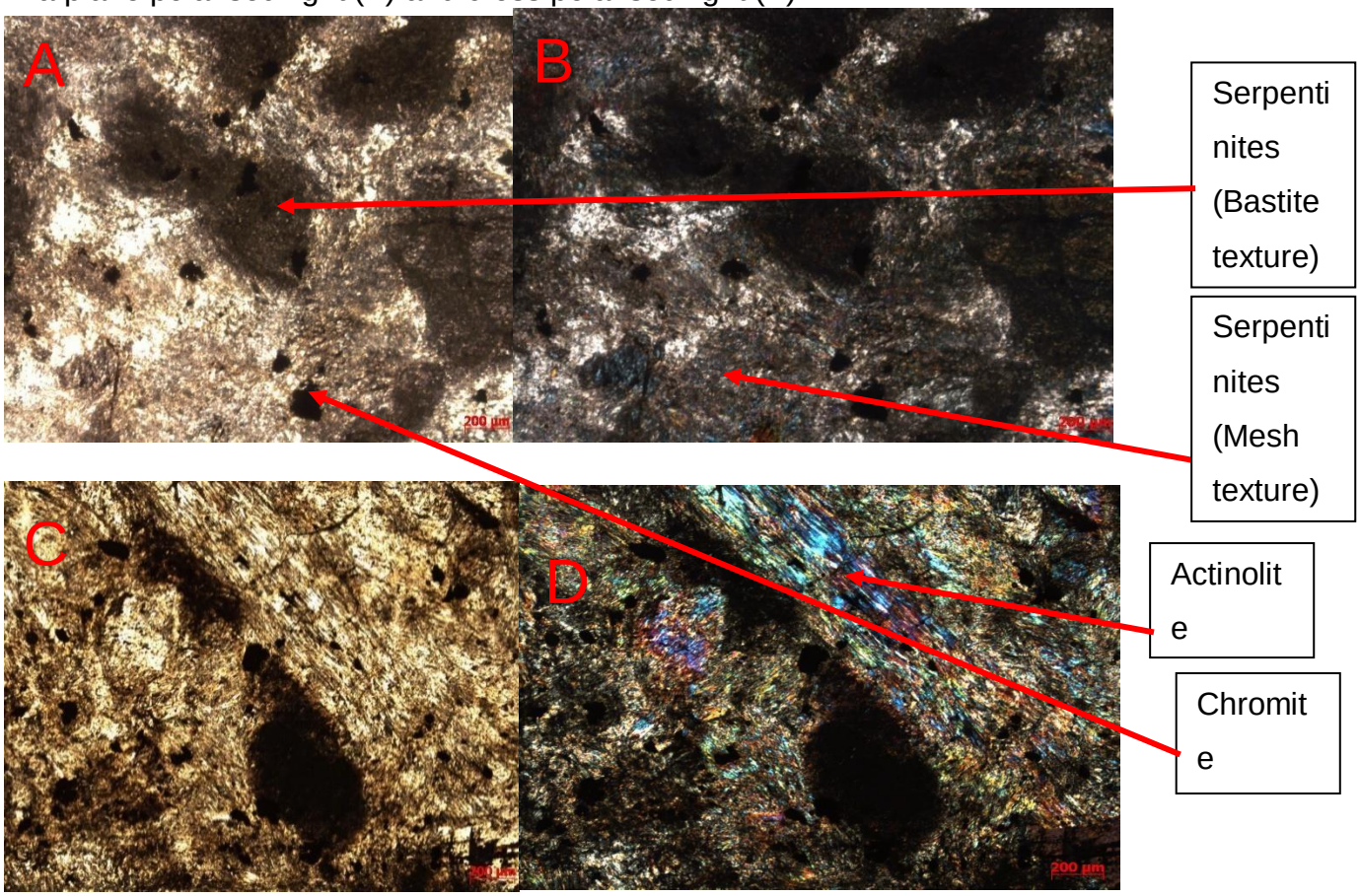

Figure 3.18: Photomicrograph of altered serpentinite rock. Serpentine that developed as an alteration after olivine has a mesh texture while that formed after orthopyroxene has a bastite texture (Azer and Khalil, 2005). The thin section has both mesh and bastite texture, due to the alteration of olivine and orthopyroxene. Photomicrography are in a plane polarised light (A and C) and cross polarised light (B and D).

Talc Schist

The talc schist outcrop was grey to brown, due to weathering and exposure to the environment (Fig. 3.19). It had a sharp contact with basalt and quartzite in the Muyexe area. The outcrop breaks in layers which were a result of the strong schistosity of the rock, due to mineral alignment in parallel form. The hand specimen of the rock is pale green to grey and has aligned platy minerals, which were large enough to be seen by the unaided eye. It had a fine to medium grain size. It was also soft and has a soapy feel and slippery due to talc minerals. It comprises mainly talc and chlorite minerals with carbonate crystals. It had a lepidoblastic texture with well-developed schistosity.

In the thin section (Fig. 3.20) talc dominates the rock, with chlorite. Accessory mineral chromite can be seen in the thin section.

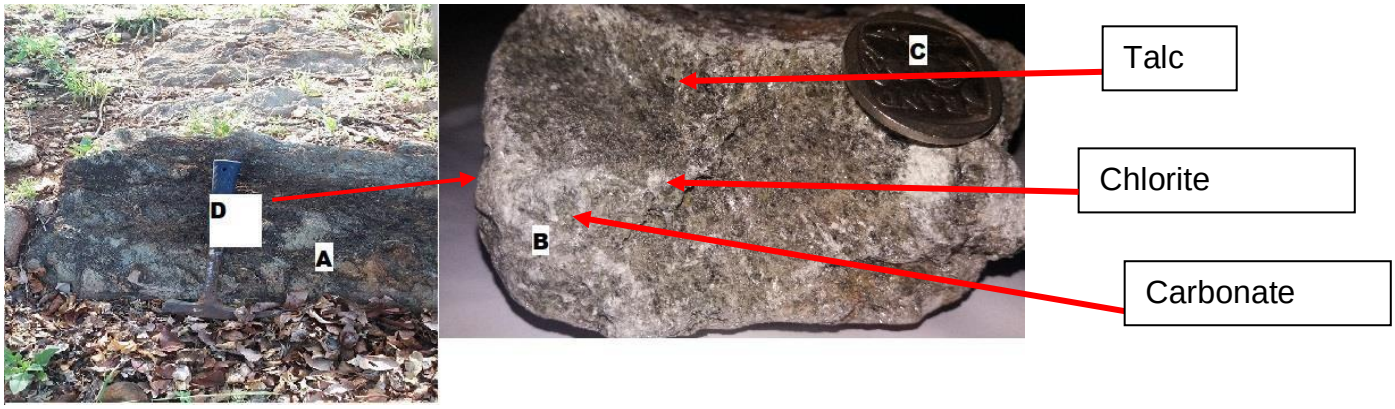

Figure 3.19: A photograph of: A-Talc schist; B-Hand specimen; C-Coin; and DGeological hammer as a scale.

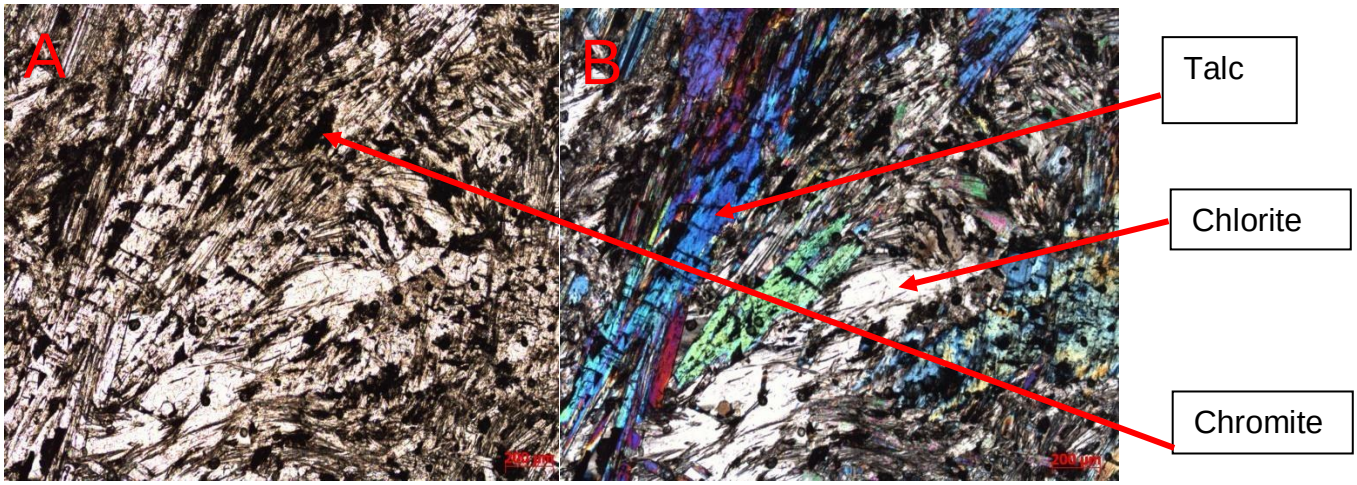

Figure 3.20: Photomicrograph of talc schist rock. Photomicrography are in a plane polarised light (A) and cross polarised light (B).

Basalt

The basalt outcrop in the area was mostly intrusive into other rocks, like quartzite and schists (Fig. 3.21). Some of the basalt outcrops were weathered and brown while the un-weathered once was dark grey. The outcrop was compact and hard to break. It had a sharp contact with quartzite and schist rocks. The hand specimen was dark-grey and had a fine grain size. It comprises of mainly plagioclase and pyroxene minerals.

In the thin section (Fig. 3.22) Under plane polarised light (PPL), plagioclase was colourless, clinopyroxene was pale green, brownish to colourless, orthopyroxene was colourless, and chromite was dark. Both pyroxenes had high relief, while plagioclase had a low relief. A typical pyroxene cleavage can be identified. Under the cross polarised light (XPL), low interference colours can be observed between the pyroxenes, which ranges from yellowish, brown, pale green to bluish. Twinning can be observed on the mineral grains of plagioclase and clinopyroxene.

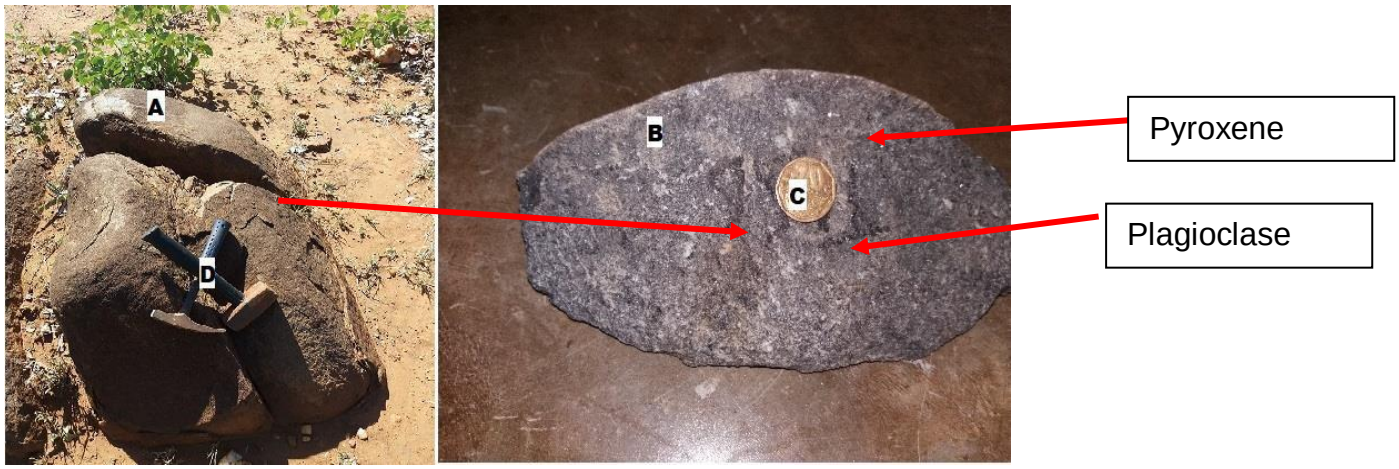

Figure 3.21: A photograph of: A-Basalt outcrop; B-Hand specimen; C-Coin; and DSledgehammer and geological hammer as scale.

Figure 3.22: Photomicrograph of basalt rock. Photomicrography are in a plane polarised light (A) and cross polarised light (B).

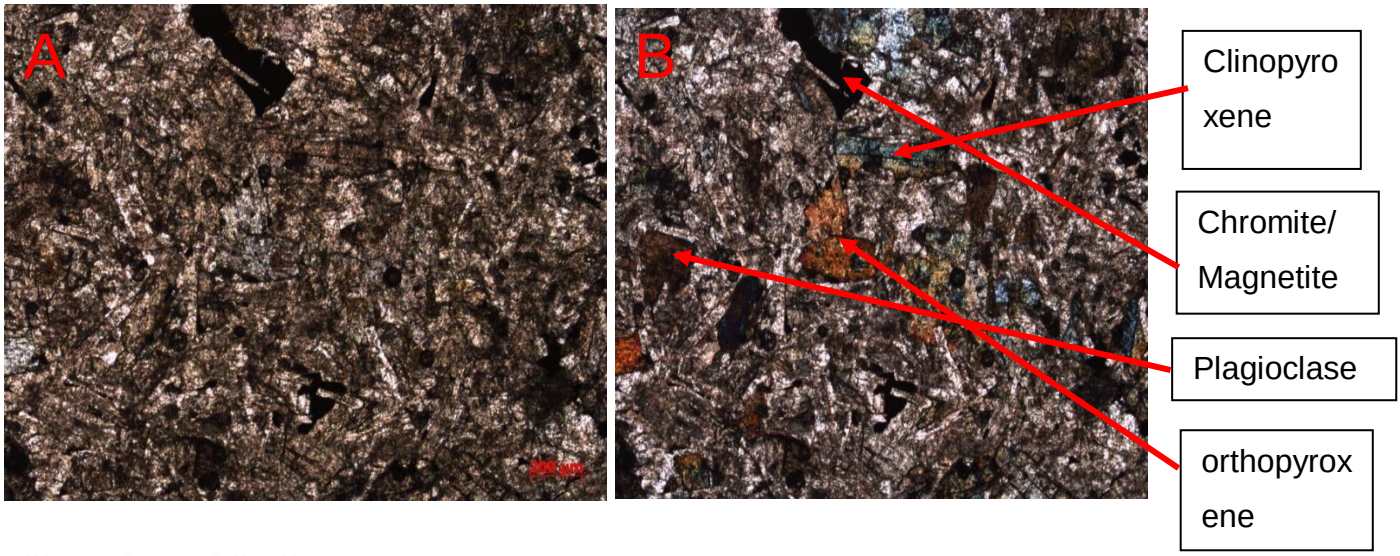

Pillowed Amphibolite

The outcrop of the pillowed amphibolite comprises of extrusive pillowed boulders with facies, of white and dark grey coloured minerals (Fig. 3.23). It was very compact and tough to break. The hand specimen was white to dark grey. It was very heavy and comprises of aligned minerals. It had a weakly foliated texture. It comprises mostly amphibole hornblende and plagioclase feldspar. It had a mineral alignment of white and black.

In the thin section (Fig. 3.24) the brown greenish minerals are hornblende while the white mineral is quartz and the whitish to blueish mineral being Albite. The rock contains some amounts of opaque minerals, iron oxide (the black part), which results in the rock being heavy. The hornblende has two distinct cleavages at 120^0 and 60^0.

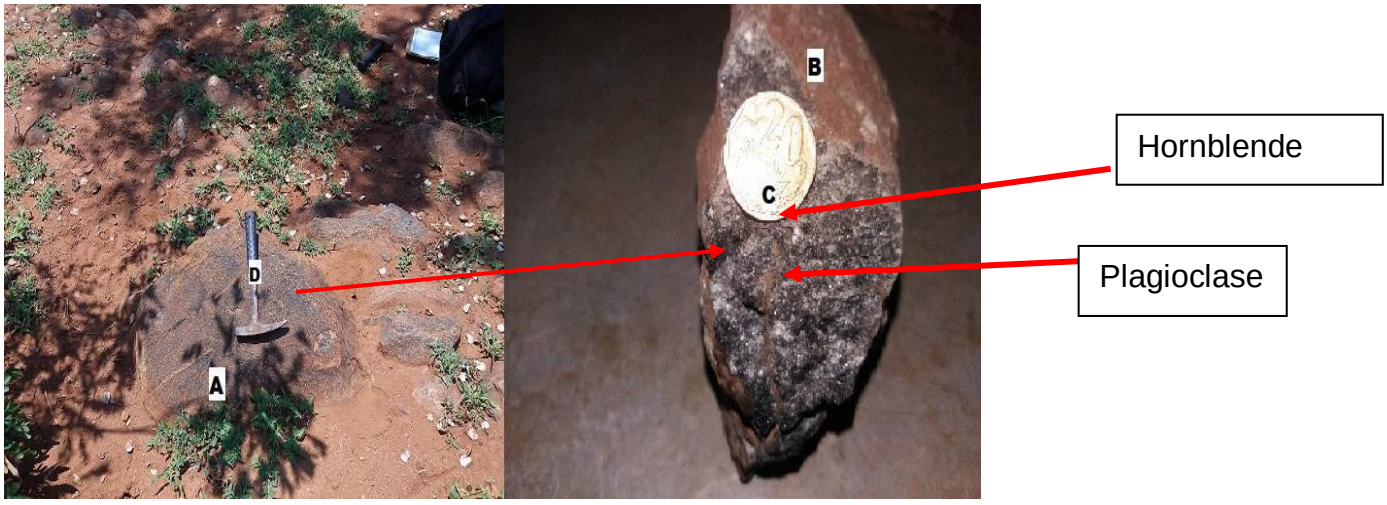

Figure 3.23: A photograph of: A-Pillowed amphibolite rock; B-Hand specimen; C-Coin;

and D-Geological hammer as a scale.

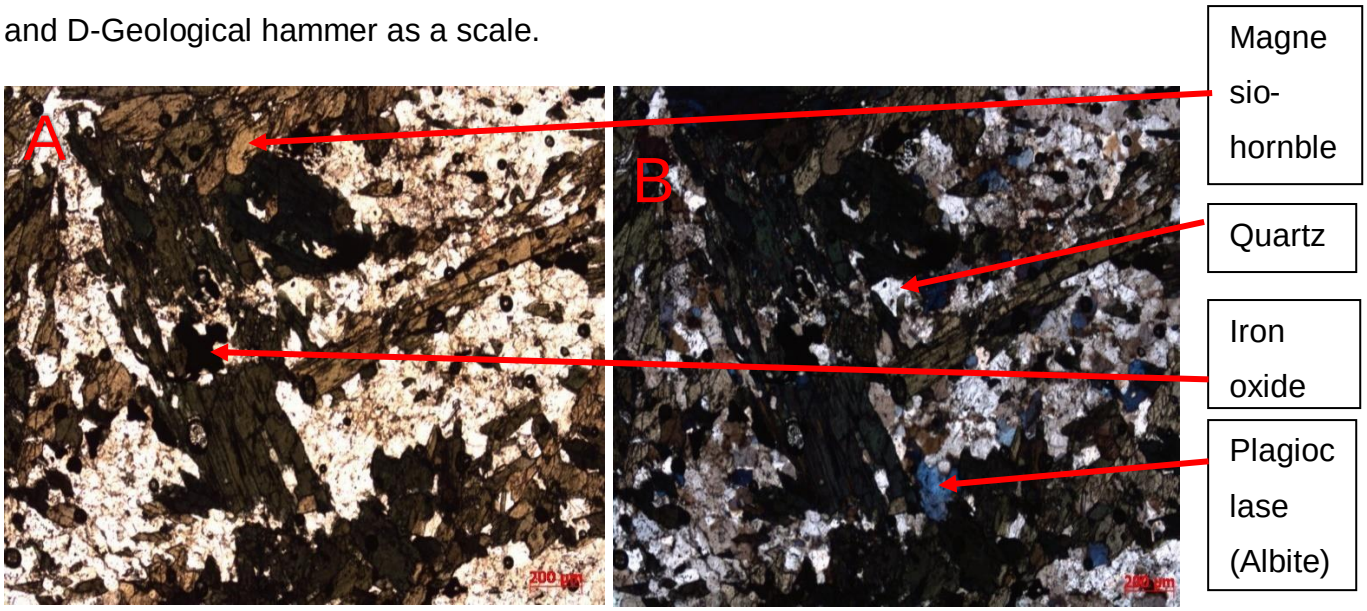

Figure 3.24: Photomicrograph of pillowed amphibolite. Photomicrography are in a plane polarised light (A) and cross polarised light (B).

Weathered Serpentinites Schist

The outcrop of this rock was located along the edges of a hill. It was brown and has stains of grey to black colour which was a result of weathering (Fig. 3.25). The rock break in layer due to a well-developed schistosity. The hand specimen was brown, with a foliation texture. The serpentinite minerals were mostly weathered which gives it its brown colour and a schistose komatiite weathered pattern and, in some area, an elephant skin weathered pattern, while it also exhibits a serpentinite weathered pattern. The rock was too weathered that there was no possible way of making a thin section from it but according to XRD data, the rock contains the following minerals clinochlore, anthophyllite and fluoro-edenite.

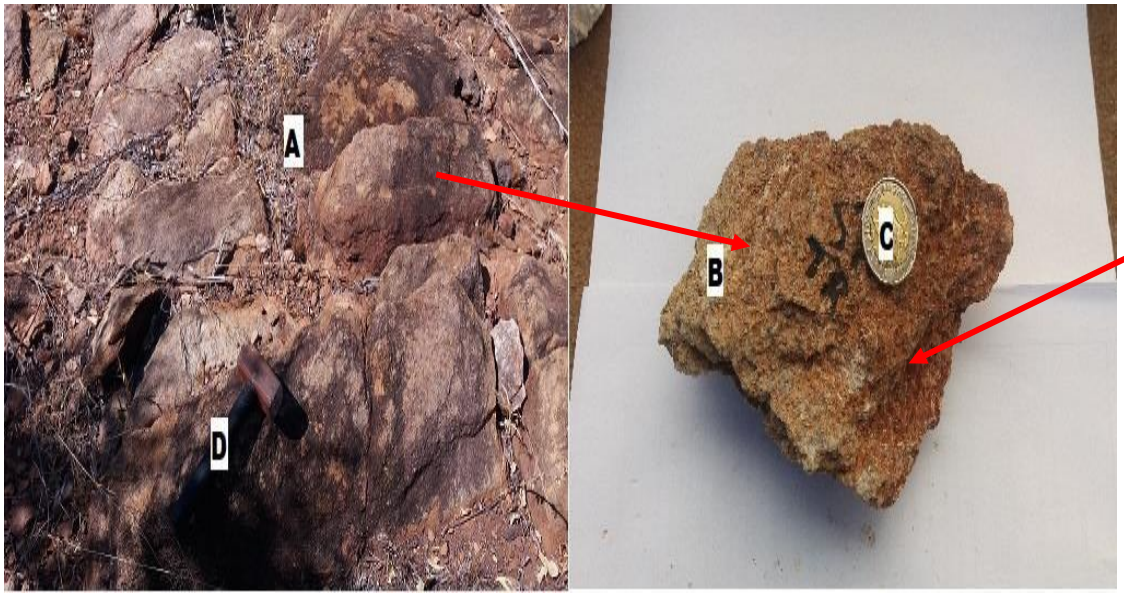

Figure 3.25: A photograph of: A-Weathered serpentinite schist; B-Hand specimen; CCoin; and D-Sledgehammer as a scale.

Birbirite

The birbirite outcrop extends over a large area, with most of the area, covered by its floats, (Figure 3.26). The outcrop was dark red to brown, with a lot of holes or vesicular due to the oxidation of the iron oxide. It was very compact, hard, and tough to break. The hand specimen was red to brown. It had fine grain sizes. It had a vesicular texture and very shinny. It made a metallic sound when hit with a metal. It comprises mostly iron oxide (limonite), and silica veins.

Under the microscope (Fig. 3.27), the rock consists of silica veins cutting through the limonite matrix, which makes up the rock. Chlorite, which is blueish to whitish can be seen in the thin section. The opaque mineral chromite is present in the thin section as an accessory mineral. According to XRD data, the rock is composed of the following minerals, quartz, clinochlore, and ferro-gedrite.

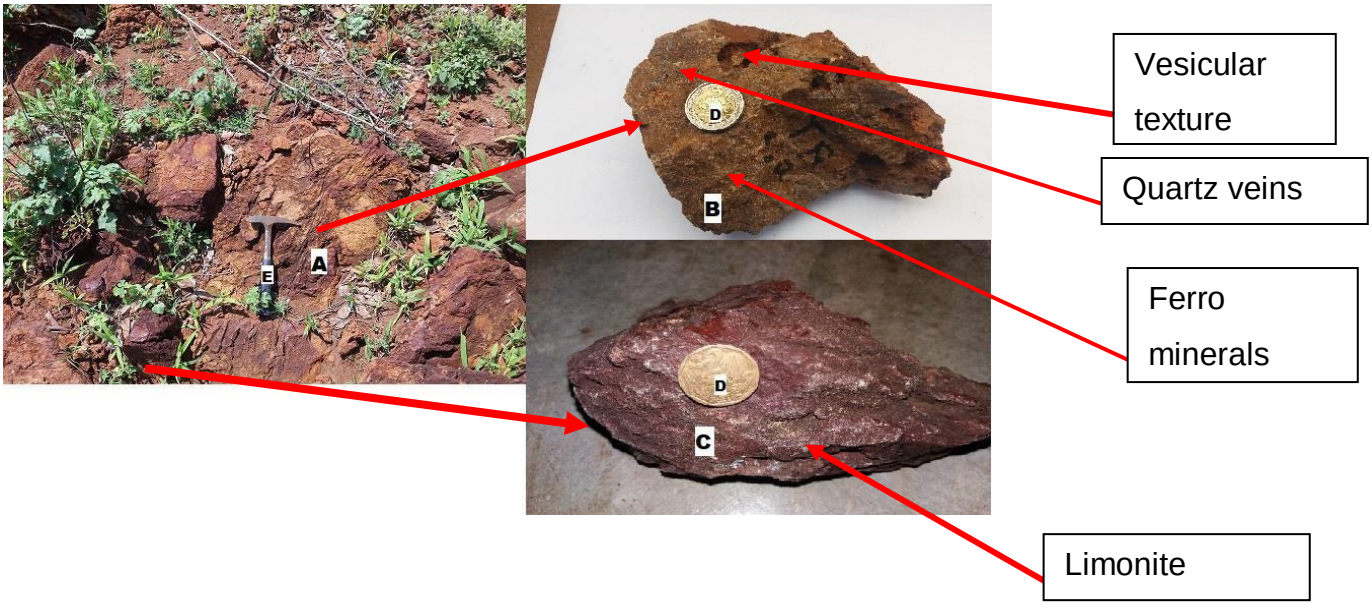

Figure 3.26: A photograph of: A-Birbirite outcrop; B, C-Hand specimens; D-Coins; and E-Geological hammer as a scale.

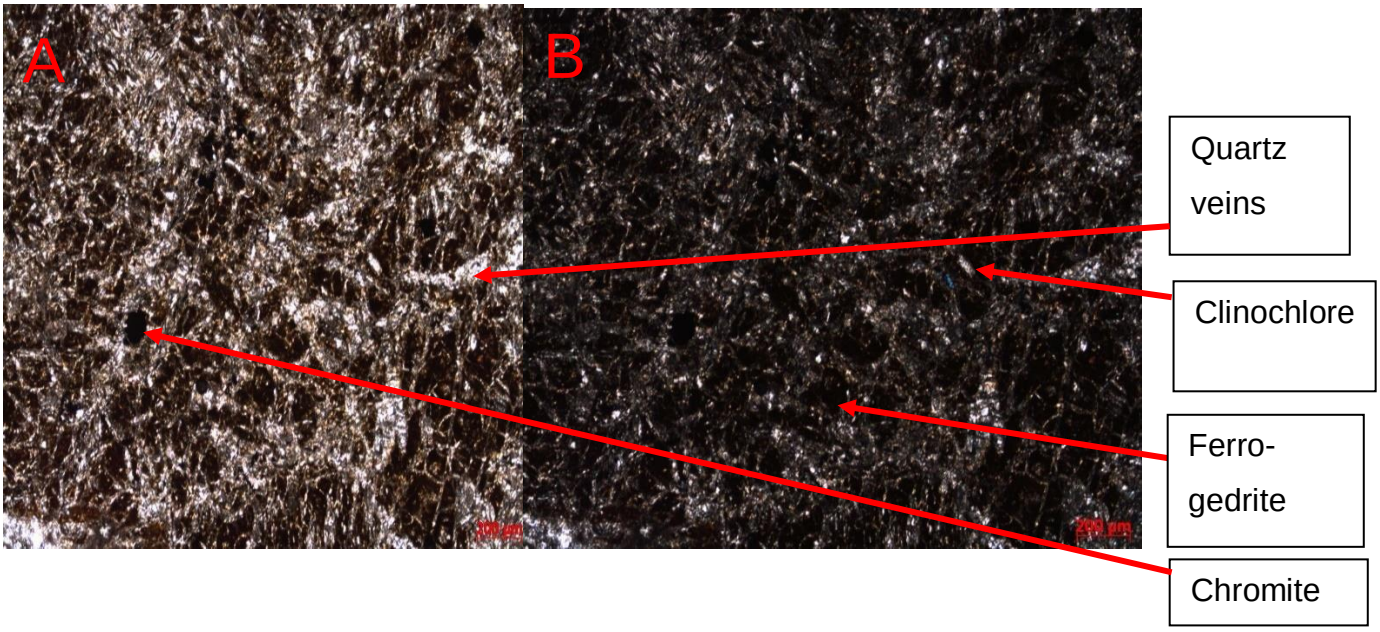

Figure 3.27: Photomicrograph of birbirite rock, with dark minerals (ferro-gedrite) and light silica veins and opaque chromite. Photomicrography are in a plane polarised light (A) and cross polarised light (B).

Peridotite

The outcrop of this rock was grey and has a stain of brown due to weathering. Most of the outcrop was weathered and altered, and where it was not it was compact and tough to break. The hand specimen was dark grey. It had a fine to medium-grained (Fig.

3.28). It had a glassy texture with green dots of olivine mineral dominating the rock. It mainly comprises of olivine.

In the thin section (Fig. 3.29 and Fig. 3.30) the rock comprises olivine and serpentinites. The olivine was going through the process of serpentinisation, where the mafic minerals are being replaced by serpentinites minerals. serpentinite is showing a mesh structure after olivine alteration in the thin section. According to XRD data, the rock is composed of the following minerals: olivine (forsterite), clinochlore, magnesite, ferri-fluoro-katophorite, lizardite, and tremolite. These minerals were also viewed under the microscope.

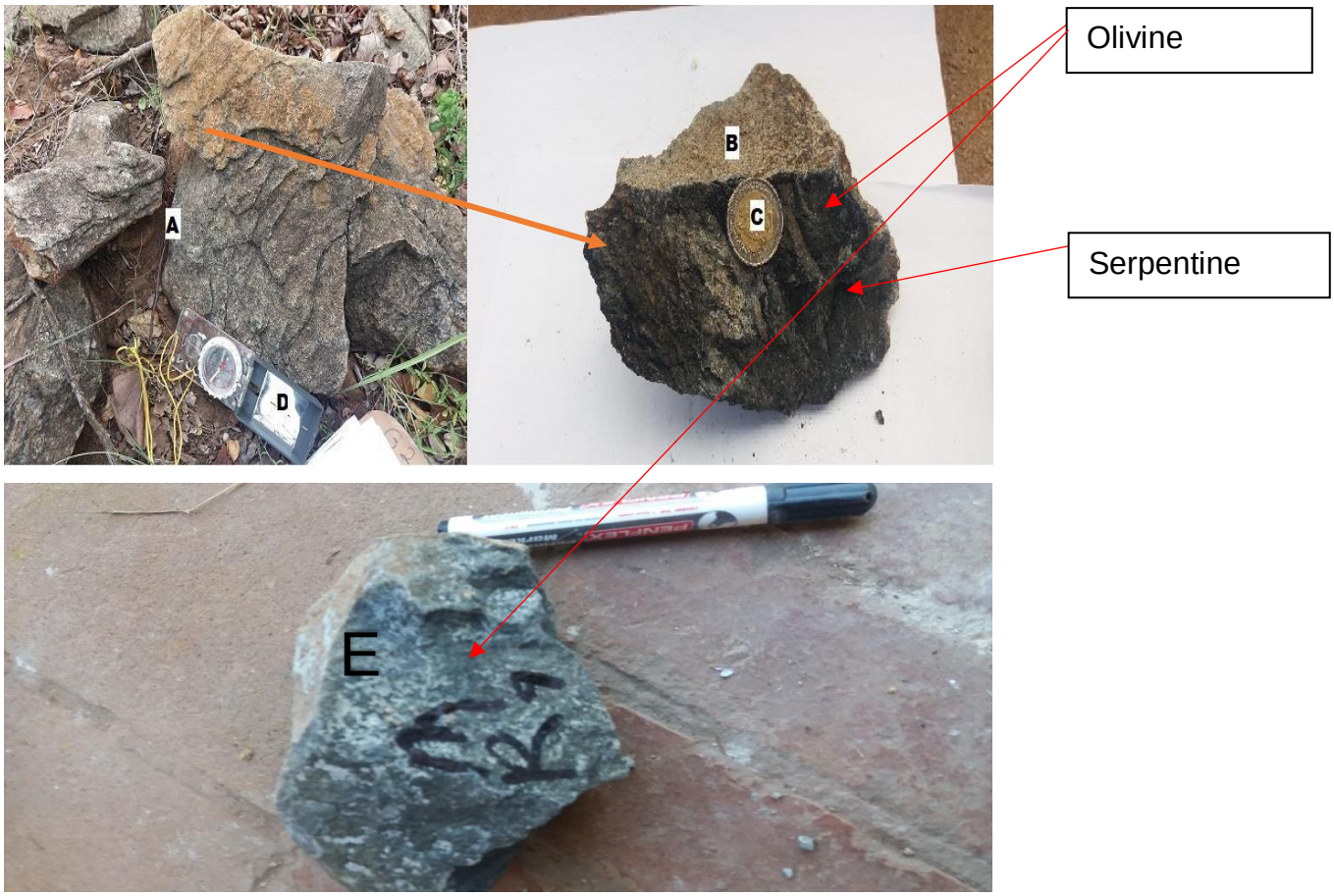

Figure 3.28: A photograph of: A-Altered peridotite outcrop; B-Hand specimens of altered peridotite; C-Coin; D-Compass as a scale; and E-Hand specimen of Peridotite.

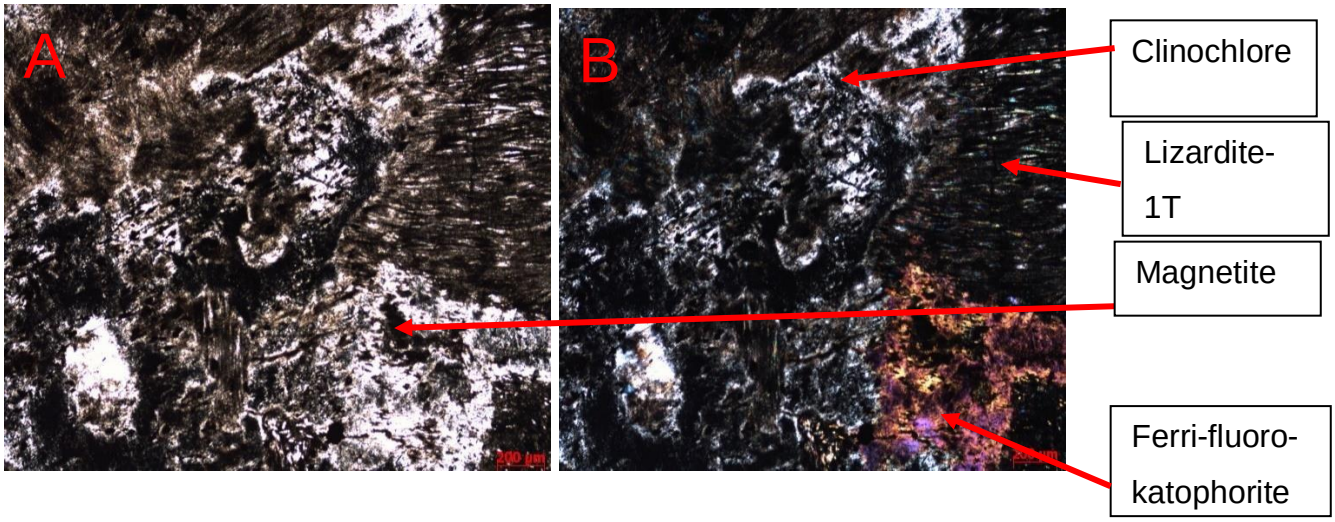

Figure 3.29: Photomicrograph of altered peridotite. Photomicrography are in a plane polarised light (A) and cross polarised light (B).

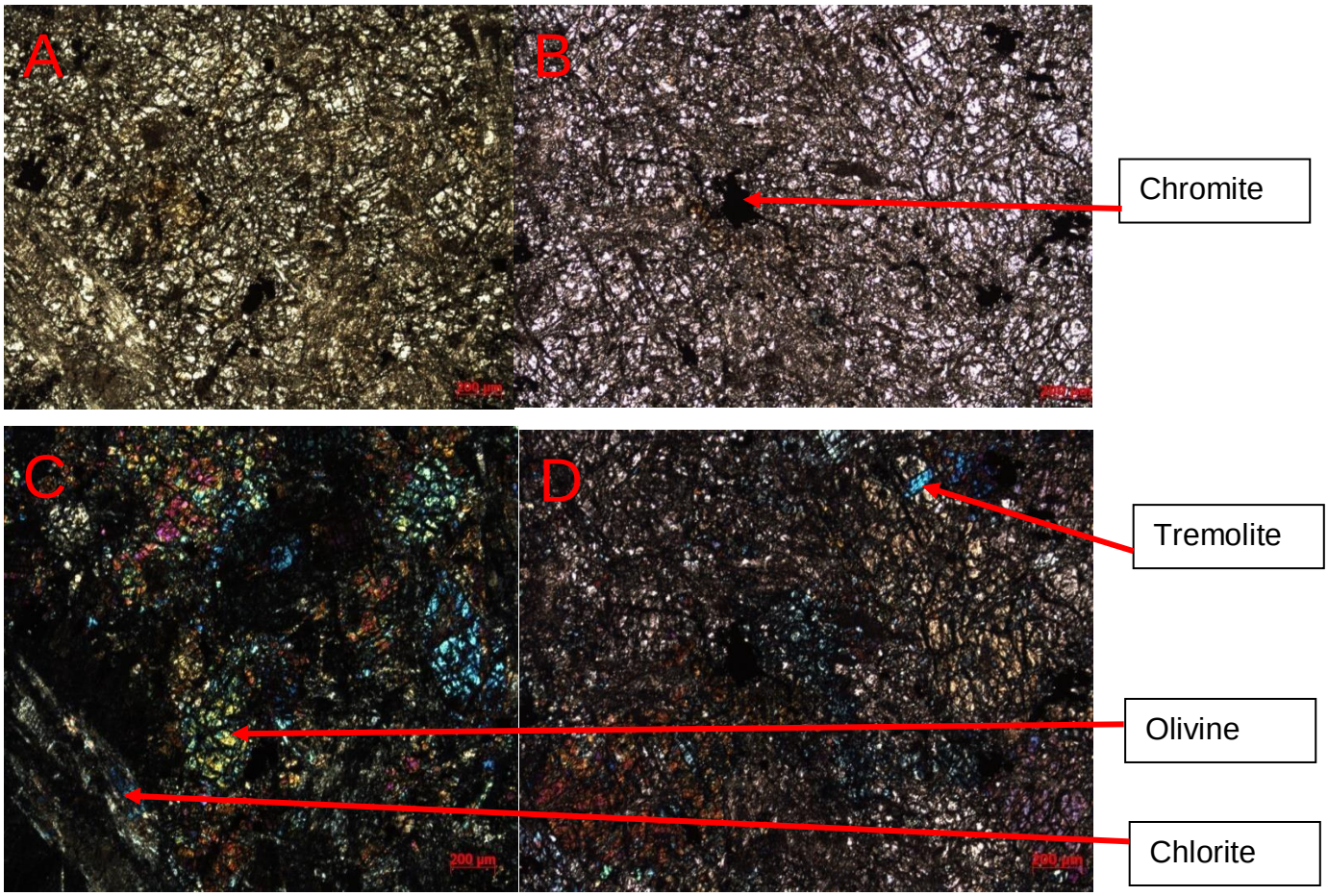

Figure 3.30: Photomicrograph of peridotite. The rock is characterized by large metamorphic olivine (with mesh structure), with only minor tremolite and chlorite. olivine has a high reflective. Photomicrography are in a plane polarised light (A and B) and cross polarised light (C and D).

3.3.2.2 Loss of Ignition Test

Loss of ignition test was performed to determine the concentration of carbon dioxide in magnesite. The following equipment and tools were used during the loss of ignition test (Fig. 3.31).

- Scale (resolution 0.001 g) was used to weigh the samples and crucibles;
- Muffle furnace was used to ash the sample at 1000^{0}C (Fig. 3.31B/D);
- Porcelain crucibles were used to put the samples during heating (Fig. 3.31C);
- Glass desiccator was used to place the crucibles during cooling;
- Hand gloves were used to protect the hand when holding the crucibles (Fig. 3.31A); and
- Furnace handheld claw was used to carry the crucible inside the furnace.

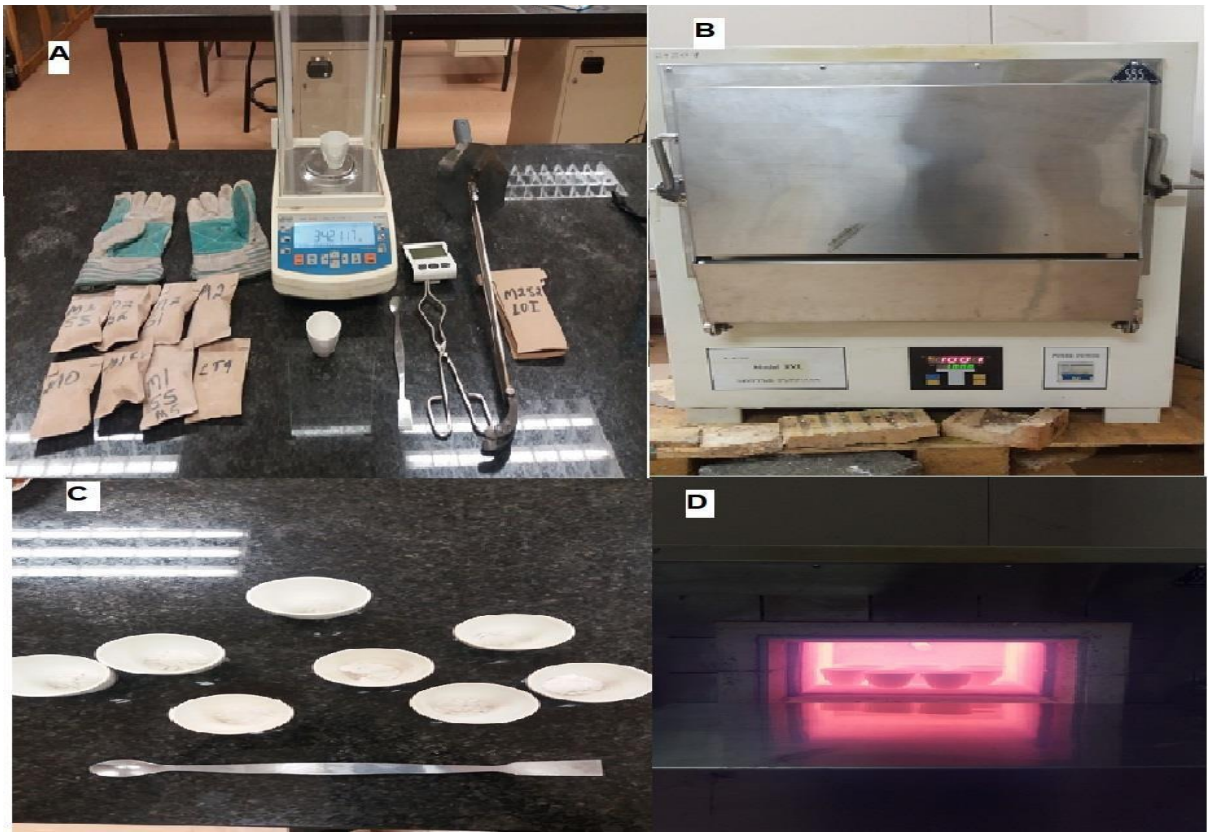

Figure 3.31: Laboratory equipment and tools used for loss of ignition test: A-Scale, handheld claws, hand gloves and samples; B-Muffle furnace; C-Crucibles and spoon; and D-Crucibles inside a furnace.

Determination of carbon content from 20 magnesite samples was executed using the loss-on-ignition method. About 2 kg of the sample was jaw-crushed to less than 4 mm of grain particle size. About 50 g of the crushed sample was milled to about 75-micron

meter. Before the sample is taken out of the sample box provided, good mixing of the sample should be ensured (Evonik Industries, 2014). Sample assaying was then done by extracting about 1 g of magnesite sample and placed in weighed silica crucible (Brix, 2008). Then about 1 g of the sample was weighed and recorded together with the crucible and recorded as initial weight. The sample and crucible were placed in a furnace to 1000°C for 2 hours (Evonik Industries, 2014; Ebrahimi-Nasrabadi, 2015) to completely oxidize the magnesite and then cooled in a desiccator for 20 minutes and weighed and recorded as final weight (Table 3.3). The magnesite content was then calculated using the following equation (Brix, 2008):

$$LOI = \frac{initial\ weight - final\ weight}{initial\ weight} \times 100 \qquad \text{.....equation 3.1}$$

Note, Crucibles that were for the first time were ignited empty prior use (Evonik Industries, 2014).

Table 3.3: Loss of ignition test results

Sample	Initial weight	final weight	LOI
M1S1	36,5	23,2	36,4
M1S2	34,5	21,8	36,8
M1S3	34,6	21,9	36,7
M1S4	37,2	23,5	35,8
M1S5	36,2	22,7	37,3
M1S6	36,4	23,1	36,5
M1S7	36,5	23,7	35,1
M1S8	36,3	23,4	35,5
M1S9	37,1	24,1	35
M1S10	34,8	21,9	38,2
M2S1	36,3	22,9	36,9
M2S2	34,6	22,1	36,1
M2S3	34,9	21,7	37,8
M2S4	36,5	27,7	35
M2S5	36,8	23,9	35,1
M2S6	37,1	23,7	36,1
M2S7	36,4	23,6	35,2
M2S8	34,8	22,92	34,1
M2S9	34,5	21,9	35,5
M2S10	34,6	22,2	35,8

3.3.2.3 Geochemical Analysis

Selecting an analytical method for the determination of elements/metals depends on the precision, accuracy, determination limit, cost, availability, and simplicity of operation of the instrument. Some of the common analytical methods used in geochemistry for analysis include X-Ray Fluorescence (XRF), X-Ray Diffraction (XRD), Inductively Coupled Plasma Emission Spectrometry (ICP) and Atomic Absorption Spectrophotometry (AAS) (Rollinson, 1993). The final decision as to which analytical methods to be used for analysis is based on scientific comparison and careful analysis of each of the conditions involved. Both XRD and XRF were used in this study to analyse the samples because of their availability, simplicity, reliability, and cost-effectiveness.

Whole Rock Geochemistry

Whole-rock geochemical analysis of major oxides and trace elements was undertaken using an S2 Ranger XRF (Fig. 3.32). A total number of 38 pellets, which included 18 for rock samples and 20 for magnesite samples were analysed. The pressed pellet was loaded in the sample port of the X-Ray Fluorescence analyzer which was connected to a computer system and the XRF analysed the sample for about ten minutes after which the values of the analysed major oxides and elements concentration were displayed on the monitor. This was saved directly on the computer system and then printed out as the result of the analysis.

Prior to each cycle of analysis, the spectrometer was calibrated using a copper disk. A sample was designated as a check sample to ensure the precision of the analysis, this sample was analysed after a cycle of analysis. The standardised control sample SARM 42 (South African Reference Materials) from Mintek was also used to ensure the accuracy of the instrument. The XRF results in weight percentage and parts per million were recorded in Tables 3.4 and 3.5, respectively.

Figure 3.32: A Ranger S2 XRF machine used for geochemical analysis.

Mineralogical Analysis

PANalytical X'Pert Diffractometer instrument was used for mineralogical analysis. A total of 14 total number of samples, which included 12 rock samples and 2 magnesite samples were analysed. The X-ray diffractometer (XRD) machine uses the "Data collector'' software from PANalytical to run the required measurement settings. The parameters that were used for the XRD analysis are as follows:

- Instrument running parameters: Start Position [°2θ]: 4.0124, End Position [°2θ]: 89.9814
- Step Size [°2θ]: 0.0170
- Scan Step Time [s]: 177.8000
- PSD Length [°2θ]: 2.12
- Divergence Slit Type: Fixed
- Divergence Slit Size [°]: 0.2500
- Specimen Length [mm]: 10.00
- Measurement Temperature [°C]: 25.00
- Anode Material: Cu

- Generator Settings: 40 mA, 40 kV
- Goniometer Radius [mm]: 240.00
- Spinning: Yes

Once the measurements were completed, PANalytical's "HighScore Plus" software was used to assess the various XRD spectra. The K-Alpha2 peaks were stripped to eliminate interference and remaining spectra peaks were matched to standards found in the "HighScore Plus" database. When these peaks were matched, they were done so with the assumption that the samples are completely unknown. This position ensured that only the exact phases are accepted as authentic. The mineralogy of the rocks and magnesite analysed through XRD, are presented in Tables 3.6 and 3.7, respectively.

Table 3.4: XRF results of major oxides in weight percent (wt. %)

Sample	**SiO_2**	**TiO_2**	**Al_2O_3**	**Fe_2O_3**	**MnO**	**MgO**	**CaO**	**Na_2O**	**K_2O**	**P_2O_5**
Altered serpentinite 1	50,14	0,09	0,59	4,86	0,13	27,95	9,74	6,45	0,03	0,07
Altered serpentinite 2	49,34	0,13	1,52	6,90	0,16	27,17	7,43	0,61	0,00	0,05
Altered serpentinite 3	42,25	0,10	1,31	11,91	0,26	26,97	7,42	3,52	0,00	0,06
Altered serpentinite 4	36,23	0,07	0,05	8,19	0,19	27,11	10,70	0,00	0,02	0,09
Basalt	48,38	0,15	2,04	11,11	0,27	25,25	3,07	3,59	0,03	0,06
Peridotite	39,00	0,08	0,00	10,07	0,24	41,98	0,06	0,00	0,01	0,00
Serpentinite	42,34	0,29	5,72	10,01	0,21	21,20	7,66	3,49	0,02	0,07
BIF	77,77	0,22	0,89	19,81	0,17	1,49	0,49	0,00	0,10	0,39
Weathered Serpentinite	65,15	0,10	1,01	10,98	0,24	20,04	0,14	2,96	0,02	0,03
Birbirite	83,03	0,08	1,36	7,38	0,14	10,79	0,23	0,00	0,02	0,02
Amphibolite	50,11	0,41	7,84	8,23	0,14	7,60	13,43	3,13	0,23	0,40
Altered peridotite	39,81	0,16	0,66	11,75	0,23	40,96	0,64	0,00	0,00	0,01
Pillowed amphibolite	54,46	1,38	10,38	12,78	0,16	3,31	7,74	3,79	0,35	0,27
Hornblende schist	43,78	0,25	6,38	9,68	0,18	22,18	6,58	0,42	0,05	0,08
Talc schist	54,74	0,15	1,65	8,83	0,19	28,73	3,07	15,46	0,01	0,04
Quartzite	99,50	0,00	0,00	0,47	0,00	0,00	0,00	0,00	0,00	0,10

Table 3.5: XRF results of selected trace elements in part per million (ppm)

Sample	Sr	Ba	Rb	Th	U	Y	Zr	Nb	Hf	Sc	V	Cr	Co	Ni	Cu
Altered serpentinite 1	57,1	126,3	5,6	10,6	0	3,5	15,4	1	0	0,9	19,3	1287,4	11,4	1208,6	3,3
Altered serpentinite 2	23,5	158,8	4,2	3,9	4,3	2,4	9,2	1,1	0	0,7	36,7	1617,5	19,3	1102,2	0
Altered serpentinite 3	23,7	98,9	9,7	51,2	9,9	2,1	9,2	0,9	0	0,7	36,4	4437,5	27,1	5142,9	0
Altered serpentinite 3	39,5	111,1	5,4	1,8	0,8	0,6	9,9	1,5	0	1	18,1	3244	22,3	4427,4	0
Basalt	7,9	168,2	12,1	46,7	12,3	2,6	7,5	0,8	0	0,3	51	2355	29,7	1869	0,2
Peridotite	1,1	94,8	7,2	5	7,3	2	3,8	0	1,2	0	23,5	4031	30	5451,7	0,2
Serpentinite	10,4	273,3	9,3	5,7	0,5	5,8	22,8	1,2	0	0,7	87,4	1875,7	26,7	1373	0
BIF	14,4	224,6	19,5	14,8	25	8,9	23,7	1,5	155	0	66,6	204,3	46,7	0	1408,8
Weathered serpentinite	3	132	11,2	6,2	11,4	3	7,2	2,2	1,5	0	32,1	2626,5	27,9	3709,8	15
Birbirite	4,2	117	5	4,3	5,1	2,7	7,6	0,7	2,3	0	50,9	2721,7	17,1	3287	17,3
Amphibolite	185,1	362,9	8	31,4	0,8	7,8	66,1	2,7	6,1	1,2	111,8	287,2	17,7	207,7	84
Altered Peridotite	1,9	180,1	11,1	50,1	11,3	1,7	10,6	1,2	0	0,1	38,9	2054,1	27,5	6721,6	0
Pillowed Amphibolite	60,8	1088,6	17	11	17,3	25	106,1	7,5	0	0,7	332,8	71,5	27,4	105	0
Hornblende Schist	24,2	244	9	39,8	1,5	5,6	23,7	1	7,7	0,6	77,3	1319,5	21,5	2207	83,3
Talc Schist	28,2	170,9	7,5	5	7,7	4,8	17,2	0,4	0	0,3	45,5	1315,4	20,3	3789,4	32,3
Quartzite	4,8	58,3	0,8	0	0	0	1,4	5	2,1	0	0,8	4,9	1,2	6,7	9,2

Table 3.6: XRD results for the mineralogical composition of magnesite

Sample	Magnesite	Dolomite	Quartz
M1S1	94%	2%	4%

M2S3	91%	-	9%

Table 3.7: XRD results of the mineralogy of rocks

Samples	HR3 (HR3M2)	HR4 (HR4M2)	T1S13 (MR2)	T1S12 (MR3)	T3S9 (MR4)	T1S16 (MR6)	MR8	T2S (MR9)	T2S11 (MR10)	T1S1	M1S1	M2S3	T2S13 (M2R5)
Clinochlore		×	×		×		×	×	×	×			×
Edenite	×						×		×				
Talc									×				
Clino-ferriholmquistite									×				
Calcium Aluminium Hydroxide Hydrate	×												
Anthophyllite							×			×			
Magnesio-hornblende				×		×				×			
Sodium Cobalt Aluminum Silicate	×												
Forsterite								×					
Tremolite								×					×
Albite						×							
Quartz	×	×	×	×		×					×	×	
Ferri-fluorokatophorite					×								
Lizardite	×				×								
Magnetite					×								
Anorthite				×									
Ferro-gedrite			×										
Actinolite													×

Cummingtonite													×
Magnesite		×									×	×	
Willemseite		×											
Dolomite	×	×									×		

CHAPTER 4: DATA ANALYSIS AND INTERPRETATION

4.1 Geological Map and Cross-Section of Muyexe Area

The Muyexe area forms part of the northern limb of the Giyani Greenstone Belt. The area is dominated by metamorphosed mafic and ultramafic rock as well as metasedimentary rocks. A total of 10 different rock types were identified based on the mineral composition and textural difference. These are schists composed of hornblende-talc-chlorite-anthophyllite-tremolite, weathered serpentinite schist, birbirite, pillowed amphibolite, amphibolite, peridotite, serpentinites, quartzite, basalt, and banded iron formation (Fig. 4.1).

The rocks in the area are intruded by basalt and peridotite. Most of the exposure has a sharp contact, dipping between 10^0- 45^0 (Fig. 4.2) and striking northwest to the south-east and southwest. Some lithologies such as talc schist, tremolite schist, and weathered serpentinites schist are sheared and foliated.

Quartzite is abundantly distributed in the area, especially towards the north-eastern side, where it is a low-lying area due to flooding by the rivers in the area. Thus, leaving the hard and resistant quartzite and basalt as the dominant rocks along that side, while other rocks were weathered by the rivers. Some areas which were covered by quartzite float were mapped as quartzite on the geological map. The birbirite seems to dominate the edges of the hills in the area. Birbirite had a sharp contact with serpentinite in the area.

Serpentinite rock dominated the hills of the Muyexe area. The serpentinite rock in the area contains magnesite mineralisation. The rock seems to be cut across by a normal fault that divides the serpentinite rock. Peridotite dykes are present in the area as intrusions. The peridotite is mostly altered, and it is the source rock for both serpentinisation and magnesite mineralisation.

The shearing of the peridotite, foliations of the schist rocks and shearing of quartz rock in some area, suggest that the area was subjected to strong tectonic forces which subjected the rocks to different kinds of strength resulting in shearing, foliating and tilting. Some of the rocks in the area have joints and alignment of minerals, thus providing proof of the regional metamorphism that took place in the area. However, the peridotite and some of the ultramafic rocks in the area seems to be subjected to a

different kind of metamorphism. The presence of serpentinites and magnesite mineralisation in the area suggests that the mafic and ultramafic rocks were also subjected to contact metamorphism by the hydrothermal fluids that resulted in mineralisation in the area.

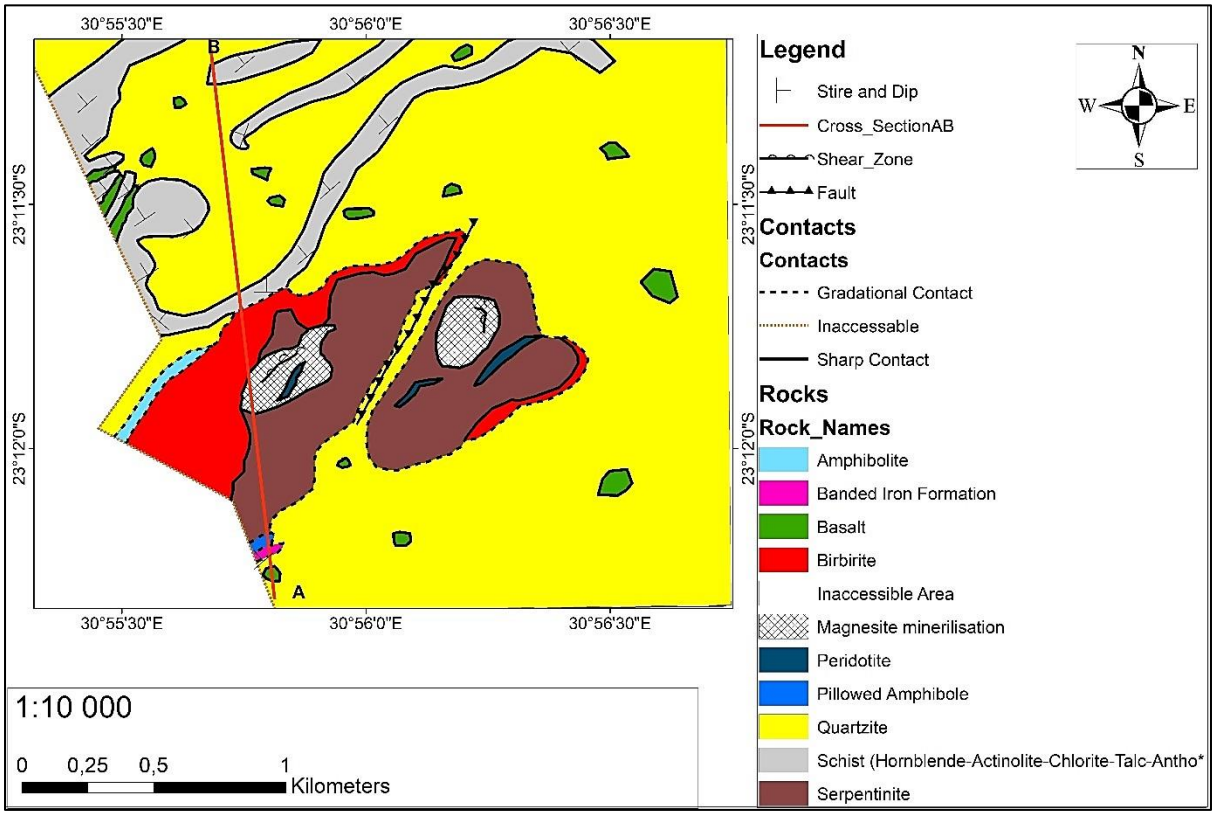

Figure 4.1: Geological map of the Muyexe area.

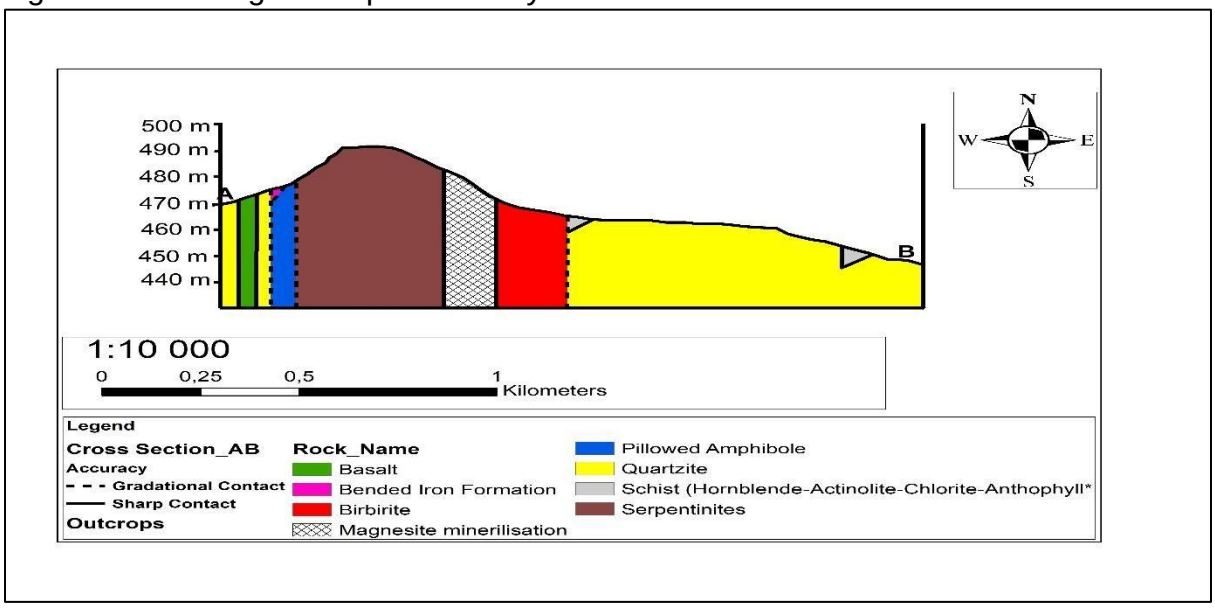

Figure 4.2: Cross-section view of the Muyexe area.

4.3 Mineralogy of Rocks at Muyexe

Detailed mineralogical study of the rocks at Muyexe was already carried out in the petrographic study, however mineralogical analysis of some of the selected rocks was also analysed using XRD to verify the mineralogical composition. Mineralogical information is valuable to imminent the role of host rocks in the formation of magnesite and other allied minerals.

The XRD analysis of 12 selected rock samples revealed that most of the rocks in the study area are dominated by amphibole facies mineral assemblage. This is because the rocks of the Giyani Greenstone Belt have been subjected to amphibolite facies metamorphism (De Wit *et al*., 1992), and peak metamorphism was at 2715 Ma (Kreissig *et al*., 2001; Kramers *et al*., 2014). The lithologies are dominated by minerals such as clinochlore, quartz, edenite, and magnesio-hornblende, followed by anorthite, tremolite, lizardite, actinolite, and talc among others (Table. 3.7). Most of these minerals are rich in magnesium composition.

Amphiboles minerals that were analysed in the rock samples at Muyexe are secondary, meaning they replaced the original primary mineralogy of the rocks during retrograde metamorphism of the mafic and ultramafic rocks. The amphibole minerals in the study area included the following: edenite, anthophyllite, magnesio-hornblende, actinolite, ferro-gedrite, ferri-fluoro-katophorite, cummingtonite, tremolite, and clinoferri-holmquistite. Sample HR3, MR8, T2S11, T1S1, T1S12, T1S13, T3S9, and T1S13 are mostly dominated by amphiboles mineralogy.

Monoclinic amphiboles, edenite, magnesio-hornblende, ferri-fluoro-katophorite cummingtonite, and clino-ferri-holmquistite are common mineral in both igneous and metamorphic rocks. In igneous rocks, these minerals are found in andesites, dacites, and rhyolites, as well as in gabbro, diorites, and granites. In metamorphic rocks, they are a common constituent of meta-basalts that have been metamorphosed to intermediate grades of regional metamorphism. According to Deer *et al*. (1992), magnesium-rich cummingtonite occurs together with anthophyllite in iso-chemically metamorphosed ultrabasic rocks. Cummingtonite is also found in hybrid rocks of intermediate composition and may occur as the middle member in the transition of orthopyroxene to hornblende (Deer *et al.,* 1992). Sample T2S13 in composed of cummingtonite. It was suggested by de Waal *et al.* (2006) that the edenite and

magnesio-hornblende amphiboles are found in the high-Ti suite samples stabilized after clinopyroxene in the paragenetic sequence.

According to Deer *et al.* (1992), orthorhombic amphiboles are unknown in igneous rocks. Anthophyllite and gedrite do however occur in metamorphic and metasomatized rocks, and these minerals are also commonly found in the reaction zone between ultramafic rocks and country rocks. These two minerals may also develop during lower amphibolite facies conditions (Deer *et al.,* 1997). Orthorhombic amphiboles may be derived from calcic amphiboles by metasomatism, e.g. hornblende or actinolite, in the latter due to hydrothermal alteration involving the addition of Mg and the loss of Fe, Ti and Ca (Deer *et al.,* 1997). The formation of anthophyllite may also be due to the addition of Fe, Mg or Al and the removal of Ca during metamorphism (Deer *et al.,* 1992). Anthophyllite commonly occurs as an alteration product in rocks rich in olivine (Deer *et al.,* 1997). Anthophyllite may also form due to retrograde metamorphism of earlier thermally metamorphosed rocks (Deer *et al.,* 1992). In the study area sample T1S1, MR8 and T1S13 contain the composition of both anthophyllite and ferro-gedrite.

Tremolite and actinolite are metamorphic minerals that may occur in both contact and regionally metamorphosed rocks. Actinolite is a common product of retrograde metamorphism of ultrabasic rocks. Actinolite usually develops in pyroxene-rich rocks as an alteration product of both orthopyroxene and clinopyroxene (Deer *et al.,* 1997). In ultrabasic rocks, actinolite is usually associated with assemblages of tremolite-talc and or tremolite-carbonate-antigorite (Deer *et al.,* 1997). Tremolite and actinolite are found in sample T2S and T2S13.

Plagioclase was also present in the rocks in a form of albite and anorthite in sample T1S16 and T1S12. Both minerals are associated with mafic rocks. The difference between the two minerals is that albite is sodium-rich while anorthite is calcium-rich, meaning that the two rocks samples, T1S12 and T1S12 are both sodium and calciumrich, respectively.

Clinochlore is a secondary mineral that forms due to deuteric or hydrothermal alteration of primary ferromagnesian minerals such as mica, pyroxenes, amphiboles, garnets, and olivine at a temperature of up to 400 °C (Deer *et al.,* 1992). Clinochlore is found in most of the rocks analysed (XRD), notable in samples HR4, T1S13, T3S9, MR8, T2S, T2S11, T1S1, and T2S13, suggesting that the original mineralogy of these

rock samples were mafic in nature, as the clinochlore is also both magnesium and iron-rich.

Quartz is the second most abundant mineral in the rock samples, this is no surprise because of its widespread occurrence in the earth crust, thus most of the rock would constitute of quartz in its lattice. However, sample T2S3, MR8, T2S, T2S11, and T2S13 are depleted of silica (quartz) as this may be due to the silica being utilised in the formation of other minerals during the metamorphism of these rocks.

Other important minerals that were analysed in rock sample include lizardite and forsterite. These two minerals indicate the presence of ultramafic rocks in the study area. Minerals such as calcium aluminium hydroxide hydrate and sodium cobalt aluminium silicate were also present in rock sample HR3. The presence of these minerals probably replaced serpentine in the host rock, during metamorphism. Besides these minerals, the selected rock samples contain several other minerals in varying proportions (Appendix F). These include dolomite, magnesite, and magnetite.

4.4 Whole Rock Geochemistry

The whole-rock geochemical analysis was undertaken to determine the concentrations of major oxide, trace, and rare-earth elements from rock samples within the study area. The rock samples were analysed by an X-ray fluorescence spectrometry (XRF). The detail of the methodology was discussed in Chapter 3. In total, 16 rock samples representing about 62 rocks from the Muyexe area were analysed and studied.

4.4.1 Major Oxides

Major oxides are useful for the classification and identification of rocks. The analysis of major and is important for understanding the conditions under which the rocks where formed, as well as their economic potential. The major oxides that were analysed in this study included SiO_2, TiO_2, Al_2O_3, Fe_2O_3, MnO, MgO, CaO, Na_2O, K_2O, and P_2O_5. Statistical analysis of the major oxide is presented in Table 4.1. The mean values of the major oxides revealed their abundance in rocks in the following order:
SiO_2>MgO> Fe2O_3> CaO> Na_2O> Al_2O_3>TiO_2>MnO> P_2O_5>K_2O (Table 4.1).

Table 4.1: Statistical analysis of major oxides

	SiO_2	TiO_2	Al_2O_3	Fe_2O_3	MnO	MgO	CaO	Na_2O	K_2O	P_2O_5
Count	16	16	16	16	16	16	16	16	16	16
Min value	36,23	0,00	0,00	0,47	0,00	0,00	0,00	0,00	0,00	0,00
Max value	99,50	1,38	10,38	19,81	0,27	41,98	13,43	15,46	0,35	0,40
Mean	54.75	0,23	2,59	9,56	0,18	20,80	4,90	2,71	0,06	0,11
Std. dev	17,88	0,32	3,17	4,09	0,06	12,90	4,45	3,95	0,10	0,13

Major oxide concentrations from Table 3.4 were plotted using histogram plots (Fig. 4.3). Histograms are useful in interpreting the whole-rock geochemical data.

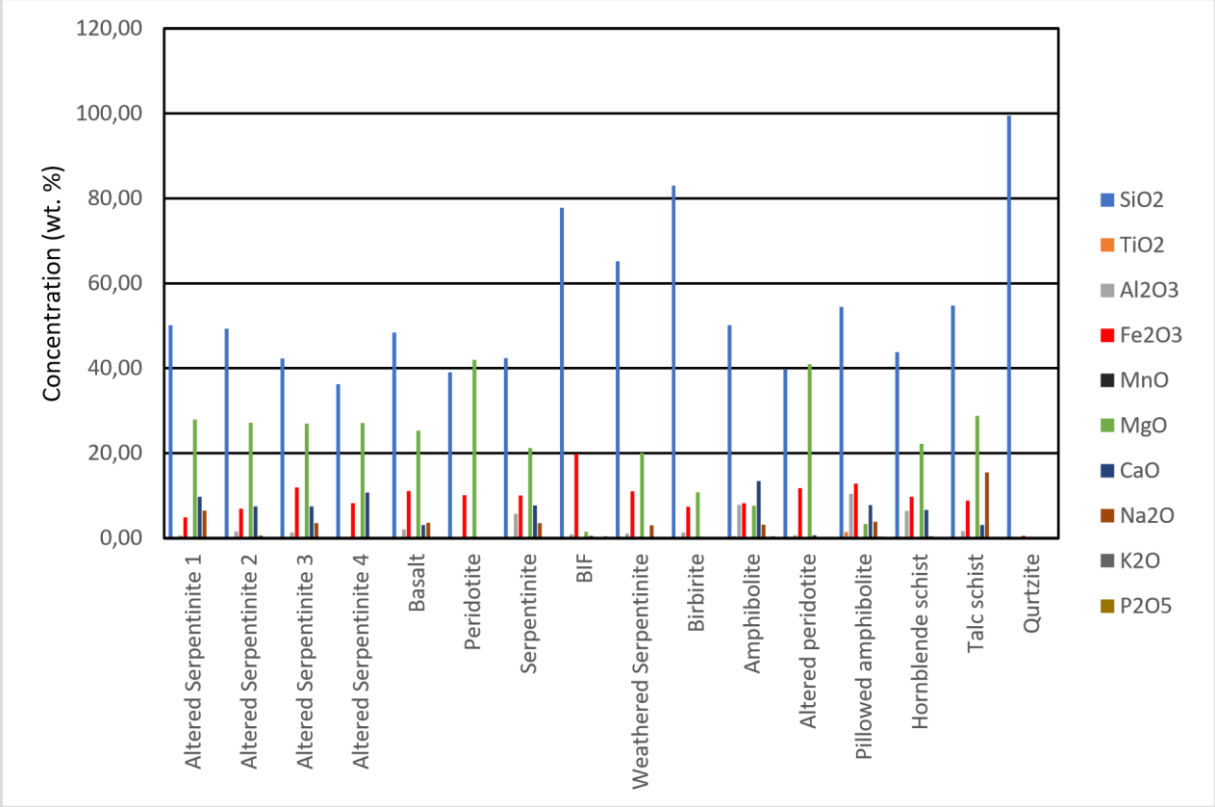

Figure 4.3: Histogram plot showing Major oxides in rock samples.

Based on the data presented in the histogram (Fig. 4.3), the major oxide distribution varied based on their mineralogy. SiO_2 is the most common oxide in the rocks, with

higher concentration up to 99.50 wt. % in quartzite. SiO_2 was dominating in all the rock types.

MgO seems to be the second most common oxide in the rocks of Muyexe. The magnesium oxide (MgO) content values range from 0 wt. % to 41.98 wt. %, with the least value recorded in quartzite and the highest value recorded in a peridotite. TiO_2 concentrations in rocks from Muyexe are mostly clustered, ranging from 0 wt. % in quartzite to 1,38 wt. % in pillowed amphibolite. The Al_2O_3 compositions have a wide range between 0 wt. % in peridotite and quartzite and 10.38 wt. % in pillowed amphibolite.

Fe_2O_3 concentration has a range of 0.47 – 19.81 wt. %, with the highest being concentrated in the banded iron formation and the least found in quartzite. MnO and CaO concentration also showed a wide range of 0 – 0.27 wt. % and 0 – 13.43 wt. % with the highest being in basalt and amphibolite, respectively. Na_2O contents have a wide range of 0 –15.46 with the highest value being in talc schist. Similarly, K_2O and P_2O_5 contents have a range of 0.0 – 0.35 wt. %, and 0.00 – 0,40 wt. %, respectively (Fig. 4.3). SiO_2 has a higher enrichment in the selected rocks, followed by the MgO, while Na_2O, K_2O, and P_20_5 are depleted within the rocks and has a very low concentration.

4.4.3 Trace Elements

Trace elements are those elements with low concentric levels in rock, i.e. <01% by weight and expressed in part per million (ppm). Trace element varies with major elements and they tend to concentrate on fewer minerals. Therefore, this provides a useful key tool for geochemist in formulating models of magmatic differentiation, discriminant diagram, prediction of the phases of fractionating from magma, and predicting sources of magma using trace elements (Vandecasteele and Block, 1993). Trace elements can be grouped on how they behave in the silicate portion of the earth, the mantle, and the crust. Generally, they are grouped according to their chemical behaviour. Four groups of trace elements are normally used for analysis which are the Large-ion Lithophile Elements (LILE), the High Field Strength Elements (HFSE), the Rare Earth Elements (REE) and the transition elements. Concentrations of these trace elements will vary with different rock types (Mason and Moore, 1982). Trace elements

were used to reflect chemical composition, origin, alteration, and classification of rocks.

Large Ion Lithophile Elements

Large ion lithophile elements (LILE) are characterized by large ionic radius, and low charges, and will therefore preferentially concentrate in the liquid until a phase with large enough sites to accommodate them begins to crystallize (Best, 2003). These elements will, therefore, be largely "incompatible" particularly with respect to mantle phases (Ol, Opx, Cpx, Gt). K, Rb, Cs, Sr, and Ba, are often collectively termed the large-ion-lithophile-elements (LILE) elements (White, 2013).

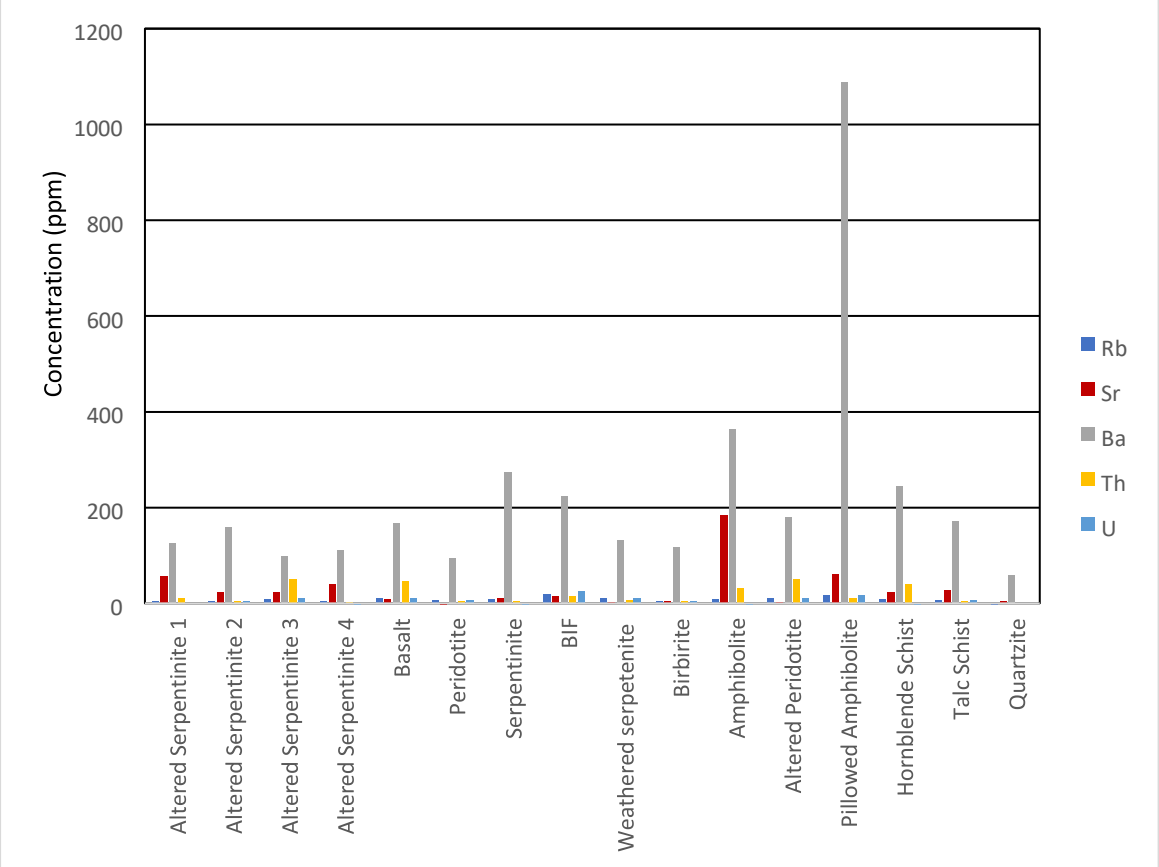

Figure 4.4: Histogram plot showing Large Ion Lithophile Elements in rock samples.

According to the histogram above (Fig. 4.4), the concentration of Rb in the rock samples ranged between 0.8 ppm to 19.5 ppm with an average of 8.9 ppm compared to the 84 ppm for the upper crust (Rudnick and Gao, 2003). According to Mielke (1979), ultramafic rocks have an average concentration of 0.2 ppm, however, the ultramafic rocks of the study area have an average of 8.05 ppm of Rb which is higher.

The rocks of the study area seem to be depleted in Rb concentration and this may be attributed to the depletion of biotite in the samples and equally may be indicative of fine-grained sili-clastic material present within the sample.

The concentration of Sr in rock samples ranges between 1.1 – 185.1 ppm with an average of 30.6 ppm which is low compared to the 320 – 384 ppm of the upper crust (Rudnick and Gao, 2003). Amphibolite has the highest concentration of Sr at 185,1 ppm while peridotite has the lowest concentration at 1.1 ppm. Mielke (1979) cites levels of Sr in ultramafic, basaltic, and granitic rocks as 1, 465 and 100 – 440 ppm, respectively. The Sr concentration of the rocks of the study area seems to be around the ultramafic and basaltic values, but they are depleted. The occurrence of Sr in the samples may be indicative of carbonate materials whereas the low content of Sr may be attributed to leaching during weathering.

The concentration of Th in rock samples ranges between 0 ppm to 51.2 ppm with an average of 17.97 ppm compared to 10.5 ppm for Upper Crust (Rudnick and Gao, 2003). Altered serpentinite 3 has the highest concentration of Th, while quartzite has the lowest concentration. The rocks of the study area are enriched in Th, averaging more than that of the upper crust. The concentration of U in the rock samples of the study area ranges between 0 – 25 ppm with an average of 7.2 ppm compared to the 2.7 ppm of the Upper Crust concentration (Rudnick and Gao, 2003). U is enriched in the banded iron formation (BIF), followed by sample pillowed amphibolite. Altered serpentinite 3 and quartzite are depleted in U, with their values being 0 ppm. The enrichment of U and Th in samples is indicative of the felsic composition of the source rock or the presence of their major host minerals such as zircon and iron oxide.

The concentration of Ba in rock samples ranges between 58.3 ppm and 1088.6 ppm with an average of 225.6 ppm compared to 628 ppm for Upper continental crust (Rudnick and Gao, 2003). Pillowed amphibolite is enriched in Ba and this is due to Ba^{2+} ion also substitutes for Ca^{2+} in the plagioclase, pyroxenes, and amphibole, and in the non-silicate minerals apatite and calcite. Quartzite, peridotite, and altered serpentinite 3 have the lowest abundance of Ba with a concentration of 58.3 ppm, 94.8 ppm, and 98.9 ppm respectively thus indicating depletion, and these can be attributed to weathering and alterations resulting in mobilisation of the element in the rock.

High Field Strength Elements

Trace elements comprised in this group are Y, Zr, Nb, and Hf. These elements are particularly insoluble due to their high ionic potential thus making them immobile during weathering and metamorphism (Cann, 1970). HFSE elements are enriched in felsic rather than mafic rocks (Bauluz *et al.,* 2000 and Bauluz *et al.,* 2005). In general, Y–Nb–REE-rich minerals are spatially associated with Fe-rich phases (e.g., pyrite, magnetite, greenalite, and hematite) (Graupner *et al.,* 2014).

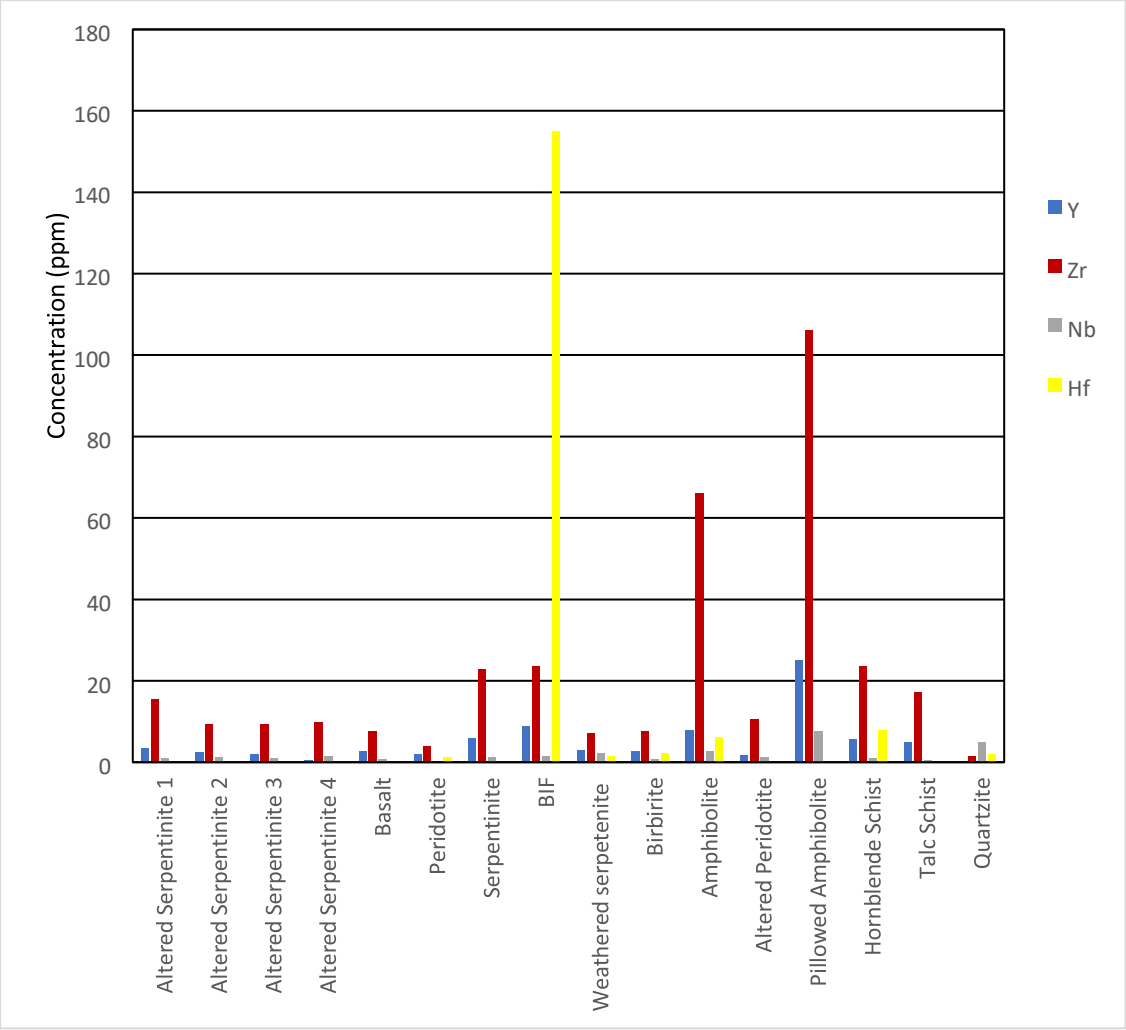

Figure 4.5: Histogram plot showing High Field Strength Elements in rock samples.

The concentration of Y in rock samples ranges between 0 ppm and 25 ppm with an average of 4.90 ppm (Fig. 4.5) compared to 21 ppm for Upper continental crust (Rudnick and Gao, 2003). All the collected samples are depleted in Y except for pillowed amphibole with a concentration of 25 ppm. The enrichment of Y in these

samples can be associated with the concentration of hornblende, biotite, feldspar and clinopyroxene where they can be present as an accessory element.

The concentration of Zr in rock samples ranges between 1.4 ppm and 106.1 ppm with an average of 21.34 ppm compared to 193 ppm for Upper continental crust (Rudnick and Gao, 2003). Zr is depleted in all the samples but minor enrichment can be detected in pillowed amphibolite. The minor enrichment of Zr in the rock can be attributed to the abundance of clinopyroxene, amphibole, and mica.

The concentration of Nb in rock samples ranged between 0 ppm and 7.5 ppm with an average of 1.79 ppm compared to 12 ppm for Upper continental crust (Rudnick and Gao, 2003). Nb is depleted in all the samples, however, minor enrichment can be found in pillowed amphibolite rock. The minor enrichment of Nb in the rock can be attributed to the abundance of biotite, rutile, sphene, cassiterite, and zircon.

The concentration of Hf in rock samples ranged between 0 ppm and 155 ppm with an average of 10.99 ppm compared to 5.3 ppm for Upper continental crust (Rudnick and Gao, 2003). Hf is depleted most of the samples, however, there is a major enrichment in BIF, hornblende schist, and amphibolite. Their concentrations are 155 ppm, 7.7 ppm, and 6.1 ppm respectively, which are higher than the average concentration of the upper continental crust (5.3 ppm). The enrichment of Hf in these samples can be attributed to alkali-rich lava which is commonly enriched with Hf. The high concentration of Hf and Zr elements implies an enriched source or extensive liquid evolution (Winter, 2014).

Transition Trace Elements

Trace elements comprised in this group are V, Co, Cu, Ni, Cr, and Sc. The solubility of transition metals varies and is influenced by valence state and obtainability of anions with which they can form soluble coordination complexes. They range from moderately incompatible to very compatible. High concentrations of highly compatible elements such as Cr, Ni, and Co point toward a mantle source or crystal accumulation. They are considerably more complex as they have two or more valence states of nature and they have higher electronegativity than LILE. They range from moderately incompatible e.g. (Ti, Cu, and Zn) to very compatible e.g. (Cr, Ni, and Co). High

concentrations of the highly compatible elements (Cr, Ni, and Co) indicate a mantle source or crystal accumulation (Best, 2003).

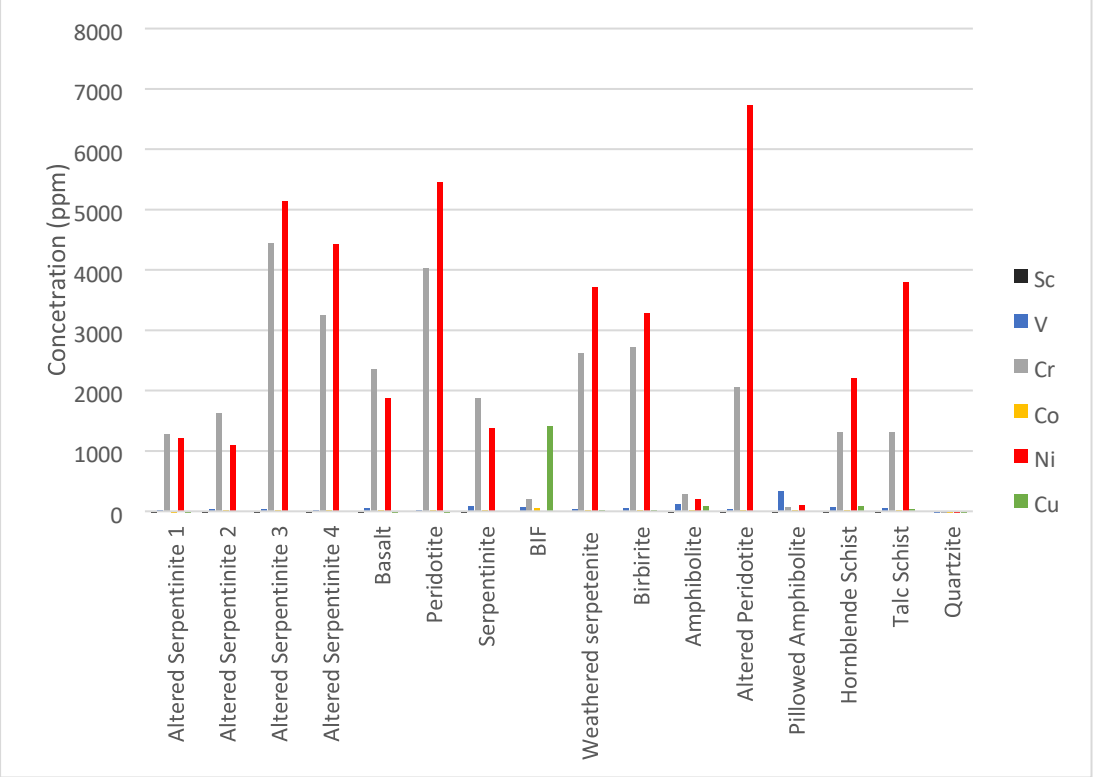

Figure 4.6: Histogram plot showing Transition Trace Elements in rock samples.

According to the histogram above (Fig. 4.6), chromium (Cr) exhibited high concentration values in the rock samples of the study area, with its concentration being between 4.9 - 4437.5 ppm averaging 1840.83 ppm which is higher than the Upper continental crust of 92 ppm (Rudnick and Gao, 2003). Quartzite and pillowed amphibolite are depleted of Cr. The major enrichment of Cr can be attributed to that Cr is very enriched in ultramafic rocks (1000–3000 ppm) and that the majority of the rocks were dominated by Cr as an accessory mineral as seen for the thin section in the petrographic study.

Sc, V, Co, Cu, and Ni concentration ranged between 0 – 1.2 ppm, 0.8 – 332.8 ppm, 1.2 – 46.7 ppm, 0 – 1480.8 ppm and 0 – 6721.6 ppm, respectively. Their average concentration area 0.45 ppm, 64.32 ppm, 23.36 ppm, 103.35 and 2538.06 ppm compared to the Upper continental crust (Rudnick and Gao, 2003) of 14.0 ppm, 97 ppm, 17.3 ppm, 28 ppm, and 47 ppm, respectively. Sc in depleted from all the rock

samples of the study area, while the other elements appear to be enriched. Enrichment of these elements is associated with mafic rocks and Cu-Fe-Cr rich rocks.

Trace Elements Normalisation

The concentrations of the trace elements in the rock samples were compared to those of the same elements in primitive upper mantle-PUM described by McDonough and Sun (1995). According to the Figure below (Fig. 4.7), Sr, Ba, V, and Cr are enriched in the rocks of the study area. Cu is enriched in some rocks, like quartzite, BIF but it is also depleted in rocks such as serpentinites and peridotite. Co, Ni, and Zn are also depleted, but just like Cu, they show a little bit of enrichment in some rock samples.

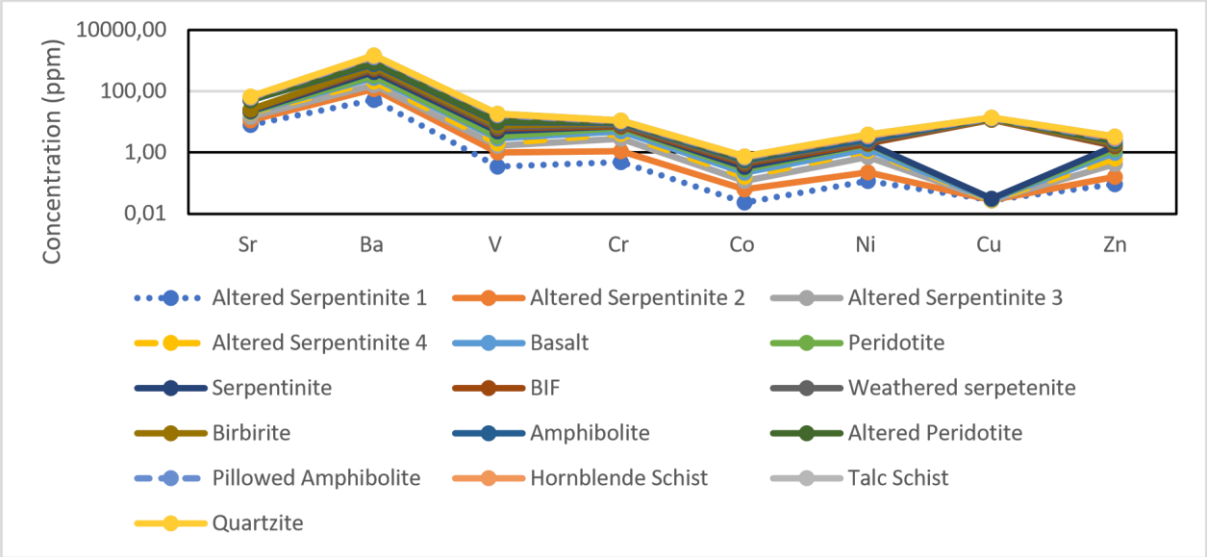

Figure 4.7: Trace elements normalised to primitive upper mantle (PUM) composition

4.4.4 Rare Earth Elements

La, Ce, Pr, Nd, Pm (N.B. promethium is unstable and not present as a natural element), Sm and Eu being described as light rare-earth elements (LREEs) and Gd, Tb, Dy, Ho, Er, Tm, Yb and Lu as heavy rare-earth elements (HREEs) (Henderson, 1984). They are strongly electropositive and have electronegativity of at most 1.2. They are relatively insoluble in aqueous solutions because of their higher charge and high ionic potential. They are regarded as incompatible elements due to their large ionic charge and large ionic radii (Best, 2003). The degree of incompatibilities varies due to the ionic radii.

These elements are valuable in studying altered or weathered rocks as they are highly insoluble and immobile with their patterns often remain unchanged during

metamorphism. The patterns of REEs make available information on the premetamorphic history of rock. The study revealed the occurrence of La, Ce, Sm, Eu, Gd, Tb, Dy, Er, and Yb (Fig. 4.8).

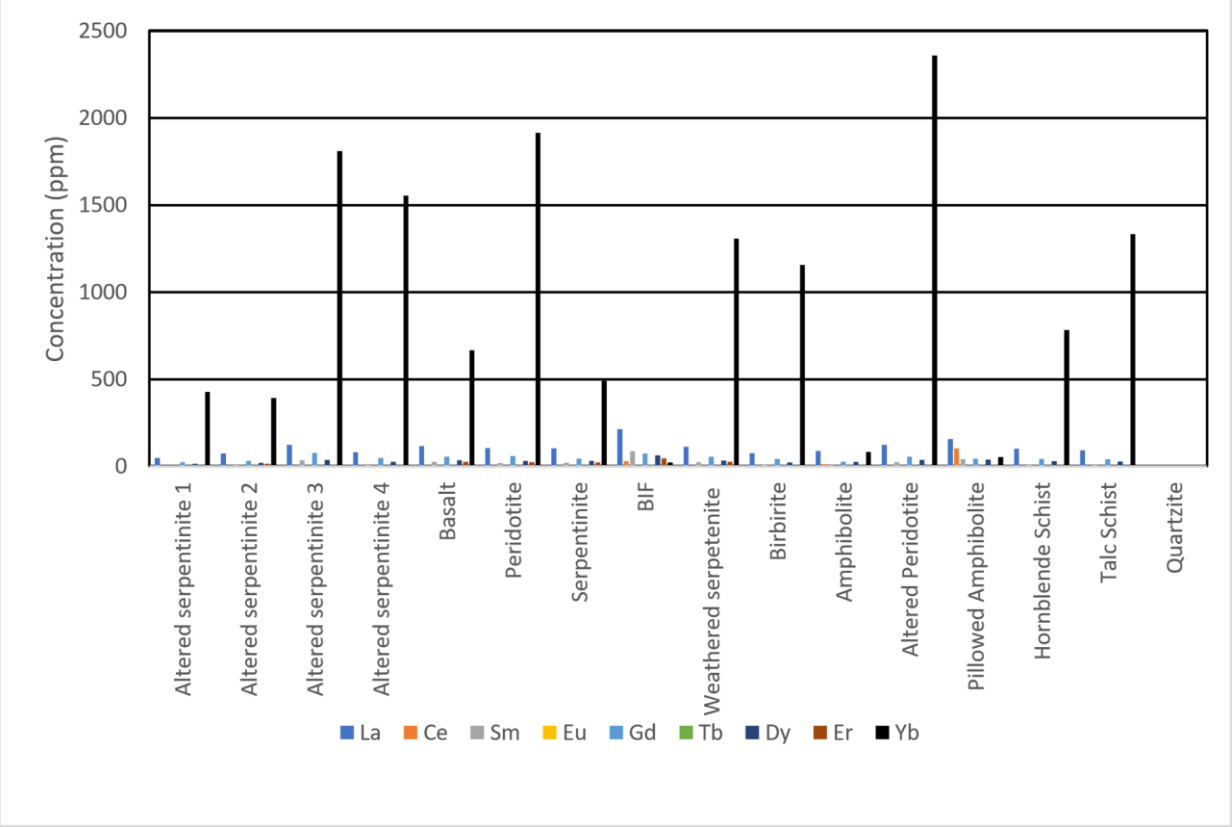

Figure 4.8: Histogram plot showing Rare Earth Elements in rock samples.

REE Concentration in Rocks

Ce had an average concentration of 9.59 ppm, with a wide range of 0 ppm to 104.7 ppm (Fig. 4.8). Ce was highly depleted from most of the rocks; however, pillowed amphibolite indicated a major enrichment. The concentration of La was ranging from 4.8 ppm to 215.3 ppm with an average concentration of 102.31 ppm. The least concentration was recorded in quartzite, with the highest concentration recorded in BIF.

Dy concentration ranges from 1.5 ppm to 63 ppm with an average concentration of 30.4 ppm. The highest concentration was found in BIF and the lowest was found in quartzite. Sm had an average concentration of 22.72 ppm and ranging from 0 ppm into 88.2 ppm in BIF (T1S17).

Yb concentration ranges from 3 ppm to 2360.5 ppm with an average concentration of 898.13 ppm. The highest concentration was found in altered peridotite and the lowest was found in quartzite. Eu concentration ranges from 0 ppm to 2.7 ppm with an average concentration of 1.84 ppm. The highest concentration was found in basalt and the lowest was found in quartzite.

Gd concentration ranges from 0 ppm to 78.8 ppm with an average concentration of 46.01 ppm. The highest concentration was found in altered serpentinite 3 and the lowest was found in quartzite. Tb concentration ranges from 0.2 ppm to 6.4 ppm with an average concentration of 2.99 ppm. The highest concentration was found in BIF and the lowest was found in quartzite. Er concentration ranges from 1.1 ppm to 46.6 ppm with an average concentration of 12.91 ppm. The highest concentration was found in BIF and the lowest was found in quartzite.

Rare Earth Elements Normalisation

The REE are commonly normalised rather than being presented as absolute values. They are usually normalised against the composition of the upper continental crust and in this study, normalisation was undertaken using McDonough and Sun (1995) REE Primitive mantle values. By normalising the data, it is possible to look at the patterns in REE relative abundance to determine features, such as high-pressure or low-pressure formation.

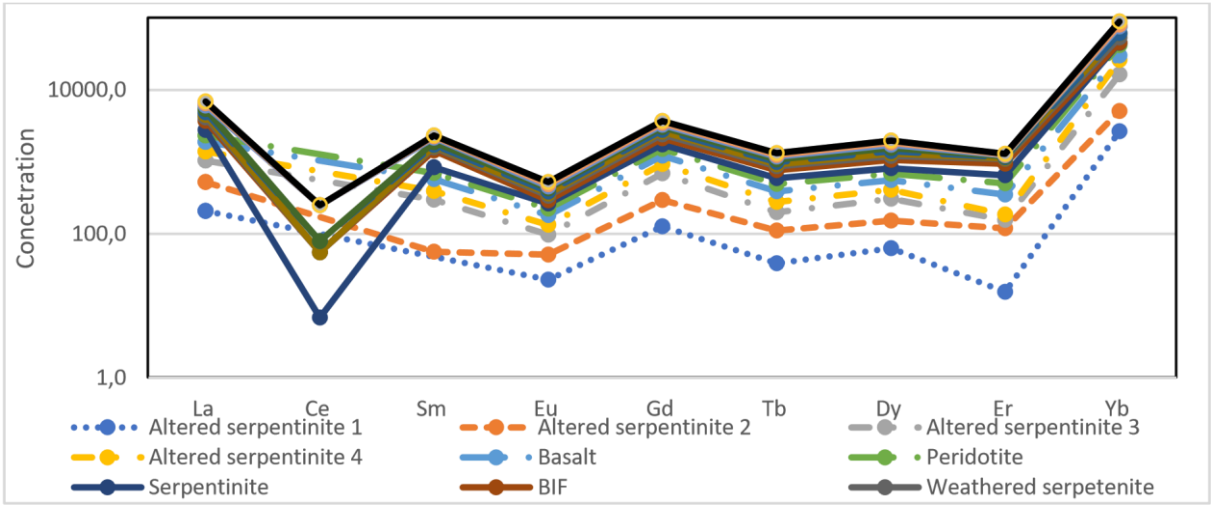

Figure 4.9: Spider diagram plot of normalised REE in Rocks.

The REE distribution patterns of all the samples are elevated on the left, and elevated and steep flat on the right, suggesting that the LREE and HREE are fractionated in

different degrees (Fig. 4.9). The distribution pattern indicates that the rocks of the study area are enriched with Yb and depleted in Ce and Er compare to primitive upper mantle values. The rock samples generally exhibit negative Ce, Eu and Er anomaly, respectively. A moderately negative Eu anomaly is normally subscribed to fractionation of plagioclase due to the similar ionic radius and charge of Eu^{2+} and Ca^{2+} (Rollinson, 1993; Blatt *et al.,* 2006). An obvious V shape at Ce, Eu, and Er features the normalised distribution patterns. The concentrations of individual REEs tend to decrease with increasing atomic number, and REEs with even atomic numbers are more frequent than their neighbours with odd atomic numbers, according to the OddoHarkins rule as described by Wang *et al.* (2015) and Laveuf and Cornu (2009). REE concentrations are in the same order of magnitude as that in the earth's crust as described by Taylor and McLennan (1995) and like that of Humphris and Henderson (1984).

Among common petrographic minerals only amphibole, clinopyroxene, the feldspars, and garnet contain detectable amounts of REE. Neither olivine, nor orthopyroxene, muscovite, and biotite have a measurable REE concentration.

The LaN/EuN values range from 0 to 156.47 (average 908.43), which represent a slight depletion of LREE compared to the GdN/YbN ratios which vary between 0 and 14661,49 (average 1219,33), reflecting high enrichment of HREE on the REE patterns normalised relative to primitive mantle values. These features are typical of tholeiitic arc basalts (Chiaradia, 2009). The unfractionated HREE could indicate that magma was produced outside the garnet stability field (Ahmadi Khalaji *et al.,* 2007).

4.5 Classifications of Rocks and Provenance

4.5.1 Alteration Box Plot

The alteration box plot of Large *et al.* (2001) was used to determine whether the samples were affected by alteration (Fig. 4.10). This plot is very important in the sense that it will determine whether the sample represents the original geochemical composition of the rock and can be used to measure the mode and intensity of alteration of the rock or that the sample is suitable (Large *et al.,* 2001). The alteration box plot of Large *et al.* (2001) can also be used to recognize and distinguish the effects of diagenetic and hydrothermal alteration processes on the major element geochemistry of common volcanic rock types (Large *et al.,* 2001; Gifkins *et al.,* 2005). The box plot may, with some limitations, also be applied to sedimentary rocks of

immature chemical and mineralogical composition (Gifkins *et al.,* 2005). In the present context, possible volcanic and sedimentary samples can both be displayed on the box plot, as the intent is to reliably exclude geochemically altered samples, rather than to recognize the effects of such alteration processes in details (Large *et al.,* 2001).

The box plot uses the Ishikawa Alteration Index (AI) and Chlorite Carbonate-Pyrite Index (CCPI) as the axes, where:

$$AI = 100 \times (MgO + K_2O) / (MgO + K_2O + CaO + Na_2O) \quad \text{.....equation 4.1}$$

$$CCPI = 100 \times (MgO + FeO) / (MgO + FeO + K_2O + Na_2O) \quad \text{.....equation 4.2}$$

The alteration box plot of Large *et al.* (2001) shows that most of the samples were modified by alteration, which leads to the removal of mobile elements and the addition of volatiles (Fig. 4.10). The alteration box plot (Fig. 4.10) outlines the position of unaltered igneous rocks with boxes, whereas the various types of alteration are denoted by arrows that point away from the boxes (for a detailed explanation of alteration trends see Gifkins *et al.,* 2005 and Large *et al.,* 2001).

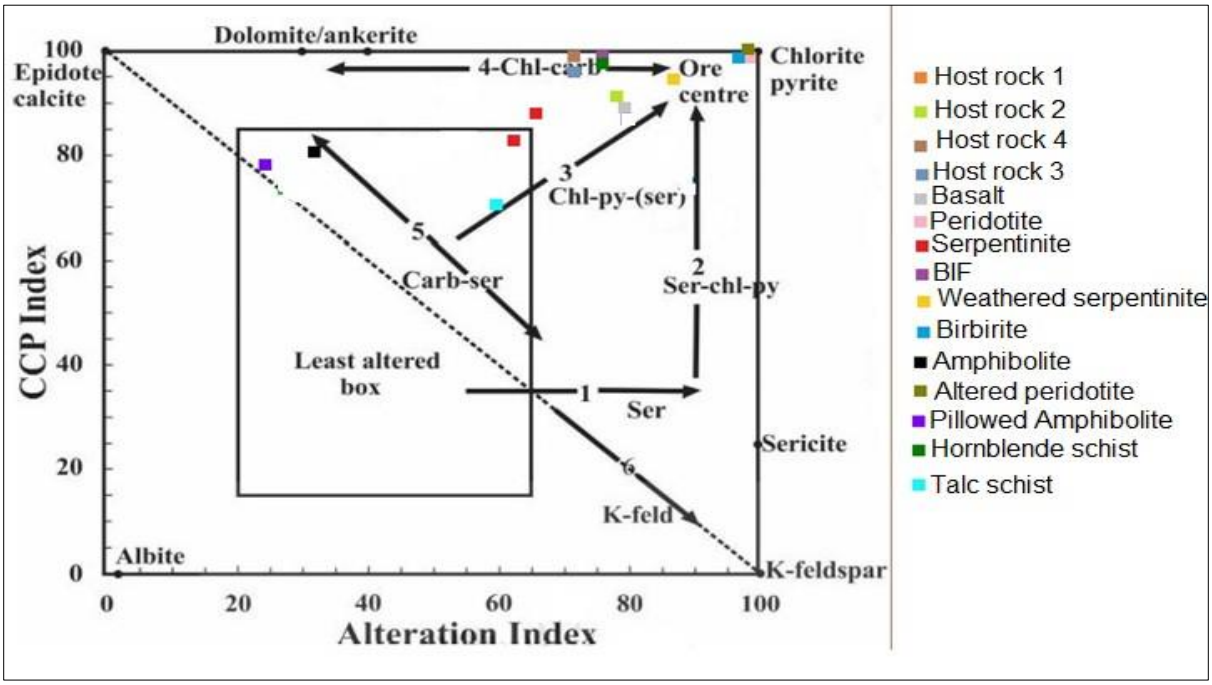

Figure 4.10: Alteration box plot of rock samples from the study area.

Although most of the rocks are altered, amphibolite, talc schist, host rock 1 (altered serpentinite 1) and pillowed amphibolite from the study area appear to be not altered and suitable for determining original geochemical composition (Fig. 4.10). Host rock 3 (altered serpentinite 3), hornblende schist, BIF, and host rock 4 (altered serpentinite

4), were altered by chlorite-carbonate alteration (Fig. 4.10). Peridotite, birbirite, and weather serpentinite schist were affected by strong chlorite pyrite alteration, while basalt, serpentinite, and host rock 2 (altered serpentinite 2) were affected by chloritepyrite-sericite alteration (Fig. 4.10). This alteration trend follows hydrothermal alteration trends 3 and 4 defined by Large *et al.,* (2001), typically associated with chlorination (Gifkins *et al.,* 2005). The geochemical data is accordingly viewed with caution especially with reference to major element geochemistry.

4.5.2 Classification of Rocks and Magma Type

Various criteria are used to classify rocks. These include mineral present in the rock (the mode), texture, colour, and chemical composition. In this study chemical composition was used to classify rocks of the study area.

Classification diagrams were used to determine the petrological characteristics of the rocks of the study area. Few discrimination diagrams are available for this purpose, but most of them are applicable to younger rocks and become less definitive with older rocks as environments of formation become less clear and secondary processes such as metamorphism and hydrothermal alteration become more dominant. Some of these plots use concentrations of mobile elements (Pecerillo and Taylor, 1976). Because of the effects of hydrothermal alteration, these plots need to be used with caution, so only least altered samples should be included. But due to behavioural variations amongst the major, trace and rare earth elements, it is possible to select classification schemes based on carefully chosen elements that are suitable to the rock suit in question. Diagrams based on immobile element concentrations, on the, should yield more reliable results (Winchester and Floyd, 1977).

AFM Diagram

Major oxides are commonly used to classify volcanic rocks, but they tend to be mobile during hydrothermal alteration and metamorphism. Oxides such as Na_2O, K_2O, MgO, and FeO are commonly utilized to decide whether a suite of volcanic rocks have a tholeiitic or calc-alkaline affinity (Floyd and Winchester, 1978). The two broad magmatic types exhibit characteristic trends on an alkali, total Fe and MgO on the AFM diagram.

The lithologies of the study area indicated an alkali depletion with a decrease in FeO concentrations and corresponding increases in MgO, except for pillowed amphibolite, which indicated the opposite (Fig. 4.11). It should also be noted that the alkalis, especially Na_2O are prone to remobilization during metamorphism, in which case rocks samples may not reflect the primary composition. Thus, because the Precambrian rocks are not pristine, these interpretations should be viewed with caution. The rocks at the study area are tholeiitic magma type, except for samples amphibolite, altered serpentinite 1, and talc schist which are calc-alkali magma type. Most of the rocks under tholeiitic magma are highly altered. This trend suggests that the rocks have a similar paragenesis. BIF and quartzite were not classified on this diagram as they are not part of mafic or ultramafic rock.

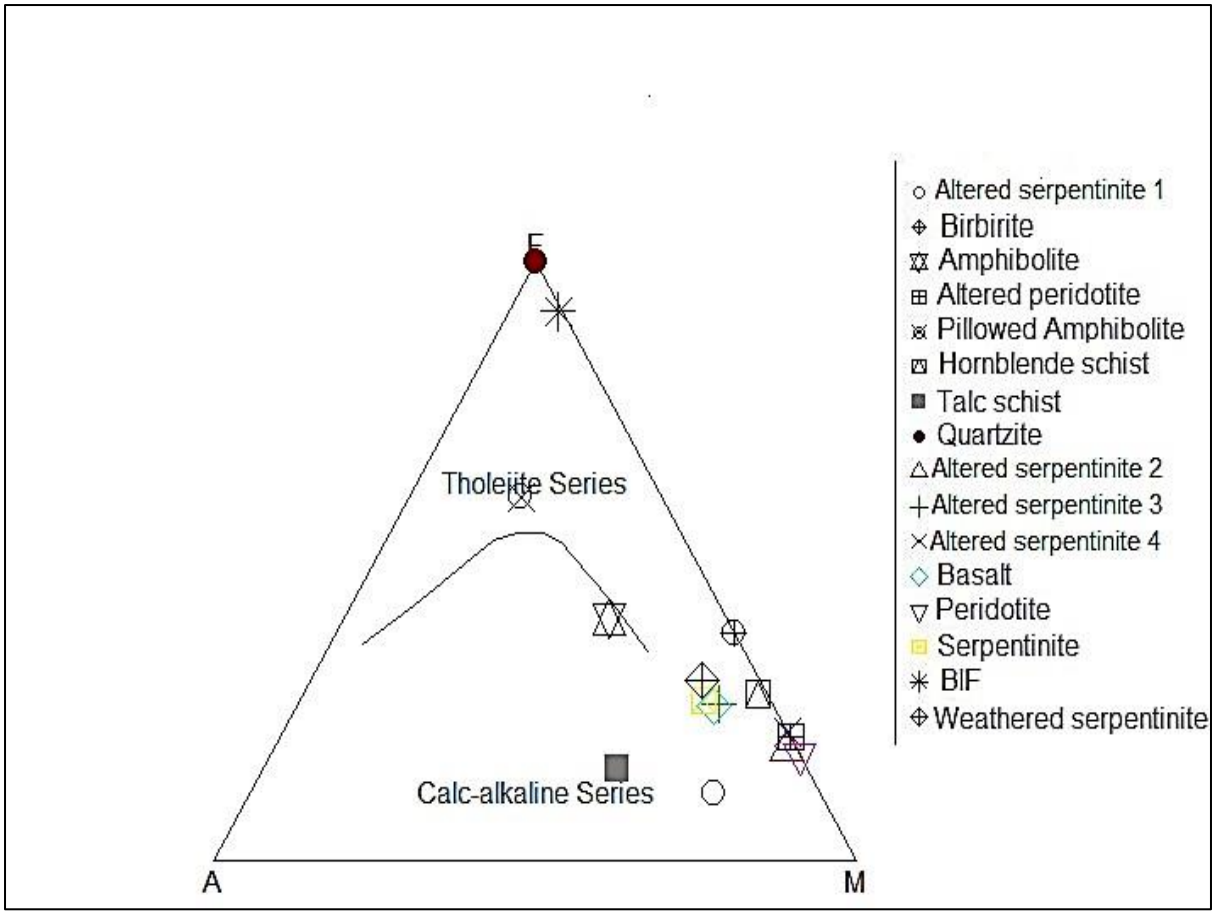

Figure 4.11: Magma classification AFM diagram for rocks in the Study area. *A = (Na_2O +K_2O), F = (FeOtotal), M = (MgO).*

Total Alkalis Diagram

The Total Alkalis (TAS) diagram of Le Bas *et al.* (1986) was also used to classify and to distinguish between various two types of magma that may have formed the rocks of the study area. On the TAS diagram (Fig. 4.12)**,** most of the rock samples plotted between; basalt, picro-basalt, trachy-basalt, basaltic andesite, basaltic trachyandesite, dacite, andesite, foidite. The banded iron formation has been classified as dacite, while quartzite was classified under rhyolite magma. Just like in the AFM diagram (Fig. 4.12) the rock classification on the TAS diagram (Fig. 4.12) suggests that the rocks at the study area are tholeiitic magma type, with a few being Calc-alkali magma type.

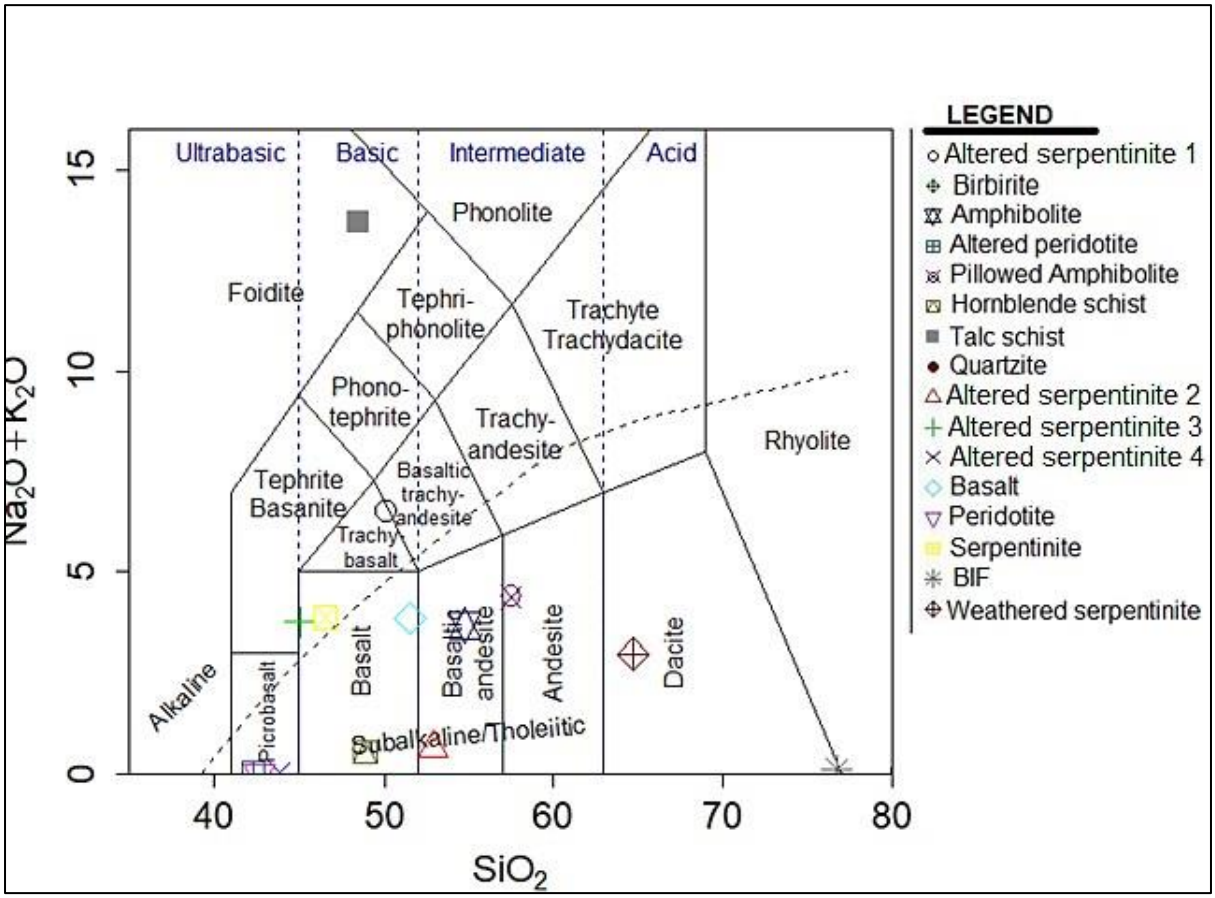

Figure 4.12: Total alkali-silica used to determine magma type

Nb/Y – Zr/Ti Plot

A diagram by Pearce (1996), making use of immobile trace element ratios, was also used to establish the original magma type of the rock samples of the study area. This diagram (Fig. 4.13) is considered more reliable than the diagram of Le Bas *et al.* (1986) for establishing original magma composition because it is based on immobile element

ratios rather than using mobile elements like sodium and potassium used in TAS diagram. On the Pearce (1996) diagram most of the samples from Muyexe are grouped closely as basalt (7 samples), basaltic andesite (4 samples), alkali basalt andesite (3 samples) and due to the chemical composition, peridotite and quartzite were unclassified on this diagram.

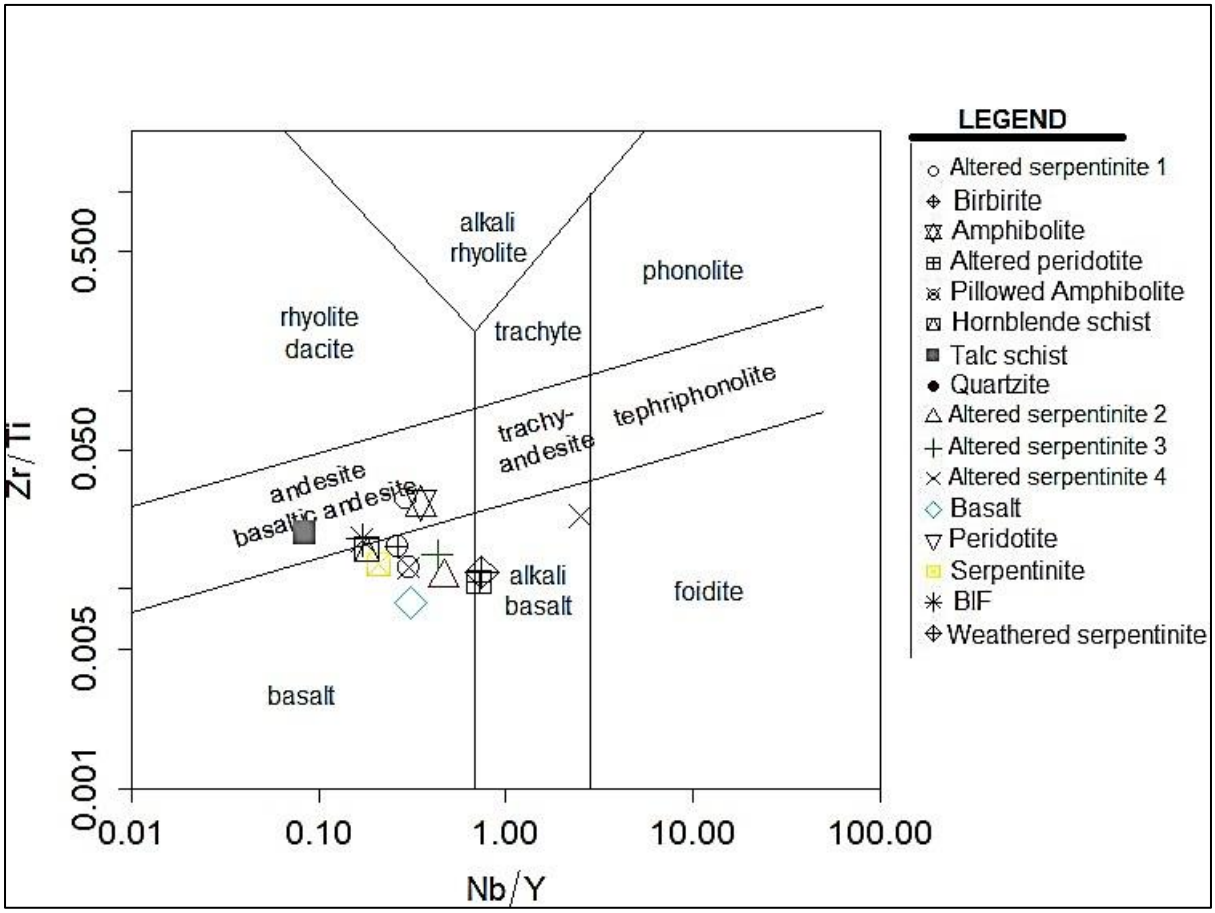

Figure 4.13: Magma type Nb/Y-Zr/Ti diagram for the rocks of the study area.

4.6 Geochemistry of Magnesite

In order to understand the geochemical characteristic of the magnesite orebody, 20 magnesite samples were chemically analysed by an X-ray fluorescence spectrometry (XRF) technique at the University of Venda Mining and Environmental Geology laboratory. Representative data of the major, trace and rare-earth elements of magnesite are presented in Appendix C.

4.6.1 Major Oxide Geochemistry

Major oxides geochemistry of magnesite is reported as a weight percentage of MgO, CaO, SiO_2, Fe_2O_3 and Loss of ignition (LOI). Stoichiometrically, the purest magnesite

is composed of 47.81% of MgO and 52.19% CO_2 (Bashir, 2008) but the average mined magnesite has a concentration of 43.3 wt. % MgO, 2.5 wt. % CaO, SiO_2 2.0 wt. %, 2.4 wt. % Fe_2O_3 and LOI of 49.8 wt. % (Ebner and Prochaska 2001). The deviation from the ideal composition in magnesite is due to the introduction of SiO_2, CaO and other impurities under varying geochemical controls. The statistical average concentration of major elements in magnesite is presented in the form of a table (Table 4. 2). Major elements concentrations from Table 4.2 were plotted on a bar graph (Fig. 4.14). A histogram is useful in interpreting the geochemical data of magnesite. The bulk chemical composition of magnesite analyse can be found in Appendix C.

Table 4.2: Statistical analysis of major oxide and LOI in magnesite

	MgO	SiO_2	CaO	Fe_2O_3	AL_2O_3	LOI
No of values	20	20	20	20	20	20
Min value	51,9	6,34	0,58	0,04	0	34.1
Max value	57,28	10,24	4,57	0,25	0	38.2
Range	5,38	3,9	3,99	0,21	0	4.1
Mean	54,02	7,85	1,76	0,14	0	36.05
Standard Deviation	1,33	0,00	0,00	0,06	0,00	1,53

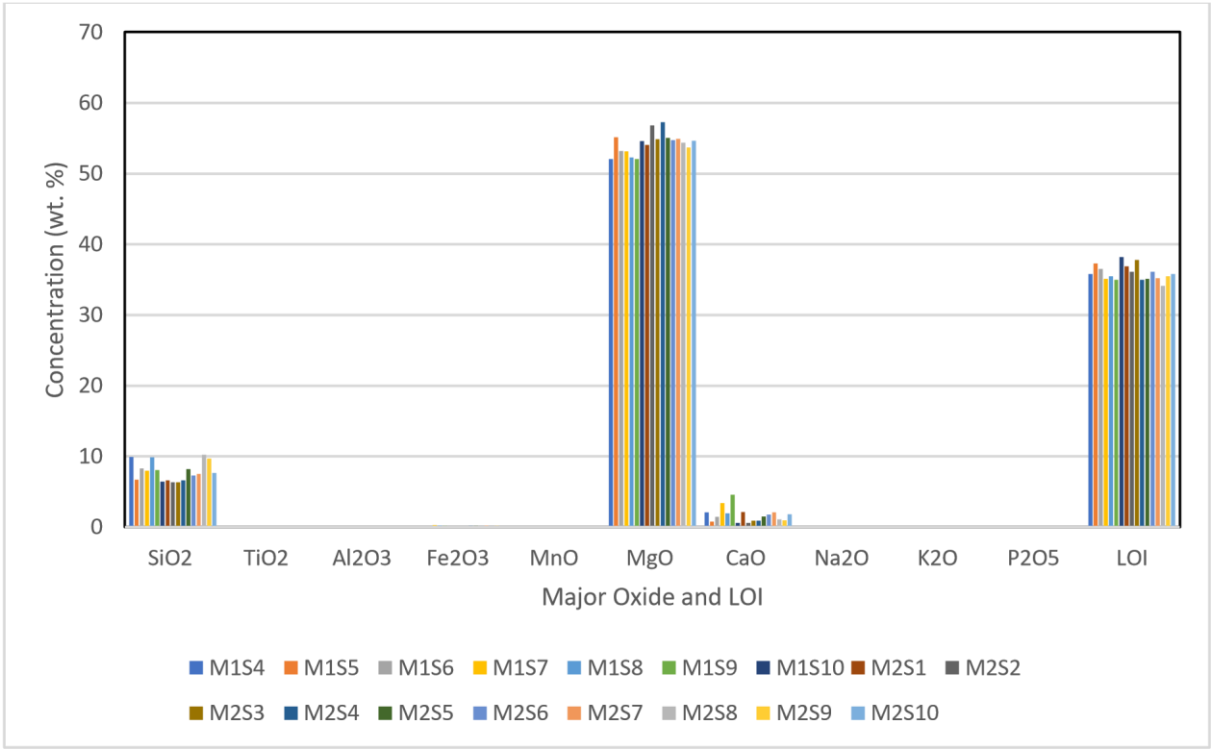

Figure 4.14: Concentration of major oxides and LOI in magnesite samples.

The chemical composition of magnesite samples from the mining sites showed some variations. From the magnesite geochemistry data (Fig. 4.14) of the study area, Magnesium Oxide range between 51.9 – 57.27 wt. % with an average of 54.01 wt. %. Sample M2S4 has the highest concentration of MgO while sample M1S1 has the lowest concentration of MgO.

The concentration of CaO in the magnesite ranges from 0.58 to 4.57 wt. % with an average of 1.8 wt. %. The distribution of CaO in magnesite is low and quite consistent with little spread (SD=1.05) (Table 4.2). The low concentration of CaO supports that host rocks of magnesite in the study area are Mg-rich and Ca deficient rocks.

Silica (SiO_2) is a bit high in the magnesite of the study area when compared to the theoretical 2.0 wt. % of the Indian Mineral Yearbook of 2012. The SiO_2 in the magnesite of the study area ranges between 6.34 – 10.24 wt. %, with an average of 7.9 wt. %. Sample M2S2 with the lowest concentration, while sample M2S8 has the highest concentration. This high concentration of silica is mostly due to the mobilization during metamorphism and dominant in the study area. The high SiO_2 content could also be derived from birbirite, talc and sometimes quartz rocks that are within the magnesite deposit in the study area.

Iron is an isomorphic admixture for Mg^{2+} in the crystal framework of magnesite and Fe_2O_3 contents are due to Fe substitution in the magnesite crystal lattice. Thus, the Fe_2O_3 in the magnesite ranges from 0.04 to 0.25 wt. %, with an average of 0.14 wt. % which is lower than the maximum allowable limit of iron oxide in magnesite of 2.4 wt. % (Ebner and Prochaska, 2001). The magnesite samples from the study have no concentration of aluminium oxide.

4.6.2 Trace Elements Geochemistry

Trace elements in magnesite have been studied in order to use their signatures as a hint to the source rocks from which the Mg^{2+} ions have been derived (Moller, 1989). Magnesite which occurred in different environments indicates unlike enrichments such as Cr, Ni, Co, and Ti contents. Magnesite related to ultramafic host rocks has enriched in Cr, Ni and Co content, magnesite in the marine-evaporitic environment has Cr, Ni, B, and Ti, magnesite in the lacustrine environment has Ni and Cu enrichment (Moller,

1989; Schroll, 2002; Kuşcu *et al.,* 2017). The occurrence of trace elements in different carbonate lattice (calcite, dolomite, aragonite, and magnesite) is largely depending upon ionic size, charge, abundance, and coefficient of distribution. Different sets of trace elements of the magnesite ore body were analysed to depict their geochemical behaviour. To characterize the individual geochemical environment of important magnesite forming processes (Moller, 1989), different groups of trace elements (SrBa, Ti, Fe-Mn, and Cr-Ni-Co) were studied (Table 4.3; Appendix C). The substitution of the trace elements into the lattice of magnesite is limited and most commonly occurs as impurities (Schroll, 2002). The concentrations of the trace elements in the whole samples were compared to those of the same elements in the upper continental crust by Rudnick and Gao (2003).

Table 4.3: Statistical analysis of trace element data in magnesite

	Sr	Ba	Cr	Co	Ni	Ti*	Fe*	Mn*
Count	20	20	20	20	20	20	20	20
Min	6,6	58,5	1,9	0	514,8	0	280	0
Max	65	60,1	48,3	3,9	3929,9	11,99	1749	116,17
Range	58,4	1,6	46,4	3,9	3415,1	11,99	1469	116,17
Mean	25,76	58,76	17,37	0,58	1578,9	3,9	996,75	31,38
Std.dev	13,31	0,53	14,41	0,81	894,97	5,25	445,19	26,99

Note these trace elements were calculated from the major oxide data (Appendix E)*

Titanium

The titanium concentration of all magnesite samples of the study area ranges from 0 to 11.99 ppm. Magnesite in ultramafic rocks usually has very low Ti concentrations (<3 ppm) (Toulkeridis *et al.,* 2010), whereas the Ti from magnesite of the study is was depleted in most samples and it had an average of 3.9 ppm, which is slightly higher than that of Moller (1989). Martiny and Rojkovic (1977) and Moller (1989) showed that Ti is not preferentially hosted in magnesite itself, but rather in the insoluble accessory minerals such as ilmenite or titanite. In the Moller (1989) magnesite vs environment diagram, Ti has a Log CTi range from 0 to 1.08. It is lower than the magnesite deposited in the marine/evaporates, metamorphic rocks and Mg^{2+}- metasomatism

environment (Fig. 4.15). Ti concentration covers the range of magnesite which were deposited in the altered ultramafic environment (Fig. 4.15).

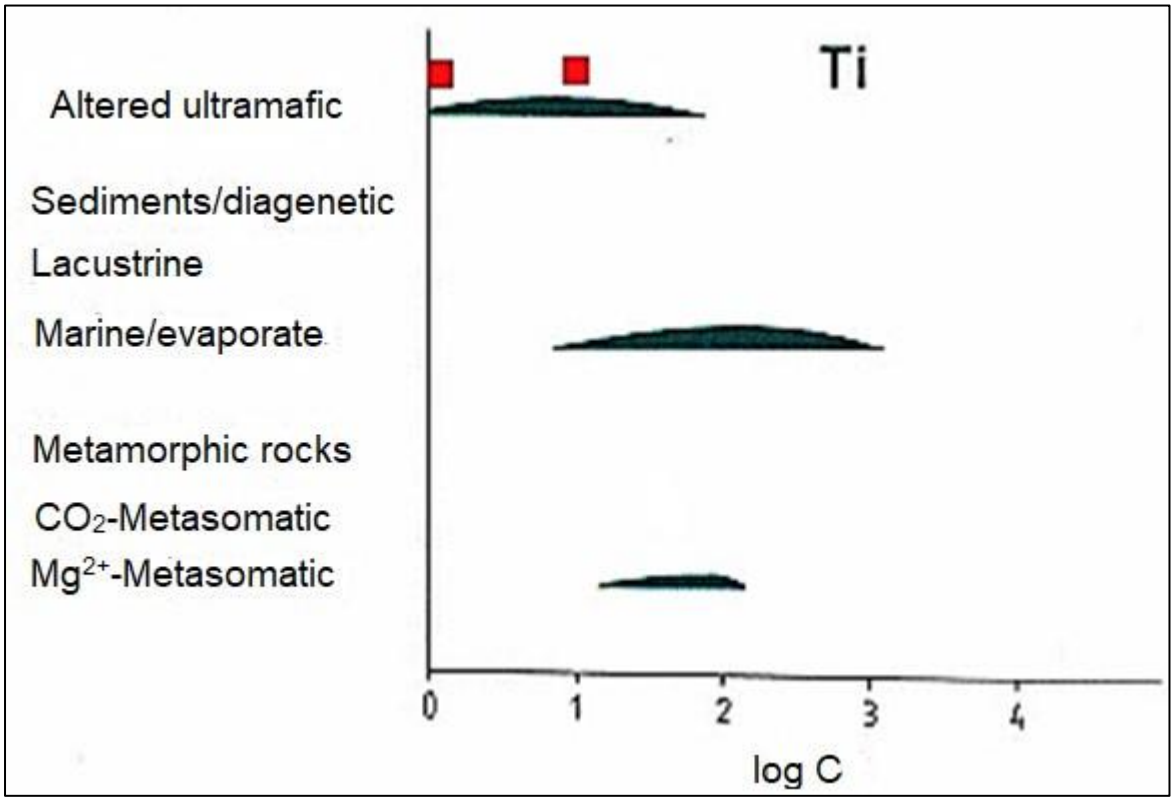

Figure 4.15: Distribution of Ti in magnesite from the study area plotted on the Log of concentration versus environment diagram proposed by Moller (1989). Red square indicates the range of Ti.

Strontium and Barium

Sr^{2+} and Ba^{2+} have the same ionic charge and their ionic radii are 1.32 A° and 1.49 A°, respectively. Both elements belong to large ion lithophile (LIL) elements and low filed strength (LFS) elements, therefore they have similar geochemical behaviour. But in all studied magnesite samples of the study area, there is no meaningful correlation between Sr and Ba (Appendix D). The Sr and Ba concentration of the studied magnesite range between 6.6 – 65.0 ppm (av. 25.7) and 58.50 – 60.1 ppm (av. 58.76), compared to the 320 and 628 ppm of the for Upper continental crust (Rudnick and Gao, 2003) respectively. The carbonates of Sr and Ba crystallize in the aragonite structure, for that reason, Sr and Ba substitution in calcite-structure magnesite should be of minor relevance. The Sr and Ba ions will be constantly rejected during magnesite crystallization and recrystallization because they are too large and cannot enter the

magnesite lattice (Moller, 1989). Therefore, low Sr and Ba concentration in magnesite samples does relate to ionic radii differences between the large Sr and Ba ions and the smaller Mg and Fe ions. The relatively high Sr concentrations in some samples probably reflect dolomite inclusions and re-dolomitization of magnesite

The concentration of Sr and Ba of all magnesite samples indicate Log CSr: 0.8 – 1.8 and Log CBa: 1.8 – 1.8. These values compared to the marine/evaporitic, lacustrine, altered ultramafic and Mg^{2+}metasomatism magnesite for Sr concentration (Fig. 4. 16). The Ba concentration covers between the magnesite which were deposited due to Mg^{2+}-metasomatism, marine/evaporates and altered ultramafic rocks (Fig. 4.17).

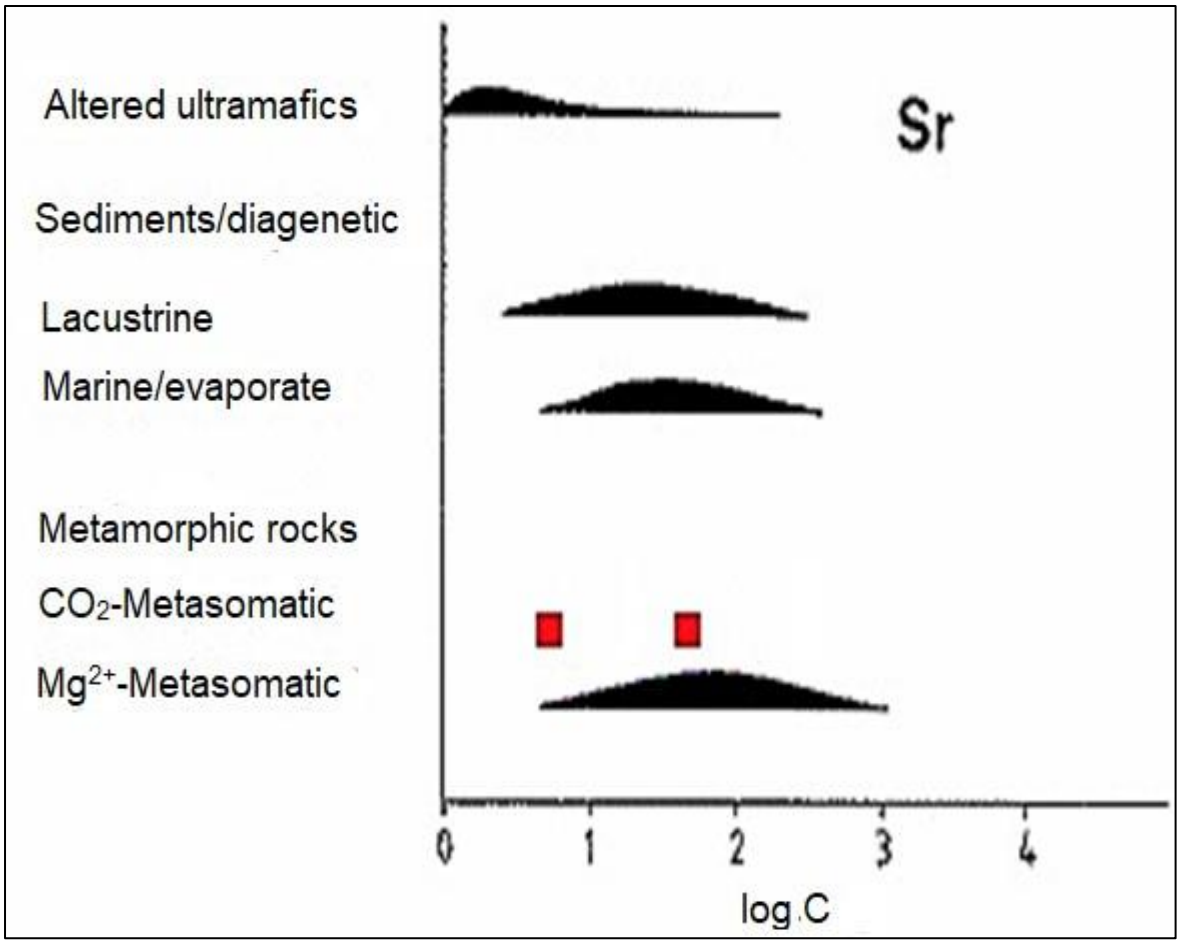

Figure 4.16: Distribution of Sr in magnesite from the study area plotted on the Log of concentration versus environment diagram proposed by Moller (1989). Red square indicates the range of Sr.

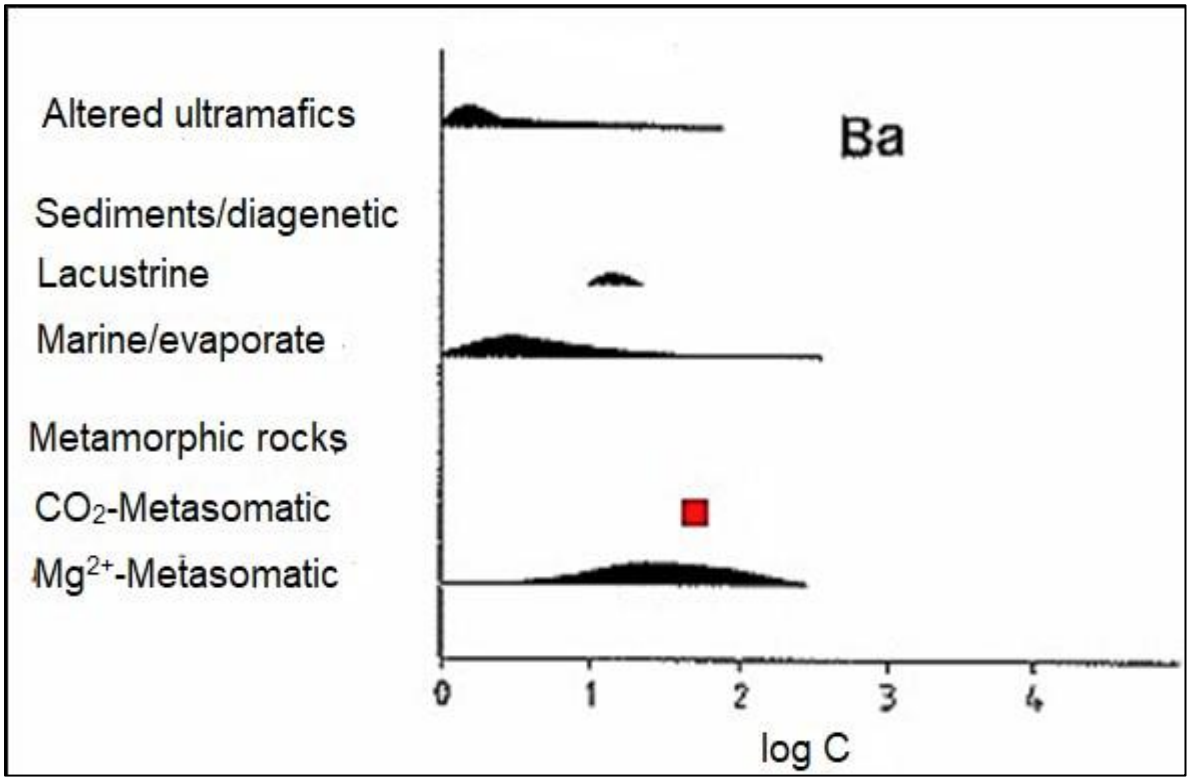

Figure 4.17: Distribution of Ba in magnesite from the study area plotted on the Log of concentration versus environment diagram proposed by Moller (1989). Red square indicates the range of Ba.

Iron and Manganese

Fe and Mn have similar geochemical behaviour in all magnesite samples analysed and they show a positive correlation (correlation coefficient r = 0.82, Appendix D). Both elements are partly hosted in the magnesite. Positively correlated Mn with Fe is interpreted to indicate that Mn was incorporated into the magnesite lattice during magnesite formation.

Fe and Mn concentrations range between 280 – 1749 ppm (av. 996.75 ppm) and 0 – 116.17 ppm (av. 31.38 ppm). Fe and Mn concentrations cover ranges typical for lacustrine as well as marine/evaporitic magnesite and their concentration is high in Mg^{2+}-metasomatism magnesite. Fe and Mn concentrations of all magnesite samples from the study area indicate Log CFe: 2.5 to 3.2 and Log CMn: 1.56 to 2.1. These values fit the lacustrine, altered ultramafic and marine/evaporitic environment (Fig. 4.18 and Fig. 4.19).

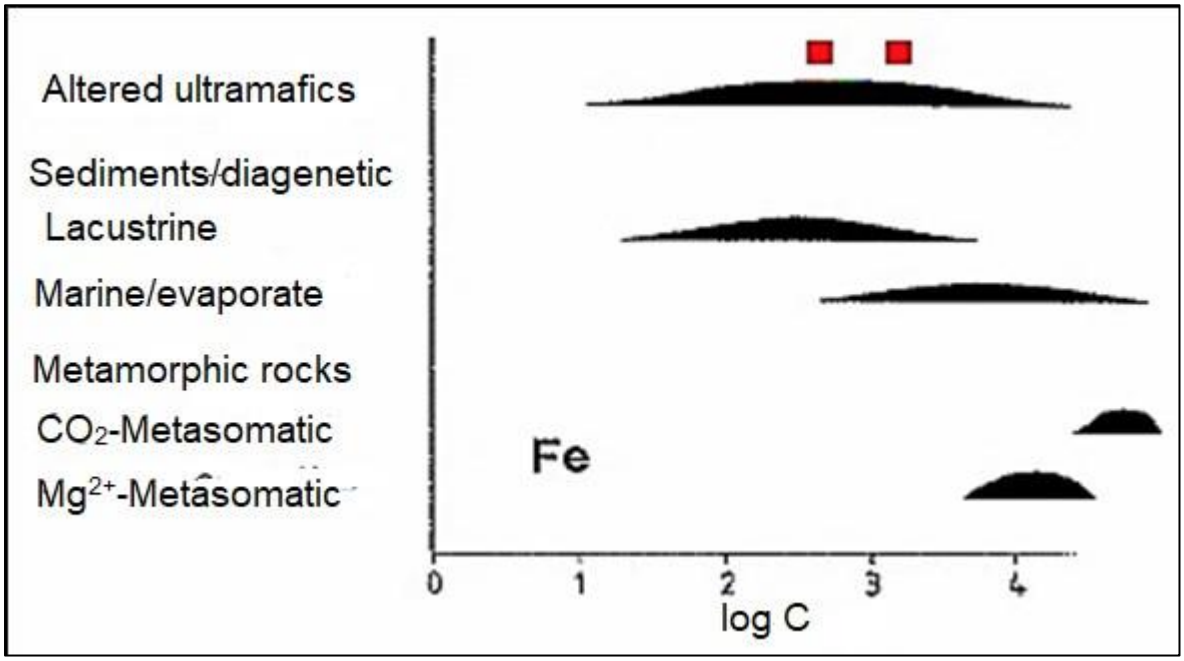

Figure 4.18: Distribution of Fe in magnesite from the study area plotted on the Log of concentration versus environment diagram proposed by Moller (1989). Red square indicates the range of Fe.

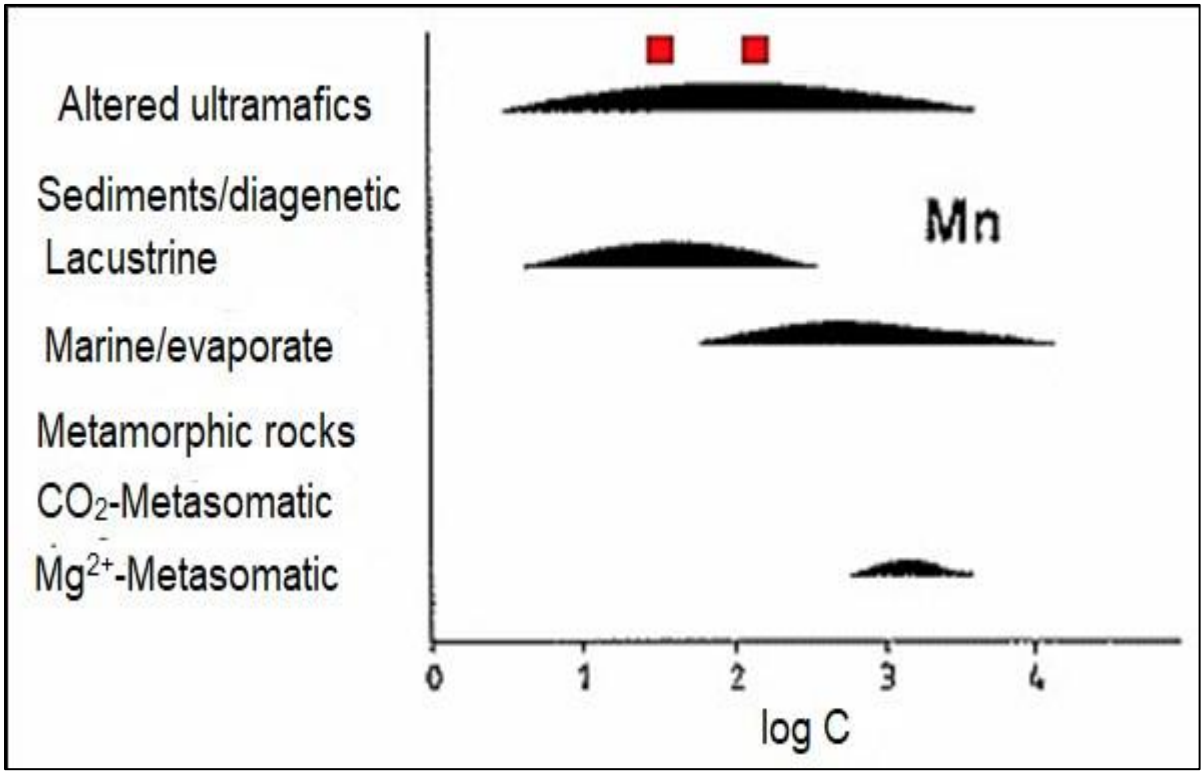

Figure 4.19: Distribution of Mn in magnesite from the study area plotted on the Log of concentration versus environment diagram proposed by Moller (1989). Red square indicates the range of Mn.

Chromium, Nickel, Cobalt

Cr, Ni, and Co concentrations values in magnesite range between 1.9 – 48.3 ppm (av. 17.37 ppm), 514.8 – 3929.9 pm (1578.9 ppm), 0 – 3.9 ppm (av. 0.58) compared to the upper continental crust (Rudnick and Gao, 2003) of 92 ppm, 48 ppm, and 28 ppm respectively. Cr, Ni and Co concentrations of all magnesite samples from the study area indicate Log CCr: 0.3 - 1.9, Log CNi: 2.7 to 3.6 and Log CCo:0 - 0.6. The concentration of Cr cover mainly ranges of marine/evaporitic magnesite and Mg^{2+}metasomatism magnesite, lacustrine magnesite and Altered ultramafic magnesite (Fig. 4.20). In the lacustrine environment, Mg^{2+} is largely derived from ultramafic rocks in contrast to Mg^{2+} in the marine environment (Moller, 1989). Therefore, the concentration of Cr can indicate marine/evaporitic and Mg^{2+}-metasomatism environment. Ni has a high concentration in magnesite of the study area and reflects altered ultramafic. Co concentration of magnesite samples is very low in contrast to magnesite from different environments. Co for magnesite of the study area mainly ranges of marine/evaporitic magnesite and Mg^{2+}-metasomatism magnesite, lacustrine magnesite, and Altered ultramafic magnesite.

Trace Elements Normalisation

Trace elements composition of magnesite were normalised again the primitive upper mantle (PUM) values of that of McDonough and Sun (1995). The Figure below indicates that Sr, Sb, and Ba are enriched in the magnesite samples compared to the primitive upper mantle (Fig. 4.21). Ni and Cu are enriched in the samples from mine site 2, while depleted from mine site 1. This is mostly due to the difference in the depositional environment of the magnesite. Cr, V, Zn, As, and Co are depleted in the magnesite samples relative to the primitive upper mantle and this is due to an indication for impoverishing and purification in these elements during a process of precipitation of magnesite in veins (Hamdy, 2007). Trace elements normalisation is similar to those of the host rocks.

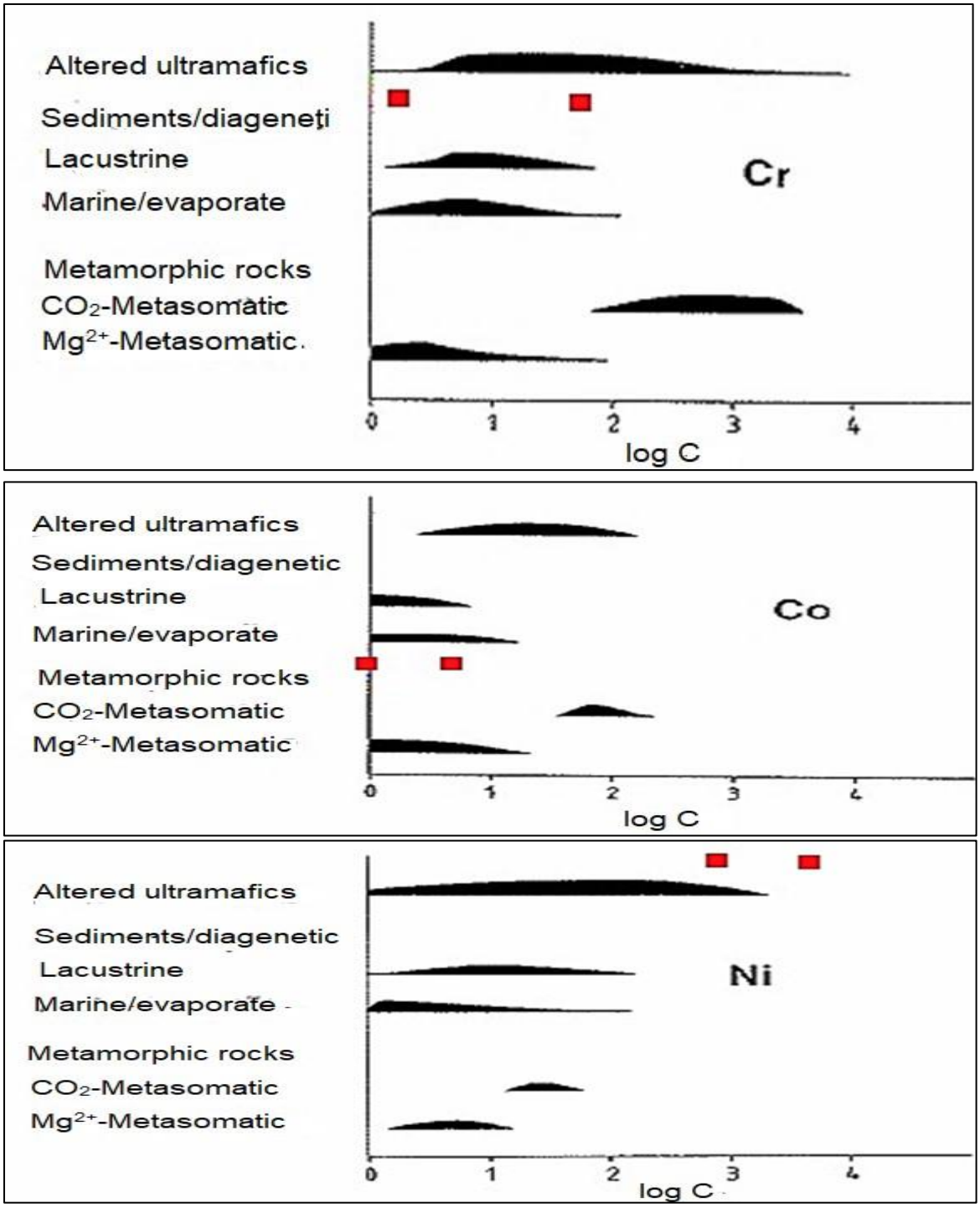

Figure 4.20: Distribution of Cr, Ni and Co in magnesite from the study area plotted on the Log of concentration versus environment diagram proposed by Moller (1989). Red square indicates the range of Cr, Ni, Co.

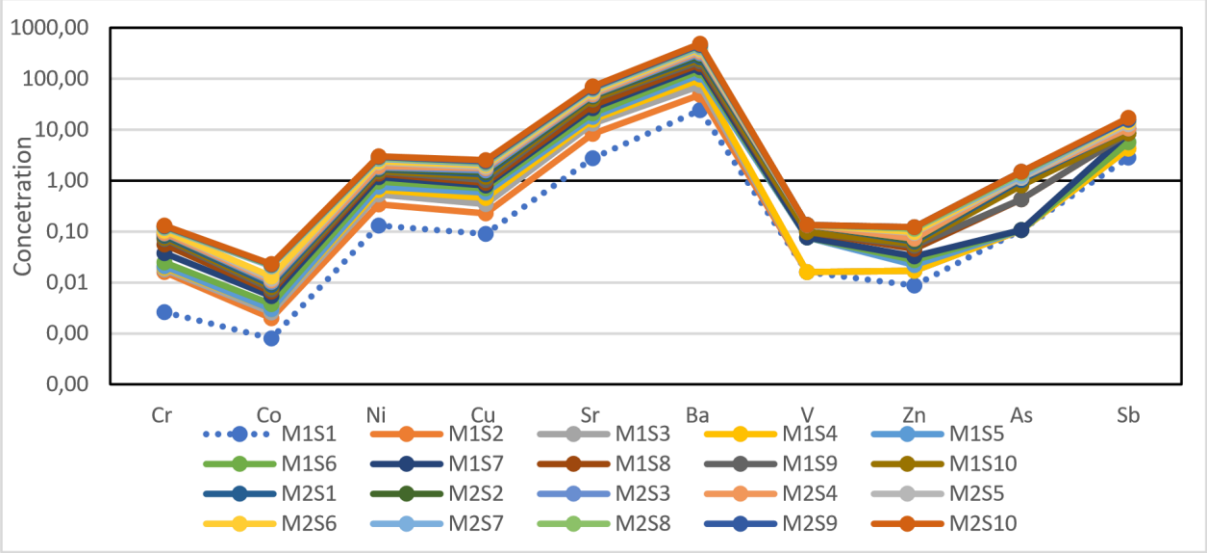

Figure 4.21: Trace elements normalised to primitive upper mantle (PUM).

4.6.3 Rare Earth Elements

Rare earth element (REEs) contents of rocks and minerals give important clues for the origin and geological history of the materials. Many of the magmatic, metamorphic, and sedimentary processes strongly keep their story within rocks and minerals. Rare earth elements play an important role to understand the formation processes. Because REE have larger ionic radii, they supposed not to join any chemical reactions during the formation of minerals and rocks.

REE patterns of the magnesite have been used as proper tools to solve the formation of magnesite and the source of Mg, especially for crystalline magnesites (Morteani *et al.,* 1982; Schroll, 2002). According to Moller (1989), only a few amounts of heavyREE can intrude the magnesite lattice. On the other hand, seawater and ultramafic rocks also have low REE (Schroll, 2002), thus the magnesite deposits occurred as either crystalline or cryptocrystalline should have very low REE concentrations. Crystalline magnesite deposits of Eugui (Western Pyrenees, Spain) studied by Lugli *et al.* (2000), have similar REE patterns with host rock dolomite indicating replacement of magnesite by dolomite.

It may be possible to distinguish between the main lines of thought of magnesite formation, i.e. precipitation and metasomatism, by studying the REE distribution in magnesite (Morteani *et al*.,1982, 1983). Among the trace elements in carbonates, the lanthanides are most useful to know about the probable sources of magnesite forming

Mg2+ ions (Moller, 1989). Because their concentration levels are well below 1000 ppm, their trivalent ionic radii (1.17-1.0 A°) correspond well with that of Ca^{2+} (1.14 A°) in coordination number VI (Shannon, 1976), and most of the chemical and physicochemical properties change a periodically within their series.

A total of 20 magnesite samples were analysed for REEs using X-ray fluoresces spectrometry (XRF), and the results are displayed in Appendix C. It must be pointed out that both the LREE and HREE were analysed in all the samples but due to the limitation of the instrument the following REEs were not measured; Pr, Nd, Ho, Tm, and Lu.

The abundance of rare earth elements in magnesite is significantly low and close to detection limits. The concentration of magnesite samples on the study area was normalised using McDonough and Sun (1995) REE Primitive mantle values (Fig. 4.22). Magnesite shows chondrite-normalised patterns very similar to those of the host rocks (Fig. 4.22), but LREE contents of magnesite are significantly lower, whereas HREE are enriched. LREE content in the magnesite seems to indicate higher mobility than the HREE because the ion radii of the HREE are much more like the Mg^{2+} ion radius than those of the LREE. Hence LREE will be enriched in the fluid phase and can thus be depleted in the solid phases. LREE which concentrates in the fluid phase can later be captured during re-dolomitization. The depletion of LREE in magnesite samples is reflected by low LREE/HREE ratios of magnesite.

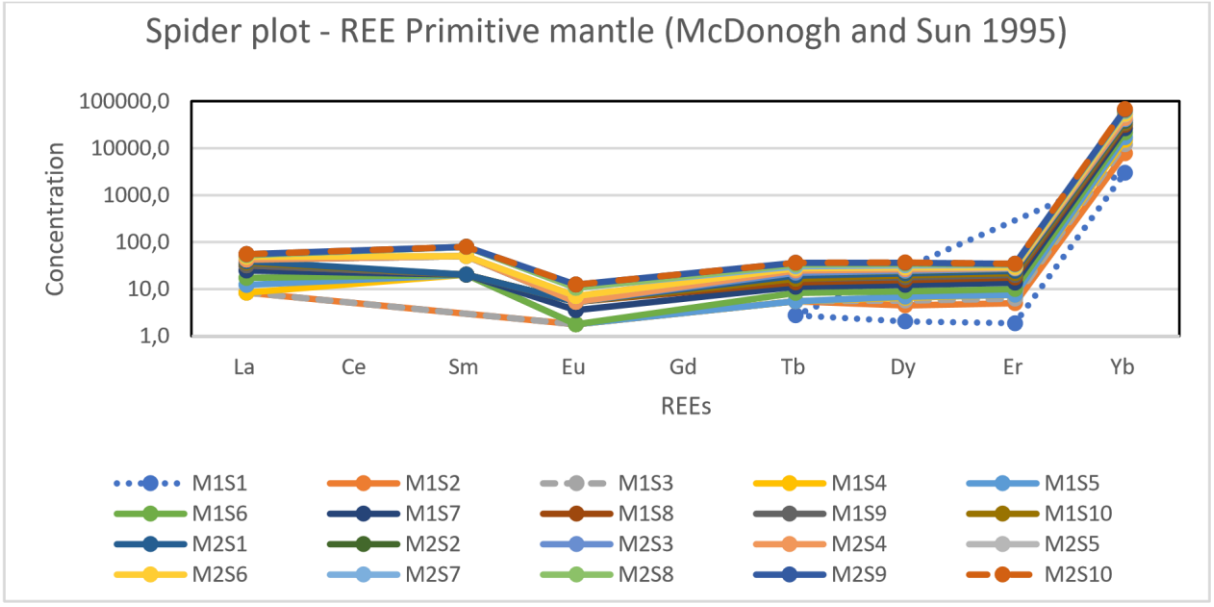

Figure 4.22: Spider diagram plot of normalised REE in magnesite.

Depletion of LREE in comparison to the host rocks is a result of mineralogical control (Krupenin, 2002). Additional, fractionation and decrease of LREE are connected to metasomatic recrystallization (Moller, 1989) because more quantity of fluids has passed through such zones (Krupenin, 2002). Normalised REE patterns of magnesite illustration consistent minor Eu negative anomalies (Eu/Eu*). These negative Euanomalies in magnesite were inherited from its ultramafic predecessors. The negative Eu-anomalies are due to magnesite formation in a chemically reducing environment (Moller, 1989). REE patterns of the magnesite display low LREE/HREE and depletion of LREE in comparison to the host rocks. This is because magnesite fractionates the HREE when crystallizing from hydrothermal fluids, whereas LREE are rejected (Bau and Moller, 1992).

4.6.4 Mineralogy of Magnesite at Muyexe

XRD analysis of 2 selected samples revealed magnesite as the major mineral, with concentration ranging between 94-91% $MgCO_3$ (Fig. 4.23).

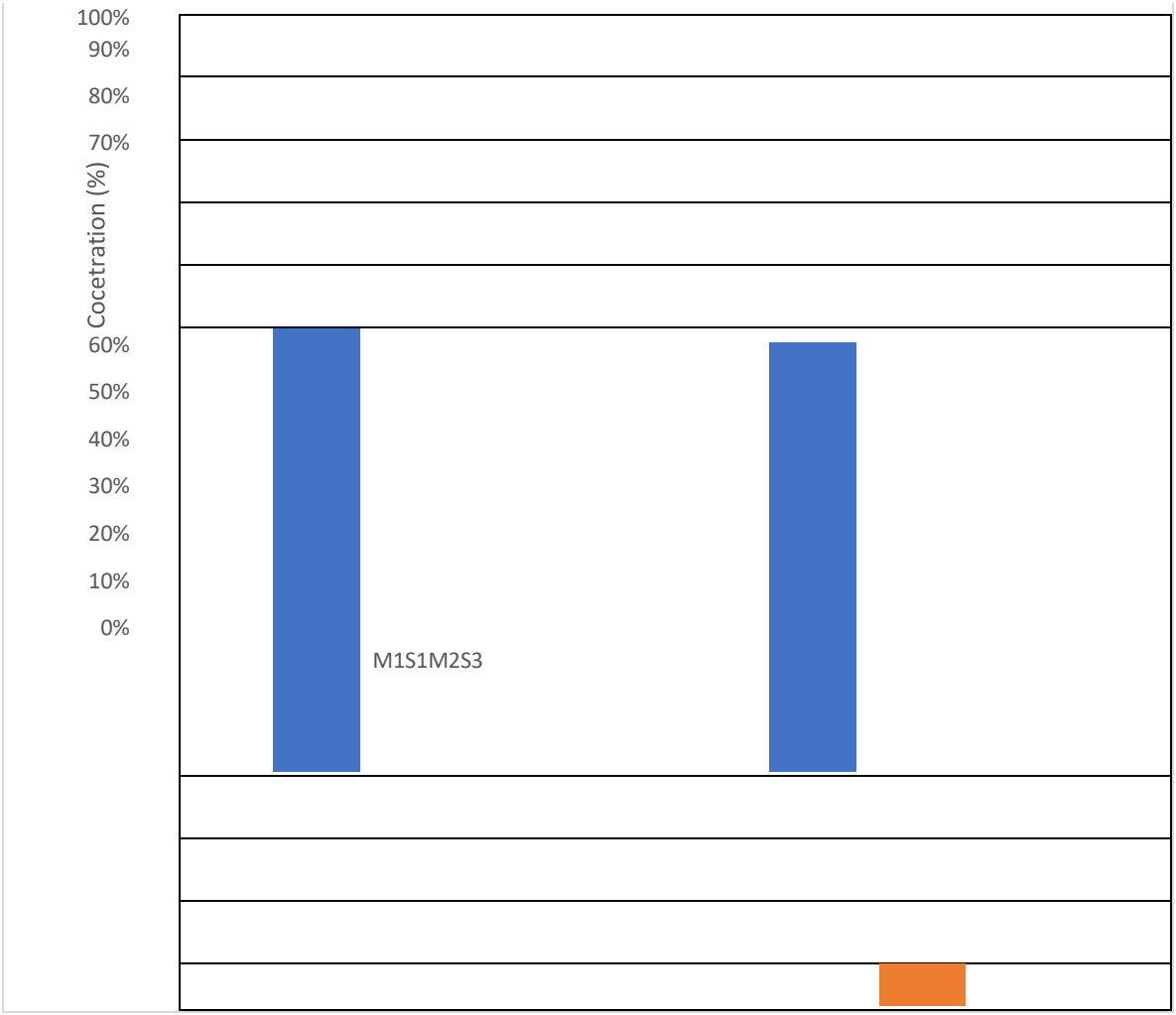

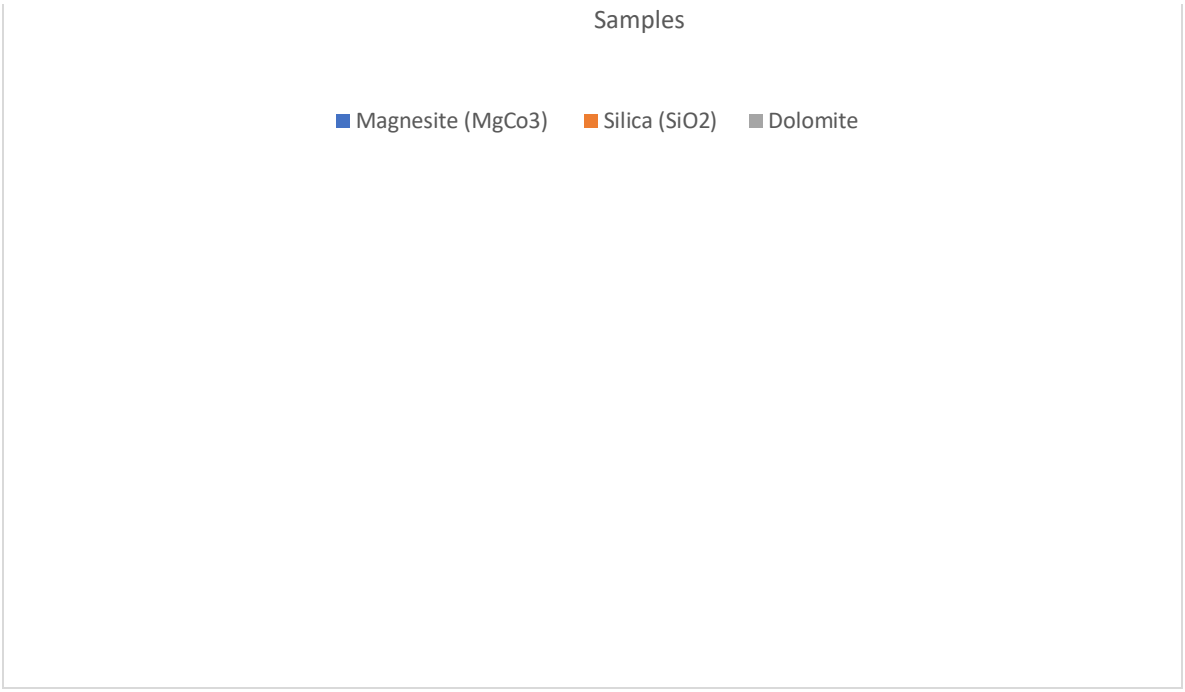

Figure 4.23: Histogram showing the mineralogy of magnesite.

Magnesite is associated with quartz (silica) and dolomite, with a concentration ranging between 9-4% and 0-2% respectively. Sample M2S3 showed no presence of dolomite as the main constituent. The low abundance of associated minerals (dolomite, silica, brucite, and huntite) reflects relatively high-temperature conditions that converted fewer stable minerals into stable magnesite phase (Bashir, 2008).

4.7 Quality and Grade of Magnesite at Muyexe Area

The mineralogical study is essentially required for better evaluation of any ore deposit (Bashir *et al.*, 2009). Magnesite deposit of the study area is cryptocrystalline in nature so only x-ray analysis is a valid analytical technique for mineralogy study. XRD analysis of magnesite ore samples indicated that magnesite, silica, and dolomite are widely distributed minerals within the Muyexe magnesite deposit. The quality of magnesite is great, and it contains >91% of magnesite while the rest is occupied by silica and dolomite in that order.

Chemical analysis of magnesites of the study area reflects a high amount of MgO (av. 54.02 wt. %) and loss on ignition (av. 36.04 %). Silica (SiO_2) averaged 7.85 wt. %, calcium (CaO) averaged 1.76 wt. % and iron (Fe_2O_3) averaged 0.14 wt. % respectively as impurities (Fig. 4.24). Harben and Bates (1990) mentioned the specification in terms of the chemical composition of good cryptocrystalline magnesite for used in different

industrial applications as 46.6% MgO, 49.9% CO_2, 0.70% SiO_2, 1.35% CaO, 0.85% Fe_2O_3 and Al_2O_3.

The samples of the study area show that the av. MgO content (54.01%) is high than the specified values, in all the magnesite samples. Calcium is objectionable in many industries. In the studied samples, it ranges between 0.58 – 4.57 wt. % (av. 1.76 wt. %), which is higher than the specified value of 0.70 %. Silica is also high in comparison to 0.75% and combined Fe and Al-oxides (av. 0.14 %) is below the specified value of 0.85 %. High iron content adversely affects the refractory properties of the final product. The loss of ignition ranges between 34.1-38.2 % (av. 36.05 %).

According to Cao *et al.* (2016), magnesite with concertation of above 46% MgO is of a high grade. The concentration of MgO for magnesite of the study area ranged between 51.90 – 57.28 wt. % with an average of 54.7 wt. %. Therefore, the magnesites of the study area are of a high grade.

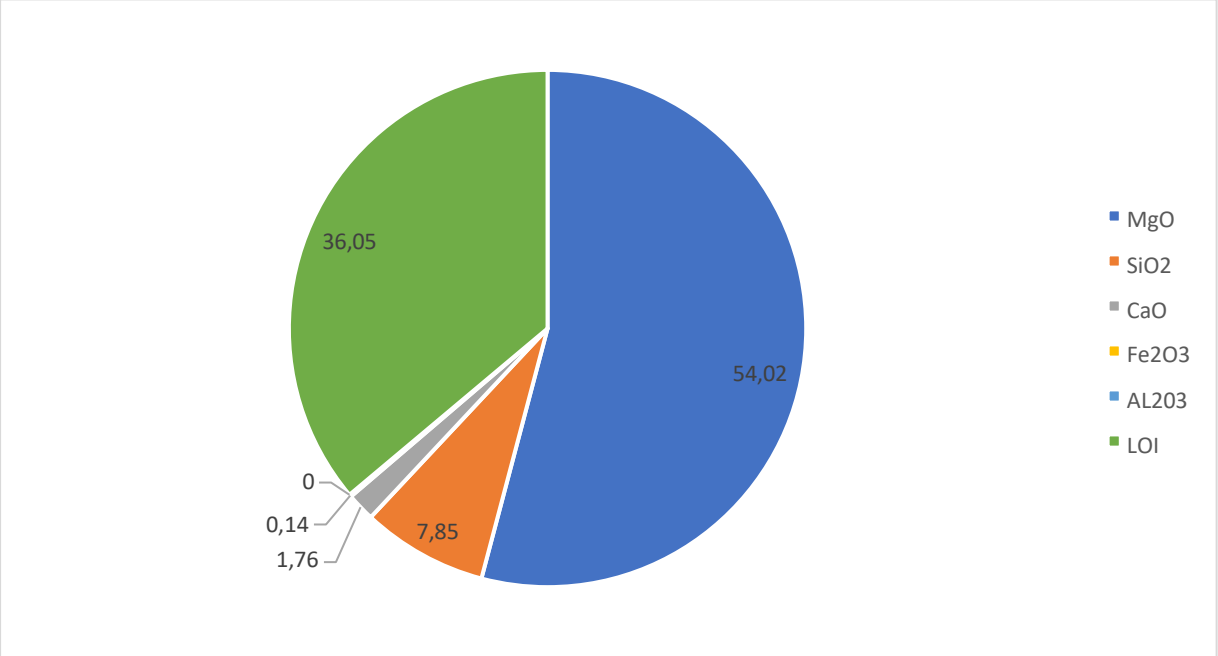

Figure 4.24: Pie chart illustrating the average concentration of major constituents of the studied magnesites.

CHAPTER 5: DISCUSSIONS, CONCLUSIONS AND RECOMMENDATIONS

5.1 Discussions

According to Pohl (1989), Abu-Jaber and Kimberly (1992) and Schroll (2002), magnesite deposits commonly occur in 4 types of geological environments. These are: (a) alteration product of ultramafic; (b) vein fillings in ultramafic; (c) replacement terrarossa types in carbonate rocks; and (d) bedded sedimentary deposits. Prinsloo (1977) noted that serpentinite which is the host rock was derived from altered peridotite harzburgite. The geological, petrographic, and geochemical features shown by the Muyexe magnesite deposit are confined to ultramafic rocks of the Giyani Greenstone Belt. The particular evidence that was considered in this study is outlined below.

5.1.1 Geological Evidence

In Muyexe, magnesite veins are found as fracture fillings of massive cryptocrystalline variety (Fig. 5.1). These veins mainly occur in several steeply dipping to shallow dipping shear planes and along strike and oblique and sheet joint planes. Most of the veins thin-out and disappear within a short distance, both in length and depth. The prominent veins have a thickness of 5 cm to 20 cm and extend to a length of 100 to 200 m. Compact magnesite is found with silica veinlets and stringers of sheared serpentinites. The deposit occurs in an area of about a kilometre long and 100 – 500 m wide in some areas. Magnesite mineralization took place along the minor faults and shear zone, within the host rock.

Detailed observation and delineation of the magnesite deposit in the area, further indicate some sort of structural control of localization. The shear zones in the area mainly serve as pathfinders for the magnesite occurrence. Based on nature, extent, and altitude, the magnesite mineralisation can be classified into three mineralised zones: (a) Those in the weathered ultramafic rocks, (b) those in the sheared ultramafic rocks and (b) veins fillings in the serpentinites (Fig. 5.1). The magnesite veins did not migrate into the adjacent birbirtite and basalt and this may be due to the fact that these rocks were not subjected to alteration like serpentinite and peridotite.

The geological map (Fig. 4.1) of the study area revealed that magnesite is associated with both metamorphic, ultramafic, and mafic rocks. Geological mapping revealed the following rock types in the area: hornblende chlorite schist, quartzite, banded iron formation, amphibolite, serpentinites, talc schist, basalt, pillowed amphibolite, weathered serpentinites schist, birbirite, and peridotite. The map further confirms that magnesite occurred in serpentinites and sheared peridotite rocks.

Ultramafic rocks of the study area were subjected to complex deformation and metamorphism (McCourt and van Reenen, 1992). The deformation of ultramafic rocks and metamorphism resulted in the over thrusting, development of shear zones, partial melting, and high heat flow, which in turn played a significant role during serpentinisation in the area. The presence of low to medium grade rocks such as serpentinites, amphibolite and schists is evidence that the whole Muyexe area was subjected to regional metamorphism.

The hand specimens of magnesite were yellowish to cream-white (Fig. 5.2). Magnesite in the area had a cryptocrystalline texture, that was noticed during fieldwork and on the hand specimen. The magnesite was hard and compact, and it exhibits porcelaneous lustre, breaks with a conchoidal to sub-conchoidal fracture.

5.1.2 Petrographic and Mineralogical Evidence

According to mineralogical and petrological studies of both magnesite veins and host rocks, the source rock of magnesite mineralisation and the serpentine in this study was peridotite-type protolith of harzburgite composition. The altered serpentinite rocks were formed from olivine-rich protolith. This evidence is indicated by the abundance of pseudomorphic of serpentine structure with abundant hourglass pseudomorphs of

serpentine after olivine (Fig. 3.18) in thin sections of the rocks. Serpentine that developed as an alteration after olivine has a mesh texture while that formed after orthopyroxene has a bastite texture (Azer and Khalil, 2005). This evidence was seen in the host rock samples under the microscope.

Both petrographic and mineralogical study revealed that the rocks in the study area are mostly dominated by amphibole-chlorite-anorthite, amphibole-quartz-plagioclase, and amphibole-chlorite-actinolite-talc-olivine mineral assemblage.

Figure 5.1: Magnesite veins in different depositional environments at Muyexe: (A)-Magnesite veins in serpentinite; (B)-Magnesite veins in sheared peridotite; (C)Magnesite veins in weathered serpentinite; and (D)-Magnesite veins outcrops).

Figure 5.2: Cryptocrystalline magnesite texture (top left image and top right image) and magnesite vein with sharp contact in weathered serpentinite rock (bottom image).

The dominance of magnesium-rich amphibole minerals in the rocks here is because the rocks of the Giyani Greenstone Belt were subjected to amphibolite facies metamorphism, with peak metamorphism being around 2715 Ma (De Wit *et al.,* 1992). Mineralogical analysis of host rocks revealed that only lizardite is present as a serpentine mineral. The presence of lizardite signified continental serpentinisation, formed during syntectonic metamorphism and that lizardite was persistence during progressive metamorphism. The petrographic study also showed the presence of streaks and gains of variable sizes of opaque minerals (chromite and magnetite). According to Bashir (2008), the occurrence of chromite is an indication of the harzburgite sub-type peridotite. Other minerals that are associated with host rocks include, calcium-aluminium-hydroxide-hydrate and sodium-cobalt-aluminium silicate. These minerals probably replaced serpentine in the host rock during metamorphism. Besides these minerals, the host rock comprises several minerals that are related to magnesite mineralisation such as dolomite and magnesite in varying proportion.

The mineralogy of magnesite indicated that magnesite is the major component. Other minerals that are present in magnesite included quartz and dolomite (Fig. 4.23).

Minerals that are associated with magnesite such as brucite, hunite and hydromagnesite were missing. Bashir (2008) stated that the lack of these associated minerals reflects relatively high-temperature conditions that converted fewer minerals into a stable magnesite phase.

5.1.3 Geochemical Evidence

Geochemical studies of rocks demonstrated the high concentration of SiO_2 followed by MgO. As silica is the most abundant oxide on earth, rocks can be classified according to their silica content i.e. acidic (>63 wt. %), intermediate (63-52 wt. %), mafic (52-45 wt. %) and ultramafic (<45 wt. %) (Bucher and Grapes, 2010). Considering this classification, rocks in the study area such as peridotite, altered peridotite, hornblende schist, serpentinite, altered serpentinite 4 and altered serpentinite 3 are ultramafic, rocks such as altered serpentinite 1, altered serpentinite 2, basalt, amphibolite, pillowed amphibolite and talc schist are mafic rocks, while rocks such as quartzite, birbirite, BIF, and weathered serpentinite schist are acidic rocks (Table 3.4; Fig. 4.3). The alteration box indicates that the rocks of the study area are mostly altered. They follow hydrothermal alteration trends 3 and 4 defined by Large *et al.* (2001), typically associated with chlorination (Gifkins *et al., 2005)*, that is why most of the rocks in Muyexe are dominated by chlorite. On the AFM diagrams of Irvine and Baragar (1971) (Fig. 4.10), most of the rocks of the study area plot under tholeiitic magma. Some of the rocks plot under calc-alkali magma type. On the TAS diagram most of the rock samples plotted between; basalt, picro-basalt, trachy-basalt, basaltic andesite, basaltic trachyandesite, dacite, andesite and foidite. Just like in the AFM diagram (Fig. 4.11) the rock classification on the TAS diagram (Fig. 4.12) suggests that the rocks in the study area are tholeiitic magma type, with a few being calc-alkali magma type. This means that most of the rocks in the study area have the same petrogenesis.

The geochemical study of the Muyexe magnesite deposit revealed that the magnesite is relatively pure (MgO ranges between 51.9-57.28 wt. % and magnesite above 90 %). Magnesite has a moderately high SiO_2 and low Fe_2O_3, CaO (Fig. 4.14). Trace elements play an important role in evaluating the genetic environment of the magnesite. Each type of magnesite deposit contains a specific assemblage of the trace elements, thus, magnesite related to ultramafic host rocks is enriched in Cr, Ni, Cu, Hg, As, Sb and Co content, while magnesite in the marine-evaporitic environment has Cr, Ni, Cu, B, and

Ti enrichment and magnesite in the lacustrine environment has Ni and Cu enrichment (Moller, 1989; Abu-jaber and Kimberly, 1992; Schroll, 2002). Based on this classification, the current study confirms that Muyexe magnesite deposit is of ultramafic origin. Likewise, the dominate trace element content of magnesite was found to be similar to the once identified by Moller (1989) and Abu-jaber and Kimberly (1992). Trace elements of the studied magnesite indicated an enrichment in Sr, Ba, Sb, Ni and Cu (Ni and Cu are enrichened in magnesite from mine site 2) relative to the primitive upper mantle (PUM) (Fig. 4.21). The depletion of V, Cr, and Co relative to PUM indicate that magnesite was impoverished and purified of these elements during a process of precipitation of magnesite in veins. Schroll (2002) stated that ultramafic associated magnesite is characterized by higher Fe content, up to 5%, whereas those from sedimentary environments have low Fe content (<1% Fe). Kuscu *et al.* (2017) had also noted that sedimentary Aşağıtırtar magnesite bearing huntite had a low Fe content (0.13 wt. %). In this study, it was noted that Fe content was up to 0.25 wt. %. The low Fe content on magnesite of the study area is due to the oxidation of iron, as near-surface magnesite deposits are oxidised of iron (Schroll, 2002). The concentrations of selected trace elements (Sr-Ba, Ti, Fe-Mn and Cr-Ni-Co) in magnesite illustrate altered ultramafic and/or Mg^{2+}-metasomatism origin of magnesite mineralization (Fig. 4.15-Fig. 4.20). This confirms that the Muyexe magnesite deposit is of ultramafic origin, apparently from altered peridotite and serpentinite, which is a product of peridotite alteration. The REE patterns of the magnesite display low LREE/HREE (Fig. 4.22) and depletion of LREE in comparison to the host rocks (Fig. 4.9). This is because magnesite fractionates the HREE when crystallizing from hydrothermal fluids, whereas LREE are rejected (Bau and Möller, 1992).

5.1.4 Genetic Model

Combination of geological, petrological, mineralogical, and geochemical results provides initial constraints on establishing a genetic model for the genesis of magnesite at the Muyexe magnesite deposit. The characteristics of this deposit points towards that of vein-type formation.

In the Muyexe magnesite deposit, magnesite was found to occur as veins along with the fractures and shear zones in peridotite and serpentinite. MgO with values up to 41.98 wt. % in peridotite and 29.95 wt. % of altered serpentinite was established. The

study confirmed that serpentinite was a product of peridotite alteration during regional metamorphism. From these observations, it is envisaged that formation of magnesite in this deposit could have been as a result of the reaction of ascending CO_2-bearing solution that extracted Mg^{2+} from either altered peridotite or serpentinite through the process of pneumatolytic and metasomatism hydrothermal alteration. The following observation support this genetic model:

a) presence of pure veins of magnesite filling fractures and shear zones
b) the serpentine minerals in the vein deposits are minor and occur as angular fragments restricting to the vein margins
c) magnesite is predominantly cryptocrystalline in texture and absence of talc which is usually formed by metasomatism 'in situ' replacement
d) carbonate veinlets in altered host rocks are composed of magnesite, silica, and dolomite
e) brucite or any hydrous magnesium carbonate minerals are absent in the magnesite veins
f) The magnesite deposit is depleted in the transition elements of V, Cr, Co and Ni relative to PUM.

The above-mentioned results of field and laboratory investigations could favour the following origin of the magnesite in question.

(a) The presence of pure veins of magnesite filling fractures and shear zones. This suggests that magnesite precipitated along the fractures and shear zones of the host rock, which evidence of it was seen from field observation of magnesite deposit, where magnesite veins are precipitated along the fractures of serpentinites and shear zones of peridotite.
(b) The presence of angular fragments of host rock and no other relics of serpentinites including chromite spinel in magnesite veins suggest that magnesite was not formed by metasomatic "in situ" replacement of the serpentinite rocks but it precipitated from ascending solutions rich in Mg^{2+} (Dulski and Morteani, 1989; Pohl, 1990).
(c) The cryptocrystalline texture of magnesite indicates that the input of the CO_2rich fluids must have been fairly rapid causing the abundant precipitation of magnesite from solutions (Jancić and Grootsholten, 1984; Abu-Jaber and

Kimberley, 1992) under near-surface conditions (Abu-Jaber and Kimberley, 1992) at a temperature below 300ºC as indicated by an absence or very scarce occurrence of talc (Johannes, 1970).

(d) As dolomite and silica are filling cavities and fissures in magnesite veins, they had to form after the main crystallization ended. According to the T-X diagram of Johannes (1970), two factors controlled the formation of dolomite. These factors are temperature and the ratio Ca/ (Ca + Mg) in mineralisation fluids. The increase of Ca/(Ca + Mg) value of the parent fluids due to magnesite crystallisation as well as the decrease of temperature caused crystallisation of dolomite.

(e) The low abundance of associated minerals (dolomite, silica, brucite, and huntite) reflects relatively high-temperature conditions that converted fewer stable minerals into stable magnesite phase (Bashir, 2008), which is a process of metasomatic hydrothermal alteration and not metasomatism 'in situ' replacement.

(f) This is an indication for impoverishing and purification in these elements during a process of precipitation of magnesite in veins. If the deposit were formed by metasomatism 'in situ' replacement, it would be richer in these elements.

The possible mechanism of magnesite formation is summarised below. The ultramafic and mafic rocks of the Giyani Greenstone Belt were subjected to three phases of complex deformation (De Wit *et al.,* 1992; McCourt and van Reenen, 1992; Roering *et al.,* 1992; Smit and van Reenen *et al.,* 1997; Kramers *et al.,* 2014) and amphibolite facies metamorphism (De Wit *et al.,* 1992), and peak metamorphism was at 2715 Ma (van Reenen *et al.,* 1987, 2011; Barton and van Reenen, 1992; Roering *et al.,* 1992; Perchuk *et al.,* 1996; Passeraub *et al.,* 1999; Kreissig *et al.,* 2001; Kramers *et al.,* 2014). The deformation of ultramafic rocks and metamorphism resulted in the over thrusting, development of shear zones, partial melting, and high heat flow, which in turn played a significant role during serpentinisation in the area. The presence of low to medium grade (schist rocks, serpentinites, and amphiboles) in the area justify the event of metamorphism. The process of serpentinisation is thoroughly discussed by Guild (1947). A summary of this is as follows, ultramafic rocks were subjected to metamorphism by hydrothermal fluids to form serpentinites as indicated below (Guild, 1947):

Olivine + Quartz + Water ⟶ Serpentine

$3Mg_2SiO_4 + SiO_2 + 4H_2O \longrightarrow Mg_6SiO_{10}(OH)_8$ .....*equation 4.3*

Olivine + Water ⟶ Serpentine + Limonite

$6MgFeSiO_4 + 11H_2O + 3O_2 \longrightarrow Mg_6Si_4O_{10}(OH)_8 + 6FeO(OH)_2H_20$.....*equation 4.4*

The ultramafic rocks of the Giyani Greenstone Belt were subjected to this process of serpentinisation. This evidence can be seen from the presence of serpentinites and mineralogy of lizardite, which is related to serpentinisation.

Serpentinites were formed from a peridotite-type protolith of harzburgite composition, as confirmed by their petrographic and geochemical features. According to Azer and Khalil (2005), serpentines that developed as an alteration of olivine has a mesh texture while that formed after orthopyroxene has a bastite texture. These textures can be seen under the microscope on the magnesite host rocks.

After the serpentinisation process ended, serpentinite rocks of the study area were subjected to hydrothermal alteration by CO_2-rich hydrothermal fluids, which precipitated magnesite along the cracks, joints, and shear zones of the serpentinite rocks. From the above evidence, hydrothermal fluids were responsible for the precipitation of magnesite in the area. The reaction of hydrothermal fluids was as follows (Fournier, 1985).

When carbon dioxide reacts with hydrothermal water, carbonic acid (H_2CO_3) is generated as;

$CO_2 + H_2O$ (hydrothermal) ⟶ H_2CO_3 (carbonic acid) .....*equation 4.5*

Carbonic acid then dissolves magnesium as bicarbonate from serpentinite, leaving silica (SiO_2) behind (Henderson and Fortey, 1982):-

$2Mg_3Si_2O_5(OH)_4$ (serpentinite) + $6H_2CO_3 \longrightarrow 4SiO_2 + 6MgCO_3 + 10H_2O$.....*equation 4.6*

$MgCO_3 + H_2CO_3 \longrightarrow$
$Mg^{+2} + 2HCO_3$.....*equation 4.7*

And as this fluid rises along the suitable channel ways (fractures and shear zones) pressure loss leads to the sudden release of carbon dioxide from bicarbonate (HCO_3) causing rapid magnesite precipitation at shallow depths;

$$Mg^{+2} + 2HCO_3 \longrightarrow MgCO_3 + H_2O + CO_2 \quad \text{.....equation 4.8}$$

If the precipitation is along the joints and shear zones then vein-type magnesites would be expected, in the case of fluid flow along with fractures then stockwork-type magnesites are generated (Fallick *et al.,* 1991). On the other hand, if serpentinisation of the ultramafic rocks had not already been established the bicarbonate-rich fluids (dissociates of carbonic acid: $H_2CO_3 \rightarrow H^+ + HCO_3$ (Fournier, 1985)) can serpentinite them (Abu-Jaber and Kimberley, 1992);

$$2Mg_2SiO_4 + H_2O + H^+ + HCO_3 \longrightarrow Mg_3Si_2O_5(OH)_4 + MgCO_3 \quad \text{.....equation 4.9}$$

It is important to note that the buffering of H + from the fluid during this reaction causes an increase of pH of the fluid up to 12 (Neal and Stanger, 1984). When serpentinisation is completed, according to Barnes *et al.* (1973) and Stanger (1985), silica may also be dissolved by the reaction of highly alkaline solutions with serpentinite; $2Mg_3Si_2O_5(OH)_4 + 6H^+ + 6HCO_3 \longrightarrow 4SiO_2 + 6MgCO_3 + 10H_2O$ .....*equation 4.10*

As the reaction progresses the pH of the fluid is probably high enough to dissolve silica. So hydrothermal solutions would be initially rich in dissolved silica. When these first fluids rise along channel ways, precipitation of silica would be expected followed by magnesite.

For magnesite to precipitate in the rocks, there must be three general requirements: a) There must be a magnesium source; b) there must be a suitable water supply, and c) there must be a carbon dioxide source.

Source of Magnesium

As the vein magnesite deposits are hosted by serpentinite rocks and peridotites, the probable magnesium source is the magnesium-rich minerals within the serpentinites and peridotites, such as serpentine, olivine and/or pyroxene. The concentration of Co, Ni and Ti contents of magnesite and associated rocks indicate that Mg was derived from serpentinised ultramafic rocks. This was also supported by the restriction of magnesite veins to only serpentinite and peridotite suggesting that these rocks are

probably the source of magnesium. In general, serpentine has a larger surface area per unit volume. Therefore, serpentine alters more rapidly than non-phyllosilicates (Meunier, 1983) making it the most appropriate source of Mg^{2+}.

Source of Suitable Water Supply

At Muyexe area, the source of suitable water supply was meteoric water. The cold meteoric water, along the fractures, was sucked by gravity into deeper terrain parts (2-3 km), then was heated (most probably at 75-100^{0}C) and was enriched with CO_2 content (the gas was released during thermal decarboxylation of the organic matter that begins at about 75^{0}C) (Zadef, 1994), and after that, along fractures, too, flowed towards the surface. Therefore, meteoric water was subjected to convection flow (most probably artesian) and was heated at depth due to the Earth's heat.

Sources of Carbon Dioxide (CO_2)

As mention earlier, there are various models regarding the source of CO_2 for the formation of vein-type magnesite deposits. These are: a) soil-derived organic CO_2 (decomposition of plant material and plant-root respiration); b) decarbonisation of carbonate rocks; c) decarboxylation of organic-rich sediments; d) atmospheric CO_2; and e) magmatic CO_2 (including volcanogenic CO_2). A through isotope study of the fluid will need to be undertaken at Muyexe magnesite deposit in order to find the source of the carbon dioxide.

5.2 Conclusions

The current study came up with several conclusions and recommendations that are presented below.

a) A detailed geological map of Muyexe magnesite deposit was produced, and the following rocks are associated with magnesite: hornblende chlorite schist, quartzite, banded iron formation, amphibolite, serpentinites, talc schist, basalt, pillowed amphibolite, weathered serpentinites schist, birbirite, and peridotite. These rocks strike to the south-west and north-east.

b) The study confirmed that serpentinites and altered peridotite found are the source rock for magnesite mineralisation in the area.

c) XRD analysis revealed that the magnesite in the Muyexe deposit is associated with silica and dolomite, while XRF data revealed that the following major oxides are present in magnesite as impurities; Silicon dioxide (SiO_2), calcium oxide (CaO), and iron oxide (Fe_2O_3). Sr, Ba, Cr, Cu, Ni, Sb and Co are trace elements found in magnesite of the study area.

d) Magnesite was found to be of high quality with few impurities. Chemical analysis of magnesites reflects a high amount of MgO (54.02 wt. %) and loss on ignition (36.04 %). Silica (SiO_2) averaged 7.85 wt. %, calcium (CaO) averaged 1.76 wt. % and iron (Fe_2O_3) averaged 0.14 wt. % respectively. The grade of the magnesite was also found to be high, with an average of MgO 54.02 %.

e) Magnesite in the area was formed due to the reaction of ascending CO_2-bearing water with serpentinites and peridotite which caused leaching of Mg^{2+} away from the rocks and precipitating magnesite in fractures and shear zones.

f) The genetic type of Muyexe magnesite deposit is a vein-type cryptocrystalline magnesite deposit of the Kraubath-type.

5.3 Recommendations

The following recommendations were made based on the study:

- Cathodoluminescence and fluid inclusion studies should be undertaken to investigate magnesite morphology and internal structure.
- Electrostatic and froth flotation is recommended during mineral processing as these methods are known to reduce the concentration of impurities like quartz in magnesite.
- A through isotope study of the fluid will need to be undertaken at Muyexe deposit in order to find the source of the Carbon dioxide.

REFERENCES

Abu-Jaber, N.S., and Kimberley, M.M. (1992). Origin of Ultramafic-Hosted Vein Magnesite Deposits. *Ore Geology Reviews*, Vol. 7, pp. 155-191.

Afonin, Y. A., and Maryasev, I. G. (2006). Cryptocrystalline Magnesite in Weathering Crust of Ultrabasic Rocks. *Refractories and Industrial Ceramics,* Vol. 47**,** pp. 269-274.

Aharon, P. (1988). A Stable-Isotope Study of Magnesites from the Rum Jungle Uranium Field, Australia: Implications for the Origin of Strata-Bound Massive Magnesites. *Chemical Geology*, Vol. 69, pp. 127–145.

Ahmadi Khalaji, A., Esmaeily, D., Valizadeh, M. V., and Rahimpour Bonab, H. (2007). Petrology and Geochemistry of the Granitoid Complex of Boroujerd, Sanandaj-Sirjan Zone, Western Iran. *Journal of Asian Earth Sciences*, Vol. 29, pp. 859–877.

Alloway, B.J. (1998). The Origin of Heavy Metals in Soils. In: Alloway, B, J. (Ed.). Heavy Metals in Soil. 2nd Edition, Chapman, and Hall, UK, Chapter. 3. pp. 38-57.

Anhaeusser, C., R. (2006). Ultramafic and Mafic Intrusions of the Kaapvaal Craton. In: Johnson, M.R., Anhaeuser, C.R., and Thomas, R.J. (Eds.). *The Geology of South Africa*. Geological Society of South Africa, Johannesburg/Council for Geoscience, Pretoria, pp. 95-134.

ArcGIS Software 10.04. (2018). Online Base Maps. Sources: Esri, HERE, DeLorme, Intermap, Increment P Corp., GEBCO, USGS, FAO, NPS, NRCAN, GeoBase, IGN, Kadaster NL, Ordnance Survey, Esri Japan, METI, Esri China (Hong Kong), Swisstopo, MapmyIndia, © OpenStreetMap Contributors, and the GIS User Community.

Armstrong, R.C., Compston, W., De Wit, M.J., and Williams, I.S. (1990). The Stratigraphy of the 3.5–3.2 Ga Barberton Greenstone Belt Revisited: A Single Zircon Ion Microprobe Study. *Earth Planetary Science Letters*, Vol. 101, pp. 90-106.

Azer M. K., and Khalil, A. E. S. (2005). Petrological and Mineralogical Studies of PanAfrican Serpentinites at Bir Al-Edeid Area, Central Eastern Desert, *Egypt Journal African Earth Sciences*, Vol. 43, pp. 525-536.

Barnes, I., and O'Neil, J.R. (1969). The Relationship Between Fluids in Some Fresh Alpine-Type Ultramafics and Possible Modern Serpentinisation, Western United States. *Geological Society of America Bulletin*, Vol. 80, pp. 1947-1960.

Barton, J.M., and van Reenen, D.D. (1990). Constraints on the Timing of the Limpopo Orogeny. In: Barton, J. Jr (Ed.). The Limpopo Belt: A Field Workshop on Granulite and Deep Crustal Tectonics. Extended Abstracts, Rand Afrikaans University, Johannesburg and Foundation for Research and Development, Pretoria, pp. 10-12.

Barton, J.M., and van Reenen, D.D. (1992). When was the Limpopo Orogeny? Precambrian Research, pp. 7-16.

Bashir, E., Kaleem, M., and Hamza, S. (2008a). Economic Evaluation of Magnesite Deposits of Khuzdar, Balochistan, Pakistan. *Karachi University Journal of Science*, Vol. 36, pp. 9-14.

Bashir, E., Naseem, S., Arkhtar, T., and Shireek, K. (2008b). Characteristics of Ultramafic Rocks and Associated Magnesite Deposits, Nal Area, Khuzdar, Balochistan, Pakistan. *Journal of Geology and Mining Research*, Vol. 1, No. 2, pp. 034-041.

Bashir, E., Naseem, S., Sheikh, A.S., and Kaleem, M. (2009). Mineralogy of the Kraubath Type Magnesite Deposits of the Khuzdar Area, Balochistan, Pakistan,

Journal of the Earth Sciences Application and Research Centre of Hacettepe University, Vol. 30, No. 3, pp. 169–180.

Bashir, E. (2008). Geology and Geochemistry of Magnesite Ore Deposits of Khuzda Area, Balochistan. PhD Thesis, University of Karachi, Karachi, Pakistan (Unpublished), 432 pp.

Bau, M., and Moller, P. (1992). Rare Earth Elements Fractionation in Metamorphogenic Hydrothermal Calcite, Magnesite and Siderite. *Mineralogy and Petrology*, Vol. 45, pp. 231–246.

Best, M.G. (2003). Igneous and Metamorphic Petrology 2nd Edition. Blackwell Science Ltd, 108 Crowley Road, Oxford OX4 1JF, UK, 729 pp.

Bhilisse, M., Wafik, A., Admou, H., Maacha, L., and Constantin, M. (2014). Geochemical and Mineralogical Characteristics of Serpentinite and Carbonated Serpentinite: Case of Magnesite (Bou Azzer Inlier, Central Anti-Atlas, Morocco). *Journal of Tethys*, Vol. 2, pp. 287–313.

Billay, A., Sadeghi, M., and Carranza, E. I. M. (2014). Predictive Bedrock and Mineral Prospectivity Mapping in the Giyani Greenstone Belt, South Africa. Mineral Resources Development Unit Meeting Points Mining Project. Report Number: 2014-0027, 70pp.

Birch, R, E., and Wicken, O. M. (1949). Magnesite and Related Minerals. In: Industrial Minerals and Rocks, 2nd Edition. The American Institute of Mining and Metallurgical Engineers. New York.

Brandl, G., Cloete, M., and Anhaeusser, C.R. (2006). Archean Greenstone Belts. In: Johnson, M.R., Anhaeuser, C.R., and Thomas, R.J. (Eds.). The Geology of South Africa. Geological Society of South Africa, Johannesburg/Council for Geoscience, Pretoria, pp. 9-56.

Brix, H. (2008). Soil Moisture and Loss-On-Ignition. 3pp.

Brock University. (2017). Variation Diagrams. [Online]. Available at: https://brocku.ca/earthsciences/people/gfinn/petrology/variatn.html [Accessed: 27 February 2018].

BUEHLER. Ltd. (2004). Preparations of Petrographic Thin Sections. Vol. 1, Issue No. 3. [Online]. Available at www.buehle.com for more info [Accessed: 28 February 2018].

Cao, Y., Wang, Z., Wang, J., and Li, G. (2016). Experimental Study on Magnesite and Mineral Components Electrostatic Separation Methods. *Electrostatics Joint Conference*, 11pp.

Carranza, E, J, M., Sadeghi, M., and Billay, A. (2014). Predictive Mapping of Prospectivity for Orogenic Gold, Giyani Greenstone Belt (South Africa), *Ore Geology Reviews*. doi: 10.1016/j.oregeorev.10.030, 48pp.

Chiaradia, M. (2009). Adakite-Like Magmas from Fractional Crystallization and Melting-Assimilation of Mafic Lower Crust (Eocene Macuchi Arc, Western Cordillera, Ecuador). *Chemical Geology*, Vol. 265, pp. 468–487.

Dabitzias, S. G. (1980). Petrology and Genesis of the Vavdos Cryptocrystalline Magnesite Deposits, Chalkidiki Peninsula. *Economic Geology*, Vol. 75, pp. 1138–1151.

Dar, J. A., and Dubey, R.K. (2012). Genetic Aspects of Magnesite Deposits of Lesser Himalaya, India. In: *Geology, Biodiversity and Natural Resources of Himalaya*. India: Department of Applied Geology, Indian School of Mines, Dhanbad-826 004, pp. 447453.

De Waal, S., Graham, I., and Armstrong, R. (2006). The Lindeques Drift and Heidelberg Intrusions and the Roodkraal Complex, Vredefort, South Africa: Comagmatic Plutonic and Volcanic Products of a 2055 Ma Ferrobasaltic Magma. South Africa. *Journal of Geology South Africa,* Vol. 109, pp. 279-300. 10.2113/gssajp.109.3.279.

Deer, W. A., Howie, R.A., and Zussman. J. (1997). Rock-Forming Minerals. *Geological Society*. London, Vol. 4, 973 pp.

Deer, W.R., Howie, R.A., and Zussman, J. (1992). An Introduction to the RockForming Minerals. Longman, Essex, U.K, 498 pp.

DMR. (2013). South African's Mineral Industry. Department of Mineral Resources, Republic of South Africa. Director: Mineral Economics, Travenna Campus, Pretoria, 0002. [Online]. Available at www.dmr.gov.za. [Accessed 22 May 2018]

Dulski, P., and Morteani, G. (1989). Magnesite Formation by CO_2 Metasomatism During Regional Metamorphism of the Ultrabasic Rocks of the Ochsner Serpentine,

Zillertaller Alpen, Tylor, Austria. In: Moller, P. (Ed.). Monograph Series on Mineral Deposits: Gebr. Borntaeger, Berlin–Stuttgart, Vol. 28, pp. 99–104.

DWAF: Department of Water Affairs and Forestry. (2004), Luvuvhu/Letaba Water Management Area: Internal Strategic Perspective Directorate National Water Resource Planning, Pretoria, South Africa, report no; PWMA 02/000/00/0304, 166pp.

Ebner, F., and Prochaska, W. (2001). Die Magnesit lagerstätte Sunk/Hohentauern und ihr Geologischer Rahmen. *Joannea Geol Paläont*, Vol. 3, pp. 63–103.

Ebrahimi-Nasrabadi, K., Barati, M., and Scott, P. (2015). Time-TemperatureTransformation Diagram of Caustic Calcined Magnesia. *CIM Journal*, Vol. 6, Issue No.
1, pp. 42-50.

Ellmies, R., Voigtla¨nder, G., Germann, K., Krupenin, M.T., and Moller, P. (1999). Origin of Giant Stratabound Deposits of Magnesite and Siderite in Riphean Carbonate Rocks of the Bashkir Mega-anticline, Western Urals. *Geologische Rundschau*, Vol.

87, pp. 589–602.

Erdoğan, N. (2016). The Most Suitable Beneficiation Method for Magnesite Ore. Aksaray University, Aksaray / Turkey, 7pp.

European Union. (2014). List of Critical Minerals. [Online]. Available at http://ec.europa.eu/research/participants/portal/desktop/en/opportunities/h2020/topics/sc5-13a-2014.html [Accessed: April 2018].

Evonik Industries. (2014). Analytical Test Method Aerosil.1pp.

Floyd, P.A., and Winchester, J.A. (1978). Identification and Discrimination and Altered and Metamorphosed Volcanic Rocks Using Immobile Elements. *Chemical Geology,* Vol. 21, pp. 291-306.

Fournier, R.O. (1985). Carbonate Transport and Deposition in the Epithermal Environment. In: Berger, B.R., and Bethke, P.M. (Eds.). Geology and Geochemistry of Epithermal Systems. *Society of Economic Geologists*, El Paso, Texas, pp. 63-72.

Frank, T.D., and Fielding, C.R. (2003). Marine Origin for Precambrian, Carbonate Hosted Magnesite. *Geology*, Vol. 31, pp. 1101–1104.

Gan, S., and van Reenen, D.D. (1995). Geology of Gold Deposits in the Southern Marginal Zone of the Limpopo Belt and the Adjacent Sutherland Greenstone Belt, South Africa, Franke Mine. *South African Journal of Geology*, Vol. 98, pp. 263-275.

Gifkins, C.C., Hermann, W., and Large, R.R. (2005). Altered Volcanic Rocks-A Guide to Description and Interpretation, Centre for Ore Deposit Research, University of Tasmania, Hobart, 275pp.

Gold T. (1979). Terrestrial Sources of Carbon and Earthquake Outgassing. *Journal of Petrology and Geology*, Vol. 1, pp. 3-19.

Greater Giyani Local Municipality LED Strategy. (2018-2019). [Online]. Available at http://www.greatergiyani.gov.za/docs/reports/FINAL%20IDP%202018-19.pdf [Accessed: May 2018]. 97pp.

Griffis, R. (1972). Genesis of a Magnesite Deposit, Deloro Twp., Ontario. *Economic Geology*, Vol. 67, pp. 63–71.

Guild, P.W. (1947). Petrology and Structure of the Moa District, Orient Province, Cuba. Am. Union Trans. *Geophysics*, Vol. 28, pp. 218-246.

Hajjar, Z., Wafik, A., and Constantin, M. (2015). Magnesite Veins from Ultramafic Massif of Beni Bousera (Internal Rif, Morocco). *Journal of Tethys*, Vol. 3, Issue No. 2, pp. 152–162.

Hamdy, M. (2007). Stable Isotope and Trace Element Characteristics of Some Serpentinite-Hosted Vein Magnesite Deposits from the Eastern Desert of Egypt. Arguments for Magmatism and Metamorphism-Related Mineralising Fluids. *MERC Bull*, Vol. 21, pp. 29-50.

Harben, P.W. (2008). Uses. [Online]. Available at www.peterharben.com/index.html [Accessed: January 2018].

Harben, P.W., and Bates, R.L. (1990). Industrial Minerals Geology and World Deposits. Industrial Minerals Division, Metal Bulletin, London, 312pp.

Hassan, Z. H. (2017). Beneficiation and Mineral Processing of Magnesium Minerals. [Online]. Available at https://www.slideshare.net/hzharraz [Accessed: March 2018].

Hogmalm, K. J., Hellingwerf, R., Cornell, D. H., and Finger, F. (2012). An Epigenetic Magnesite Deposit in the Bergslagen Area, Central Sweden, *GFF*, Vol. 134, Issue No. 1, pp. 7-18.

Hughes, W. (2008). Magnesite Processing. [Online]. Available at www.azom.com/details.asp?articleID=1343 [Accessed: May 2018].

Humphris, S. E., and Henderson, P. (1984). The Mobility of the Rare Earth Elements in the Crust. *Rare Earth Element Geochemistry*, Vol. 2, pp. 317-342.

Ilich, M. (1968) Problems of the Genesis and Genetic Classification of Magnesite Deposits. Bratislava, *Geologicky Zbornik-Geologica Carpathica XIX*, Vol. 1, pp. 149160.

Indian Minerals Yearbook. (2012). Magnesite (Final Release). The Government of India Ministry of Mines, Indian Bureau of Mines, Indira Bhavan, Civil Lines, NAGPUR–440 001. Part- III: Mineral Reviews, 51st Edition, 15pp.

Irvine, T.N., and Baragar, W.R.A. (1971). A Guide to the Chemical Classification of the Common Volcanic Rocks. *Canadian Journal of Earth Sciences*, Vol. 8, pp. 523–548.

Jancic, S.J., and Grootsholten, P.A. (1984). Industrial Crystallization. Delft Univ. Press, Dordrecht, Netherlands, 434 pp.

Jedrysk, M.O., and Halas, S. (1990). The Origin of Magnesite Deposits from the Polish Forsesudetic Block Ophiolites. Preliminary d13C and d18O Investigations. *Terra Nova*, Vol. 2, pp. 54-159.

Jeleni, M. N., Gumbo, J. R., Muzerengi, C., and Dacosta, F. A. (2012). An Assessment of Toxic Metals in Soda Mine Tailings and a Native Grass: A Case Study of an Abandoned Nyala Magnesite Mine, Limpopo, South Africa. *WIT Transactions on Ecology and the Environment,* Vol. 164**,** pp. 415-426.

Kadir, S., Kolayli, H., and Eren, M. (2013). Genesis of Sedimentary and Vein-type Magnesite Deposits at Kop Mountain, NE Turkey. *Turkish Journal of Earth Sciences*, Vol. 22, pp. 98–114.

Kleywegt, R.J., De Beer, J.H., Stettler, E.H., Brandl, G., Duvenhagen, W.A., and Day, R.W. (1987). The Structure of the Giyani Greenstone Belt as Derived from Geophysical Studies. *South African Journal of Geology*, Vol. 90, pp. 282.

Kralik, M., Aharon, P., Schroll, E., and Zachmann, D. (1989). Carbon and Oxygen Isotype Systematics of Magnesite: Review: In P. Moller (Ed.). Magnesite: Geology, Mineralogy, Geochemistry, Formation of Mg-carbonates, Gebru¨der Borntraeger, Berlin, pp. 197–206.

Kramer D.A. (2005). Magnesium Compounds. In*:* United States Geological Survey. Compiler. Mineral Commodity Summaries*.* United States Department of the Interior, pp. 100–101.

Kramers, J.D., Henzen, M., and Steidle, L. (2014). Greenstone Belts at the Northern Most Edge of the Kaapvaal Craton: Timing of Tectonic Events and a Possible Crustal Fluid Source. *Precambrian Res*, Vol. 253, pp. 96–113.

Kreissig, K., Holzer, L., Frei, R., Villa, I.M., Kramers, J.D., Kröner, A., Smit, C.A., and van Reenen, D.D. (2001). Geochronology of the Hout River Shear Zone and the Metamorphism in the Southern Marginal Zone of the Limpopo Belt, Southern Africa.

Precambrian Research, Vol. 109, pp. 145-173.

Kröner, A., Jaeckel, P., and Brandl, G. (2000). Single Zircon Ages for Felsic to Intermediate Rocks from the Pietersburg and Giyani Greenstone Belts and Bordering Granitoid Orthogneisses, Northern Kaapvaal Craton, South Africa. *Journal of African Earth Sciences*, Vol. 30, pp. 773-793.

Krupenin, M.T. (2002). Comparison of Lower and Middle Riphean Sparry Magnesite Deposits of the Southern Urals Province. *Spec Iss Bol Paran Geoci*, Vol. 50, pp. 43–50.

Kuşcu, M., Cengiz, O., and Kahya, A. (2017). Trace Element Contents and C-O Isotope Geochemistry of the Different Originated Magnesite Deposits in Lake District (Southwestern Anatolia), Turkey. *Arabian Journal of Geosciences*, Vol. 10, Issue No. 15, 21pp.

Lakehead University. (2014). Preparations of Thin Sections. Geology Department [Online]. Available at https://lucas.lakeheadu.ca/luil/uploads/geoprep.pdf. [Accessed; June 2018].

Lambert, I.B., Donnelly, T.H., Etminan, H., and Rowlands, N.J. (1984). Genesis of Late

Proterozoic Copper Mineralization, Copper Claim, South Australia. *Economic Geology*, Vol. 79, pp. 461–475.

Large, R.R., Gemmell, J.B., Paulick, H., and Huston, D.L. (2001). The Alteration Box Plot: A Simple Approach to Understanding the Relationship Between Alteration Mineralogy and Lithogeochemistry Associated with Volcanic Massive Sulphide Deposits. *Economic Geology*, Vol. 95, Issue No. 5, pp. 957-972.

Laveuf, C., and Cornu, S. (2009). A Review on the Potentiality of Rare Earth Elements to Trace Pedogenetic Processes. *Geoderma*, Vol. 154, Issue No. 1, pp. 1-12.

Le Bas, M.J., Le Maitre, R.W., Streckeisen, A., and Zanettin, B. (1986). A Chemical Classification of Volcanic Rocks Based on the Total Alkali-Silica Diagram. *Journal of Petrology*, Vol. 27, pp. 745–750.

Lefond, S.J. (1975). Industrial Minerals and Rocks. Am. Inst. Mining and Metallurgical and Petroleum Engin. Inc. New York.

Li and Ghilotti. (2017). Fused Magnesia Prices in April 2017 [Online]. Available at http://www.indmin.com/Article/3709216/Fusedmagnesia-prices-increase-in China.html [Accessed: May 2019].

Lian, D., Yang, J., Dilek, Y., and Rocholl, A. (2018). Mineralogy and Geochemistry of Peridotites and Chromitites in the Aladag Ophiolite (Southern Turkey): Melt Evolution of the Cretaceous Neotethyan mantle. *Journal of the Geological Society*, Vol. 176, pp. 958-974.

Lugli, S., Torres-Ruiz, J., Garuti, G., and Olmedo, F. (2000). The Origin of the Eugui Magnesite Deposit (Western Pyrenees, Spain): Petrological, Geochemical, and REE Study. *Economic Geology*, Vol. 95, pp. 1775–1791.

Marshall, D. (1996). Ternplot: An Excel Spreadsheet for Ternary Diagrams. *Computers and Geosciences*, Vol. 22, Issue NO. 6, pp. 697-699.

Martiny, E., and Rojković, I. (1977). Trace Elements in Magnesites of Slovakia (Central West Carpathians). *Geologica Carpathica*, Vol. 28, pp. 311-322.

Masindi, V. (2015). Remediation of Acid Mine Drainage Using Magnesite and Its Bentonite Clay Composite. Ph. D. Department of Ecology and Resource Management, School of Environmental Sciences, University of Venda, (Unpublished), 230pp.

Masindi, V., Gitari, M., Tutu, H., and De Beer, M. (2015). Passive Remediation of Acid Mine Drainage Using Cryptocrystalline Magnesite: A Batch Experimental and Geochemical Modelling Approach. *Water SA*, Vol. 41, Issue No: 5, pp. 677-682.

McCourt, S., and van Reenen, D.D. (1992). Structural Geology and Tectonic Setting of the Sutherland Greenstone Belt, Kaapvaal Craton, South Africa. *Precambrian Research*, Vol. 55, pp. 93-110.

McDonough, W.F., and Sun, S. S., (1995). The Composition of the Earth. *Chemical Geology*, Vol. 120, pp. 223-253.

Melezhik, V.A., Fallick, A.E., Medvedev, P.V., and Makarikhin, V.V. (2001). Palaeoproterozoic Magnesite: Lithological and Isotopic Evidence for Playa/Sabkha Environments. *Sedimentology*, Vol. 48, pp. 379–397.

Meunier, A. (1983). Micromorphological Advances in Rock Weathering Studies. In: Bullock, P., and Murphy, C.P. (Eds.). *Soil Micromorphology*, Vol. 2. pp. 467-483.

Mielke, J.E. (1979). Composition of the Earth's Crust and Distribution of the Elements. In: Siegel, F.R., (Ed.). Review of Research on Morden Problems in Geochemistry, Paris, International Association for Geochemistry and Cosmochemistry, *Earth Sciences Series*, Vol. 16, pp. 13-37.

Moller P. (1989). Minor and Trace Elements in Magnesite. In: Moller, P. (Ed.) Magnesite: Geology, Mineralogy, Geochemistry, Formation of Mg Carbonates. Monograph Series on Mineral Deposits, Gebrüder Borntraeger, Berlin-Stuttgart, Vol. 28., pp. 173–195.

Morteani, G., Moller, P., and Schley, F. (1982). The Rare Earth Elements Contents and the Origin of the Sparry Magnesite Mineralizations of Tux/Lanersbach, Entanchen Alm, Spiessnägel, Hochfilzen, Austria, and the Lacustrine Magnesite Deposits of Ainai/Kozani, Greece, and Bela Stena, Yugoslavia. *Economic Geology*, Vol. 77, pp. 617–631.

Morteani, G., Schley, F., and Moller, P. (1983). On the Formation of Magnesite: In Schneider, H.J. (Ed.). Minerals Deposits of the Alps and of the Alpine Epoch in Europa. Berlin, *Springer-Verlag*, pp. 106–116.

Naidoo, D. (2008). Overview of South Africa's Mineral-based Fertilizer Industry.

Department of Minerals and Energy, 25pp.

Nasedkin V. V., Krupenin M. T., Safonov Y. G., Boeva N. M., Efremova S. V., and Shevelev A. I. (2001). Comparison of Amorphous (Cryptocrystalline) and Crystalline Magnesite. *Mineral Slovaca*, Vol. 33, pp. 567-574

Nelson, S. A. (2011). General Classification of Igneous Rocks. [Online]. Available at: http://www.tulane.edu/~sanelson/eens212/igrockclassif.htm [Accessed: February 2017].

Nesse, W. D. (2012). Introduction to Mineralogy, 2nd Edition. Oxford University Press, New York, pp. 63–78.

Neubauer F. R. (1983). Bericht 1982 Uber Geologische Aufnahmen im Renfeld-und Gleinalmkristallin und in der Grauwackenzone auf Blatt 134 *Passail. - Jb. Geol. B.-A,* Vol. 126, pp. 315-316.

Nuffield, E. W. (1966). “X-ray Diffraction Methods”, John Wiley and Sons, Inc. New York, London, Sydney, pp. 29-45.

O'Neil, J.R., and Barnes, I. (1971). C13 and O18 Composition in Some Fresh-Water Carbonate Associated with Ultramafic Rocks. Western United States. *Geochimica et Cosmochimica Acta*, Vol. 35, pp. 687-697.

Operta, M., and Bušatlić, N. (2018). Contribution to the Knowledge of the Magnesite Deposits in Bosnia and Herzegovina. *Geografski Pregled*, Vol. 39. Issue No. 39, pp. 2303-8950.

Passeraub, M., Wüst, T., Kreissig, K., Smit, C.A., and Kramers, J.D. (1999). Structure, Metamorphism and Geochronology of the Rhenosterkoppies Greenstone Belt, South Africa. *South Africa Journal of Geology*, Vol. 102, pp. 323-334.

Pearce, J. A. (1996). A User's Guide to Basalt Discrimination Diagrams. In: Wyman, D. (Ed.). Trace Element Geochemistry of Volcanic Rocks: Application for Massive Sulphide Exploration. Winnipeg: Geological Association of Canada, Mineral Deposits Division, pp. 79-113.

Pecerillo, R., and Taylor, S.R. (1976). Geochemistry of Eocene Calc-Alkaline Volcanic Rocks from the Kastamonu Area, Northern Turkey. *Contribution of Mineral Petrology*, Vol. 58, pp. 63-81.

Perchuk, L.L., Gerya, T.V., van Reenen, D.D., Safonov, O.G., and Smit, C.A. (1996). The Limpopo Metamorphic Complex South Africa, 2. Decompression-cooling Regimes of Granulites and Adjacent Rocks of the Kaapvaal Craton. *Petrology*, Vol. 4, pp. 571-599.

Peter, B.N. (2010). Theory of XRF. 3rd Edition. Netherland: Panalytical BV, 4pp.

Pohl, W., and Siegl, W. (1986). Sediment-Hosted Magnesite Deposits. In: Wolf, K. H. (Ed.): Handbook of Strata-Bound and Stratiform Ore Deposits. *Elsevier*, Amsterdam, Vol. 14. pp. 223–310.

Pohl, W. (1990). Genesis of Magnesite Deposits: Models and Trends. *Geol. Rund*, Vol. 79, pp. 291-299.

Prasannakumar, V., Vikas, C., and Kumar, S.N. (2002). Constraints on the Origin of South Indian Magnesite Deposits. *Boletim Paranaense de Geociência,* Vol. 50, Issue No. 50, pp. 15-20.

Pressacco, R., Hall, D., and Ling, P. (2010). Technical Report on the Initial Mineral Resource Estimate for the Timmins Talc-magnesite Deposit. [Online]. Ontario, Canada: Available at MICON International Limited. Available at: https://www.globexmining.com/docs/TR_20100224_TimminsTalc.pdf. 149pp.

Price, W. J. (1972). Analytical Atomic Absorption Spectrometry. London: Heyden.

Prinsloo, M.C. (1977). The Geology of the Giyani Region, North-Eastern Transvaal Showing Easy Economic Mineral Settings. M.Sc. Thesis, Rand Africans Univ., Johannesburg. Unpublished, 44pp.

Raith, M.M., Raase P., and Reinlhardt, J. (2012). Guide to Thin Sections Microscopy. 2nd Edition. ISBN 978-3-00-037671-9.

Ramovha, D.A. (2016). Socio and Economic Impact of Comprehensive Rural Development Programme: A Case Study of Muyexe Comprehensive Rural Development Programme Site in the Greater Giyani Local Municipality in Limpopo Province, South Africa. Research Dissertation: MSc. UNISA, Department of Geography. Unpublished, 139pp.

Ratlabala, M. E. (2003). An Overview of South Africa's Mineral Based Fertilizers. Department of Minerals and Energy, pp. 1-28.

Roering, C., van Reenen, D.D., De Wit, M.J., Smit, C.A., De Beer, J.H., and van Schalkwyk, J.F. (1992). Structural Geological and Metamorphic Significance of the Kaapvaal Craton – Limpopo Belt Contact. *Precambrian Research*, Vol. 55, pp. 69-80.

Rollinson, H. R. (1993). Using Geochemical Data: Evaluation, Presentation, Interpretation. Harlow, Essex, England: New York. Longman Scientific and Technical, 352pp.

Rudnick, R. L. and Gao, S. (2003). Composition of the Continental Crust. In: D. H. Heinrich and K. T. Karl (Eds). Treatise on Geochemistry. Oxford: Pergamon, pp. 1-64.

Rutherford, M. C. Mucina, L. Lotter, M.C and Bredenkamp, G.J. (2006). Savanna Biome. In: Mucina, L. and Rutherford, M.C (Eds.): The vegetation of South Africa, Lesotho, and Swaziland, Strelitzia 19. South African Biodiversity Institution, Pretoria, pp. 440-438.

SACS: South African Committee for Stratigraphy. (1980). Lithostratigraphy of the Republic of South Africa, South West Africa/Namibia, and Republic of Bophuthatswana, Transkei, and Venda. Handbook of Geological Survey of South Africa, Vol. 8, 690pp.

Schroll E. (2002). The Genesis of Magnesite Deposits in the View of Isotope Geochemistry. Institute of Mineralogy and Crystallography, University Vienna, Althanstraße 14, A-1090 Wien. *Boletim Paranaense de Geociências*, Vol. 50, pp. 59-68.

Schulze, R. K., Hill, M. A., Field, R. D., Papin, P. A., Hanrahan, R. J., and Byler, D. D. (2004). Characterization of Carbonated Serpentine Using XPS and TEM. *Energy Conversion and Management,* Vol. 45, pp, 3169–3179.

Shannon, R.D. (1976). Revised Effective Ionic Radii and Systematic Studies of Interatomic Distances in Halides and Chalcogenides. *Acta CrystaUogr Sect A*, Vol. 32, pp.751-767.

Sibanda, Z., Amponsah-Dacosta, F., and Mhlongo, S. E. (2013). Characterization and Evaluation of Magnesite Tailings for their Potential Utilization: A Case Study of Nyala

Magnesite Mine, Limpopo Province of South Africa. *ARPN Journal of Engineering and Applied Sciences,* Vol. 8**,** pp. 606-613.

Smit, C.A., and Van Reenen, D.D. (1997). Deep Crustal Shear Zones, High-grade Tectonites, and Associated Metasomatic Alteration in the Limpopo Belt, South Africa: Implications for Deep Crustal Processes. *Journal of Geology*, Vol. 105, pp. 37-57.

South African Weather Service. (2019). Greater Giyani Weather Forecast Pretoria, South Africa.

Steenkamp, N. C., and Clark-Mostert, V. (2012). Inferred Historic Gold Mining Approaches, Giyani Greenstone Belt, South Africa. TWP Projects Level 1, Building 54, Melrose Arch, Johannesburg, 2107, South Africa, 11pp.

Strydom, J. H. (1998). Magnesite: In Wilson, M. G. C., and Anhaeusser, C. R. (Eds.). The Mineral Resources of South Africa: Handbook, *Council for Geoscience*, Vol. 16, pp. 447–448.

Takahashi, G. (2015). Sample Preparation for X-ray Fluorescence Analysis. *Rigaku*, Vol. 1, Issue No. 31, pp. 26-30.

Taylor, S. R., and McLennan, S. M. (1995). The Geochemical Evolution of the Continental Crust. *Reviews of Geophysics, Vol.* 33, Issue No. 2, 241pp.

Teir, S., Kuusik, R., Fogelholm, C. J., and Zevenhoven, R. (2007). Production of Magnesium Carbonates from Serpentinite for Long-Term Storage of CO_2. *International Journal of Mineral Processing*, Vol. 85, pp. 1–15.

Thompson, M., and Walsh, J. N. (1983). A Handbook of Inductively Coupled Plasma Spectrometry. Glasgow: Blackie.

Toulkeridis, T., Peucker-Ehrenbrink, B., Clauer, N., Kröner, A., Schidlowski, M., and Todt, W. (2010). Pb–Pb Age, Stable Isotope and Chemical Composition of Archaean Magnesite, Barberton Greenstone Belt, South Africa. *Journal of the Geological Society*, Vol. 167, Issue No. 5, pp. 943-952.

U.S. Geological Survey. (2013). Minerals Yearbook, Magnesium Compounds [Advance Release], 11pp.

U.S. Geological Survey. (2018). Mineral Commodity Summaries 2018: U.S.

Geological Survey, 200 pp. Available at https://doi.org/10.3133/70194932.

Valdiya, K.S. (1968). Origin of the Magnesite Deposits of Southern Pithoragarh. Kumaun Himalaya, India. *Economic Geology*, Vol. 63, pp. 924–934.

Van Reenen, D.D. (1986). Hydration of Cordierite and Hypersthene and a Description of the Retrograde Isograd in the Limpopo belt, South Africa. *American Mineralogist*, Vol. 71, pp. 900-915.

Van Reenen, D.D., and Hollister, L.S. (1988). Fluid Inclusions in Hydrated Granulite Facies Rocks, Southern Marginal Zone of the Limpopo Mobile Belt, South Africa. *Geochimica et Cosmochimica Acta*, Vol. 52, pp. 1057-1064.

Van Reenen, D.D., Perchuk, L.D., Roering, C., and Boshoff, R. (2011). Thrust Exhumation of the Neoarchean Ultra-High Temperature Southern Marginal Zone, Limpopo Complex: Convergence of Decompression–Cooling paths in the Hanging Wall and Prograde P–T Paths in the Footwall. In: van Reenen, D.D., Kramers, J.D. McCourt, S., and Perchuk, L.L. (Eds.). Origin and Evolution of Precambrian HighGrade Gneiss Terranes, with Special Emphasis on the Limpopo Complex of Southern Africa. Geological Society of America Memoir, Vol. 207, pp. 189–212.

Wang, L., and Liang, T. (2015). Geochemical Fractions of Rare Earth Elements in Soil Around a Mine Tailing in Baotou, China. Scientific Reports No 5.

Wang. N., Chen. M., Yue-Yuan. L., and Hong-Wei, T. (2011). Non-Ferrous Met. *Soc*. China, pp. 2061-2065.

Ward, J.H.W., and Wilson, M.G.C. (1998). Gold Outside the Witwatersrand Basin. In: Wilson, M.G.C., and Anhaeusser, C.R. (Eds.). The Mineral Resources of South Africa. Handbook, Council for Geoscience, Vol. 16, pp. 350-386.

White, W. (2013). Chapter 7: Trace Elements in Igneous Processes. In: White, W. (Ed.). *Geochemistry*. New York, United States: John Wiley and Sons Inc, pp. 259-313.

Williams, K. L. (1987). Introduction to X-ray Spectrometry. London: Allen and Unwin.

Wilson, I., and Ebner, F. (2005). A Review of the World's Current and Potential Magnesite Resources. Industrial Minerals, *MagMin*, Vienna-Austria, 100pp.

Wilson, I. (2013). Global Update of Magnesite Resources. *In: MagMIn Conference*. Oslo, Norway, 14th MAY 2013. Norway: Industrial Mineral Events. 100.

Wilson, M. (1989). Igneous Petrogenesis., Chapman and Hall, London, 466 pp.

Wilson, M. (2007). Igneous Petrogenesis: A Global Tectonic Approach. 10th Edition. Dordreebt: Springer.

Winchester, J.A., and Floyd, P.A. (1977). Geochemical Discrimination of Different Magma Series and Their Differential Products Using Immobile Elements. *Chemical Geology*, Vol. 20, pp. 325-343.

Zachmann, D.W. (1977). Untersuchung von Magnesit-Hydromagnesit und Huntitvorkommen in Nordgriechenland. 262pp. PhD-Thesis Univ. Stuttgart.

Zachmann, D.W., and Johannes, W. (1989). Cryptocrystalline Magnesite. In: Moller, P (Ed.) Magnesite: Geology, Mineralogy, Geochemistry, Formation of Mg Carbonates. Monograph Series on Mineral Deposits, Vol. 28. Gebrüder Borntraeger, BerlinStuttgart, pp. 15-28.

Zadeh, A.M.A. (2009). The Genetic Model of the Hohentauern/Sunk Sparry Magnesite Deposit (Eastern Alps/Austria). PhD Thesis, Department of Applied Geosciences and Geophysics, Geology and Economic Geology, University of Leoben, Austria, 208pp.

Zedef, V. (1994). Origin of Magnesite in Turkey, A Stable Isotope Study. PhD, Department of Geology & Applied Geology, University of Glasgow, Konya, Turkey, 174pp.

Zedef, V., Russell, M., Fallick, A., and Hall, A. (2000). Genesis of Vein Stockwork and Sedimentary Magnesite and Hydromagnesite Deposits in the Ultramafic Terranes of Southwestern Turkey: A Stable Isotope Study. *Economic Geology*, Vol. 95, pp. 429–445.

APPENDICES

Appendix A: GPS Coordinates and Physical Description of Rocks

SAMPLE I. D	COORDINATES		ELEVATION	MINERAL COMPOSITION	COLOR AND TEXTURE	DESCRIPTION OF ROCK	STRIKE	DIP ANGLE	DIP DIRECTION	ROCK NAME
	LAT	LONG								
T1S1	$23^0$11'25.1'' S	$30^0$55'28.3'' E	458 m	Hornblende, Chlorite, Anthophyllite, Talc	Pale green to grey and has lepidoblastic texture, fine to medium grain sizes	Breaks in layers due to a well-developed schistosity	S230 ^{0}W N50^0 E	42_0	S140^{0}E	Schist
T1S2	$23^0$11'26.1'' S	$30^0$55'29.0'' E	459 m	Plagioclase, Clinopyroxene, and Chromite	Dark grey, Aphanitic texture	Very fine, and slightly weathered, contact with schist rocks				Basalt
T1S3	$23^0$11'26.6'' S	$30^0$55'29.2'' E	462 m	Hornblende, Chlorite, Anthophyllite, Talc	Pale green to grey and lepidoblastic texture, fine to medium grain sizes	Breaks in layers due to a well-developed schistosity, it has a soapy feel and it is slippery.	S230 ^{0}W N50^0 E	35_0	S140^{0}E	schist
T1S4	$23^0$11'27.0'' S	$30^0$55'29.4'' E	462 m	Plagioclase, Clinopyroxe	Dark grey, Aphanitic texture	Weathered on top to				Basalt

				ne, and Chromite		brown and fine-grained				
T1S5	$23^0$11'27.7'' S	$30^0$55'30.3'' E	464 m	Talc, Tremolite, Chlorite, and Chromite	Pale green to grey and lepidoblastic texture, fine to medium grain sizes	Breaks in layers due to a well-developed schistosity, it has a soapy feel and it is slippery.	S235 ^{0}W N55^0 E	29^0	S14 5^0E	Schist
T1S6	$23^0$11'21.6'' S	$30^0$55'31.1'' E	465 m	Plagioclase, Clinopyroxene, and Chromite	Dark grey, Aphanitic texture	Lightly weathered, fine-grained				Basalt
T1S7	$23^0$11'31.1'' S	$30^0$55'32.3'' E	470 m	Hornblende, Chlorite, Anthophyllite, Talc	Pale green to grey and lepidoblastic texture, fine to medium grain sizes	Breaks in layers due to a well-developed schistosity	S236 ^{0}W N56^0 E	30^0	S14 6^0E	Schist
T1S8	$23^0$11'34.4'' S	$30^0$55'32.2'' E	476 m	Quartz, Iron oxide, and the silica cement	White to slightly pink and granular texture	Hard, conchoidal fracture, a pink stain of iron oxide. Medium				Vitreous Quartzite

						grained can be seen by				
						the unaided eye				
T1S9	$23^0$11’36.1’’S	$30^0$55’32.0’’E	476 m	Hornblende, Chlorite, Anthophyllite, Talc	Pale green, to grey and lepidoblastic texture, fine to medium grain sizes	Breaks in layers due to a well-developed schistosity.	S238 ^{0}W N50^0 E	29_0	S14 8^{0}E	Schist
T1S10	$23^0$11’37.9’’S	$30^0$55’32.7’’E	477 m	Hornblende, Chlorite, Anthophyllite, Talc	Pale green, to grey and lepidoblastic texture, fine to medium grain sizes	Breaks in layers due to a well-developed schistosity.	S230 ^{0}W N50^0 E	35^0	S14 0^{0}E	Schist

T1S11	$23^0$11’43.7’’S	$30^0$55’35.1’’E	465 m	Hornblende, Chlorite, Anthophyllite, Talc	Pale green, to brown and lepidoblastic texture, fine to medium grain sizes	Breaks in layers due to a well-developed schistosity. Has two layers of different colours, brown and pale green	N310 ^{0}W	28^0	S22 0^0W	Schist
T1S12	$23^0$11’47.9’’S	$30^0$55’40.0’’E	457 m	Quartz, Plagioclase and Amphibole	Dark greenish, a mixture of phaneritic and	Very heavy, glassy, rough and shiny				Amphibolite

					porphyritic texture					
T1S13	$23^0$11’54.7’’S	$30^0$55’40.8’’E	476 m	Chlorite, limonite, and Silica	Red to brown, vesicular texture	Very compact and hard to break, has some veins of magnesite				Birbirite

T1S14	23^{0}12’04.4’’S	30^{0}55’44.9’’E	486 m	Serpentine, Tremolite, Actinolite and chromite	Greyish to Green colour and has a serpentine texture	It had magnesite veins, coarsegrained and light				Serpentinites
T1S15	23^{0}12’10.09’’ S	30^{0}55’45.1’’E	470 m	Serpentine, Tremolite, Actinolite and chromite	Brown	a schistose komatiite weathered pattern and, in some area, an elephant skin weathered pattern	S190^{0}E	20^0	N290	Weathered Serpentinite Schist
T1S16	23^{0}12’12.2’’S	30^{0}55’46.0’’E	470 m	Hornblende, Quartz, Plagioclase	Dark grey and white. Foliated texture	Minerals are aligned, very heavy, Amphibolite				Pillowed Amphibolite

				and Iron oxide		facies texture				

T1S17	$23^0$12'13.2'' S	$30^0$55'46.8'' E	470 m	Cherts, iron oxide and jasper	Red to dark grey and white. Banded trellis texture	Bended layers, with veins of carbonate minerals. Coarse to Large grained	S189 ^{0}E	40^0	S22 9^0W	Banded iron formation
T1S18	$23^0$12'15.3'' S	$30^0$55'48.5'' E		Plagioclase and pyroxene	Dark grey, Aphanitic texture	Finegrained and compact				Basalt
T2S1	$23^0$11'17.8'' S	$30^0$55'37.0'' E	450 m	Plagioclase and pyroxene	Dark grey, Aphanitic texture	Finegrained and weathered, with a stain of red and not compact breaks easily				Basalt
T2S2	23011'21.2''S	30055'44.5 E	457 m	Hornblende, Chlorite, Anthophyllite, Talc	Pale green, to brown and lepidoblastic texture, fine to medium grain sizes	Breaks in layers due to a well-developed schistosity. Has two layers of different colours,	S200 ^{0}W N20^0 E	31_0	S10 ^{0}E	Schist

						brown and pale green				
T2S3	23011’19.9 S	30055’43.58’’E	457 m	Quartz, Iron oxide, and the silica cement	White to slightly pink and granular texture	Hard, conchoidal fracture, a pink stain of iron oxide. Medium grained can be seen by the unaided eye				Vitreous Quartzite
T2S4	$23^0$11’22.2’’S	$30^0$55’44.6’’E	457 m	Hornblende, Chlorite, Anthophyllite, Talc	Pale green, to brown and lepidoblastic texture, fine to medium grain sizes	Breaks in layers due to a well-developed schistosity. Has two layers of different colours, brown and pale green	S230 ^{0}W N50^0 E	18_0	S14 0^{0}E	Schist
T2S5	$23^0$11’21.8 S	$30^0$55’45.2 E	459 m	Quartz, Iron oxide, and the silica cement	White to slightly pink and granular texture	Hard, conchoidal fracture, a pink stain of iron oxide.				Vitreous Quartzite

						Medium grained can				

						be seen by the unaided eye				
T2S6	$23^0$11’26.4’’S	$30^0$55’47.1’’E	454 m	Plagioclase and pyroxene	Dark grey, Aphanitic texture	Finegrained and compact				Basalt
T2S7	$23^0$11’29.5’’S	$30^0$55’48.7’’E	456 m	Plagioclase, Clinopyroxene, and Chromite	Dark grey, Aphanitic texture	Lightly weathered, fine-grained				Basalt
T2S8	$23^0$11’36.8’’S	$30^0$55’52.4’’E	451 m	Hornblende, Chlorite, Anthophyllite, Talc	Pale green, to brown and lepidoblastic texture, fine to medium grain sizes	Breaks in layers due to a well-developed schistosity. Has two layers of different colours, brown and pale green	S230 ^{0}W N50^0 E	18^0	S14 0^0E	Schist

T2S9	$23^0$11’40.3’’S	$30^0$55’53.2’’E	455 m	Quartz, Iron oxide, and the silica cement	White to slightly pink and granular texture	Hard, conchoidal fracture, a pink stain of iron oxide. Medium grained can be seen by				Vitreous Quartzite
						the unaided eye				
T2S11	$23^0$11’47.0’’S	$30^0$55’55.4’’E	485 m	Serpentine, Tremolite, Actinolite and chromite	Greyish to Green colour and has a serpentine texture	It had magnesite veins, coarsegrained and light				Serpentinite
T2S12	$23^0$11’50.5’’S	$30^0$55’58.8’’E	479 m	Serpentine, Tremolite, Actinolite and chromite	Greyish to Green colour and has a serpentine texture	It had magnesite veins, coarsegrained and light				Serpentinites

T2S13	$23^0$11’56.9’’S	$30^0$56’01.6’’E	473 m	Serpentine, Tremolite, Actinolite and chromite	Greyish to Green colour and has a serpentine texture	It had magnesite veins, coarsegrained and light				Serpentinites
T2S14	$23^0$12’01.1’’S	$30^0$56’03.0’’E	475 m	Serpentine, Tremolite, Actinolite and chromite	Brown, Coarsegrained and schistose komatiite weathered pattern	Easily splits into slabs, has flake-aligned minerals				Weathered serpentinite schist

T2S15	$23^0$12’10.9’’S	$30^0$56’04.2’’E	463 m	Plagioclase and pyroxene	Dark grey, Aphanitic texture	Finegrained and compact				Basalt
T2S17	$23^0$12’12.2’’S	$30^0$56’08.7’’E	459 m	Quartz, Iron oxide, and the silica cement	White to slightly pink and granular texture	Hard, conchoidal fracture, a pink stain of iron oxide. Medium grained can be seen by the unaided eye				Vitreous Quartzite

T3S1	23^{0}11’56.1’’S	30^{0}56’15.0’’E	464 m	Chlorite, limonite, and Silica	Red to brown, vesicular texture	Very compact and hard to break, has some veins of magnesite				Birbirite
T3S2	23^{0}11’52.4’’S	30^{0}56’16.1’’E	467 m	Serpentine, Tremolite, Actinolite and chromite	Greyish to Green colour and has a serpentine texture	It had magnesite veins, coarsegrained and light				Serpentinites

T3S4	23^{0}11’38.7’’S	30^{0}56’07.0’’E	450 m	Serpentine, Tremolite, Actinolite and chromite	Greyish to Green colour and has a serpentine texture	It had magnesite veins, coarsegrained and light				Serpentinites
T3S5	23^{0}11’32.9’’S	30^{0}56’04.9’’E	441 m	Quartz, Iron oxide, and the silica cement	White to slightly pink and granular texture	Hard, conchoidal fracture, a pink stain of iron oxide. Medium grained can be seen by the unaided eye				Vitreous Quartzite

T3S6	$23^0$11’31.1’’S	$30^0$56’01.4’’E	444 m	Hornblende, Chlorite, Anthophyllite, Talc	Pale green, to brown and lepidoblastic texture, fine to medium grain sizes	Breaks in layers due to a well-developed schistosity. Has two layers of different colours, brown and pale green	S229 ^{0}W N49^0 E	40^0	S13 9^{0}E	Schist
T3S7	$23^0$11’29.5’’S	$30^0$56’00.4’’E	445 mm	Plagioclase, magnetite,	Dark grey, Aphanitic texture	Finegrained and compact				Basalt

				and pyroxene						
T3S8	$23^0$11’27.6’’S	$30^0$55’56.5’’E	453 m	Tremolite, Actinolite, Chlorite, Chromite, and Talc	Pale green, to brown and lepidoblastic texture, fine to medium grain sizes	Breaks in layers due to a well-developed schistosity. Has two layers of different colours, brown and pale green	S228 ^{0}W N48^0 E	20^0	S14 8^{0}E	Schist

T4S1	$23^0$11’14.5’’S	$30^0$55’58.2’’E	411 m	Hornblende, Chlorite, Anthophyllite, Talc	Pale green, to brown and lepidoblastic texture, fine to medium grain sizes	Breaks in layers due to a well-developed schistosity. Has two layers of different colours, brown and pale green	S230 ^{0}W N50^0 E	37^0	S14 0^0E	Schist
T4S2	$23^0$11’30.9’’S	$30^0$55’58.0’’E	449 m	Plagioclase and pyroxene	Dark grey, Aphanitic texture	Finegrained and compact				Basalt
T4S3	$23^0$11’36.7’’E	$30^0$56’20.1’’E	454 m	Quartz, Iron oxide, and	White to slightly pink	Hard, conchoidal fracture, a				Vitreous Quartzite

				the silica cement	and granular texture	pink stain of iron oxide. Medium grained can be seen by the unaided eye				
T4S4	$23^0$11’28.2’’S	$30^0$56’77.1’’E	457 m	Plagioclase and pyroxene	Dark grey, Aphanitic texture	Finegrained and compact				Basalt

T4S5	$23^0$11’48.3’’S	$30^0$56’17.3’’E	466 m	Olivine, serpentine and chromite	Dark grey, Aphanitic texture	Finegrained, altered and weathered				Peridotite
T4S6	23°11'51.30"S	30°56'23.14"E	462 m	Serpentine, Tremolite, Actinolite and chromite	Greyish to Green colour and has a serpentine texture	It had magnesite veins, coarsegrained and light				Serpentinites
T4S7	23°11'53.61"S	30°56'24.95"E	458 m	Iron oxide, limonite, and Silica	Red to brown, vesicular texture	Very compact and hard to break, has some veins of magnesite				Birbirite

T4S8	23°12'11.13"S	30°56'22.57"E	458 m	Plagioclase and pyroxene	Dark grey, Aphanitic texture	Finegrained and compact				Basalt

T5S1	23^{0}11’09.7’’S	30^{0}56’25.6’’E	416 m	Hornblende, Chlorite, Anthophyllite, Talc	Pale green, to brown and lepidoblastic texture, fine to medium grain sizes	Breaks in layers due to a well-developed schistosity. Has two layers of different colours, brown and pale green	S228^{0}W N48^{0}E	20^0	S148^{0}E	Schist
T5S2	23^{0}11’10.2’’S	30^{0}56’27.6’’E	420 m	Quartz, Iron oxide, and the silica cement	White to slightly pink and granular texture	Hard, conchoidal fracture, a pink stain of iron oxide. Medium grained can be seen by the unaided eye				Vitreous Quartzite
T5S3	23^{0}11’12.3’’S	30^{0}56’28.1’’E	423 m	Plagioclase and pyroxene	Dark grey, Aphanitic texture	Finegrained and compact				Basalt
T5S4	23^{0}11’14.7’’S	30^{0}56’30.0’’E	427 m	Quartz, Iron oxide, and	White to slightly pink	Hard, conchoidal fracture, a				Vitreous Quartzite

				the silica cement	and granular texture	pink stain of iron oxide. Medium grained can be seen by the unaided eye				
T5S5	$23^0$11’23.6’’S	$30^0$56’30.9’’E	429 m	Plagioclase and pyroxene	Dark grey, Aphanitic texture	Finegrained and compact				Basalt
T5S6	23°12'10.77"S	30°56'33.79"E	450 m	Plagioclase and pyroxene	Dark grey, Aphanitic texture	Finegrained and compact				Basalt
TRS1	$23^0$12’03.’’S	$30^0$55’45.5’’E	482 m	Serpentine, Tremolite, Actinolite and chromite	Brown, Coarsegrained and schistose komatiite weathered pattern	Easily splits into slabs, has flake-aligned minerals	S198 ^{0}E N18^0 W	42^0	N29 0^0W	Weathered serpentinite schist
TRS2	23°11'54.14"S	30°55'33.35"E	470 m	Quartz, Plagioclase and Amphibole	Dark greenish, a mixture of phaneritic and porphyritic texture	Very heavy, glassy, rough and shiny				Amphibolite
TRS3	23°11'42.19"S	30°56'16.78"E	468 m	Serpentine, Tremolite, Actinolite	Pale green to grey, coarse grain size and	light and not heavy, some of the serpentine				Serpentinites

				and chromite	a serpentine texture	had magnesite veins				
TRS4	23°11'23.9" S	30°55'33.2" E	450 m	Plagioclase and pyroxene	Dark grey, Aphanitic texture	Finegrained and compact				Basalt
TRS5	23°11'39.9" S	30°55'47.8" E	450 m	Hornblende, Chlorite, Anthophyllite, Talc	Pale green, to brown and lepidoblastic texture, fine to medium grain sizes	Breaks in layers due to a well-developed schistosity. Has two layers of different colours, brown and pale green	S230 ^{0}W N50^0 E	22$_0$	S14 0^{0}E	Schist
TRS6 (T2S)	23°11'52.80"S	30°55'51.60"E	487 m	Olivine, serpentine and chromite	Dark grey, Aphanitic texture	Finegrained, altered and weathered				Peridotite
TRS7 (T3S9)	23°11'52.80"S	30°56'6.00" E	485 m	Olivine, serpentine and chromite	Dark grey, Aphanitic texture	Finegrained, altered and weathered				Peridotite

TRS8	23°11'24.00"S	30°55'24.90"E	458 m	Hornblende, Chlorite, Anthophyllite, Talc	Pale green, to brown and lepidoblastic texture, fine to	Breaks in layers due to a well-developed	S230 ^{0}W	42^0	S140^{0}E	Schist
					medium grain sizes	schistosity. Has two layers of different colours, brown and pale green	N50^0 E			
TRS9	23°11'17.05"S	30°55'25.15"E	450 m	Hornblende, Chlorite, Anthophyllite, Talc	Pale green, to brown and lepidoblastic texture, fine to medium grain sizes	Breaks in layers due to a well-developed schistosity. Has two layers of different colours, brown and pale green	S229 ^{0}W N49^0 E	30^0	S149^{0}E	Schist

TR10	23°11'12.10"S	30°55'44.50"E	449 m	Hornblende, Chlorite, Anthophyllite, Talc	Pale green, to brown and lepidoblastic texture, fine to medium grain sizes	Breaks in layers due to a well-developed schistosity. Has two layers of different colours, brown and pale green	S230 ^{0}W N50^0 E	30^0	S14 0^{0}E	Schist

Appendix B: Whole-rock geochemical analyses of rocks from the Muyexe area

Sample	**HR1**	**HR2**	**HR3**	**HR4**	**T2S7**	**T2S**	**T2S13**	**T1S17**	**T2S11**	**MR10**	**T1S18**	**T1S13**	**T1S12**	**T3S9**	**T1S16**	**MR8**	**T1S1**	**T1S5**	**T2S3**
SiO_2	50,14	49,34	42,25	36,23	48,38	39	42,34	77,77	65,15	53,52	50,41	83,03	50,11	39,81	54,46	50,61	43,78	54,74	99,5
TiO_2	0,091	0,134	0,103	0,071	0,147	0,078	0,288	0,223	0,099	0,142	1,524	0,078	0,408	0,163	1,381	0,145	0,249	0,151	0
Al_2O_3	0,59	1,52	1,31	0,05	2,04	0	5,72	0,89	1,01	1,51	13,72	1,36	7,84	0,66	10,38	2,21	6,38	1,65	0
Fe_2O_3	4,86	6,9	11,91	8,19	11,11	10,07	10,01	19,81	10,98	9,77	12,89	7,38	8,23	11,75	12,78	9,98	9,68	8,83	0,47
MnO	0,128	0,162	0,257	0,194	0,265	0,241	0,214	0,171	0,236	0,255	0,183	0,135	0,14	0,228	0,164	0,166	0,177	0,186	0

MgO	27,953	27,1656	26,9654	27,1133	25,2496	41,9836	21,2026	1,4949	20,0373	28,5985	3,831	10,7903	7,5974	40,957	3,3104	29,6452	22,181	28,7264	0
CaO	9,74	7,43	7,42	10,7	3,07	0,06	7,66	0,49	0,14	2,72	9,42	0,23	13,43	0,64	7,74	1,83	6,58	3,07	0
Na_2O	6,452	0,605	3,521	0	3,592	0	3,49	0	2,962	8,108	3,808	0	3,128	0	3,792	5,36	0,42	15,461	0
K2O	0,03	0	0	0,02	0,03	0,01	0,02	0,1	0,02	0,05	1,37	0,02	0,23	0	0,35	0,03	0,05	0,01	0
P_2O_5	0,065	0,053	0,056	0,085	0,061	0,002	0,074	0,394	0,03	0,045	0,308	0,019	0,399	0,01	0,271	0,066	0,075	0,044	0,1
FeO*	4,37	6,21	10,72	7,37	10,00	9,06	9,01	17,83	9,88	8,79	11,60	6,64	7,41	10,57	11,50	8,98	8,71	7,95	0,42

Total	100,05	93,31	93,79	82,65	93,94	91,44	91,02	101,34	100,66	104,72	97,46	103,04	91,51	94,22	94,63	100,04	89,57	112,87	100,07
Mg#	86,47	81,40	71,56	78,63	71,64	82,25	70,18	7,74	66,98	76,49	24,83	61,90	50,64	79,48	22,35	76,75	71,80	78,33	0,00
Sc	0,9	0,7	0,7	1	0,3	0	0,7	0	0	0,2	0,9	0	1,2	0,1	0,7	0,2	0,6	0,3	0
V	19,3	36,7	36,4	18,1	51	23,5	87,4	66,6	32,1	42,1	344,3	50,9	111,8	38,9	332,8	46,5	77,3	45,5	0,8
Cr	1287,4	1617,5	4437,5	3244	2355	4031	1875,7	204,3	2626,5	1995,1	117,1	2721,7	287,2	2054,1	71,5	2961,9	1319,5	1315,4	4,9
Co	11,4	19,3	27,1	22,3	29,7	30	26,7	46,7	27,9	22,7	27,5	17,1	17,7	27,5	27,4	25,3	21,5	20,3	1,2
Ni	1208,6	1102,2	5142,9	4427,4	1869	5451,7	1373	0	3709,8	2270	79,7	3287	207,7	6721,6	105	2952,9	2207	3789,4	6,7

Cu	3,3	0	0	0	0,2	0,2	0	1408,8	15	17,4	220,7	17,3	84	0	0	11,1	83,3	32,3	9,2
Zn	28,1	20,8	79,8	65,6	104,3	89,1	106,3	5,9	58,6	47,9	131,4	63,5	89,2	60,1	76,7	61,6	90,8	100,9	1,5
Ga	3,8	4,3	2,8	3,3	4,3	3,1	7,6	2,9	4,1	3,1	13,6	3,9	9,5	3,5	16,2	6,2	6,9	4,7	3,3
Ge	1,2	1,4	1,2	1,2	1,2	1,2	1,2	1,8	1,3	1,4	1,2	1,2	1,2	1,2	1,2	1,5	1,2	1,2	1,2
As	2,4	2,8	2,4	1,3	0,9	3	0	0,1	3,7	4,5	0,8	9,4	0,9	0,6	0,5	1	0,2	0,6	0,7
Rb	5,6	4,2	9,7	5,4	12,1	7,2	9,3	19,5	11,2	9,6	32,1	5	8	11,1	17	9,1	9	7,5	0,8
Sr	57,1	23,5	23,7	39,5	7,9	1,1	10,4	14,4	3	14,5	128,7	4,2	185,1	1,9	60,8	6,6	24,2	28,2	4,8
Y	3,5	2,4	2,1	0,6	2,6	2	5,8	8,9	3	2,1	22,6	2,7	7,8	1,7	25	2,1	5,6	4,8	0

Zr	15,4	9,2	9,2	9,9	7,5	3,8	22,8	23,7	7,2	9,6	126,9	7,6	66,1	10,6	106,1	7,8	23,7	17,2	1,4
Nb	1	1,1	0,9	1,5	0,8	0	1,2	1,5	2,2	1,4	7,4	0,7	2,7	1,2	7,5	0,7	1	0,4	5
Mo	0	0	0,1	0,3	0,1	0,1	0,1	0,2	0,2	0	1,7	0,1	0,1	0,1	0,4	0,1	0	0	0,5
Ag	0,2	0,4	0,3	0,5	0,3	0,4	0,2	0,2	0,4	0,6	0,2	0,4	0,3	0,3	0,2	0,4	0,3	0,4	1,2
Cd	0,1	0,1	0	0,1	0	0	0	0	0	0	0	0	0	0,1	0	0	0	0	0,1
Sn	2,5	2,7	2,3	2,9	2,7	2,8	2,4	1,7	2,7	2,7	2,1	2,9	2	2,7	2,3	2,5	2,2	2,7	3,7
Sb	0,4	0,5	0,3	0,6	0,4	0,6	0,4	0,3	0,3	0,6	0,2	0,7	0,3	0,5	0,4	0,3	0,2	0,2	0
Cs	5,4	5,4	5,4	5,4	5,4	5,4	5,4	5,4	5,4	5,4	5,4	5,4	5,4	5,4	5,4	5,4	5,4	5,4	11,1

Ba	126,3	158,8	98,9	111,1	168,2	94,8	273,3	224,6	132	164,8	1195,3	117	362,9	180,1	1088,6	166,5	244	170,9	58,3
La	49,3	74,7	124,3	82,4	116,5	106,6	104,3	215,3	113,3	106,1	163,1	76,3	89,4	125,1	158,3	107,3	102,3	94	4,8
W	116,1	107,8	491,8	423,3	181,1	516	132	0	357,7	218,4	10,7	316,1	21,5	640,8	13,3	284,8	219,1	360,8	0
Ta	0,4	1,2	1,1	1,2	0,3	5,9	0,2	15,5	4,1	0,5	2,7	0,9	1,2	1,4	0,2	0,9	1,2	0,7	0,4
Hf	0	0	0	0	0	1,2	0	155	1,5	0	22,1	2,3	6,1	0	0	3,2	7,7	0	2,1
Tl	0	1,6	2,3	0,2	0,5	0	0	0,4	0	0	0	0	3,7	0	0,3	0,4	1,4	0,3	0
Pb	22,4	25,7	22,6	12	8,1	27,9	0	1,5	34,1	41,8	7,6	87,6	8	5,2	4,2	9,2	2,1	5,4	6,4
Bi	0,5	0,4	0,4	0,5	0,4	0,4	0,4	0,4	0,5	0,4	0,5	0,5	0,4	0,4	0,5	0,5	0,4	0,5	0,4
Ce	0	0	0	0	0	0	4,2	29,8	0	0	128,5	0	14,7	0	104,7	0	0	0	0
Sm	0	8,3	35,6	14,1	27,2	18,6	20,5	88,2	24,2	18,5	46,8	9,9	7,7	24,6	41,5	20,7	12,7	12,5	0
Eu	1,3	1,6	2,6	2	2,7	2,4	2,2	1,7	2,4	2,6	1,9	1,4	1,4	2,3	1,7	1,7	1,8	1,9	0
Gd	25,3	33,2	78,8	48,1	56,7	60,4	46	74,5	55,9	51,3	47,4	43,6	27,1	56,5	45,8	53	43,1	41,2	0
Tb	1,4	2,6	3,2	2,8	4	3,8	3,6	6,4	3,6	2,7	3,5	2,1	2,3	3,2	3,5	3,2	2,6	2,5	0,2
Dy	15,5	21,9	37,9	26	35,3	32	31,8	63	34,9	31	41	23,5	26,2	37,4	40,6	31,7	30,8	28,1	1,5
Er	2,5	16,6	5,9	4,8	26,4	24,2	23,7	46,6	26	4,9	6,1	3,7	3,9	6	6,1	5,5	4,7	4,4	1,1

Yb	428,2	393,9	1810,1	1555,4	667,1	1915,3	492,6	23,7	1309	805,1	45,4	1156,6	83,7	2360,5	54,1	1043,6	783	1333,8	3
Th	10,6	3,9	51,2	1,8	46,7	5	5,7	14,8	6,2	5,6	64	4,3	31,4	50,1	11	6,5	39,8	5	0
U	0	4,3	9,9	0,8	12,3	7,3	0,5	25	11,4	9,8	3,5	5,1	0,8	11,3	17,3	1,1	1,5	7,7	0
S	14,7	7,1	31,7	82,3	0	38,5	23,7	1569,2	1,1	30,1	175,4	6,5	19,1	41,5	1	83,4	35,8	15,3	0

Appendix C: Magnesite Geochemical Data

Sample	**M1 S1**	**M1 S2**	**M1 S3**	**M1 S4**	**M1 S5**	**M1 S6**	**M1 S7**	**M1 S8**	**M1 S9**	**M1 S10**	**M2 S1**	**M2 S2**	**M2 S3**	**M2 S4**	**M2 S5**	**M2 S6**	**M2 S7**	**M2 S8**	**M2 S9**	**M2 S10**
SiO_2	9,86	7,26	7,34	9,93	6,7	8,3	7,98	9,85	8,05	6,44	6,63	6,34	6,35	6,6	8,21	7,3	7,51	10,24	9,7	7,65
TiO_2	0,002	0,002	0	0,001	0,002	0	0,001	0,002	0	0	0,001	0	0	0,002	0	0	0	0	0	0
Al_2O_3	0	0	0	0	0	0	0	0	0	0	0	0	0	0	0	0	0	0	0	0
Fe_2O_3	0,14	0,2	0,1	0,07	0,04	0,15	0,25	0,24	0,18	0,13	0,15	0,15	0,07	0,17	0,16	0,05	0,24	0,15	0,16	0,05

MnO	0,002	0,005	0,003	0	0,001	0,004	0,007	0,009	0,005	0,003	0,003	0,002	0,001	0,004	0,007	0,001	0,015	0,003	0,005	0,001
MgO	51,90	52,24	53,08	52,06	55,15	53,18	53,15	52,29	52,06	54,61	54,04	56,82	54,87	57,28	55,04	54,76	54,93	54,38	53,69	54,65
CaO	1,5	3,39	2,72	2,08	0,75	1,44	3,4	1,94	4,57	0,59	2,14	0,58	0,92	0,92	1,51	1,75	2,07	1,06	0,94	1,79
Na_2O	0	0	0	0	0	0	0	0	0,045	0	0	0	0	0	0	0	0	0	0	0
K_2O	0	0	0,01	0	0	0	0	0,02	0	0,01	0	0	0	0,01	0	0,01	0	0	0	0
P_2O_5	0,029	0,063	0,052	0,038	0,015	0,029	0,063	0,037	0,086	0,011	0,041	0,011	0,017	0,017	0,028	0,032	0,037	0,007	0,005	0,032
Sc	0,1	0,3	0,3	0,2	0,1	0,1	0,3	0,2	0,4	0	0,2	0,1	0,1	0,1	0,1	0,2	0,2	0,1	0,1	0,2
V	0,9	0	0	0	3,4	0	0	1,2	0	0	2,1	0	0	0	0	0	0	0	0	0
Cr	7	35,6	5,1	4,5	3,4	10,5	33,7	48,3	42,3	9,3	19,8	13,9	9,5	6,4	27,3	1,9	36	12	14,3	6,6
Co	0,4	0,6	0,3	0,2	0	0,4	0,8	0,6	0,4	0,4	0,4	0,5	0,1	0,4	0,4	0,7	3,9	0,4	0,4	0,2
Ni	1389,1	2201,4	2044,4	1293,2	1028,6	2049,7	2326,5	2239,4	1194,5	580,8	1300,8	514,8	833,6	1200,9	3929,9	978,3	3092,9	1180,4	1196,4	1002,5

Cu	10,8	16,8	14,2	13,1	15,8	13,7	12,4	12,5	14,5	20,1	15,8	16,5	14,2	19,9	14,4	16	18,4	13,2	14,3	18,9
Zn	2,7	2,6	0	0	1,6	1,6	1,6	4,1	2,1	1,4	2,1	1	1,6	0	6,8	1,4	4,6	0	2,7	0
Ga	3,6	5	3,1	4,3	4,9	4,4	3,4	1,8	4,6	3,7	0,7	5,6	5,9	3,7	3,6	3,9	4,9	5,4	5,1	6,1
Ge	1,5	1,5	1,2	1,2	1,2	1,4	1,2	1,2	1,8	1,2	1,2	1,4	1,2	1,2	1,5	1,2	1,2	1,2	1,8	1,2
As	0,2	0	0	0	0	0	0	0,6	0	0,7	0,4	0,2	0	0	0	0,2	0	0,3	0,2	0
Rb	2,7	0	1,3	1,6	1,6	2,4	0	0,6	1,4	6,1	0	2,4	1,5	0,8	1,6	0	0	1,1	0	2,7
Sr	20,1	40	35,6	18,1	15,7	23,5	39,3	28,3	65	8,3	33,8	6,6	15,7	15,1	25,9	25,6	33,5	20,8	15,9	28,4

Y	1,9	1,6	0	0	1,1	0,7	0	1,2	0	0	0	0	0	0	0	1,7	0	1,4	0,8	1,5
Zr	3,5	6,8	5,5	4,9	3,2	1,8	6,2	3,6	10,3	3,2	4,3	3,2	1,7	3,4	2,9	4,9	3,2	2,9	0,9	3,6
Nb	0	0	0	0	2,3	0,7	1,3	0	0	0	1,7	1,9	0	0	0	0,7	0	0	1,3	2,3
Mo	0,1	0	0	0	0	0,3	0,2	0	0,1	0	0	0,2	0,1	0,2	0	0,1	0,1	0	0	0,2
Ag	2,3	1,3	1,1	2,2	1,1	1,1	1,9	2,3	1	1,4	0,5	1,4	0,7	1,4	1,1	1,2	1,2	1,1	1,1	0,9
Cd	0,1	0,2	0,2	0,1	0,1	0,2	0,1	0,1	0,1	0,1	0,1	0,1	0,1	0,1	0,1	0,1	0,1	0,1	0,1	0,2
Sn	4,5	4	5,2	4,2	4,5	4,6	3,3	3,8	4,1	4,4	4,7	4,3	4,7	4,6	4,3	4,7	4,9	3,9	4,3	5
Sb	0,4	0,2	0	0	0,2	0	0,4	0	0	0	0,3	0	0	0	0,3	0,2	0,2	0	0	0,2
Cs	5,4	5,4	10,4	5,4	5,4	5,4	5,4	5,4	5,4	8,4	5,4	5,4	5,4	5,4	5,4	5,4	5,4	5,4	5,4	5,4
Ba	58,5	58,5	58,5	58,5	58,5	58,5	58,5	59,6	58,5	58,5	58,5	58,5	58,5	60,1	58,5	58,5	58,5	59,9	58,5	59,5
La	0	2	0	0	0,9	1,2	1,8	1,7	0	1,1	0,6	0,7	0	0	1,5	0	1,1	0	0,6	0
W	10,4	218,6	200,3	122,8	102,8	194	222,9	212,8	113,6	54,6	11,1	4,1	75,9	10,4	376,5	6,5	23,3	119,9	116,1	100,2
Ta	1,5	2,5	0,5	0,5	0,5	2,2	0,5	2,4	0,5	0,5	0,5	0,5	0,5	0,5	1,2	0,5	3,4	0,5	0,5	0,5
Hf	0	5,6	2	0	0	1,8	4,1	0	2,3	1,4	1,6	3,2	1,5	3,9	3,5	3,2	4,7	3,6	1,8	0
Tl	0,4	0	0	0,7	0	0	0	0,6	0	0,4	0	0	0	0	0	0,3	0	0,3	0	0
Pb	1,9	0	0	0	0	0	0	5,3	0	5,4	3,1	0	0	0	0	0	0	2,5	1,9	0
Bi	0,4	0,4	0,4	0,4	0,4	0,4	0,4	0,4	0,4	0,4	0,4	0,4	0,4	0,4	0,4	0,4	0,5	0,4	0,5	0,4
Ce	0	0	0	0	0	0	0	0	0	0	0	0	0	0	0	0	0	0	0	0
Sm	0	0	0	3	0	0	0	0	0	0	0	4,5	0	0	0	0	4,3	0	0	0
Eu	0	0,1	0	0	0	0	0,1	0,1	0	0	0	0	0	0	0,1	0	0,2	0	0,1	0
Gd	0	0	0	0	0	0	0	0	0	0	0	0	0	0	0	0	0	0	0	0
Tb	0,1	0,1	0	0	0	0,1	0,1	0,1	0,1	0	0,1	0,1	0	0,1	0,1	0	0,1	0,1	0,1	0
Dy	0,5	0,6	0,3	0,2	0,1	0,5	0,8	0,8	0,6	0,4	0,5	0,5	0,2	0,5	0,5	0,2	0,7	0,5	0,5	0,2
Er	0,3	0,5	0,2	0,2	0	0,4	0,6	0,6	0,4	0,3	0,4	0,4	0,1	0,1	0,1	0,1	0,6	0,1	0,1	0

Yb	484,7	768,1	713,2	451,1	358,8	715,1	811,8	781,4	416,9	202,7	453,9	179,8	290,8	419,1	1370,9	341,3	1079,1	411,9	417,5	349,7
Th	0,9	0	1	1,2	0	0	2,6	0	0	0	0	0	3,8	4,6	0	0	0	1,1	0	1
U	1,1	0,6	0	0,6	0	0,9	0	1,4	0,6	0	0	0	1,5	0	1,7	0	2,4	0,7	0	2,4
S	3,7	4,3	4,7	2,1	1,6	1,4	4,5	2,4	7,8	3,9	6,7	1,2	2,9	3,4	0,5	1,4	6,9	0	2,3	3,5

Appendix D: Correlation matrix for magnesite

	SiO_2	TiO_2	Fe_2O_3	MnO	MgO	CaO	Cr	Co	Ni	Cu	Sr	Ba	Ti	Fe	Mn
SiO_2	1														
TiO_2	0,10	1													
Fe_2O_3	0,21	0,19	1												
MnO	0,12	-0,01	0,82	1											
MgO	-0,60	-0,20	-0,19	-0,06	1										
CaO	0,10	0,07	0,38	0,28	-0,63	1									
Cr	0,16	0,14	0,82	0,76	-0,36	0,61	1								
Co	-0,04	-0,15	0,50	0,81	0,10	0,14	0,41	1							
Ni	0,21	0,04	0,54	0,72	-0,20	0,34	0,55	0,47	1						
Cu	-0,68	-0,13	-0,12	0,06	0,64	-0,23	-0,15	0,25	-0,21	1					
Sr	0,07	-0,02	0,38	0,36	-0,53	0,95	0,64	0,20	0,37	-0,18	1				
Ba	0,22	0,23	0,11	0,02	0,29	-0,22	-0,01	-0,11	-0,12	0,19	-0,14	1			
Ti	0,10	1,00	0,19	-0,01	-0,20	0,07	0,14	-0,15	0,04	-0,13	-0,02	0,23	1		
Fe	0,21	0,19	1,00	0,82	-0,19	0,38	0,82	0,50	0,54	-0,12	0,38	0,11	0,19	1	
Mn	0,12	-0,01	0,82	1,00	-0,06	0,28	0,76	0,81	0,72	0,06	0,36	0,02	-0,01	0,82	1

Appendix E: Excel sheet used to convert major elements Into elements

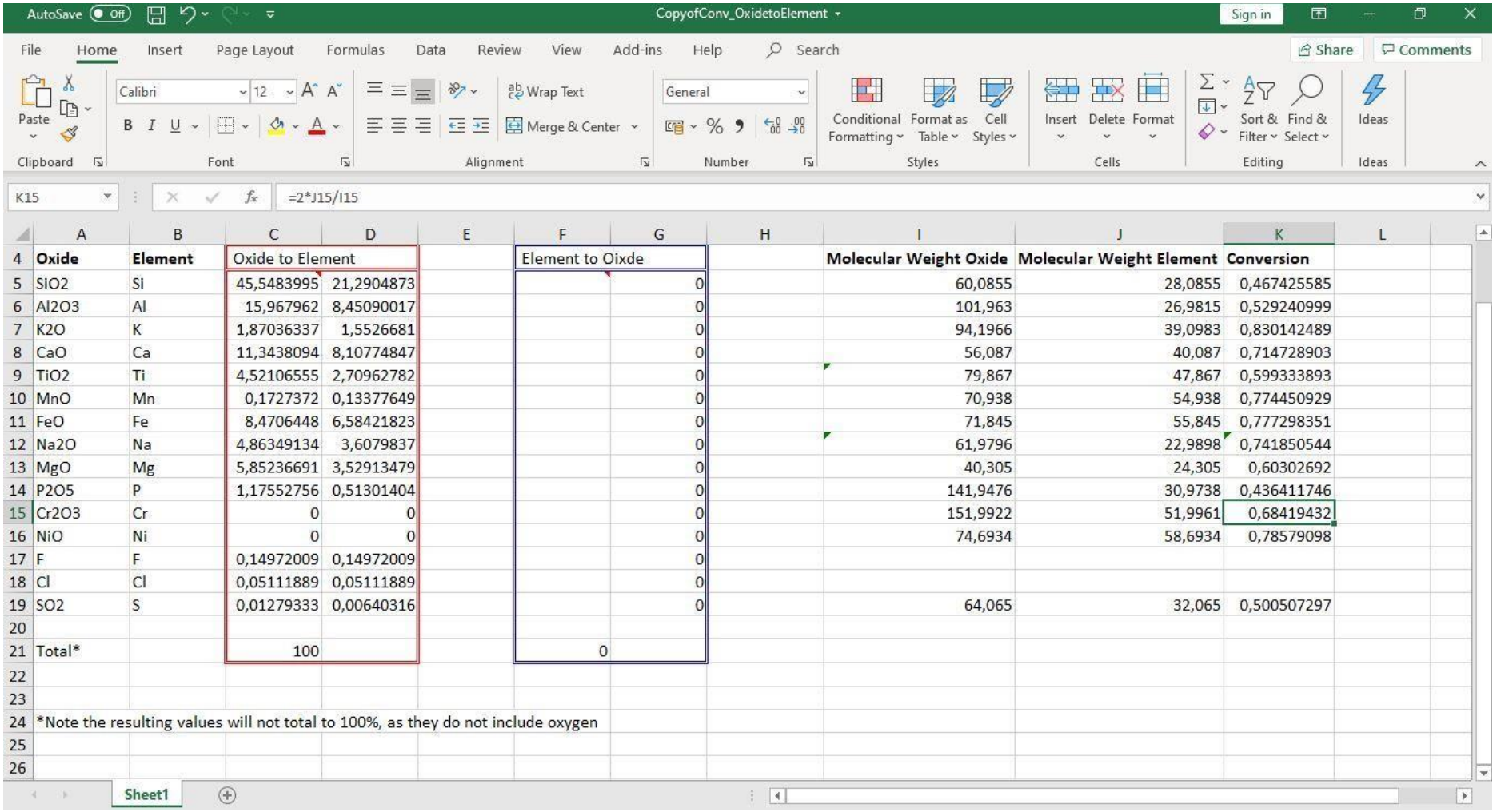

AutoSave Off | CopyofConv_OxidetoElement | Sign in

File Home Insert Page Layout Formulas Data Review View Add-ins Help Search | Share | Comments

Paste | Calibri 12 | Wrap Text | General | Conditional Formatting | Format as Table | Cell Styles | Insert | Delete | Format | Sort & Filter | Find & Select | Ideas

Clipboard | Font | Alignment | Number | Styles | Cells | Editing | Ideas

K15 =2*J15/I15

	A	B	C	D	E	F	G	H	I	J	K	L
4	**Oxide**	**Element**	Oxide to Element			Element to Oixde			**Molecular Weight Oxide**	**Molecular Weight Element**	**Conversion**	
5	SiO2	Si	45,5483995	21,2904873			0		60,0855	28,0855	0,467425585	
6	Al2O3	Al	15,967962	8,45090017			0		101,963	26,9815	0,529240999	
7	K2O	K	1,87036337	1,5526681			0		94,1966	39,0983	0,830142489	
8	CaO	Ca	11,3438094	8,10774847			0		56,087	40,087	0,714728903	
9	TiO2	Ti	4,52106555	2,70962782			0		79,867	47,867	0,599333893	
10	MnO	Mn	0,1727372	0,13377649			0		70,938	54,938	0,774450929	
11	FeO	Fe	8,4706448	6,58421823			0		71,845	55,845	0,777298351	
12	Na2O	Na	4,86349134	3,6079837			0		61,9796	22,9898	0,741850544	
13	MgO	Mg	5,85236691	3,52913479			0		40,305	24,305	0,60302692	
14	P2O5	P	1,17552756	0,51301404			0		141,9476	30,9738	0,436411746	
15	Cr2O3	Cr	0	0			0		151,9922	51,9961	0,68419432	
16	NiO	Ni	0	0			0		74,6934	58,6934	0,78579098	
17	F	F	0,14972009	0,14972009			0					
18	Cl	Cl	0,05111889	0,05111889			0					
19	SO2	S	0,01279333	0,00640316			0		64,065	32,065	0,500507297	
20												
21	Total*		100			0						
22												
23												
24	*Note the resulting values will not total to 100%, as they do not include oxygen											
25												
26												

Sheet1

Appendix F: XRD Diffractogram for analysed rocks and magnesite XRD

Diffractogram for MR2 Rock sample.

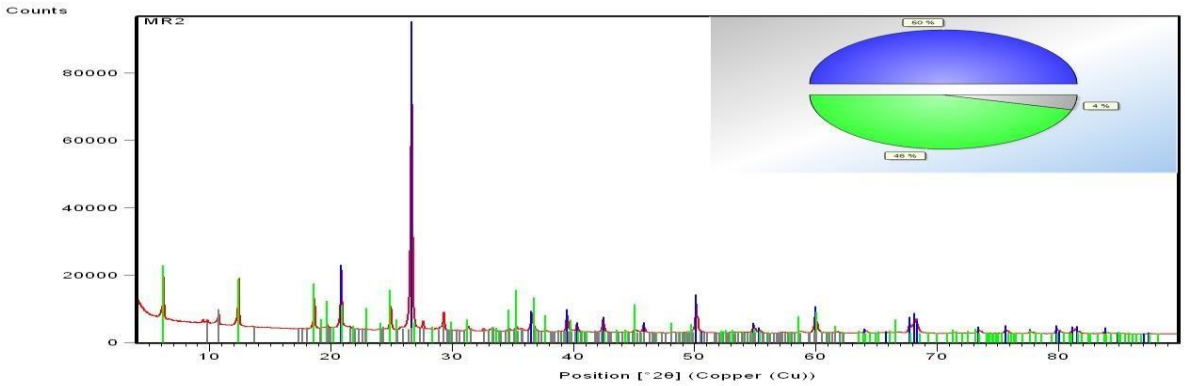

XRD Diffractogram for HR4-M2 Rock sample.

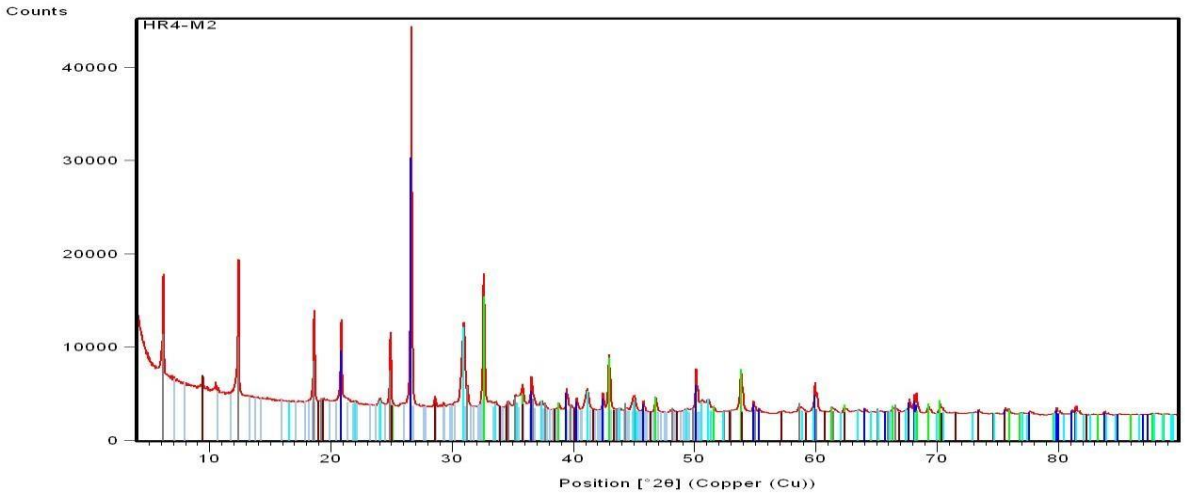

XRD Diffractogram for M2R5 Rock sample.

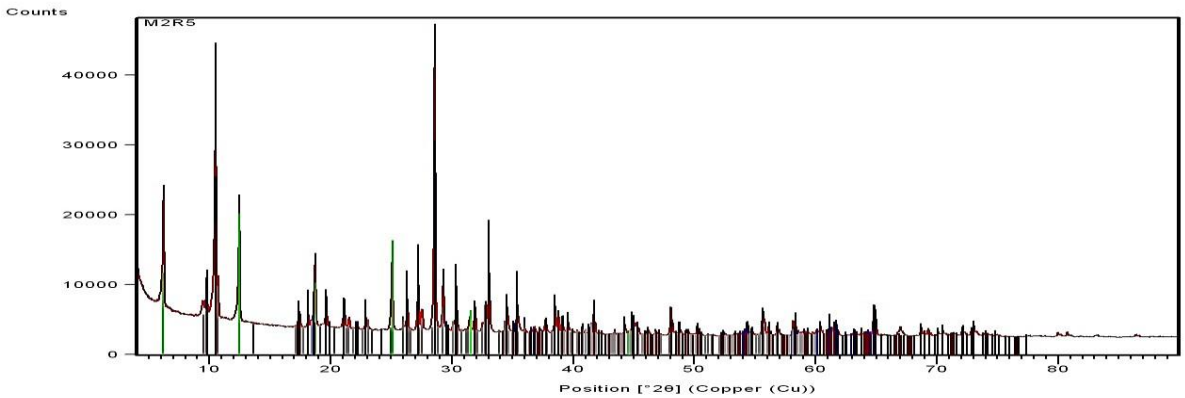

3 Rock sample.

XRD Diffractogram for MR

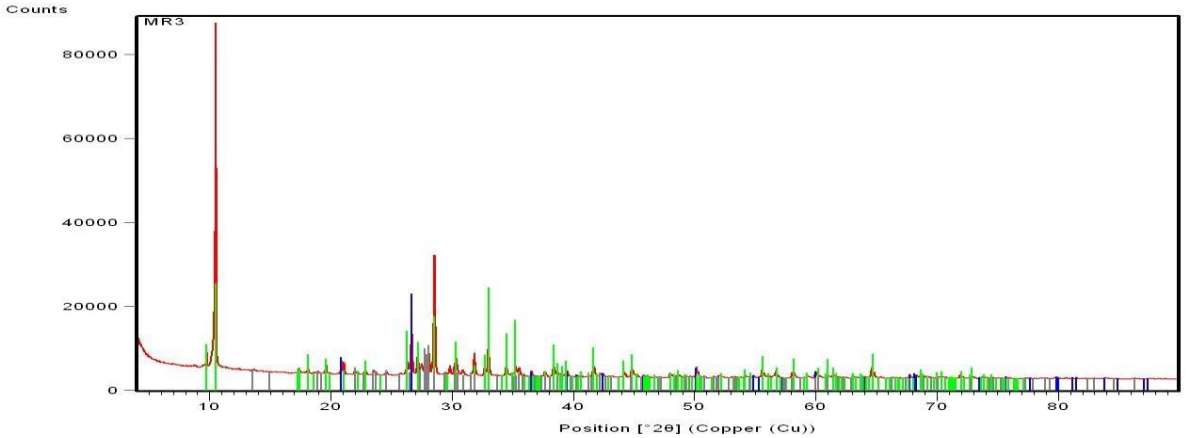

XRD Diffractogram for MR4 Rock sample.

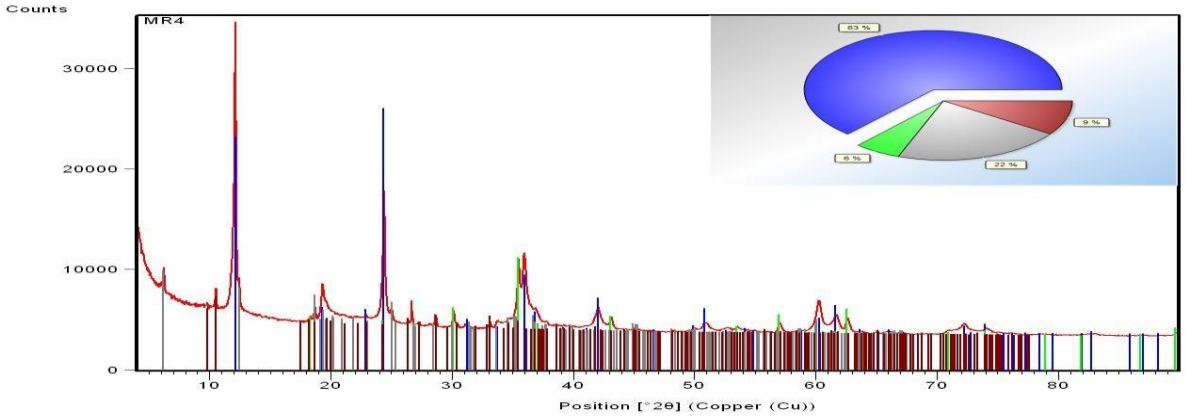

XRD Diffractogram for MR6 Rock sample.

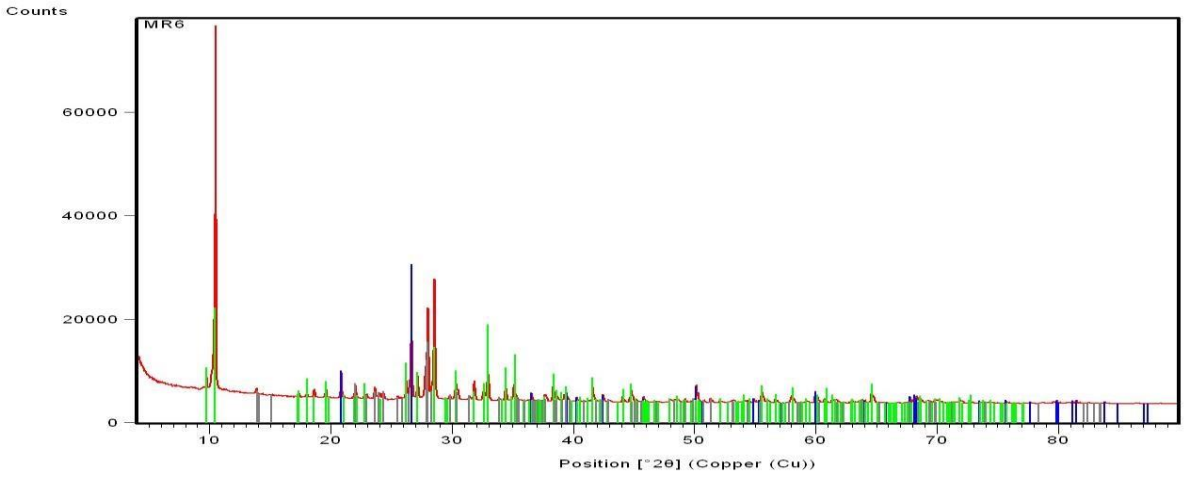

7 Rock sample.

XRD Diffractogram for MR

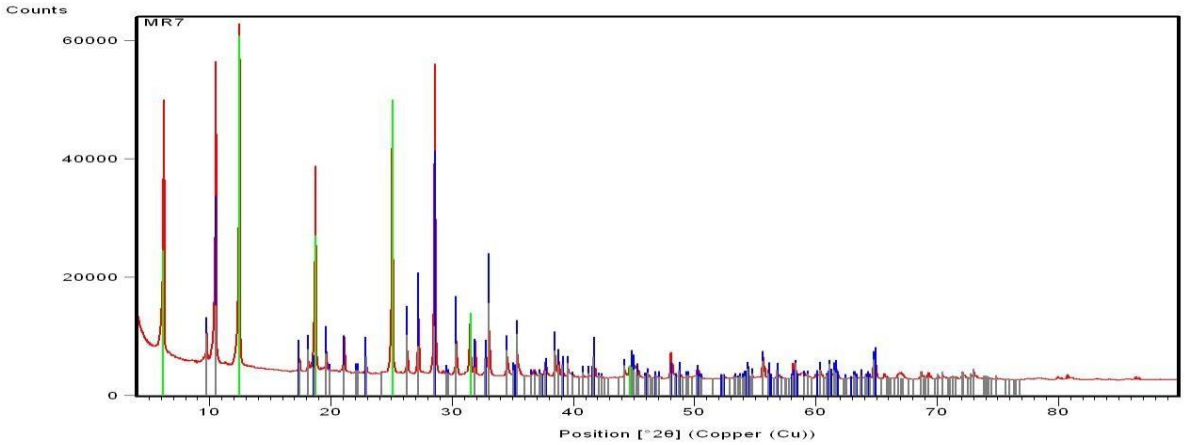

XRD Diffractogram for MR8 Rock sample.

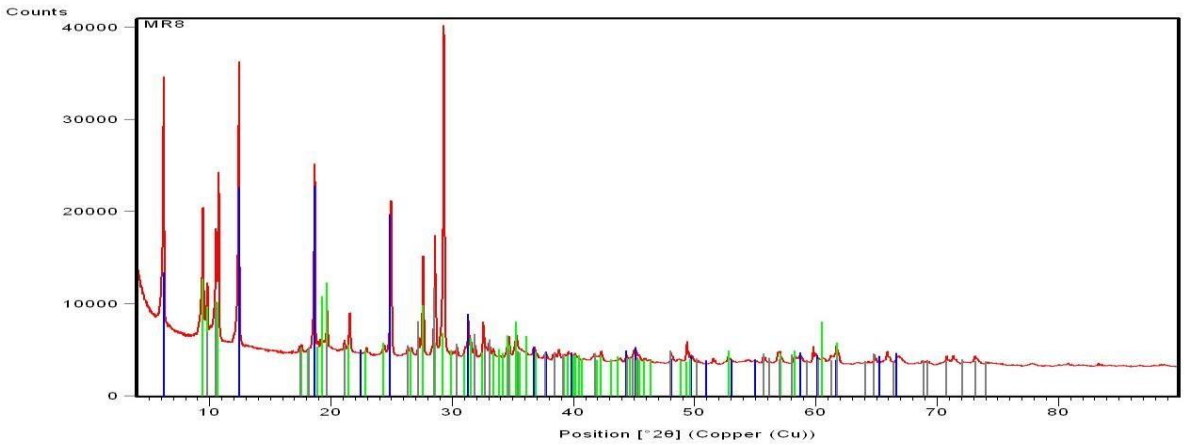

XRD Diffractogram for MR9 Rock sample.

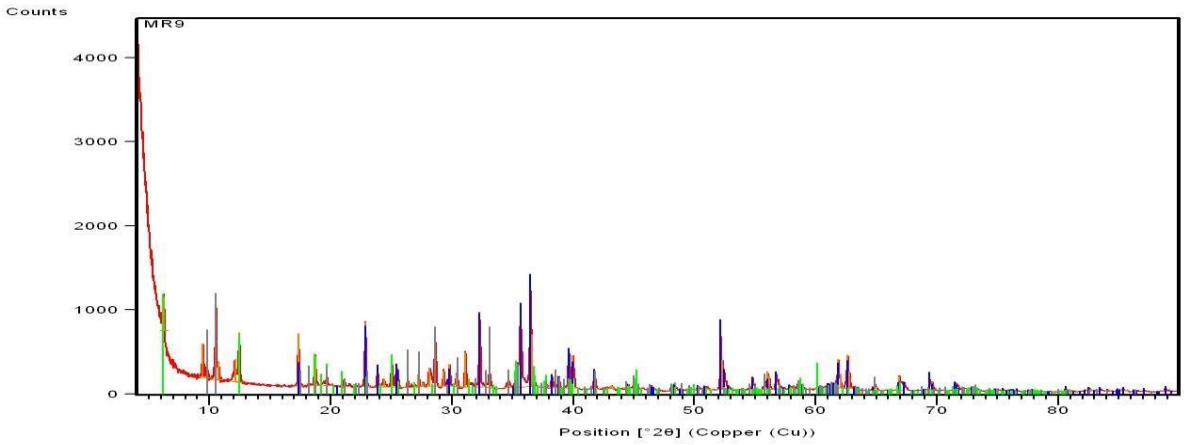

10 Rock sample.

XRD Diffractogram for MR

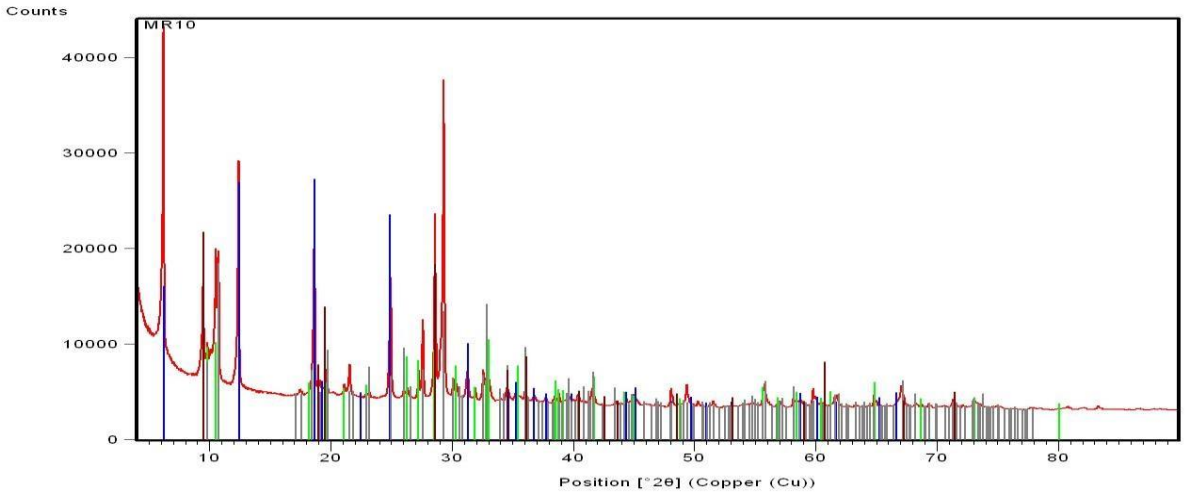

XRD Diffractogram for T1S1 Rock sample.

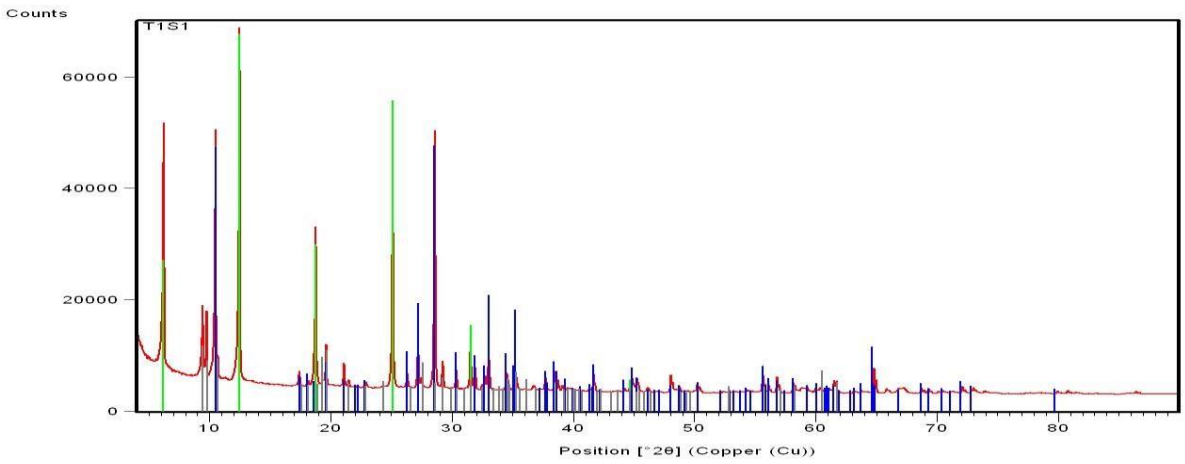

XRD Diffractogram for M2S3 Rock sample.

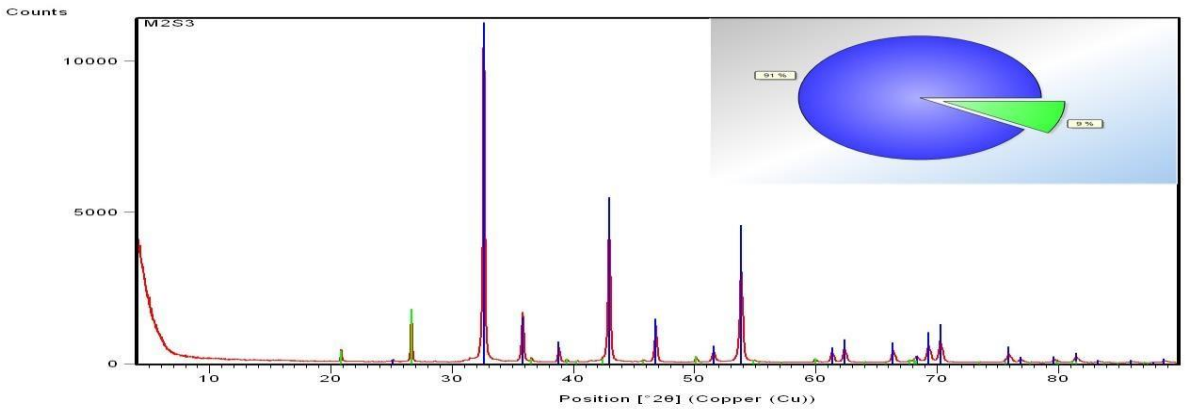

Diffractogram for M1S1 Rock sample.

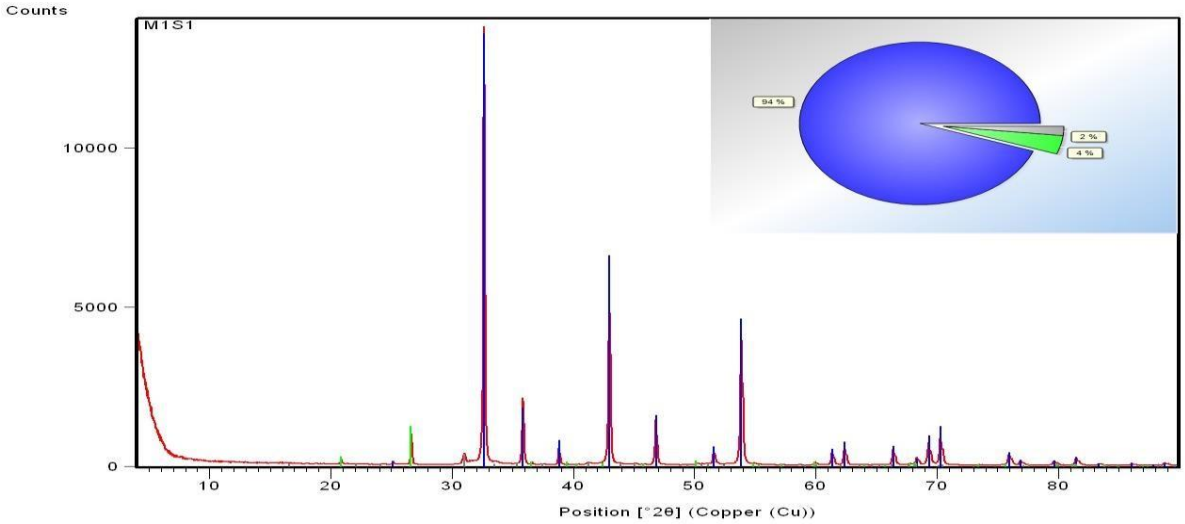

XRD Diffractogram for HR3-M2 Rock sample.

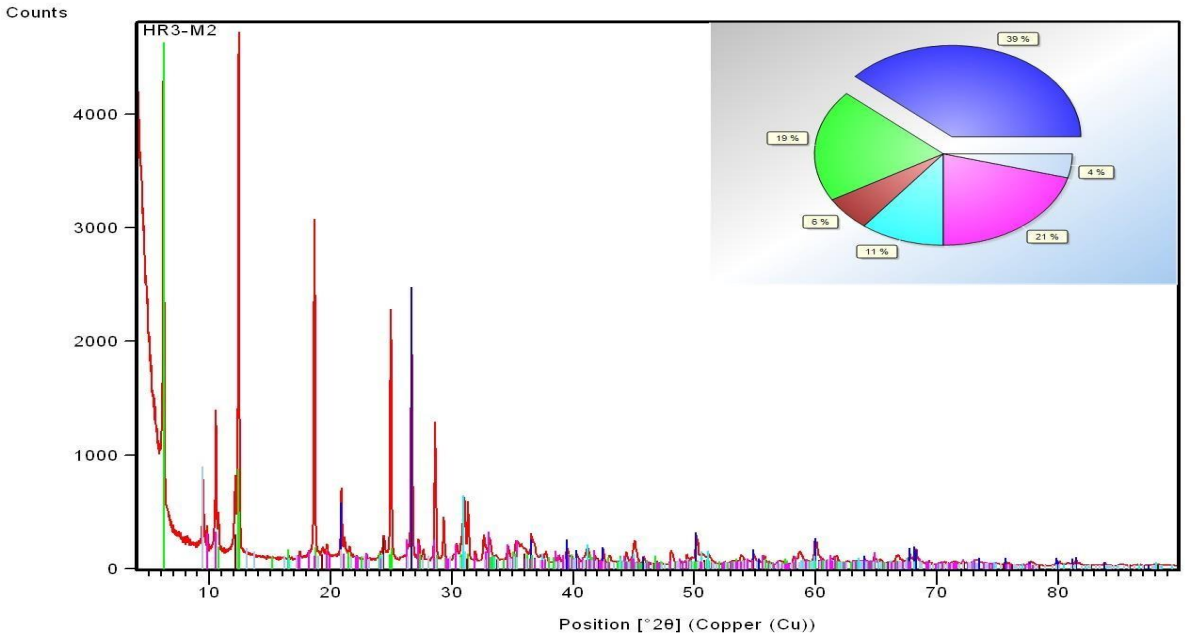

XRD

Appendix G: UNIVEN research ethics certificate

RESEARCH AND INNOVATION
OFFICE OF THE DIRECTOR

NAME OF RESEARCHER/INVESTIGATOR:
Mr T Chauke

Student No:
11622901

PROJECT TITLE: **Geology and geochemistry of Muyexe Magnesite deposit, Giyani Greenstone Belt, Limpopo Province, South Africa.**

PROJECT NO: **SES/19/MEG/01/2305**

SUPERVISORS/ CO-RESEARCHERS/ CO-INVESTIGATORS

NAME	INSTITUTION & DEPARTMENT	ROLE
Prof JS Ogola	University of Venda	Supervisor
Ms HR Mundalamo	University of Venda	Co - Supervisor
Mr T Chauke	University of Venda	Investigator – Student

ISSUED BY:
UNIVERSITY OF VENDA, RESEARCH ETHICS COMMITTEE

Date Considered: May 2019
Decision by Ethical Clearance Committee Granted
Signature of Chairperson of the Committee: .....
Name of the Chairperson of the Committee: Senior Prof. G.E. Ekosse

UNIVERSITY OF VENDA
DIRECTOR
RESEARCH AND INNOVATION
2019-06-10
Private Bag X5050
Thohoyandou, 0950

University of Venda
PRIVATE BAG X5050, THOHOYANDOU, 0950λ LIMPOPO PROVINCEλ SOUTH AFRICA
TELEPHONE (015) 962 8504/8313 **FAX** (015) 962 9060
"A quality driven financially sustainable, rural-based Comprehensive University"